

Status of Simulation Capability of 3D System-scale Thermal- hydraulic (TH) Analysis Codes

Unclassified

English text only

27 May 2024

**NUCLEAR ENERGY AGENCY
COMMITTEE ON THE SAFETY OF NUCLEAR INSTALLATIONS**

**Status of Simulation Capability of 3D System-scale Thermal-hydraulic (TH)
Analysis Codes**

This document is available in PDF format only.

JT03544485

ORGANISATION FOR ECONOMIC CO-OPERATION AND DEVELOPMENT

The OECD is a unique forum where the governments of 38 democracies work together to address the economic, social and environmental challenges of globalisation. The OECD is also at the forefront of efforts to understand and to help governments respond to new developments and concerns, such as corporate governance, the information economy and the challenges of an ageing population. The Organisation provides a setting where governments can compare policy experiences, seek answers to common problems, identify good practice and work to co-ordinate domestic and international policies.

The OECD member countries are: Australia, Austria, Belgium, Canada, Chile, Colombia, Costa Rica, Czechia, Denmark, Estonia, Finland, France, Germany, Greece, Hungary, Iceland, Ireland, Israel, Italy, Japan, Korea, Latvia, Lithuania, Luxembourg, Mexico, the Netherlands, New Zealand, Norway, Poland, Portugal, the Slovak Republic, Slovenia, Spain, Sweden, Switzerland, Türkiye, the United Kingdom and the United States. The European Commission takes part in the work of the OECD.

OECD Publishing disseminates widely the results of the Organisation's statistics gathering and research on economic, social and environmental issues, as well as the conventions, guidelines and standards agreed by its members.

NUCLEAR ENERGY AGENCY

The OECD Nuclear Energy Agency (NEA) was established on 1 February 1958. Current NEA membership consists of 34 countries: Argentina, Australia, Austria, Belgium, Bulgaria, Canada, Czechia, Denmark, Finland, France, Germany, Greece, Hungary, Iceland, Ireland, Italy, Japan, Korea, Luxembourg, Mexico, the Netherlands, Norway, Poland, Portugal, Romania, Russia (suspended), the Slovak Republic, Slovenia, Spain, Sweden, Switzerland, Türkiye, the United Kingdom and the United States. The European Commission and the International Atomic Energy Agency also take part in the work of the Agency.

The mission of the NEA is:

- to assist its member countries in maintaining and further developing, through international co-operation, the scientific, technological and legal bases required for a safe, environmentally sound and economical use of nuclear energy for peaceful purposes;
- to provide authoritative assessments and to forge common understandings on key issues as input to government decisions on nuclear energy policy and to broader OECD analyses in areas such as energy and the sustainable development of low-carbon economies.

Specific areas of competence of the NEA include the safety and regulation of nuclear activities, radioactive waste management and decommissioning, radiological protection, nuclear science, economic and technical analyses of the nuclear fuel cycle, nuclear law and liability, and public information. The NEA Data Bank provides nuclear data and computer program services for participating countries.

This document, as well as any data and map included herein, are without prejudice to the status of or sovereignty over any territory, to the delimitation of international frontiers and boundaries and to the name of any territory, city or area.

Corrigenda to OECD publications may be found online at: www.oecd.org/about/publishing/corrigenda.htm.

© OECD 2024

You can copy, download or print OECD content for your own use, and you can include excerpts from OECD publications, databases and multimedia products in your own documents, presentations, blogs, websites and teaching materials, provided that suitable acknowledgement of the OECD as source and copyright owner is given. All requests for public or commercial use and translation rights should be submitted to neapub@oecd-nea.org. Requests for permission to photocopy portions of this material for public or commercial use shall be addressed directly to the Copyright Clearance Center (CCC) at info@copyright.com or the Centre français d'exploitation du droit de copie (CFC) contact@cfcopies.com.

COMMITTEE ON THE SAFETY OF NUCLEAR INSTALLATIONS

The Committee on the Safety of Nuclear Installations (CSNI) addresses the Nuclear Energy Agency (NEA) programmes and activities that support maintaining and advancing the scientific and technical knowledge base of the safety of nuclear installations.

The Committee is a forum for the exchange of technical information and for collaboration between organisations, which can contribute to its activities from their respective backgrounds in research, development and engineering. It has regard to the exchange of information between member countries and safety R&D programmes of various sizes in order to keep all member countries involved in and abreast of developments in technical safety matters.

The Committee reviews the state of knowledge on important topics of nuclear safety science and techniques and of safety assessments, and ensures that operating experience is appropriately accounted for in its activities. It initiates and conducts programmes identified by these reviews and assessments in order to confirm safety, overcome discrepancies, develop improvements and reach consensus on technical issues of common interest. It promotes the co-ordination of work in different member countries that serves to maintain and enhance competence in nuclear safety matters, including the establishment of joint undertakings (e.g. joint research and data projects), and assists in the feedback of the results to participating organisations. The Committee ensures that valuable end-products of the technical reviews and analyses are provided to members in a timely manner, and made publicly available when appropriate, to support broader nuclear safety.

The Committee focuses primarily on the safety aspects of existing power reactors, other nuclear installations and new power reactors; it also considers the safety implications of scientific and technical developments of future reactor technologies and designs. Further, the scope for the Committee includes human and organisational research activities and technical developments that affect nuclear safety.

Acknowledgements

The members of the Nuclear Energy Agency (NEA), the Committee on the Safety of Nuclear Installations (CSNI) and the Working Group on the Analysis and Management of Accidents (WGAMA) acknowledge the significant contributions of those individuals who had a key role in the preparation of this summary report, and those who had a leadership role in the conduct and success of the NEA activity “Status on simulation capability of 3D system-scale thermal-hydraulic (TH) analysis codes”, such as Christophe Herer. Additional thanks are extended to Imogen Ryan for her editorial support.

Leading author

Christophe Herer (IRSN)

Authors

Dominique Bestion (CEA)

Kyungdoo Kim (KAERI)

Philipp Schöffel (GRS)

Valeria Parrinello (NINE)

Anis Bousbia Salah (BelV)

Contributors

Henrique Austregesilo (GRS)

Sebastian Buchholz (GRS)

Aleksandar Delja (CNSC)

Philippe Fillion (CEA)

Pierre Gaillard (FRAMATOME)

Jae Jun Jeong (PUSAN)

Junichi Kaneko (NRA)

Calogera Lombardo (ENEA)

Raphael Pr ea (CEA)

NEA Secretariat

Martin Kissane

Nils Sandberg

Martina Adorni

This report was approved by the 67th meeting of the CSNI in 4-5 June 2020 (as recorded in the “Summary Record of the 67th Meeting of the Committee on the Safety of Nuclear Installations” [NEA/SEN/SIN(2020)2] [not publicly available]) and prepared for publication by the NEA Secretariat.

Table of contents

Executive summary	15
List of abbreviations and acronyms.....	19
1. Introduction	25
1.1. Background.....	25
1.2. Objectives and scope; safety issues with 3D T/H phenomena.....	26
1.3. Related CSNI and international activities	27
1.3.1. Transients, physical phenomena and experimental support	27
1.3.2. Transverse studies	28
1.4. Structure of the report	30
References.....	31
2. Needs of 3D system-scale T/H codes for nuclear safety	34
2.1. Plant types, components and transients.....	34
2.2. Identification of 3D phenomena for selected transients.....	35
2.2.1. Loss-of-coolant accident – large break LOCA.....	35
2.2.1.1. Transient description	35
2.2.1.2 Key processes	40
2.2.1.3 Main 3D phenomena.....	40
2.2.1.4 Known applications and main drawbacks of these applications.....	41
2.2.2. Intermediate and small break LOCA.....	42
2.2.2.1 Transient description	42
2.2.2.2 Key processes	43
2.2.2.3 Known applications	44
2.2.3. Main steam line break	44
2.2.3.1 Transient description	44
2.2.3.2 Key processes	46
2.2.3.3 Known applications	46
2.2.4. Feed water line break	47
2.2.4.1 Description of the transient.....	47
2.2.4.2 Key parameters	47
2.2.4.3 Main 3D phenomena involved.....	48
2.2.4.4 3D applications	48
2.2.5. Pressurised thermal shock (PTS).....	49
2.2.5.1 Description of the transient.....	49
2.2.5.2 Key parameters	50
2.2.5.3 Main 3D phenomena.....	50
2.2.5.4. 3D applications	51
2.2.6. Spent fuel pool loss-of-cooling and LOCA.....	52
2.2.6.1. Description of the transient.....	52

2.2.6.2.	Key parameters to be calculated.....	53
2.2.6.3.	Main 3D phenomena	54
2.2.6.4.	Known applications and main drawbacks of these applications.....	54
2.2.7.	Passive safety systems.....	54
2.2.7.1.	Introduction	54
2.2.7.2.	Phenomena involved in the PSS.....	55
2.2.7.3.	Key parameters.....	59
2.2.7.4.	Main 3D phenomena	59
2.2.7.5.	Known applications.....	60
References.....		61
3.	Physical models.....	64
3.1.	Flow regime identification.....	64
3.2.	Scale-dependent modelling and mesh convergence.....	64
3.3.	Wall friction and singular pressure losses.....	65
3.4.	Interfacial friction	68
3.5.	Wall heat transfer.....	69
3.6.	Interfacial heat transfer	69
3.7.	Turbulence and dispersion.....	69
3.8.	Modelling of the chimney effect and other crossflows.....	70
References.....		72
4.	Implementation of 3D capabilities in 3D system-scale T/H Codes.....	73
4.1.	Approaches	74
4.1.1.	Field equations	74
4.1.2.	Numerical scheme and solution algorithms	75
4.2.	Simplifications and limitations	76
4.3.	Review of 3D system-scale analysis codes.....	77
4.4.	MARS-KS code	78
4.4.1.	Description	79
4.4.2.	Field equations of MULTID component.....	79
4.4.3.	Field equations of the VESSEL component.....	80
4.4.4.	Simplifications and limitations.....	80
4.5.	SPACE code	83
4.5.1.	Governing equations	84
4.5.2.	Simplifications and limitations.....	87
4.6.	ATHLET code	87
4.6.1.	Description	87
4.6.2.	3D model description	89
4.6.3.	Simplifications and limitations.....	92
4.7.	CATHARE code.....	92
4.7.1.	Description	95
4.7.2.	Simplifications and limitations.....	96
References.....		99
5.	Experimental support with 3D capabilities.....	101
5.1.	Separate effects tests	101
5.1.1.	ROCOM	101
5.1.1.1	Objective of the experiment.....	101
5.1.1.2	Description of the test loop.....	101
5.1.1.3	Tests performed	102
5.1.1.4	Application for system code validation	104

5.1.2. INKA.....	104
5.1.2.1 Objective of the experiment.....	104
5.1.2.2 Description of the test loop.....	104
5.1.2.3 Tests performed	106
5.1.2.4 Application for system code validation	106
5.1.3. Upper plenum test facility	106
5.1.3.1 Objective of the experiment.....	106
5.1.3.2 Description of the test loop.....	107
5.1.3.3 Tests performed	109
5.1.3.4 Application for system code validation	111
5.1.4. CCTF and SCTF.....	112
5.1.4.1 Objective of the experiment.....	112
5.1.4.2 Description of the test loop.....	112
5.1.4.3 Test performed.....	116
5.1.4.4 Application for system code validation	118
5.1.4.5 Main advantages and drawbacks of the facility	119
5.1.5. PERICLES 2D.....	120
5.1.5.1 Objective of the experiment.....	120
5.1.5.2 Description of the test loop.....	120
5.1.5.3 Tests performed	121
5.1.5.4 Application for system code validation	122
5.1.6. PRIUS	122
5.1.6.1 Objective of the experiment.....	122
5.1.6.2 Description of the test loop.....	123
5.1.6.3 Tests performed	125
5.1.6.4 Application for system code validation	126
5.1.7. ACOP	126
5.1.7.1 Objective of the experiment.....	126
5.1.7.2 Description of the test loop.....	127
5.1.7.3 Tests performed	131
5.1.7.3 Application for system code validation	132
5.1.8. DYNAS	133
5.1.8.1 Objective of the experiment.....	133
5.1.8.2 Description of the test loop.....	133
5.1.8.3 Tests performed	136
5.1.8.4 Application for system code validation	136
5.1.9. DOBO	137
5.1.9.1 Objective of the experiment.....	137
5.1.9.2 Description of the test loop.....	138
5.1.9.3 Tests performed	142
5.1.9.4. Application for system code validation	143
5.1.10. MIDAS.....	145
5.1.10.1. Objective of the experiment.....	145
5.1.10.2. Description of the test loop.....	146
5.1.10.3. Tests performed	148
5.1.10.4. Application for system code validation	149
5.1.11. PSBT	149
5.1.11.1. Objective of the experiment.....	149
5.1.11.2. Description of the test loop.....	150
5.1.11.3. Tests performed	158
5.1.11.4. Application for system code validation	160
5.1.12. BFBT.....	161

5.1.12.1. Objective of the experiment.....	161
5.1.12.2. Description of the test loop.....	162
5.1.12.3. Tests performed	169
5.1.12.4. Application for system code validation	170
5.1.13. Other test facilities	171
5.1.13.1. PIERO.....	171
5.1.13.2. OMEGA.....	172
5.1.13.3. GRAZIELLA	173
5.1.13.4. AGATE.....	173
5.1.13.5. MR-2/MR-2A atmospheric pressure water loop	174
5.1.13.6. MR-3.....	174
5.1.13.7. Header test facility	175
5.1.13.8. MTF.....	175
5.1.13.9. CREARE	176
5.1.13.10. METERO-V.....	176
5.2. Integral effect tests.....	179
5.2.1. ATLAS	179
5.2.1.1. Objective of the experiment.....	179
5.2.1.2. Description of the test loop.....	179
5.2.1.3. Tests performed	185
5.2.2. ROSA/LSTF.....	187
5.2.2.1. Objective of the experiment.....	188
5.2.2.2. Description of the test loop.....	188
5.2.2.3. Tests performed	190
5.2.2.4. Application for system code validation	194
5.2.2.5. Main advantages and drawbacks of the facility.....	194
5.2.3. LOFT.....	194
5.2.3.1. Objective of the experiment.....	194
5.2.3.2. Description of the test loop.....	195
5.2.3.3. Tests performed	203
5.2.3.4. Application for system code validation	205
5.2.3.5. Main advantages and drawbacks of the facility.....	205
References.....	206
6. Verification and validation matrix for 3D T/H Codes	211
6.1. Verification tests.....	212
6.2. Validation procedure.....	215
6.2.1. MARS-KS code: validation	216
6.2.2. SPACE code: validation.....	217
6.2.3. ATHLET code: validation.....	218
6.2.4. CATHARE code: validation	218
6.3. Examples of code validation prepared by the developers.....	220
6.3.1. Validation cases done for CATHARE	220
6.3.2. Validation cases for MARS-KS	220
Rensselaer Polytechnic Institute (RPI) air-water experiment.....	220
MIDAS bypass tests	223
LOFT L2-5 test.....	227
6.3.3. Validation cases for SPACE.....	233
DYNAS experiment	233
6.3.4. Validation cases for ATHLET	235
6.3.4.1. ROCOM test 1.1	235
6.3.4.2. ROCOM test 2.1	240

6.3.4.3. UPTF test 7	244
6.4. Independent code validation	246
6.4.1. CATHARE 3D natural circulation flow mixing	247
CATHARE modelling	247
Calculation vs. experimental results	248
Conclusion	248
6.4.2. Validation of CATHARE with the SPES-2 facility	250
CATHARE model	250
“2-inch direct vessel injection line break” in SPES	252
Comparison between experimental data and CATHARE results	253
Conclusions	254
Acknowledgements	255
6.4.3. Validation of MARS with the LOFT facility	255
References	257
7. Main challenges to the improvement of 3D capabilities of SYSTH codes	260
7.1. 3D phenomena	260
7.1.1. Flow in the core with radial power distribution	260
7.1.2. Flow in the downcomer	260
7.2. Limitation of PIRT	261
7.3. Field equations and closure laws	262
7.4. Mesh size dependence	262
References	264
8. Recommendations for future R&D activities	265
8.1. Revisiting the PIRT	265
8.2. Physical models	267
8.3. Suggestions for verification and numerical improvements	268
8.4. Suggestions for validation	269
8.4.1. Separate effect validation for 3D applications	270
8.4.2. Combined effect validation for 3D applications	271
8.4.3. Role of multiscale validation	271
References	272
9. Conclusion	273
References	276
10. Glossary	277

List of figures

Figure 2.1. The lower plenum voiding during the blowdown phase of a PWR LB-LOCA	36
Figure 2.2. Ideal sketch of the refill phase of a PWR LB-LOCA with bypass of the ECCS' water	36
Figure 2.3. Contour plot of fluid temperature distribution in downcomer during the refill phase of a LB-LOCA as observed in a UPTF test	37
Figure 2.4. Phenomena in the upper plenum during the refill phase in case of hot leg ECC injection	37
Figure 2.5. Downflow area versus ECC flowrate for UPTF hot leg injection tests	38
Figure 2.6. Sketch of the core reflooding in case of cold leg injection	39
Figure 2.7. Radial transfers during reflooding due to radial power differences	40
Figure 2.8. Core-averaged total power time history for scenario 2 of OECD MSLB benchmark problem	47
Figure 2.9. 1D vs. 3D loop mass flow rates in the loop with inactive SG (loop-A) and the loop with active SG (loop-B) during FWLB+LOOP	49
Figure 3.1. Chimney (right) and diverging (centre) effect phenomena (radial power profiles appear in grey)	71

Figure 4.1. SPACE code interfaces [4.5-4]	84
Figure 4.2. Momentum cells in the SPACE staggered mesh system	87
Figure 4.3. ATHLET code interfaces	89
Figure 4.4. Staggered-grid approach of ATHLET	91
Figure 4.5. Illustration of the nodalisation of a PWR pressure vessel using a 3D module. On the left an old coarse nodalisation; on the right a recent finer nodalisation particularly in the core	93
Figure 4.6. Illustration of a CATHARE advanced pressure vessel 3D modelling [4.7-1]	94
Figure 4.7. Scheme for non-conformal junctions	94
Figure 5.1. The ROCOM facility	102
Figure 5.2. The INKA Facility	105
Figure 5.3. The UPTF Test Facility	109
Primary system (top) and test vessel (bottom)	109
Figure 5.4. Overview of the CCTF	113
Figure 5.5. CCTF core-II pressure vessel	114
Figure 5.6. CCTF pressure vessel cross sections	115
Figure 5.7. Overview of the SCTF	117
Figure 5.8. Cross-section of SCTF core-II pressure vessel	118
Figure 5.9. Reflood phase of CCTF C2-16 test	119
Figure 5.10. The PERICLES 2D experiment	120
Figure 5.11. Boil-up tests of the PERICLES 2D experiment	121
Figure 5.12. Schematic of the test facility (PRIUS-I)	124
Figure 5.13. Geometry of 4x6 rod bundles	124
Figure 5.14. Schematic diagram of test facility	125
Figure 5.15. Experimental setup of PIV-MIR measurement system	125
Figure 5.16. Bird's eye view of ACOP test facility	129
Figure 5.17. Core simulator	129
Figure 5.18. Single pump failed condition flow diagram	130
Figure 5.19. Pressure drop instrumentation network at downcomer and core	131
Figure 5.20. 257 core simulator inlet flow distribution	132
Figure 5.21. Schematic of the test facility	134
Figure 5.22. Design of test section	135
Figure 5.23. Effect of the gap void distribution	136
Figure 5.24. Measured parameters and nozzle definition	136
Figure 5.25. Comparison of visualisation and measured void fraction profile (AB04)	137
Figure 5.26. Main T/H phenomena occurring in APR1400 during LB-LOCA reflood	138
Figure 5.27. Geometry comparison of downcomer: simulated part of APR1400 and test facility	140
Figure 5.28. Schematic diagram of DOBO test facility	141
Figure 5.29. Profile of the channel area averaged void fraction	144
Figure 5.30. Typical local void fraction in the test section	145
Figure 5.31. DVI mode versus standard CLI mode	146
Figure 5.32. T/H phenomena during a reflood period of LB-LOCA in the APR1400	146
Figure 5.33. Schematic diagram of MIDAS test facility	147
Figure 5.34. Schematic diagram of primary piping system	148
Figure 5.35. ECC bypass fraction	149
Figure 5.36. System diagram of NUPEC PWR test	153
Figure 5.37. Test section for rod bundle void distribution measurement facility	154
Figure 5.38. View of simple spacer grid (left), non-mixing vane spacer grid (centre) and mixing vane spacer grid (right)	155
Figure 5.39. Cross-sectional view heater rod	155
Figure 5.40. Void fraction measurement procedure	157
Figure 5.41. Location of thermocouples for test assemblies	158
Figure 5.42. Test assembly and radial power distribution for void distribution measurements	163
Figure 5.43. System diagram of test facility for NUPEC rod bundle test series	164
Figure 5.44. Cross-sectional view of test section	165
Figure 5.45. Cross-sectional view of heater rod	165
Figure 5.46. Unheated rods arrangements in test assembly type 0	166
Figure 5.47. Schematic of the grid spacer (left) and the ferrule spacer design (right)	166
Figure 5.48. Void fraction measurement system	168
Figure 5.49. Void fraction measurement methods	168
Figure 5.50. Location of thermocouples for critical power measurement (C2A assembly)	169
Figure 5.51. Sketch of the PIERO test section	172

Figure 5.52. Radial view of a sketch of METERO-V test section (2 half assemblies with 8x17 unheated rods each)	176
Figure 5.53. Left: 3D view of the METERO-V facility; Right: sketch of METERO-V loop with the vertical test section.	177
Figure 5.54. Schematic diagram of loop connection of ATLAS	180
Figure 5.55. Three-dimensional view of ATLAS	181
Figure 5.56. Schematic diagram of ATLAS reactor pressure vessel	181
Figure 5.57. Schematic diagram of ATLAS steam generator	182
Figure 5.58. Schematic diagram of hybrid SIT of ATLAS	183
Figure 5.59. 2D arrangement of the DC fluid temperature sensors and example of temperature measurement in the ATLAS test	184
Figure 5.60. Distribution of core wall temperature measured in the ATLAS test	184
Figure 5.61. Distribution of liquid level measured in the ATLAS test	185
Figure 5.62. Location of profile thermocouples for measurement of fluid temperature in hot leg	185
Figure 5.63. Location of profile thermocouples for measurement of fluid temperature in plenum of SG	185
Figure 5.64. ATLAS roadmap programme	186
Figure 5.65. Schematic of ROSA/LSTF	189
Figure 5.66. Coolant flow in pressure vessel region at onset of AM action in test 6-1	190
Figure 5.67. Core steam temperature 100s after initiation of AM action in test 6-1	191
Figure 5.68. Primary and secondary pressure and accumulator flow rate in test 6-1	191
Figure 5.69. Primary and secondary pressures, primary loop flow rate, broken cold leg fluid temperature in Test 4	192
Figure 5.70. Primary and secondary pressures, primary loop flow rate, intact cold leg fluid temperature in test 5 [5.2.2-3]	193
Figure 5.71. LOFT containment section view	195
Figure 5.72 LOFT major components in cold leg break configuration	196
Figure 5.73. LOFT reactor vessel and internals arrangement	198
Figure 5.74. LOFT thermo-fluid measurement instrumentation: intact loop	199
Figure 5.75 LOFT thermo-fluid measurement instrumentation: broken loop cold leg	200
Figure 5.76 Reactor vessel downcomer instrument stalk instrument locations	201
Figure 5.77 LOFT core configuration and instrumentation	202
Figure 6.1. Comparison of the radial pressure distribution	213
Figure 6.2. Calculated liquid and vapour velocities in the mid-duct, gravity wave 3D	214
Figure 6.3. Liquid level vs. time for multidimensional component oscillating manometer	215
Figure 6.4. RPI test section and qualitative flow pattern (region (A) bubbly/slug, (B), (D) single-phase, (C) slug, (E) bubbly, (F) bubbly/slug, (G) pure liquid and (H) air-pocket)	221
Figure 6.5. MARS nodalisation of the RPI test section	221
Figure 6.6. MARS-KS simulation results for test 2AN4	222
Figure 6.7. Comparison of void fractions from the RPI test	223
Figure 6.8. MARS-KS nodalisation for the MIDAS test	225
Figure 6.9. Comparison of direct ECC bypass fraction	226
Figure 6.10. Comparison of condensation fraction	226
Figure 6.11. Comparison of water temperature at the lower downcomer	227
Figure 6.12. Results of input deck nodalisation qualification	228
Figure 6.13. Sequence of events for LOFT L2-5	229
Figure 6.14. Model diagram of 3D model for the LOFT vessel	230
Figure 6.15. Comparison of primary pressure of LOFT L2-5 sequence	230
Figure 6.16. Comparison of accumulator liquid level	231
Figure 6.17. Break flowrate through the hot and cold leg side	231
Figure 6.18. Clad temperature at hot rod node four of nine	231
Figure 6.19. MARS nodalisation for the LOFT L2-5 experiment simulation	232
Figure 6.20. Hot rod cladding temperatures at 0.64 m	232
Figure 6.21. Hot rod cladding temperatures at 1.0 m	233
Figure 6.22. SPACE DYNAS nodalisation	234
Figure 6.23. Comparison of void fraction (AC-01)	235
Figure 6.24. Comparison of void fraction (AC-02)	235
Figure 6.25. The 16 azimuthal nodes model: nodalisation of the reactor downcomer (together with the four loops) used for pseudo-3D as well as 3D calculations	237
Figure 6.26. Qualitative comparison of the downcomer temperature field. Left: Four ATHLET models. Right: outer sensor measurement	238
Figure 6.27. Mixing scalar comparison in second top most nodes of the downcomer channels for the DC16 ATHLET models	239
Figure 6.28. Downcomer grid and assignment of 193 core inlet openings to the central channel and two innermost rings of the cylindrical grid	241

Figure 6.29. Comparison of the temperature fields derived from measured data and simulated by means of the 3DLP and BRLP models, in the downcomer and at the core inlet at temporal key points of the experiment	243
Figure 6.30. Average core inlet temperature	243
Figure 6.31. Temperature trends at the CI for channel 6B adjacent to MSLB affected loop	244
Figure 6.32. Temperature trends at the CI for central channel	244
Figure 6.33. The eight segments model nodalisation scheme for the DC and LP	245
Figure 6.34. Mass flow towards the lower plenum at different experimental phases	246
Figure 6.35. 3D CATHARE nodalisation model for the ROCOM vessel	248
Figure 6.36. CATHARE vs. experimental temperature distribution in the downcomer	249
Figure 6.37. CATHARE vs. experimental mixing scalar	250
Figure 6.38. Vessel and loop A nodalisations	251
Figure 6.39. Annular downcomer 3D component	251
Figure 6.40. IRWST nodalisation	252
Figure 6.41. Primary pressure	253
Figure 6.42. Break mass flow rate	253
Figure 6.43. PRHR mass flow rate	254
Figure 6.44. CMTB mass flow rate	254
Figure 6.45. MARS nodalisation for the LOFT L2-5 experiment simulation	255
Figure 6.46. Hot rod cladding temperatures at 0.64 m	256
Figure 6.47. Hot rod cladding temperatures at 1.0 m	256
Figure 8.1. Typical revisited PIRT table	267

List of tables

Table 2.1. PSS phenomena identification	55
Table 4.1. Overview of main features of 3D modules in SYSTH codes	73
Table 4.2. Turbulent length	82
Table 4.3. ATHLET flow models	90
Table 5.1. Design parameters of the ROCOM facility	103
Table 5.2. Geometry parameters of 4x6 rod bundles	123
Table 5.3. Indicative PRIUS-I test matrix	126
Table 5.4. Scaling parameters	128
Table 5.5. Test conditions	132
Table 5.6. Measurement parameter and measuring instrument summary	142
Table 5.7. Test matrix	143
Table 5.8. Range of NUPEC PWR test facility operating conditions	151
Table 5.9. Transient parameters of NUPEC PWR test facility	151
Table 5.10. Test assembly in void distribution measurement	151
Table 5.11. Test assembly in liquid temperature distribution and DNB measurement - Assembly A0	152
Table 5.12. Test assembly in liquid temperature distribution and DNB measurement - Assembly A1, A2 and A3	152
Table 5.13. Test assembly in liquid temperature distribution and DNB measurement - Assembly A4, A8, A11 and A12	153
Table 5.14. Error sources for void measurements	156
Table 5.15. Time required to perform void fraction measurements	156
Table 5.16. Estimated accuracy for DNB measurements	156
Table 5.17. Range of test conditions for steady-state bundle void distribution measurement	159
Table 5.18. Range of initial test condition for transient bundle void distribution measurement	159
Table 5.19. Range of test condition for steady-state fluid temperature distribution measurement	160
Table 5.20. Range of test condition for steady-state DNB measurement	160
Table 5.21. Range of initial test condition for transient DNB measurement	160
Table 5.22. Heater rod structure	162
Table 5.23. Test assembly types for critical power measurements	163
Table 5.24. Specification of X-ray CT scanner	167
Table 5.25. Specification of X-ray densitometer	167
Table 5.26. Estimated accuracy of main process parameters for void distribution measurements	167
Table 5.27. Range of test condition for steady-state bundle void distribution measurement	170
Table 5.28. Range of test condition for steady-state bundle void distribution measurement	170
Table 5.29. Range of test condition for steady-state bundle void distribution measurement	170
Table 5.30. Range of test condition for steady-state bundle void distribution measurement	170

Table 5.31. Test series planned in METERO-V experiment	177
Table 5.32. Test matrix of the ATLAS programme	186
Table 5.34. Major design characteristics of ROSA/LSTF to reference PWR	189
Table 5.35. Dimensional comparison for a PWR and the LOFT facility	197
Table 5.36. LOFT experiment series: 1978-1982	204
Table 5.37. NEA LOFT experiment programme: 1983 – 1985	204
Table 5.38. Initial conditions for the LOFT L2-3 experiment	205
Table 6.1. List of typical verification tests for checking 3D features of SYSTH codes	212
Table 6.2. MARS-KS code assessment problems for MULTID Component	217
Table 6.3. MARS-KS code assessment problems for 3D vessel component	217
Table 6.4. SPACE code assessment problems for 3D component of SPACE	218
Table 6.5. ATHLET code validation cases for 3D model	218
Table 6.6. Examples of SET and IET used for the CATHARE 3D module validation	219
Table 6.7. RPI flow test parameters	220
Table 6.8. Simulation matrix for SPACE validation	233
Table 6.9. Average void fraction error	234
Table 6.10. Initial and boundary conditions for ROCOM test 1.1	236
Table 6.11. Initial and boundary conditions for ROCOM test 2.1	240
Table 6.12. Steam and ECC injection mass flows for UPTF test 7	245
Table 6.13. Boundary conditions of ROCOM runs	247
Table 6.14. Sequence of events	252
Table 7.1. Example of PIRT for validation matrix for large break loss-of-coolant accidents	261
Table 8.1. 3D effects in an uncovered PWR core during a SB-LOCA	266
Table A.1. Geometries simulated with 3D capabilities	288
Table A.2. Transients simulated with 3D capabilities	289
Table A.3. Simulations performed with 3D capabilities	290

Executive summary

Thermal-hydraulic (T/H) transient and accident analyses rely heavily on computer codes to simulate system answers to physical phenomena and engineer safety feature actions. The reliability of the methods and tools used should be fully demonstrated and the approximations, lack of knowledge and an evaluation of the uncertainties identified. Improving the reliability of codes used for T/H analyses is an important objective for both regulators and operators.

All flows are by nature three-dimensional (3D). T/H system codes mostly rely on one-dimensional (1D) models and their validation is mainly based on reduced scaled 1D experiments. In some geometries and within a certain range of given parameters, there may be one predominant flow direction and the 1D approach is sufficient. Nevertheless, for most applications, this approach was used to avoid solving the equations related to complex flows where all dimensions should be considered. Later, in the 1980s, some 3D capabilities were introduced into system codes. However, developed models include an overall contribution of interactions in all dimensions through empirically adjusted coefficients. Simple extrapolation of 1D closure laws to 3D models was used. Yet there is no guarantee that these simplifications will be relevant to all situations.

This report aims to establish the status of current 3D capabilities in T/H system codes, covering all aspects and limitations, including the equations and simplifications considered, the time and space averaging procedures, the closure models and available or needed experimental support. These aspects are organised sequentially. The reasons for developing multidimensional capabilities in T/H system codes are first discussed to illustrate the variety of situations to be covered. The multidimensional phenomena and the general approach for modelling them are then described. These descriptions clarify the general picture, after which the report presents the current situation regarding codes, experiments and validation. The report presents a gap analysis between what is available and what is desirable. Finally, the main challenges are summarised and some proposals on how to tackle them are suggested.

Multidimensional phenomena that can have a significant impact occur in the course of asymmetric design basis accident scenarios, such as a feed water line break (FWLB), main steam line break (MSLB) and loss-of-coolant accident (LOCA). Furthermore, 3D phenomena can play a key role under natural circulation flow regimes, in which flow mixing and stratification are predominant, similar situations occur when passive systems are involved.

The reliability of heat removal passive systems and their components – such as core make-up tanks, passive residual heat exchanger, isolation condenser – is driven by natural circulation and depends on which local 3D phenomena are taking place. These phenomena could be temperature stratification and mixing, heat losses under prolonged transients, competing driving forces, etc.

Another scenario involves pressurised thermal shock in the reactor pressure vessel due to cold water injection in a quasi-stagnant loop condition. A local pressure stress results on the vessel wall, which can lead to crack propagation. This multidimensional phenomenon takes place under thermal stratification and inhomogeneous fluid temperature distribution.

In the case of the spent fuel cooling pool, hundreds of parallel fuel assemblies are stored in the racks. Under such conditions, 3D local vortices and 3D large recirculation structures exist, whereas temperature stratification is possible under a generally stable natural circulation convection regime.

Flow regime, wall and interfacial friction, heat transfer, turbulence dispersion and diffusion are immediately identified as the main topics to be analysed and the approaches for considering them in multidimensional thermal-hydraulic system (SYSTH) codes are presented.

The averaging hypotheses, in time and in space, are key subjects in fluid mechanics simulations. Averaging procedures filter the information and are deeply interrelated with multidimensional phenomena. The closure models are therefore linked to space and time considerations.

This report also considers the crossflows in open geometry, such as in a pressurised water reactor core. Transverse flows are related to the power radial distribution and the pressure losses. These crossflows are fundamentally 3D and require specific treatment to provide a reliable description of the full core. These transverse flows can be beneficial when a chimney effect occurs, with flows converging from the cooler channels into the hotter areas of the core, where the higher power rods also undergo the highest peak clad temperature.

Some typical T/H system codes with 3D capabilities implemented are briefly described in this report, as well as the approaches followed that enable multidimensional simulations, their advantages and drawbacks. The porous medium approach is widely adopted in T/H system codes. Although quite compatible with the geometries encountered in the reactor systems and components, this approach has inherent limitations. The relative importance of the diffusion terms highly depends on the porosity and hydraulic diameters. However, whatever the approach, computed quantities need to be time and space averaged, leading to a limited resolution of space and time variations. The associated very small scales involved in T/H phenomena, and the related computing resources and central processing unit (CPU) cost, mean that there are intrinsic limitations directly linked to the coarse nodalisation. Information on local flow processes (such as turbulence) is lost due to the averaging and has to be compensated by additional modelling. As a result, there are deficiencies due to numerical limitations and unavoidable imperfections of the closure laws. When system codes are used, attention should be paid to the following aspects:

- Many physical phenomena heavily depend on the geometry and the models may only be valid for a specific geometry.
- Closure laws can have large uncertainties due to simplification of the physics and non-modelled phenomena. Although intrinsic limitations will ultimately remain, more accurate models may be required to enhance the reliability of the computation.

Since 1D equations have been modified and extended to 3D, one or more types of multidimensional components or modules have been implemented in current T/H system codes. The available closure laws were developed in association with 1D discretisation and therefore the simplest approach was to directly extend them to multidimensional applications. However, the closure laws are based on measurements in some typical geometries (circular pipe, rod bundle or tube bundle, annuli) and do not cover all situations. Due to their intrinsic origin as an extension of the 1D component equations, the current 3D models have deficiencies. Another option was to consider some terms as non-significant, for example the 3D diffusion terms that are sometimes not present in the 3D model.

From the numerical solution perspective, the temporal discretisation is inherently

connected to the used solution method (implicit or semi-implicit). Although fully-implicit algorithms are more CPU time-consuming to solve, they have some advantages. Another option is to use the operator-splitting approach with a semi-implicit discretisation. The non-iterative semi-implicit methods enable faster calculation (low computational cost of a single time step), yet the time step sizes are limited by the material Courant–Friedrichs–Lewy condition. Time and space averaging procedures are not 3D specific and have already been addressed for the 1D approach. The problem lies in the extension of existing closure laws that are incompatible with 3D modelling.

The growing role of 3D modelling of reactor core and pressure vessel requires additional experimental data for proper validation. Elements on available experimental support, which were used to develop some of the current T/H system codes, are proposed. Some tests were not specifically designed for 3D measurements, but still provide useful information for the validation of the 3D simulations of T/H system codes. More recent tests have larger two-dimensional (2D) or 3D features. The experimental support is presented following the usual typology, separate or integral effect tests (SET and IET). Several test facilities (e.g. upper plenum test facility [UPTF], Loss-of-Fluid Test [LOFT]) are already known to have previously supported the validation of thermal-hydraulic codes; other facilities (e.g. Advanced Thermal-Hydraulic Test Loop for Accident Simulation [ATLAS]) were constructed to support the new generation of nuclear reactors.

The qualification procedure is based on verification and then validation procedures. Typical verification tests for checking the correct implementation of 3D capabilities in the codes are suggested. The validation that was performed on T/H system codes is summarised for each code, which is separated into the validation performed by the code developers and comparisons carried out by independent users. Code developers must demonstrate the validation of their codes alongside an identification of the areas of applications. The bases of their demonstrations are summarised. Independent comparisons provide another illustration of the codes' capability.

The results showed that although the 3D capabilities brought significant improvements compared to 1D usual discretisation, there are several axes for progress. Directions for developments consist of three main parts: (i) the type of geometry in relation to the identification of phenomena and their ranking (PIR), especially in the core, where radial power distribution is a major driver for 3D phenomena, and in the downcomer, because of the highly unsymmetrical geometry in case of broken loop and safety injection; (ii) the terms in the field equations; and (iii) the mesh size dependence.

The first action should be to revisit the PIR to identify the physical models where closure laws showed significant deficiencies. The porous media approach must also be taken into consideration because it globally simulates the real geometry. One of the key issues is with the diffusion/dispersion models.

Ultimately, there is a need for additional validation support. The definition of such experimental need is also associated with the mesh size dependence strategy and the measurement possibilities. The role of multiscale validation is a promising option that requires in-depth analyses to establish the limitations of this approach. Ideally, a solution to cases where local measurements are not feasible would be to evaluate them through computational fluid dynamics (CFD) calculations and then report the values in a coarser thermal-hydraulics system (SYSTH) modelling.

In conclusion, capabilities of the current T/H simulation tools have reached a certain maturity. Although relative improvements can be achieved in 3D capabilities and numerics, significant investments in experimental support and specialists' resources are needed to generate a breakthrough new step. Multiscale validation cannot provide all insights and

therefore experiments should ideally be performed and provide 3D velocity measurements. Steam is indeed preferable to using air as a surrogate. The use of heating rods with adjusted radial distribution would increase transverse velocities – which are key parameters in heat transfer in rod bundles – and consequently increase the reliability of core modelling. Regarding the more theoretical side, the derivation of equations for a porous 3D approach, in two-phase flows, must be documented in detail. All the assumptions and simplifications made must be identified and their treatment justified. Looking beyond the specific case of 3D, ongoing work in numerics and uncertainty qualification should be continued.

List of abbreviations and acronyms

0D	Zero dimension
1D	One dimension
2D	Two dimensions
3D	Three dimensions
ACC	Accumulator
ACOP	Advanced COre flow and Pressure distribution test facilities
ADS	Automatic depressurisation system
ADV	Atmospheric relief valve
AFW	Auxiliary feed water
AHWR	Advanced heavy water reactor
AIS	Accumulator injection system
AL	Affected loop
AM	Accident management
AP-1000	Advanced Pressurised 1000
APR+	Advanced Power Reactor Plus
APR1400	Advanced Power Reactor 1400
ATHLET	Analysis of THERmal-hydraulics of LEaks and Transients
ATHLET- CD	ATHLET core degradation
ATLAS+	Advanced Thermal-Hydraulic Test Loop for Accident Simulation
BDBA	Beyond design basis accident
BDFT	Bidirectional flow tube
BE	Best estimate
BEPU	Best estimate plus uncertainty
BEMUSE	Best-estimate methods uncertainty and sensitivity evaluation
BFBT	BWR Full-size Fine-Mesh Bundle Test
BT	Boiling transition
BTD	Breakthrough detector
BWR	BWR Full-size Fine-Mesh Bundle Test
B&W	Babcock & Wilcox
CALIP	CALibration Loop for Internal Pressure drop
CANDU	Canada Deuterium Uranium

CATHARE	Code for Analysis of THERmalhydraulics during an Accident of Reactor and safety Evaluation
CCC	Containment cooling condenser
CCD	Charge-coupled device
CCTF	Cylindrical core test facility
CD	Core degradation
CEC	European communities
CET	Core exit temperature
CFD	Computational fluid dynamics
CFL	Courant–Friedrichs–Lewy condition
CHF	Critical heat flux
CLI	Cold leg injection
CMFD	Computational multi-fluid dynamics
CMT	Core make-up tank
CPU	Central processing unit
CR	Control rod
CRDM	Control rod drive mechanism
CRGT	Control rod guide tube
CSNI	Committee on the Safety of Nuclear Installations (NEA)
DBA	Design basis accident
DC	Downcomer
DEC	Design extension conditions
DEGB	Double-ended guillotine break
DNB	Departure from nucleate boiling
DNBR	Departure from nucleate boiling ratio
DOBO	DOWNcomer BOiling
DP	Pressure drop
DVI	Direct vessel injection
DWV	Drywell vessel
DYNAS	DYNAMics of Air/water System
EC	Emergency condenser
ECC	Emergency core cooling
ECCS	Emergency core cooling systems
EDF	Electricité de France
ELAP	Extended loss of AC power

EM	Evaluate model
EMDAP	Evaluation model development and assessment process
EOP	Emergency operating procedures
ESBWR	Economic simplified boiling water reactor
FA	Fuel assembly
FLB	Feedwater line break
FPV	Flooding pool vessel
FRAMATO ME	Franco-américaine de constructions atomiques
FRP	Fibre-reinforced plastic
FVM	Finite-volume method
FWLB	Feed water line break
GDIS	Gravity-driven injection system
GIF	Generation IV International Forum
GRS	Gesellschaft für Anlagen- und Reaktorsicherheit gGmbH
HPIS	High pressure injection system
HPSI	High pressure safety injection
HZDR	Helmholtz Centre Dresden Rossendorf
IAEA	International Atomic Energy Agency
IAC	Interface area concentration
IB	Intermediate break
IET	Integral effect test
INKA	INtegral Test Facility KARlstein
IRWST	In-containment refuelling water storage tank
ISP	International standard problems
JAERI	Japan Atomic Energy Research Institute
KAERI	Korea Atomic Energy Research Institute
KEPRI	Korean Electric Power Research Institute
KINS	Korean Institute of Nuclear Safety
LB	Large break
LBE	Lead-Bismuth Eutectic
LES	Large eddy simulation
LHS	Left-hand side
LIF	Laser-induced fluorescence

LOCA	Loss-of-coolant accident
LOCE	Loss-of-coolant experiment
LOOP	Loss of offsite power
LOFT	Loss-of-fluid test
LORHR	Loss of residual heat removal
LPCI	Low pressure coolant injection
LP	Lower plenum
LPI	Low pressure injection
LPSI	Low pressure safety injection
LSTF	Large Scale Test Facility
LWR	Light water reactor
MARS	Multi-dimensional Analysis of Reactor Safety
MARS-KS	Multi-dimensional Analysis of Reactor Safety - Korean Institute of Nuclear Safety
MIDAS	Multi-dimensional Investigation in Downcomer Annulus Simulation
MIR	Matching index of refraction
MOKE	Ministry of Knowledge Economy (Korea)
MOST	Ministry of Science and Technology (Korea)
MOTIE	Ministry of Trade, Industry and Energy (Korea)
MS	Mixing scalar
MSIV	Main steam isolation valve
MSLB	Main steam line break
MTF	Moderator Test Facility
MULTID	Multidimensional
MV	Mixing vane
NC	Natural circulation
NCI	Natural circulation interruption
NEA	Nuclear Energy Agency
NMV	Non-mixing vanes
NRS	Nuclear Reactor Safety
NUPEC	Nuclear Power Engineering Corporation (Japan)
NURESAFE	NUclear REactor SAFETY simulation platform
NURESIM	NUclear REactor SIMulation
ODE	Ordinary differential equation

OECD	Organisation for Economic Co-operation and Development
OPR1000	Optimised power reactor 1000
PAFS	Passive auxiliary feedwater system
PCCS	Passive containment cooling system
PCFS	Passive core flooding system
PCS	Primary coolant system
PCT	Peak clad temperature
PDE	Partial derivative equation
PDF	Probability density function
PE	Polyethylene
PHWR	Pressurised heavy water reactor
PIRT	Phenomena identification and ranking technique (or table)
PIV	Particle image velocimetry
PKL	Primär-Kreislauf
PMCS	Passive moderator cooling system
PORV	Pressure operated relief valve
PRHR	Passive residual heat removal
PRIUS	in-PWR Rod bundle Investigation of Undeveloped mixing flow across Subchannel
PSBT	PWR Subchannel and Bundle Test
PSPV	Pressure suppression pool vessel
PSS	Passive safety system
PTS	Pressurised thermal shock
PT	Pressure transmitter
PV	Pressure vessel
PVC	Polyvinyl chloride
PWR	Pressurised water reactor
PZR	Pressuriser
QA	Quality assurance
RANS	Reynolds Average Navier-Stokes
RCP	Reactor cooling pump
RELAP	Reactor excursion and leak analysis programme
RHRS	Residual heat removal system
RHS	Right-hand side (of an equality)

RIA	Reactivity insertion accident
ROCOM	Rossendorf Coolant Mixing Model
ROSA	Rig-of-safety Assessment
RPI	Rensselaer Polytechnic Institute (RPI) Air-Water Experiment
RPV	Reactor pressure vessel
RTD	Resistance temperature detector
SBO	Station blackout
SCA	Shared cost action
SCR	Silicone controlled rectifier
SCTF	Slab core test facility
SET	Separate effect test
SFP	Spent fuel pools
SG	Steam generator
SGTR	Steam generator tube rupture
SLB	Steam line break
SPACE	Safety and Performance Analysis Code
SIT	Safety injection tank
SRV	Safety relief valve
SS	Simple spacer
SWR	Siedewasserreaktor (BWR German Design)
SWR-1000	Siedewasserreaktor-1000
SYSTH	Thermal-hydraulic system
TIP	Traversing in-core probe
TFD	Thermal fluid dynamic
T/H	Thermal hydraulics
TRACE	TRAC/RELAP Advanced Computational Engine
TRAM	Transient and accident management programme
UPTF	Upper plenum test facility
US NRC	US Nuclear Regulatory Commission
V&V	Verification and validation
VVER	Russian type PWR
WGAMA	Working Group on the Analysis and Management of Accidents
WWER	cf. VVER

1. Introduction

1.1. Background

The evaluation model and computational capabilities required for engineering design and safety analyses of nuclear installations have shown significant progress compared to the first tools established in the 1960s. For the specific case of thermal hydraulics (T/Hs), first-generation codes were based on simple models associated with conservatism intended to cover the lack of knowledge, simplifications and limited computational capabilities and experimental support available at that time. The second generation included the more advanced two-fluid six-equation model, adopted a best-estimate approach and benefited from an extensive experimental programme, which was a significant improvement on the first-generation tools. However, the current tools still have some limitations and deficiencies that industries and regulatory bodies intend to address. Any progress would improve confidence in the safety demonstration and extend the application of these tools to the recently developed components and new systems offered by designers and vendors, such as the systems that rely on passive phenomena.

One of the limitations of the current evaluation tools relates to coarse nodalisation, particularly for three-dimensional (3D) aspects. Besides the loss of information due to averaging procedures, T/H system codes first focused on one-dimensional (1D) models and their validation was mainly based on reduced scaled 1D experiments, although full-height rod bundle tests were available. Large-scale multidimensional effects were identified in pressurised water reactor large break loss-of-coolant accidents (PWR LB-LOCAs) in the 80s and the two-dimensional (2D)-3D international experimental programme provided (e.g. [1-1]) large-scale 3D validation data. Alongside these developments, 3D capabilities were introduced into system codes for the pressure vessel modelling. However, some important questions about the derivation and simplifications of 3D field equations remained unanswered and experimental data was not detailed enough to justify all simplifying assumptions. Many licensing studies used zero-dimensional (0D) and 1D modelling of the pressure vessel sub-components with potential parallel channel modelling of the core and a possible addition of crossflow junctions. Detailed 3D processes are then simplified and only a global validation on full-scale mock-up was proposed for model qualification.

Progress has been made in the last two decades in the 3D modelling of two-phase flow thanks to the development of one-phase and two-phase computational fluid dynamics (CFD) tools and to the improvements of the subchannel analysis modelling and validation. Validation and international benchmarks on PWR Subchannel and Bundle Tests (PSBT) [1-2] and BWR Full-size Fine-Mesh Bundle Test (BFBT) [1-3] rod bundle tests could compare the predictions of PWR and boiling water reactor (BWR) core flow by 1D models, subchannel models and CFD in open medium. These investigations all provided a more precise identification of 3D processes in open medium and porous medium approaches and allowed a revisiting of 3D pressure vessel (PV) models of system codes to better evaluate the capabilities and limitations.

All flows are 3D by nature. However, there can be one predominant flow direction in some geometries and within a certain range of given parameters, with the result that 1D analysis is sufficient. Nevertheless, the 1D approach was initially used even for some applications in complex flows, where all dimensions should be considered. Therefore, the developed models include an overall contribution of interactions from all dimensions through empirically adjusted coefficients associated to a particular geometry. For example, the

complex 3D flow phenomena in a PWR downcomer during a large break loss-of-coolant accident (LB-LOCA) refill phase was first treated in 1D with some tuning of interfacial friction and condensation models, with many other 3D processes not being explicitly considered. 2D downcomer modelling was then used to take the azimuthal flow repartition into account for the LB-LOCA refill phase. Following the development of 3D capabilities in T/H system codes, simple extrapolation of 1D closure laws to 3D models was used instead. This method provided reasonably good results. For example, the simulation of core reflooding experiments with significant 3D effects did not require significant reformulation of the models despite the simplifications used. However, there is no guarantee that these simplifications will apply to all situations. Increased computer power enables a finer nodalisation. A careful check of all simplifications and a more complete modelling of all 3D processes is required to improve code reliability.

The current validation database of system codes is mostly 1D and only large-scale 3D LB-LOCA phenomena were experimentally simulated. A more extensive use of 3D modelling in system codes for other transients may require additional validation data. Current 3D models may also not include all phenomena. The state-of-the-art of 3D capabilities in T/H system codes should therefore cover all aspects and limitations, from the equations and simplification considered, to time and space averaging with unavoidable use of relatively coarse meshes, closure models, and a review of available or needed experimental support.

This report presents the status of the current availability and development of multidimensional capabilities of T/H system codes. Situations are identified where a multidimensional description of the geometry would improve the accuracy and reliability of the calculations. Present applications and limitations are reviewed, and experimental support described. The rationale for future developments and additional experimental support is also proposed.

1.2. Objectives and scope; safety issues with 3D T/H phenomena

The main objective of this work is to identify actions that will allow for more reliable and accurate system code simulations through a better knowledge of the various 3D phenomena and by taking advantage of increasing computer power to use good and validated 3D models of system codes with an improved space resolution. This document will:

- establish current code limitations for nuclear power plant applications;
- determine small-scale flow processes in relation to 3D set of equations and identify all simplifications of current models;
- present simplifying assumptions, checking that there is no flaw in the modelling;
- clarify the role and impact of nodalisation and strategy for mesh convergence (develop physics dedicated to a specific mesh size and validate the code with this same mesh size or accept some non-convergence and estimate the error or any other possible strategy to be defined);
- check whether the validation is sufficient or not; if not, propose additional experimental programmes;
- suggest verification and validations (V&V) matrix for 3D capabilities system codes.

1.3. Related CSNI and international activities

T/H system codes and related topics have been well documented since their initial deployment. International initiatives continue to foster collaboration and exchanges on code development, experimental support and model improvement. The present review of 3D capabilities of T/H system codes should be placed in the historical and general context of the development of scientific tools that aim to generate reliable and accurate simulations of physical phenomena.

The United States, Germany and Japan started an international programme in the early 1980s on the T/H behaviour of emergency core cooling (ECC) during the refill and reflood phases of a LOCA in a PWR, involving the assessment and use of a best-estimate computer code (TRAC). The objectives were to study the multidimensional effects during post-blowdown phases of a PWR LOCA and provide supplementary experimental data and analysis tools for this transient. Reference [1-4] presents a summary of the reactor safety issues investigated.

Most of the international co-operation projects have been supported by the NEA and IAEA. This report does not include a comprehensive survey but focuses on the major contributions related to 3D capabilities of system codes. Two main areas are discussed below: (i) the transients, related physical phenomena and experimental support; and (ii) the transverse studies.

1.3.1. Transients, physical phenomena and experimental support

Among the significant international collaborations, those related to the identification and ranking of phenomena associated with LOCAs are important because they present a comprehensive description of the transients and their phenomena.

The NEA Committee on the Safety of Nuclear Installations (CSNI) published a report [1-5] in 1987 about a code validation matrix for the assessment of T/H codes for light water reactor (LWR) LOCA and transients. This report, updated in 1996 [1-6], introduces a set of tests in support of code validation. A specific validation matrix using separate effect tests [1-7] was made available in 1993. One section in it was devoted to global multidimensional fluid temperature, void and flow distribution in the upper plenum, core, downcomer and secondary side of a steam generator. Another report [1-8] describing LOCA and non-LOCA transients, phenomena identification, code modelling capabilities and the needs for experimental data was published in 1989.

A 1996 workshop on transient T/H and neutronic codes' requirements [1-9] identified the needs for 2- or 3D hydrodynamics and their closure laws. Developments carried out in 2000 after the 1996 workshop were discussed at another workshop in Barcelona [1-10].

Other significant international collaborations concern the experimental facilities. Documents about facilities with multidimensional features are briefly described.

The need for using 3D T/H system codes for a better representation of complex phenomena that can occur during accidental transients in nuclear power plants was mentioned in 2003 in the IAEA-TECDOC-1539 [1-12]. The need for code validation was also emphasised. The validation process could be carried out within dedicated frameworks like the NEA experimental T/H Primär-Kreislauf (PKL) (2004-2020) and the Advanced Thermal-Hydraulic Test Loop for Accident Simulation (ATLAS) (2012-2020) projects. The PKL facility was built to simulate the integral behaviour of a typical 4-loop PWR [1-13]. However, the 1D geometry of the pressure vessel explains why the facility was not equipped to deal with 3D phenomena. An alternative approach was found by incorporating the Rossendorf Coolant Mixing Model (ROCOM) test facility in the project. A series of

tests were performed to set up a database for 3D code validation [1-14]. The two-loop half-height scaled ATLAS integral effect test (IET) facility [1-15] was equipped with instrumentation for performing temperature measurement in several locations of the fully annular pressure vessel downcomer. Hundreds of thermocouples have also been installed in the inlet and outlet chamber of the steam generators. These features make the ATLAS facility suitable for investigating 3D phenomena occurring during the considered experiments.

The NEA Rig-of-safety Assessment (ROSA) Project (2005-2009) [1-16] and the OECD/NEA ROSA-2 Project (2009-2012) [1-17] were performed to resolve issues in T/H analyses concerning PWR safety. The ROSA/Large Scale Test Facility (LSTF), which is a full-pressure and full-height IET facility, was used to simulate T/H phenomena in LOCAs and operational/abnormal transients of PWRs. The test data obtained in these projects is available for validation activities with 3D system-scale T/H codes. Chapter 5 summarises the experimental setup and results.

The CSNI organised a PWR main steam line break (MSLB) benchmark in 1999 to examine the coupled system T/H and 3D kinetics codes [1-18]. The benchmark assumed a hypothetical MSLB at the Three Mile Island Unit 1 system. The nuclear and T/H data for the coupled codes were provided to the participants. The break in a steam line evoked asymmetric flow behaviour in the two-loop PWR that leads to 3D flows in the reactor vessel downcomer, the lower head and the reactor core. The result was further 3D reactor kinetics behaviour. The MSLB benchmark was not based on an experiment. Instead, a numerical benchmark using code-to-code comparisons was performed. The participants used either a 1D system code, or a 3D module of a system code, or CFD codes for the reactor vessel's T/H calculations. Among the various solutions, at least four of them, provided by the CEA, Siemens, Purdue University, and the Korea Atomic Energy Research Institute (KAERI), produced complementary results [1-19, 1-44]. Although they had used completely different codes, the results were extremely similar.

The NEA organised the Nuclear Power Engineering Corporation BWR Full-size Fine-Mesh Bundle Test (NUPEC BFBT) benchmark programme [1-3] to make comparisons of currently available computational approaches and encourage the development of novel next-generation approaches that focus on more microscopic processes. The full-scale NUPEC 8x8 rod bundle test facility has a wide range of steady-state test capabilities under typical BWR operating conditions and can simulate the unsteady characteristics of operational transients. The replacement of some heater rods with water rods or unheated rods enabled the testing of four different fuel assembly types. Void distributions were measured for a fine mesh using an X-ray computerised tomography scanner at a point 50 mm above the heated zone for steady-state cases. The attained spatial resolution was as small as 0.3 mm by 0.3 mm, which is very valuable for the assessment of both subchannel codes and CFD codes [1-20]. Furthermore, three X-ray densitometers measured the cross-sectional average void fractions during transients at three different axial locations.

The NEA also organised the NUPEC PSBT benchmark programme [1-2], which is similar to BFBT but related to PWR core geometry.

1.3.2. Transverse studies

Multidimensional phenomena and their treatment in T/H system codes are considered in several international activities within a much larger framework.

A specific chapter in [1-21] examines the relationship between scaling and T/H system codes, with a section related to the specific limits of porous 3D models. The chapter outlines how closure relations used in 2D and 3D models are generally extrapolated or simply taken

from 1D models (such as wall heat coefficients, wall friction and pressure losses and flow regime map) and interfacial friction is isotropic in a non-isotropic medium. The lack of turbulent diffusion and dispersion modelling in many 3D models is also highlighted. When these last models are taken into account, they derive from subchannel analysis, and they should be extended to larger space-filtering as used in applications of system code. Distortion on scaled-down geometries – namely for IETs – is also addressed and should be carefully analysed for 3D calculations in system codes.

There are also important links between T/H system codes and passive systems, which can be highly multidimensional. The phenomena and specificities are described in several documents, most of them assembled by the IAEA. Document [1-22] provides a definition and classification of passive safety systems. Additional documents ([1-23], [1-24] and [1-25]) are dedicated to natural circulation phenomena in advanced water cooled reactors. A CSNI status report describes analytical and calculation tools focused mostly on passive systems using natural circulation as a main driver [1-26].

Another CSNI report involving multidimensional phenomena concerns the phenomena identification ranking table (PIRT) in spent fuels pools [1-27]. A CSNI status report on spent fuel pools (SFPs) under accident conditions [1-28] points out that the analysis of SFP accident scenarios requires a modelling of 3D effects in a large domain, which neither T/H system codes nor CFD methods can currently perform. The later PIRT exercise on SFPs [1-27] concludes that properly scaled experiments, model development and validation are required to study T/H behaviour and the large-scale natural circulation flow pattern from certain phases of accident scenarios.

Significant developments and increased performances made CFD a major tool for the simulation of multidimensional phenomena. Several international activities present interesting studies that can be used for the development of T/H systems codes' multidimensional capabilities. The CSNI promoted activities related to the application of CFD to nuclear reactor safety. Three Writing Groups were created under the auspices of the Working Group for the Analysis and Management of Accidents (WGAMA) to produce state-of-the-art reports on different aspects of the subject. The first group, WG1, established Best Practice Guidelines [1-29] for CFD application to Nuclear Reactor Safety (NRS); this document was revised in 2014. The second group, WG2, documented the existing assessment databases [1-30] for CFD application to some identified NRS issues; this document was also revised in 2014. The third group, WG3, established requirements for the extension of CFD codes to two-phase flow safety problems [1-31]. These activities all identified safety issues that may benefit from a 3D modelling because it would improve knowledge of turbulence in reactor components in single-phase and two-phase flows, and of the current simulation tools' capabilities.

Four benchmark activities reports have been released so far [1-32], [1-33], [1-34] and [1-35]. Three successive European projects addressed T/H multiscale analysis, including activities on CFD in open medium and porous medium approaches. The NUclear REactor SIMulation (NURESIM) Integrated Project [1-36] provided the initial step towards a common European Standard Software Platform for nuclear reactors' simulations. The overall objective of NURESIM-TH is to improve the understanding and the predictive capabilities of the simulation tools for key two-phase flow T/H processes that can occur in nuclear reactors, focusing on the critical heat flux (CHF) and the pressurised thermal shock (PTS). The NURISP project (2010-2012) continued the NURESIM activities. The publication of a state-of-the-art in two-phase CFD in a special issue of *Multiphase Science and Technology* presents contributions on the various two-phase CFD approaches [1-37], on adiabatic bubbly flow [1-38], on boiling bubbly flow [1-39], on annular-mist flow and dryout [1-40] and on stratified flow [1-41]. The NUclear REactor SAFETY simulation

platform (NURESAFE) project (2013-2015) made new advances in the two-phase flow modelling [1-42], including a modelling of turbulent effects in LOCA conditions [1-43]. The maturity of CFD for single-phase applications (including computation capacities) is sufficient for some industrial cases. Nevertheless, significant research efforts concerning their use in safety assessment still need to be made. The uncertainty quantification or the coupling with larger scale (system scale) studies is particularly concerning. The 2019-2021 activity of the task group aims for more accurate identification and to drive improvements.

1.4. Structure of the report

Chapter 2 explains the reasons for developing multidimensional capabilities in T/H system codes and describes some important transients and phenomena with multidimensional characteristics. Chapter 3 describes the 3D equations, models and closure laws. Chapter 4 reports the current implementation of 3D capabilities in T/H system codes, including simplifications and limitations. Simulation tools require qualification, which is based on a comparison of measurements and experimental data. Chapter 5 summarises the available information concerning either separate effect tests that are focused on a single specific phenomenon (such as those described in Chapter 2), or IETs, where multiple phenomena are present. Chapter 6 provides the full process of code qualification. Chapter 7 attempts to synthesise the rationale behind suggesting actions that are detailed in Chapter 8. Finally, Chapter 9 presents some recommendations and concludes the report.

References

- [1-1] Damerell, P.S. and J.W. Simons, editors (1993), “2D/3D program work summary report”, NUREG/IA—0126, Office of Nuclear Regulatory Research, US Nuclear Regulatory Commission, Washington, DC.
- [1-2] NEA (2012), “OECD/NRC Benchmark based on NUPEC PWR sub-channel and bundle tests (PSBT)”, OECD Publishing, Paris, NEA/NSC/DOC(2012)1, www.oecd-nea.org/jcms/pl_19106.
- [1-3] NEA (2005), “NUPEC BWR Full-Size Fine-Mesh Bundle Test Benchmark, Volume I. Specifications”, NEA/NSC/DOC(2005)5, OECD Publishing, Paris, www.oecd-nea.org/jcms/pl_14238.
- [1-4] Damerell, P.S. and J.W. Simons, editors (1993), “Reactor Safety Issues Resolved by the 2D/3D Program”, NUREG/IA—0127, US Nuclear Regulatory Commission, Washington, DC.
- [1-5] NEA (1987), “CSNI code validation matrix of thermo-hydraulic codes for LWR LOCA and transients”, NEA/CSNI/R132, OECD Publishing, Paris, www.oecd-nea.org/jcms/pl_15784.
- [1-6] NEA (1996), “CSNI Integral test facility validation matrix for the assessment of thermal-hydraulic codes for LWR LOCA and transients”, NEA/CSNI/R(1996)17, OECD Publishing, Paris, www.oecd-nea.org/jcms/pl_16134.
- [1-7] NEA (1993), “Separate effects test matrix for thermal-hydraulic code validation, Vol.1 and 2”, NEA/CSNI/R(1993)14, p. 83, OECD Publishing, Paris, www.oecd-nea.org/jcms/pl_15968.
- [1-8] NEA (1989), “Thermalhydraulics of emergency core cooling in light water reactors: a State of the Art Report (SOAR)”, NEA/CSNI-161 (1989), OECD Publishing, Paris, www.oecd-nea.org/jcms/pl_15836.
- [1-9] NEA (1996), “Proceedings of the OECD/CSNI workshop on transient thermal- hydraulic and neutronic codes requirements (1996: Annapolis, Maryland)”, NEA/CSNI/R(1997)4, OECD Publishing, Paris, www.oecd-nea.org/jcms/pl_16162.
- [1-10] NEA (2001), “Proceedings of the OECD/CSNI Workshop on Advanced Thermal-Hydraulic & Neutronic Codes: Current & Future Applications (2000: Barcelona)”, NEA/CSNI/ R(2001)2, OECD Publishing, Paris, www.oecd-nea.org/jcms/pl_17524.
- [1-11] NEA (2001), “Validation Matrix for the Assessment of Thermal-Hydraulic Codes for VVER LOCA and Transients”, NEA/CSNI/R(2001)4, OECD Publishing, Paris, www.oecd-nea.org/jcms/pl_17492.
- [1-12] IAEA (2007), “Use and Development of Coupled Computer Codes for the Analysis of Accidents at Nuclear Power Plants, Proceedings of a technical meeting held in Vienna, 26–28 November 2003”, IAEA-TECDOC-1539, IAEA, Vienna.
- [1-13] Guneyasu, R., H. Kremin and S. P. Schollenberger (2016), “Description of the PKL III test facility”, NTCTP-G/2007/en/0010, rev B, AREVA NP GmbH, Erlangen, Germany.
- [1-14] Kliem, S. and R. Franz (2012), “OECD PKL2 Project – Final Report on the ROCOM Tests”, HZD\FWO\2012\03, Forschungszentrum Rossendorf, Dresden.
- [1-15] Kang, K.H. et al. (2011), “Detailed description report of ATLAS facility and Instrumentation”, KAERI/TR-4316/2011, Korea Atomic Energy Research Institute.
- [1-16] NEA (2013), “OECD/NEA ROSA Project 2005-2009 Final Integration Report”, NEA/CSNI/R (2013)1, OECD Publishing, Paris, www.oecd-nea.org/jcms/pl_19244.
- [1-17] NEA (2017), “OECD/NEA ROSA-2 Project 2009-2012 Final Integration Report”, NEA/CSNI/R (2016)10, OECD Publishing, Paris, www.oecd-nea.org/jcms/pl_19728.

- [1-18] Jeong, J.J., H.G. Joo, B.O. Cho, S.Q. Zee and W.J. Lee (2001), “MARS/MASTER Coupled System Calculation of the OECD MSLB Benchmark Exercise III with Refined Core Thermal-Hydraulic Nodalisation”, ICONE-9, 8-12 April, Nice.
- [1-19] Joo, H.G., J.J. Jeong, B.O. Cho, W.J. Lee and S.Q. Zee (2003), “Analysis of the OECD MSLB Benchmark Problem using the Refined Core Thermal-Hydraulic Nodalisation Feature of the MARS/MASTER Code”, *Nuclear Technology*, Vol. 142, pp.166-179, Taylor & Francis.
- [1-20] Hwang, D.H., J.J. Jeong, B.D. Chung (2009), “The NUPEC BFBT Subchannel Void Distribution Analysis Using the MATRA and MARS Codes”, *Nuclear Engineering and Technology*, Vol. 41, pp. 295-306, Elsevier.
- [1-21] NEA (2017), “Scaling in System Thermal-Hydraulics Applications to Nuclear Reactor Safety and Design: a State-of-the-Art Report”, NEA/CSNI/R(2016)14, OECD Publishing, Paris, www.oecd-nea.org/jcms/pl_19744.
- [1-22] IAEA (1991), “Safety Related Terms for Advanced Nuclear Plants”, IAEA-TECDOC-626, IAEA, Vienna.
- [1-23] IAEA (2002), “Natural circulation data and methods for advanced water cooled nuclear power plant designs”, IAEA-TECDOC-1281, IAEA, Vienna.
- [1-24] IAEA (2005), “Natural circulation in water cooled nuclear power plants: Phenomena, models and methodology for system reliability assessments”, IAEA-TECDOC-1474, IAEA, Vienna.
- [1-25] IAEA (2009), “Passive Safety Systems and Natural Circulation in Water Cooled Nuclear Power Plants”, IAEA-TECDOC-1624, IAEA, Vienna.
- [1-26] NEA (forthcoming), “Status Report on Reliability of Thermal-Hydraulic Passive Systems”, NEA/CSNI/R (2021)2, OECD Publishing, Paris.
- [1-27] NEA (2018), “Phenomena Identification and Ranking Table (PIRT) on Spent Fuel Pools under Loss-of-Cooling and Loss-of-Coolant Accident Conditions”, NEA/CSNI/R(2017)18, OECD Publishing, Paris, www.oecd-nea.org/jcms/pl_19836.
- [1-28] NEA (2015), “Status Report on Spent Fuel Pools under Loss-of-Cooling and Loss-of-Coolant Accident Conditions”, NEA/CSNI/R(2015)2, OECD Publishing, Paris, www.oecd-nea.org/jcms/pl_19596.
- [1-29] NEA (2015), “Best Practice Guidelines for the Use of CFD in Nuclear Reactor Safety Applications”, NEA/CSNI/R(2014)11, OECD Publishing, Paris, www.oecd-nea.org/jcms/pl_19548.
- [1-30] NEA (2015), “Assessment of Computational Fluid Dynamics (CFD) for Nuclear Reactor Safety Problems”, NEA/CSNI/R(2014)12, OECD Publishing, Paris, www.oecd-nea.org/jcms/pl_19550.
- [1-31] NEA (2010), “Extension of CFD Codes to Two-Phase Flow Safety Problems”, NEA-CSNI-R(2010)2, OECD Publishing, Paris, www.oecd-nea.org/jcms/pl_18898.
- [1-32] NEA (2011), “OECD/NEA-Vattenfall T-Junction Benchmark Exercise (high-cycle thermal fatigue)”, NEA/CSNI/R(2011)5, OECD Publishing, Paris, www.oecd-nea.org/jcms/pl_19022.
- [1-33] NEA (2013), “OECD/NEA-KAERI Rod Bundle CFD Benchmark Exercise (turbulent mixing downstream of a spacer grid)”, NEA/CSNI/R(2013)5, OECD Publishing, Paris, www.oecd-nea.org/jcms/pl_19286.
- [1-34] NEA (2016), “OECD/NEA-PSI CFD Benchmark Exercise (jet erosion of a stratified atmosphere based on PANDA)”, NEA/CSNI/R(2016)2, OECD Publishing, Paris, www.oecd-nea.org/jcms/pl_19696.

- [1-35] NEA (2019), “OECD/NEA Benchmark Exercise: Computational Fluid Dynamic Prediction and Uncertainty Quantification of a GEMIX Mixing Layer Test”, NEA/CSNI/R(2017)19, OECD Publishing, Paris, www.oecd-nea.org/jcms/pl_19838.
- [1-36] Chauillac, C., J.M. Aragonés, D. Bestion, D.G. Cacuci, N. Crouzet, F.P. Weiss and M.A. Zimmermann (2009), “NURESIM – A European simulation platform for nuclear reactor safety: multi-scale and multi-physics calculations, sensitivity and uncertainty analysis”, FISA 2009, June 22-24, Praha.
- [1-37] Bestion, D., P. Coste, B. Niceno and S. Mimouni (2011), “Two-phase CFD: the various approaches and their applicability to each flow regime”, *Multiphase Science and Technology*, Vol. 23(2-4), pp. 201, Begell House.
- [1-38] Krepper, E., C. Morel, B. Niceno and P. Ruyer (2011), “CFD modeling of adiabatic bubbly flow”, *Multiphase Science and Technology*, Vol. 23(2-4), Begell House.
- [1-39] Končar, B., C. Morel, S. Mimouni, L. Vyskocil, G. Hazi and M.C. Galassi (2011), “CFD modeling of boiling bubbly flow for DNB investigations”, *Multiphase Science and Technology*, Vol. 23(2-4), Begell House.
- [1-40] Anglart H. and D. Caraghiaur (2011), “CFD modeling of boiling annular-mist flow for Dry-out investigations”, *Multiphase Science and Technology*, Vol. 23(2-4), Begell House.
- [1-41] Lucas, D., P. Coste, T. Höhne, D. Lakehal, Y. Bartosiewicz, D. Bestion, M. Scheuerer and M.C. Galassi, (2011), “CFD modeling of free surface flow with and without condensation”, *Multiphase Science and Technology*, Vol. 23(2-4), Begell House.
- [1-42] D. Bestion et al. (2014), “Multiscale thermalhydraulic analyses performed in the NURESAFE project”, ICONE-22, July, Praha.
- [1-43] Alku, T. (2016), “Modelling of turbulent effects in LOCA conditions with CATHARE-3”, Nuclear Engineering and Design, 321.
- [1-44] NEA (1999), “Pressurized Water Reactor Main Steam Line Break MSLB Benchmark, Volume 1: Final Specifications”, NEA/NSC/DOC(99)8, OECD Publishing, Paris, www.oecd-nea.org/jcms/pl_13242.

2. Needs of 3D system-scale T/H codes for nuclear safety

Thermal-hydraulic system (SYSTH) codes have been used for licensing and design issues of nuclear power plants. The purpose is to carry out numerical simulations of nuclear reactors under steady-state and transient conditions. SYSTH codes have been significantly modified and improved since the 60s. Firstly, the fluid model was progressively upgraded from homogeneous to two or three-fluid models. Secondly, a large number of facilities have been designed – such as integral effect test (IET) facilities and separate effect test (SET) facilities – that will validate codes' predictions capabilities. As a result, a greater amount of experimental data is available that then contributes to additional code improvements.

Multidimensional phenomena that have a significant impact occur in the course of many design basis accident (DBA) scenarios such as feed water line break (FWLB), steam generator tube rupture (SGTR), and (loss-of-coolant accident) LOCA (see the following chapters). Three-dimensional (3D) phenomena can also play a key role under natural circulation flow regimes, where flow mixing and stratification are predominant. More sophisticated SYSTH codes were therefore considered through the incorporation of 3D capabilities, alongside the typical one-dimensional (1D) models' representation.

Until now, limited reactor components have been concerned by 3D representations. They are generally suitable for large vertical geometry components such as boiling water reactor (BWR) cores, pressurised water reactor (PWR) cores and pressure vessels, steam generators and spent fuel pools. The need for horizontal 3D components representation such as the hot and cold legs has not yet been handled because the velocity field remains mainly 1D, except for some very specific cases. Nevertheless, validation assessments of 3D computational tools are still in progress due to the limited number of dedicated facilities. Recently, some international experimental programmes have examined this issue at the Rossendorf Coolant Mixing Model (ROCOM) [2.1-1] and Advanced Thermal-Hydraulic Test Loop for Accident Simulation (ATLAS) [2.1-2] test facilities. The outcomes show reasonable prediction capabilities in comparison with experimental and computational fluid dynamics (CFD) codes' results [2.2.5-4].

2.1. Plant types, components and transients

This report cannot provide a comprehensive survey of the identified needs of 3D system-scale thermal-hydraulic (T/H) codes for nuclear safety. Only some typical transients will be hereafter presented to illustrate the applications where 3D phenomena should be considered in order to increase the accuracy and reliability of the simulations. These transients mostly relate to pressurised water reactors (PWR), although boiling water or other water reactors type are sometimes considered. Small modular reactors (SMR) are also quite sensible to 3D phenomena, not only because of the use of passive systems (cf. para. 2.2.7), but also when water pools are surrounding the vessel. This report is not a comprehensive study of all 3D phenomena. For example, boron dilution is not presented, even though it is a transient where 3D phenomena (and mixing effects) are key aspects. Loss of residual heat removal system (RHRS) at mid-loop conditions or mixing transients inside the pressuriser are also possible examples of transients where 3D capabilities are of interest.

Vessel and core are principally mentioned in this report, although other components (e.g. steam generators, spent fuel pools, pool heat exchangers) are also places where 3D phenomena can occur.

2.2. Identification of 3D phenomena for selected transients

2.2.1. Loss-of-coolant accident – large break LOCA

The evolution of large break (LB) loss-of-coolant accidents (LOCAs) depends on the type of reactor (PWR, BWR, Canada Deuterium Uranium [CANDU], etc.), type of components (for PWR, especially the type of steam generator – U-tube, but also once-through or horizontal) and the design of emergency core cooling systems (in particular the location of the safety injection, which can be in the vessel (direct vessel injection [DVI]), in the cold and/or hot legs and the location of the break. Some general trends can be identified and significant 3D phenomena are present in most designs. However, the following description mainly addresses large break loss-of-coolant accident (LB-LOCA) in the cold leg with cold leg safety injection. Some particularities for other situations are also provided.

2.2.1.1. Transient description

The course of a PWR large break LOCA has three main phases:

- blowdown, during which the primary system depressurises and forces coolant water rapidly out of the broken leg, starting in liquid phase then coolant flashing to steam;
- refill, during which emergency cooling water refills the lower plenum to the bottom of the fuel rods;
- reflood, during which water refills the core, cools and rewets the fuel rods.

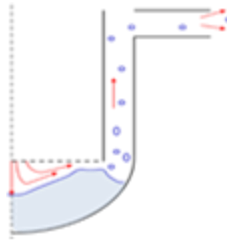
The most detrimental scenario regarding the core thermal response described here below deals with a cold leg break. This break location leads to core flow stagnation conditions during blowdown, countercurrent steam/water flow in the downcomer during refill and a steam binding effect which limits core cooling during reflood.

Blowdown

During blowdown the primary coolant flows from the intact loops and the vessel to the break, through the broken loop. In a first stage a stagnation point is located in the core, where the boiling crisis occurs that then expands in the whole core. Within few seconds, the core is almost emptied of liquid water and the clad temperatures reach a first peak. Then, the stagnation point moves to the steam generator tubes once the primary pressure is below the secondary pressure and the core flow is negative (from top to bottom) in the whole core, with some water from the upper plenum flowing downwards through the core. During this period a film boiling heat transfer allows the clad temperatures to decrease until no more water crosses the core. At the end-of-blowdown, some of the water from the lower plenum is swept out by high-velocity steam moving downwards through the core and upwards in the downcomer, up to the broken cold leg. The removal of liquid from lower plenum by the impacting jet of steam (lower plenum voiding) has been identified as a dominant phenomenon during blowdown with significant 3D effects (see Figure 2.1), which controls the minimum mass inventory during the LB-LOCA. The main process is a Kelvin-Helmholtz instability at the free surface of the liquid pool in the lower plenum, which induces some liquid entrainment from the wave crest up to the break. Core radial power distribution will develop a 3D repartition of the energy stored in the core. The clad temperature evolution during the blowdown mainly depends on the local heat flux and the

boiling crisis occurrence (within the first seconds of the transient), which depends on the core flow conditions due to the critical flow at the break and the flow resistance in the pumps. Since the departure from nucleate boiling (DNB) is reached very rapidly, the first peak clad temperature is mainly due to the stored heat before the occurrence of the break and depends on fuel properties such as pellet conductivity and gap conductance. The locations of the highest clad temperatures at the time of the first peak depend on the 3D repartition of the stored energy in the fuel.

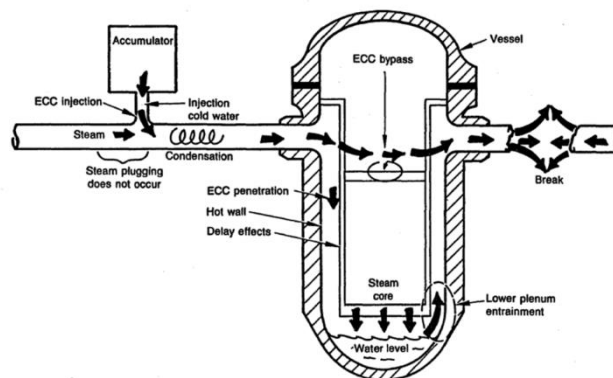
Figure 2.1. The lower plenum voiding during the blowdown phase of a PWR LB-LOCA



Refill

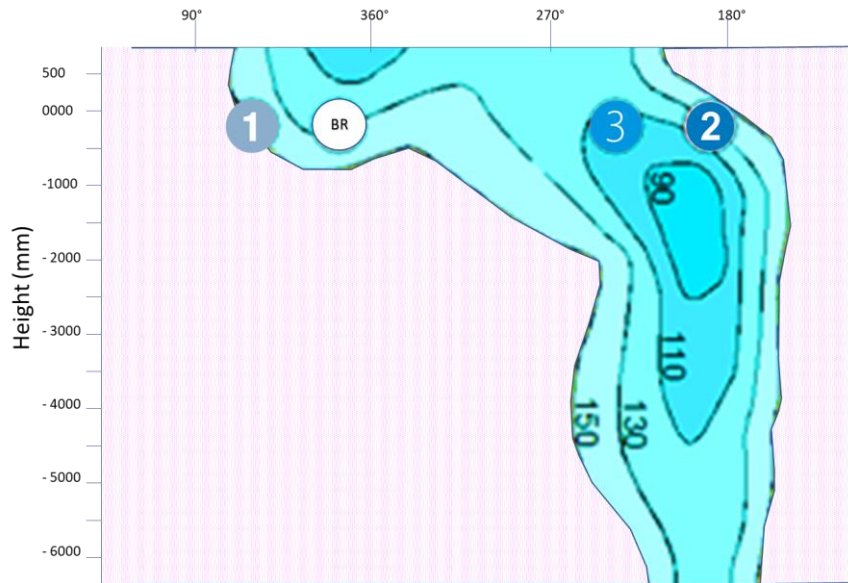
The refill phase starts at the beginning of accumulator injection – before completion of blowdown – in the cold leg, or downcomer, or hot leg or upper plenum, depending on the emergency core cooling’s (ECC’s) PWR designs. When water is injected in the intact loop cold legs or directly in the downcomer from the accumulator, it cannot reach the lower plenum. Instead, some is swept out through the broken cold leg from the downcomer by the countercurrent flow of steam. This is the “bypass phase of the refill” when some of the ECC water is lost at the break (See Figure 2.2). This bypass process depends on the difference between the pressure in the vessel and the one in the containment and decreases with time according to this pressure difference. Later, multidimensional effects occur in the downcomer, with steam converging to the broken leg and water flowing down to the opposite region [2.2.1-1]. Distribution of water in the vessel is a key parameter during the refill period. Flow is multidimensional in the downcomer during ECC bypass and the efficiency of safety injection is directed by the ratio of injected water finally reaching the lower plenum. Figure 2.3 shows a temperature field measured in an upper plenum test facility (UPTF) test (cf. Section 5.1.3), simulating a refill phase. The ECC water from the intact cold leg close to the broken leg is fully bypassed, whereas the water from the other two cold legs is only partly bypassed.

Figure 2.2. Ideal sketch of the refill phase of a PWR LB-LOCA with bypass of the ECCS’ water



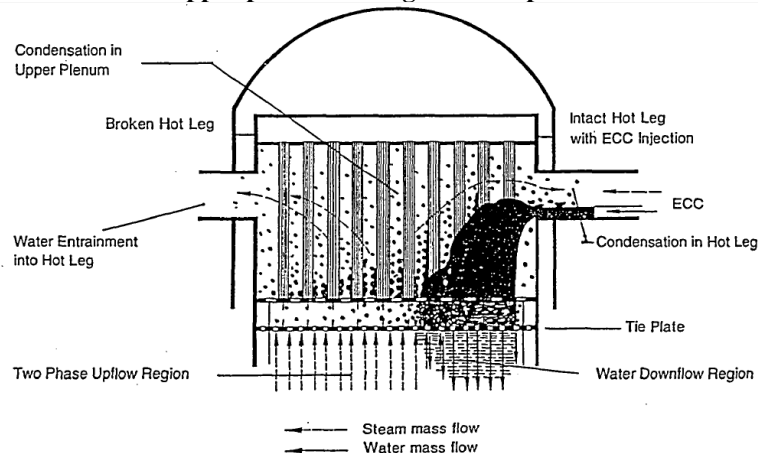
Source: US NRC, 1988.

Figure 2.3. Contour plot of fluid temperature distribution in downcomer during the refill phase of a LB-LOCA as observed in a UPTF test



Note: 1/2/3 are intact loops, and BR is the broken loop; pink region is at saturation and the blue region indicates subcooled temperatures, corresponding to the presence of liquid.

Figure 2.4. Phenomena in the upper plenum during the refill phase in case of hot leg ECC injection



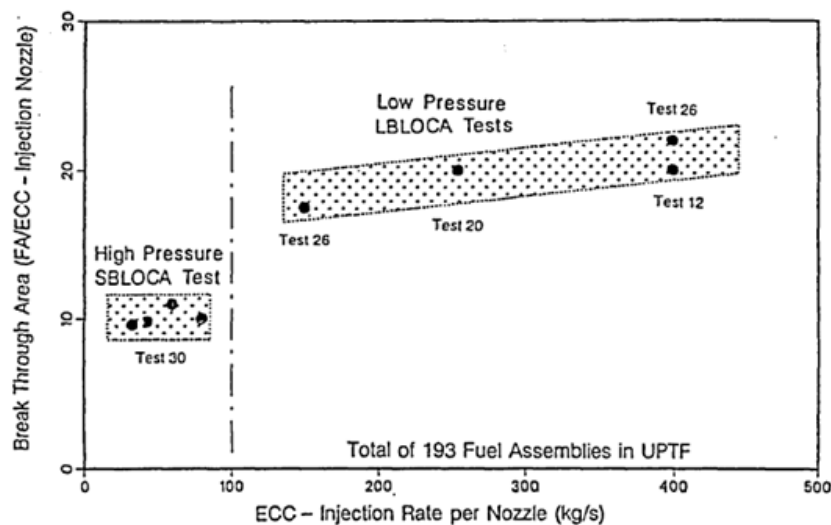
Source: Damerell and Simons, editors, 1993.

In the case of hot leg or upper plenum injection, ECC water is delivered into the local regions of the upper plenum and flows down through the core into areas located below the hot legs or injectors. This cold water creates condensation near the injection nozzle, resulting in subcooled water plugs that are intermittently delivered to the upper plenum. Despite extensive condensation in the upper plenum, ECC water still flows to the core with substantial subcooling. Fuel rods are mostly quenched in the water downflow regions, whereas they heat up in the other regions. Steam condensation by subcooled ECC water accelerates depressurisation of the primary system. However, ECC water accumulation in the upper plenum is limited (liquid fractions were about 10% in the upper plenum test facility [UPTF]) and the liquid distribution is two-dimensional (2D) (there is higher liquid accumulation above core downflow regions). Figure 2.4 illustrates the phenomena in the

upper plenum with hot leg injection. Subcooled water delivered to the upper plenum condenses steam in the upper plenum and flows down through the tie plate to the core.

Condensation in the upper plenum and delivery to the core are strongly affected by the rate of ECC delivery and water distribution in the upper plenum. Water delivery to the core is also affected by countercurrent flow phenomena at the tie plate. Figure 2.5 shows the area of the downflow region (where liquid water can reach the core) for UPTF separate effects tests (described in Section 5.1.3). The area of the downflow (or breakthrough) region is about ten fuel assemblies per injection nozzle in the high pressure tests (small break loss-of-coolant accident [SB-LOCA], test 30) and 18 to 23 fuel assemblies per injection nozzle for the low pressure tests (LB-LOCA, tests 12, 20 and 26). The size of this area increases with increased ECC injection rate.

Figure 2.5. Downflow area versus ECC flowrate for UPTF hot leg injection tests



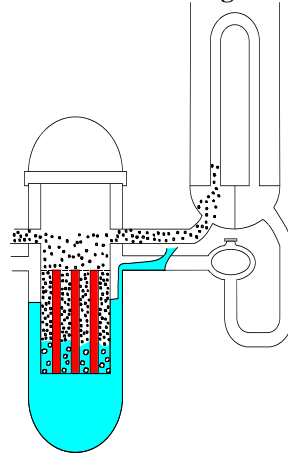
Source: Damerell and Simons, editors, 1993.

Reflood

Reflooding begins when ECC water enters the core. In the case of cold leg injection, it occurs as soon as the lower plenum is completely filled with water from the safety injection system. Water progressively quenches the fuel rods with a bottom-up quenching and a top-down quenching (falling film of de-entrained water from upper plenum). During reflood, steam flow is generated by both heat release from rod quenching and residual power in the quenched zone of the core. Various flow regimes (bubbly flow, slug flow, inverse-annular, inverse-slug, annular-mist flows) and heat transfer regimes (forced convection to liquid, subcooled boiling, saturated boiling, transition boiling, inverse-annular film boiling, inverse-slug film boiling, dispersed flow film boiling) are encountered during the reflood process [2.2.1-2]. Droplets are created and entrained by steam out of the core and can be partially de-entrained in upper plenum, hot legs and in steam generator (SG) inlet headers. The steam flow from the core through the intact and broken loops creates friction and acceleration pressure losses which are balanced by the difference of collapsed water head between the downcomer and the core. This pressure difference limits the core cooling rate. The vapourisation of entrained droplets in the SG tubes creates an additional pressure drop, which further inhibits the gravity-driven reflooding of the core. This is the “steam binding effect”, which represents the flow resistance between the core and the break (see Figure 2.6). The pressure loss is mainly due to wall friction in the SG tubes and in the pumps. There is also an acceleration pressure drop in the SGs due to evaporating drops and

superheating of the vapour. This total pressure loss and the corresponding steam flowrate in the loops are limited by the available downcomer head. In the most favourable case, the entire vapour is created in the core and participates to rod cooling. In the most realistic and less favourable case, some entrained liquid droplets vapourise in the SG, and only part of the total vapour flowrate is created in the core and participates to rod cooling. The higher the droplet entrainment to SGs, the lower the core cooling capacity. It is thus important to reliably evaluate the amount of water entrained to the SGs in order to correctly predict the reflooding duration.

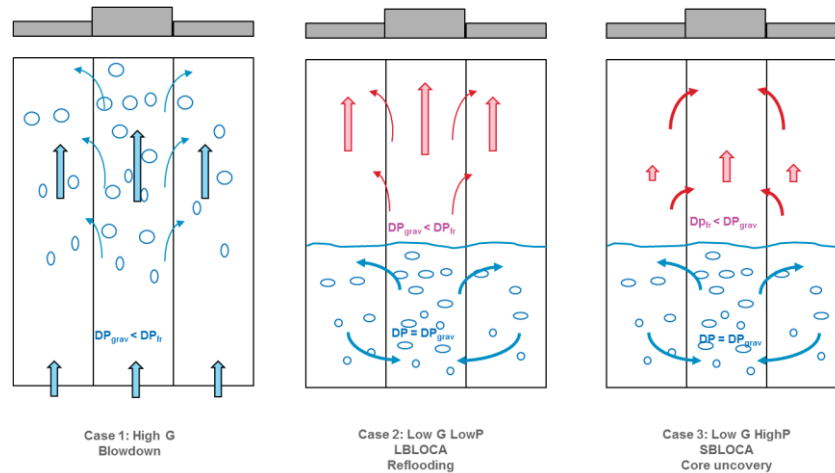
Figure 2.6. Sketch of the core reflooding in case of cold leg injection



There is a first phase of reflooding, consisting of oscillations of the collapsed levels between the core and downcomer, and a progressive damping that reduces the amplitude. A second peak clad temperature can be observed at the beginning of reflooding because the first oscillations can induce efficient cooling by film boiling. When the reflooding is stabilised, there is usually a slow heating of the cladding in the dry zone, followed by a precooling when quench front approaches. Therefore, three successive clad temperature peaks can be observed: during blowdown, at the beginning of reflooding, and during the stabilised reflooding.

The core and upper plenum coupling with steam generators drives the amount of water available. There are important multidimensional aspects due to the heterogeneous distribution of heat release with surrounding structures between the periphery and the centre of the core and between neighbouring assemblies that have different burn-up. Some of the entrained liquid is de-entrained in the core upper tie plate or in the upper plenum internals, forming a form of two-phase pool there. The liquid from this pool can re-enter (by gravity) the low-power region, where steam flow is lower, resulting in a three-dimensional (3D) flow pattern. In the core, the two-phase flow is from low to high powered regions, beneath the quench front. As a result there is an increase of the heat transfer above the quench front (referred to as the “chimney effect” cf. Section 3.8).

Above the quench front, the highest power region benefits from increased liquid carryover due to transfer from colder regions (see Figure 2.7) as observed in PERICLES-2D tests (Section 5.1.5) and in slab core test facility (SCTF) tests (Section 5.1.4). In the upper plenum, the flow is in the opposite direction.

Figure 2.7. Radial transfers during reflooding due to radial power differences

Source: Bestion and Matteo, 2015.

During the reflow phase, the quench front progresses in association with top-down and bottom-up rewetting and is multidimensional due to the radial power profile, countercurrent flows, droplet entrainment and de-entrainment in very complex geometries (e.g. upper plenum or spacer grids).

In the case of upper plenum or hot leg injection, ECC water flowing down into local regions of the core, just below the hot leg nozzles, contributes to the global reflooding process. Core cooling is enhanced in these regions and the fuel rods are quenched more quickly than those in other regions.

2.2.1.2 Key processes

One of the safety criteria is the peak clad temperature (PCT), directly related to residual power and heat transfer. Convection heat transfer is the main driver to rod and clad cooling. Flow condition is therefore one of the key parameters in determining PCT. The first peak (during blowdown) reflects the stored heat and depends mainly on hydraulic conditions in the core and time of critical heat flux (CHF) occurrence. The second peak (at the beginning of reflooding) depends on the duration of the refill phase and on all phenomena occurring in the downcomer during refill. The third peak (during reflow) is then controlled by the cooling of the dry zone of the core. The heat transfer to the steam is the main driver of rod and clad cooling with some radiation to droplets and to steam. The rod cooling depends on the steam temperature, which is also affected by convection to droplets and droplet vapourisation, which depends on the droplet size distribution. Droplet size is controlled by several processes, such as film sputtering at the quench front, dynamic break up by steam flow, break up on dry spacer grids, entrainment from liquid films along re-wetted spacer grids, coalescence between droplets, and vapourisation. Current system codes do not precisely model these processes but use an equivalent droplet size model based on prototypical reflow experimental data (e.g. PERICLES reflow tests with prototypical fuel assembly). Therefore, the equivalent droplet size is one of the key parameters in determining PCT by system codes during reflooding.

2.2.1.3 Main 3D phenomena

Core radial power distribution will result in 3D repartition of energy stored in the core. Therefore, 1D analysis may not be sufficient to depict the impact of this 3D repartition.

Additional multidimensional effects that have been identified as being of high importance ([2.2.1-3] and [2.2.1-6]) are:

- 3D flow in the lower plenum during the blowdown phase associated with the liquid entrainment by Kelvin-Helmholtz instability;
- 3D flow in the downcomer during the refill phase for cold leg or downcomer injection;
- 3D flow in the core and the upper plenum for hot leg or upper plenum injection;
- 3D flow in the core during the reflood phase (chimney effect);
- 3D flow in the upper plenum during the reflood phase (countercurrent flow limit [CCFL] at top of the core, pool formation, de-entrainment and re-entrainment of droplets).

The multidimensional influence and significance during the course of a LOCA are not the same when direct vessel injection and hot leg/cold leg combined injection are considered.

2.2.1.4 Known applications and main drawbacks of these applications

LB-LOCA is the historical transient that helps the design and sizing of ECCS. Therefore, 3D capabilities in thermal-hydraulic system (SYSTH) codes such as TRACE, Reactor excursion and leak analysis programme 5 (RELAP5), Code for Analysis of THERmalhydraulics during an Accident of Reactor and safety Evaluation (CATHARE), Multi-dimensional Analysis of Reactor Safety (MARS) and Safety and Performance Analysis Code (SPACE) – among others – have been used mainly for LB-LOCA ([2.2.1-7] and [2.2.1-8]). Another typical example of LB-LOCA applications can be found for the new advanced power reactor (APR) 1 400 reactor [2.2.1-9 and 2.2.1-13] and for the Russian type PWR (VVER) 1 000 [2.2.1-10]. Nowadays, new requirements in safety demonstration related to other transients, and especially intermediate break LOCA, have resulted in 3D applications of SYSTH codes being extended to several other types of transients (cf. the remaining paragraphs in this chapter).

3D SYSTH codes are based on the porous media approach and generally use rather coarse nodalisation that captures only large-scale 3D effects. Possible modelling strategies based on the phenomena identification and ranking technique (or table) (PIRT) could consider molecular and turbulent diffusion to be negligible (and therefore not modelled) compared to inertial force, interfacial friction and interfacial heat and mass transfer. 3D modules with coarse meshing might be required, especially when simulating the full reactor. In this case, scaling effects would be difficult to evaluate and full-scale (or at least very large-scale) experiments would be necessary for code validation, which will be restricted to specific configurations.

The main 3D-related LB-LOCA safety issues initially suspected in the 1970s have been solved thanks to the full-scale 2D/3D programme [2.2.1-6], which provides relevant data at the reactor scale to validate the 3D code prediction. UPTF (para 5.1.3) can be used to validate LB-LOCA 3D effects in the downcomer (refill and reflood phases) and SCTF, cylindrical core test facility (CCTF) (para. 5.1.4) and PERICLES-2D (para 5.1.5) may be used to validate 3D effects during reflood.

Nevertheless, finer multidimensional 3D aspects can be simulated with more recent T/H system codes (e.g. CATHARE3, SPACE, TRAC/RELAP Advanced Computational Engine TRACE). For example, modelling one mesh per assembly for the whole core and one mesh per subchannel for the hot assembly could become a standard practice in the near

future. To achieve this, experimental data will be needed to validate the code predictive capabilities at this scale on specific separate effect tests.

Water reactor fuel behaviour during LOCA phenomena - ballooning, burst, oxidation, fuel relocation and possible fracture at quench – are important aspects coupled with thermal-hydraulics. Fuel ballooning, for example, modifies the flow path and heat transfer performance is degraded for very high flow blockage (yet can enhance the cooling for low flow blockage by local flow acceleration). 3D flows should be considered to conduct a proper evaluation of both flow parameters and fuel behaviour.

2.2.2. Intermediate and small break LOCA

The intermediate break loss-of-coolant accident (IB-LOCA) described in this section is usually relevant to PWRs and corresponds to a break in the primary circuit that is between two and 14 inches (0.5% to 25% of the cold leg section). This paragraph examines the main 3D phenomena involved during this transient, where the use of 3D modules of system codes improves the simulation.

The following chapters refer mainly to IB-LOCA, for small break LOCA, and references [2.2.2-1] and [2.2.2-2] provide some general information.

2.2.2.1 Transient description

In case of an intermediate break LOCA, the transient dynamics can be very different according to the break size, location or orientation and assumptions such as pumps tripping. However, only the cold leg break with loss of off-site power will be considered, in a conservative way. The following first describes the main phases of this transient, before focusing on the phenomena where 3D modules of system codes are required to be correctly modelled. A typical reactor coolant intermediate break transient in the cold leg consists of the following sequence of events:

1. Single-phase natural circulation;
2. Two-phase natural circulation and possible reflux condensation for smaller breaks;
3. Loop seal filling and clearing with decrease in reactor pressure vessel (RPV) water level;
4. Accumulator injection, water inventory recovery and core reflooding.

Phase I: Single-phase natural circulation

This phase corresponds, at the system scale, to the draining of the pressuriser followed by single-phase depressurisation through reactor coolant draining until saturation conditions are reached in the hottest parts of the system. At the fuel assembly scale, for large size intermediate breaks, the boiling crisis can appear in the core before control rods drop, leading to a possible first but short cladding temperature increase.

Phase II: Two-phase natural circulation

At the system scale, steam production due to flashing in the hottest areas considerably slows down reactor depressurisation. The core residual power is removed during this phase via the SGs by the secondary side, which controls the primary side pressure.

After the reactor coolant pumps coast down, natural circulation replaces forced circulation. A void is created in the upper parts of the SG and at the top of the U-tubes. When overall circulation with continuous crossing at the top of the SG U-tubes is no longer possible, complete phase separation occurs (reflux condenser mode). Condensed steam then forms a countercurrent flow in the upward part of the SG U-tubes and returns towards the hot leg

and the RPV, falling into the upper plenum and the core, around and preferentially under the hot leg nozzles (3D water fall back).

Phase III: Loop seal filling and decrease with a decrease in RPV water level

The end of natural circulation creates a water slug in the crossover legs, which enables some independence between the pressure in the hot and cold legs. A pressure decrease is observed in the cold legs (partly due to the effect of the break and condensation by ECCS water) while pressure remains almost constant in the hot legs (it stabilises just above SG pressure so that the entire vapour created in the core is condensing in the SG tubes). As a result, the water level in the core decreases, possibly leading to cladding temperature excursion in the upper part of the core.

When the level in the downward part of the crossover leg passes under its horizontal section, the steam can go up into the upward part to reach the break, also removing part of the water slug (loop seal clearing). The pressure equilibrium which then follows between the upper plenum and the downcomer rebalances the core and downcomer water levels, ending any previous uncovering of the core.

Once the break has turned to steam, the volume balance between the steam produced by residual power and removed at the break (in addition to condensation in the SG tubes) is radically modified: depressurisation continues, reaching accumulator injection conditions and then low pressure safety injection (LPSI).

The core uncovering at the hot fuel assembly scale dries out of the uncovered part of the fuel rods, which are then only cooled by steam produced by water vapourisation below the swell level. This single-phase cooling is insufficient for removing the residual power and consequently the cladding temperature begins to rise. The overheated cladding also undergoes thermal-mechanical loads, possibly leading to clad deformation and subchannel blockage.

Phase IV: Accumulator injection, reactor coolant filling and core reflooding

Reaching accumulator injection pressure results in an increased flow being injected into the reactor circuit, which provides an immediate rise in the total reactor coolant mass and is followed by the core reflooding.

2.2.2.2 Key processes

This section identifies the dominant 3D phenomena regarding the PCT related to the core uncover level and duration and the downcomer water inventory during the refilling phase.

Redistribution of liquid in the primary coolant system

During the reflux condensation mode (Phases II and III), water flows back into the RPV. It flows back into the core in a multidimensional way. The downward water flow from the loops towards the core through the upper plenum takes place at the periphery of the core, where heat generation is generally lower and the steam flow weaker. This occurs preferentially close to the hot leg nozzles, from which the water from SG falls back. 3D modelling of the core in this scenario needs to account for this heterogeneous water fall back, and especially for its absence in some assemblies, including potentially the hottest assembly.

Crossflows in the core

The flow behaviour below and above the liquid during core uncovering is crucial to the core cooling. The heterogeneous core power induces 3D effects that generate crossflows whose nature is different above or below the swell level, depending on the pressure. More

powerful assemblies tend to produce more vapour below the swell level. One possible process is that the gravity tends to homogenise the void fraction and steam quality (see Figure 2.2.7 above). It is possible that the friction pressure drops above the swell level and at high pressure conditions is low compared to the gravitational component of the pressure. The hotter steam in the hotter assemblies is lighter and flows faster. It induces a crossflow from the colder to the hotter assemblies to balance the pressure field, which is also called the “chimney effect” (see Section 3.8) and has a beneficial impact for the hotter assemblies cooling.

Following the same assumption, the friction pressure drop becomes predominant when the pressure is low. A higher vapour velocity in this scenario means higher friction pressure drops. The steam crossflows thus appear from the hotter assemblies, where the velocity is higher, to the colder ones, where the velocity and the friction pressure drops are lower.

Refilling by accumulator injection

Condensation in the region surrounding the injected water for the largest intermediate breaks accelerates the primary depressurisation, leading to flashing of the downcomer water. When the cold accumulator water reaches the downcomer, it encounters boiling water and steam going upwards towards the break. The possibility to model geometrically differentiated flows in the downcomer requires the use of a 3D module in order to have different azimuths to let steam produced in the downcomer to go to the break, while accumulator cold water goes down in other azimuths below intact cold leg nozzles. In this configuration a 1D modelling of the downcomer would lead to a non-physical bypass of the accumulator water (going from intact cold leg directly to the broken leg).

For these three phenomena, 3D representation of the core is required to enable computing of the steam and liquid crossflows between assemblies of different temperatures.

2.2.2.3 *Known applications*

3D applications for IB-LOCA are increasingly more common in the literature. In [2.2.2-3], for example, a three inches’ cold leg break is simulated with CATHARE 3 and a 3D vessel. In this paper, non-conform junctions are used to combine cylindrical and Cartesian modelling for the different vessel zones (Cartesian for the core and cylindrical for the plenums, the upper-head and the downcomer).

Comparison of a Rig-of-safety Assessment/ large-scale test facility (ROSA/LSFT) test and the 3D module of CATHARE 2 is shown in [2.2.2-4]. Results provided by the 3D module showed promising capabilities.

2.2.3. *Main steam line break*

The main steam line break (MSLB) is relevant for PWR. The MSLB accident is initiated by a break of one of the main steam lines upstream from the main steam isolation valve.

Following a brief description of the transient sequence, the key processes are identified and 3D phenomena are detailed. The analyses hereafter are partially based on the reference reports [2.2.3-1] and [2.2.3-2]. Both reports are prepared for MSLB at full power condition, assuming single failure and the most reactive control rod is stuck.

2.2.3.1 *Transient description*

The initial condition for MSLB is normally assumed to be at the end of a cycle at full power, when the boron concentration is very small. The rapid decrease of moderator temperature caused by mass and energy discharge in the affected SG makes moderator density reactivity positive and the core returns to power after reactor trip.

The major concerns in a MSLB calculation are:

- the evaluation of the positive reactivity developed by the moderator temperature reactivity feedback as the core returns to power;
- the evaluation of the boron concentration injected by the safety injection system to reduce the reactivity rise;
- the large temperature and flow asymmetric effects through the vessel downcomer, lower plenum and at the core inlet;
- the heat transfer by single-phase vapour convection and nucleate boiling as the tubes start to be uncovered in the broken SG;
- the steam discharge flow rate through the break;
- the rapid radial and axial power redistribution due to moderator reactivity effect;
- the primary water inventory at the top of the pressure vessel, where voiding can appear because the primary water shrinks rapidly and this voiding can mitigate the primary pressure decrease.

According to the MSLB phenomena identification ranking table (PIRT), developed by KEPRI [2.2.3-1], the transient was divided into three phases. The first phase is the fast cooldown of primary coolant before the reactor trip on low primary pressure. The second phase corresponds to the rapid cooldown after the reactor trip and before safety injection. The third phase is after starting safety injection.

1st phase: period before reactor trip

The accident is initiated by a main steam line break. During this phase, the discharge flow through the break is choking flow. The large amount of steam discharge cools down the primary side. The primary temperature decrease makes the moderator temperature reactivity positive and reactor power increase. The reactor power increase and primary pressure decrease results in a decrease of the departure of nucleate boiling ratio (DNBR). The reactor is tripped by either high reactor power, low pressuriser pressure, low SG pressure or low DNBR.

2nd phase: period for rapid cooldown

This phase is the period between the reactor trip and start of safety injection. After the reactor trip, the pressuriser and pressure vessel dome void and the positive reactivity continuously increases. The water level of broken SG decreases or dries out if auxiliary feedwater is not supplied to the broken SG. The main steam isolation valve closes and the main feed water ceases. Minimum DNBR can occur just after the reactor trip signal due to the delay for reactor scram after the reactor trip signal and the time required for control rod drop.

3rd phase: period for safety injection

This phase is the period after broken SG dryout if no auxiliary feedwater flow exists. However, it is commonly defined as the safety injection phase when auxiliary feedwater flow is available in the plant design. The safety injection system is initiated if the pressuriser pressure falls below the safety injection set-point pressure. The reactivity reaches a maximum just before borated water enters the reactor core. The reactor power may experience return-to-power condition if the steam discharge through the broken SG cools down the primary side coolant.

2.2.3.2 Key processes

The key parameters for steam line break (SLB) are:

- possibility of a post-trip return to power;
- possible DNB before the reactor trip.

The phenomena cited below are linked with the previously mentioned key processes. The below paragraph describes the main 3D phenomena involved in this transient, phenomena for which a 3D modelling would improve the simulation performed by the system code.

The most relevant 3D phenomena affecting these processes are asymmetric power and temperature distributions.

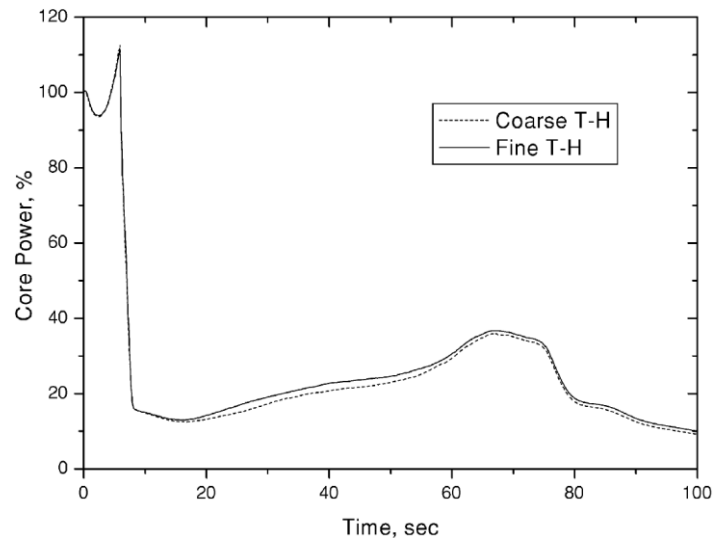
These phenomena are closely connected and a coupled 3D system T/H and 3D neutron kinetics calculation is essential for predicting the interactions between the core kinetics and fluid behaviour. Turbulent mixing and crossflow modelling in the downcomer and lower plenum are important for predicting the asymmetric moderator temperature in the core.

Due to the importance of coupled calculation of core neutronics, core T/H and system T/H simulation, OECD member countries performed PWR MSLB benchmark exercises [2.2.3-2]. Three exercises were performed, and the first two exercises were utilised to for the final exercise. A comparison of the results from the first exercise (performed using point-kinetics models) and the last (performed using 3D neutronics models and 3D -or pseudo-3D- T/H models) demonstrate that 3D analysis removes some of the conservatism inherent in point-kinetics analysis and reduces the peak local power by up to 25%. The differences are mainly caused by the inability of the standard point-kinetics approach to properly account for the detailed T/H feedback. As a result, the 3D core transient modelling provides a margin to recriticality over the point-kinetics approach during an MSLB analysis. This difference is highly significant concerning extended refuelling cycles and high burn-ups, which result in increasingly negative moderator temperature coefficients.

2.2.3.3 Known applications

In some existing safety analysis methodologies for MSLB, the T-H system, 3D reactor kinetics and hot channel analyses are performed separately (or chained) by independent codes and the results of one code are transferred to another as boundary conditions. During this process, some bounding hypotheses are introduced for a conservative analysis. For example, an accident event may have been analysed with a beginning of cycle moderator temperature coefficient and an end of cycle Doppler feedback coefficient. Although the use of these assumptions simplifies the safety analysis, it results in potentially large conservatisms. However, using coupled codes with consistent assumptions removes the excessive conservatism while sufficiently demonstrating the safety of the plant.

In this regard, numerous coupled “system T/H and 3D reactor kinetics” codes such as RELAP5/NEM, RELAP5/PARCS, RELAP5/PANBOX, CATHARE/CRONOS, TRAC-PF1/NEM and MARS/MASTER have been developed [2.2.3-3]. Their performance has been assessed using the NEA MSLB benchmark problem [2.2.3-4]. The calculation result of power history during MSLB scenario 2 is shown in Figure 2.8. In scenario 2, the problem is enforcing the return-to-power phenomenon by decreasing the negative scram rod reactivity. The NEA MSLB benchmark report concludes that the application of the state-of-the-art coupled 3D computer code systems can help improve the performance of nuclear power plants. It is necessary to develop a more in-depth knowledge of such code systems because 3D kinetic/T/H codes will play a critical role in future nuclear analysis.

Figure 2.8. Core-averaged total power time history for scenario 2 of OECD MSLB benchmark problem

Source: Joo et al., 2003.

2.2.4. Feed water line break

2.2.4.1 Description of the transient

A FWLB event is a DBA scenario for nuclear PWRs. When it occurs, it is followed by a rapid depressurisation and emptying of all the SGs' secondary sides, which triggers the reactor trip due to a low secondary-side SG level. During the reactor trip, the reactor cooling pumps (RCPs) are shut down, the steam lines are isolated via their main steam isolation valves (MSIV) and the auxiliary feedwater (AFW) starts delivering water to the unaffected SGs. The safety relief valves (SRV) evacuate the core decay power until the operator starts the cooldown procedure via the atmospheric relief valves (ADV). The objective is to reach the conditions that enable the RHRS connection.

2.2.4.2 Key parameters

A FWLB accident followed by a loss of offsite power (LOOP) is an asymmetric scenario where the presence of active and inactive SG can lead to the natural circulation (NC) interruption in the loop of the affected and isolated SG. The operators are generally instructed in these conditions to apply a prescribed linear cooldown rate in order to bring the plant to RHRS conditions. A cooldown rate limit is prescribed in the emergency operating procedures (EOP) in order to avoid both the formation of a steam bubble under the reactor vessel head during the depressurisation phase and the interruption of NC, which could be the origin of several problems, such as:

- The connection of the RHRS could be jeopardised because the temperature (in the suction lines of the loop of the affected SG) and /or the primary pressure is too high.
- A steam bubble could form during the depressurisation phase at the top of the inverted U-tubes (or elsewhere) of the corresponding SG.
- If there is poor or no circulation in a loop, the homogeneous boration of the RCS during the cooldown process could become problematic. Problems related to core recriticality could arise.

- Pressurised thermal shock phenomena could occur due to extremely low or stagnant flow and an operating safety injection (SI) system. In these conditions, fluid temperature stratification would take place and cold plumes could lead to welds and cracks appearing in thermal loads, which could threaten the pressure vessel's integrity.
- For some accidents, NC interruption leads to an increased release of radioactive products due to a longer cooldown phase; the latter also requires a larger SG feedwater supply.

2.2.4.3 Main 3D phenomena involved

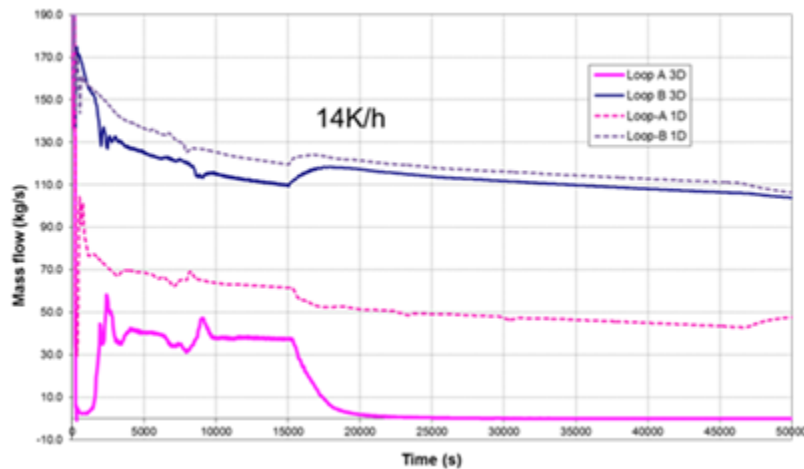
Flow mixing in the reactor pressure vessel (RPV) can play an important role in the course of the transient during a FWLB. This can impact the natural circulation flow during the cooldown phase of the primary system, particularly the flow in the affected loop. As soon as the cooldown phase begins, a counter buoyancy force in the affected loop begins to build up and this loop's mass flow rate gradually decreases. Continuous cooldown causes the counter driving force to become high enough to overcome the driving forces in the reactor vessel. As a result, the mass flow in the affected loop rapidly decreases until it stops altogether. The density difference in the downcomer and the reactor core causes the driving forces in the RPV. Consequently, the 3D flow and temperature mixing in the RPV during the cooldown phase, as well as the stratification in the downcomer, are the key parameters that govern the RPV buoyant driving forces.

2.2.4.4 3D applications

The emergency operating procedures under a postulated FWLB accident can enable the safe cold shutdown conditions by imposing a cooldown rate of 14K/h. This value was likely obtained using computational tools based on a 1D approach. However, until now, open literature has rarely investigated flow mixing in the RPV during a FWLB scenario using a 3D vessel model. The impact of a 1D or 3D RPV model on the NC interruption prediction is also not well known. An investigation using the CATHARE code shows differences in the NC interruption prediction when a 1D or 3D RPV downcomer model is examined [2.2.4-1]. The calculation results are shown below in Figure 2.9, which depicts how similar trends of the mass flow rates in the active loop have been predicted. Yet discrepancies have also been obtained between the coolant mass flow rates in the inactive loop. These differences increase when the cooldown starts. The 1D model does not predict the occurrence of natural circulation interruption (NCI) when a cooldown rate of 14 K/h is considered. However, when the 3D model with the same cooldown rate is used, NCI occurs. The presence of the stratification phenomenon and flow vortices in the downcomer is supposed to have an impact on the net flow rate through the inactive loop. Part of the total momentum goes to these vortices, and their presence forces the flow coming from the inactive loop to go in the azimuthal direction, instead of in the downward direction. Additionally, full mixing in the downcomer takes place when a 1D model is used and consequently the RPV driving force is uniform and remains high enough to allow for continuous positive flow in the inactive loop.

Overall, complex 3D mechanisms taking place during asymmetric cooldown single-phase natural circulation flow could not be accurately simulated using standard 1D code nodalisation. Detailed 3D representations would likely improve the simulation results.

Figure 2.9. 1D vs. 3D loop mass flow rates in the loop with inactive SG (loop-A) and the loop with active SG (loop-B) during FWLB+LOOP



Source: Salah and Vlassenbroeck, 2014.

2.2.5. Pressurised thermal shock (PTS)

2.2.5.1 Description of the transient

A fast depressurisation can be observed during a LOCA event in a pressurised water reactor (PWR) due to a break of the primary coolant loop. The pressure decrease induces the production of a large amount of vapour – the amount varying according to the break size – due to flashing. The flow in the core and part of the primary loop, can become two-phase. The pumps being switched off leads to a liquid vapour stratified flow in the cold legs and free surface in the downcomer with a plume of cold water, which flows from the cold leg into the downcomer in the vicinity of the wall.

The depressurisation results in the ECC being put in operation to cause primary circuit cooling. The first effect of the injection is the mixing with the ambient fluid in the cold leg and, consequently, a cooling of the flow in the downcomer and core. Large and fluctuating temperature differences between the liquid temperature and the vessel wall induce a heat exchange between the wall and the fluid. As a result, a temperature gradient appears inside the structure, which brings about a significant thermal stress in this part of the wall.

The pressure in the cold leg also slowly decreases during the ECC injection. The (still) high pressure in the primary circuit produces a mechanical stress on the vessel wall. Thermal stress in combination with high pressure is known as PTS. It can cause crack propagation through the wall in the region of the cold leg nozzle and downcomer [2.2.5-1]. A PTS analysis is thus required to ensure the vessel's integrity and monitor the reactor's life duration.

The probability of a vessel failure increases if the ECC injection induces thermal stratification in the liquid layer of the cold leg. The ECC injection is colder than the main liquid flow in the leg and therefore has greater density. Gravity effects thus tend to get the colder flow at to the bottom of the horizontal channel, with minimal mixing with the main flow until it reaches the downcomer and creates a thin cold layer along the vessel wall. It is possible to observe not only a vapour-liquid flow stratification, when there is the presence of vapour in the cold leg, but also a thermal liquid-liquid stratification in the cold leg and downcomer. The temperature of this cold layer can be much lower than the average coolant temperature in the other parts of the cold leg and downcomer. The associated

thermomechanical stress on the vessel wall can be more intense than in the case of well mixed flow.

The liquid stratified layer temperature distribution is highly important to the evaluation of the vessel wall stress. It can be calculated using a local modelling approach such as CFD codes. However, the most penalising conditions must be found for the purposes of a safety demonstration and vessel integrity has to be demonstrated for the most penalising cases. Many calculations must therefore be made. However, the required calculation time – as for a whole reactor CFD calculation – is not yet compatible for an industrial context. A calculation scheme based on short central processing unit (CPU) time is therefore extremely useful. The system code approach aims to provide calculations with an acceptable accuracy quickly. The system codes must be able to simulate the principal phenomena involved in this transient to perform this.

The envelop transient for PTS is the small break LOCA. The phenomena identified for SB-LOCA in paragraph 2.2.2 are therefore still relevant for the PTS, albeit with different levels of importance.

2.2.5.2 Key parameters

As previously mentioned, the most severe PTS conditions arise during a small break LOCA. However, the consequences are different from those caused by small break LOCAs because they are relative to the thermomechanical impact on the vessel wall. The key parameters for PTS are as follows:

- The primary circuit behaviour: the primary pressure tends to increase the thermomechanical stress in the vessel wall. Moreover, the safety injection rate is a function of the primary pressure. This parameter plays a major role.
- The vessel wall cooling: this includes both the liquid temperature near the vessel wall, and the heat transfer between the wall and liquid that influences the local wall cooling, temperature gradients and stresses inside the structure.

2.2.5.3 Main 3D phenomena

Each phenomenon that impacts either the primary circuit pressure and/or vessel wall cooling is relevant for PTS studies.

The primary pressure depends on the break flow rate and safety injection flow rate. These related processes are relevant to 3D phenomena. They are briefly mentioned below and in reference [2.2.5-2]:

- Phenomena involving safety injection in the horizontal cold legs: stratification, countercurrent flow, jet impingement on the wall (transverse flow), bubble entrainment and condensation. In system codes, these phenomena are generally modelled by a 1D module and complemented by specific closure laws, which take these 3D effects into account.
- Phenomena related to break flow: flashing and flashing delay, wall friction in the break location and interfacial friction in the break vicinity.

The phenomena which play a role in vessel cooling are:

- Phenomena involved in the downcomer liquid temperature in the vessel wall vicinity: one of the main issues of PTS studies is defining the liquid temperature in the vicinity of the vessel wall. The mixing phenomena in the downcomer are extremely important. In this scenario, the turbulent mixing, axial and transverse

mixing must be taken into account (the diffusion and dispersion of energy and momentum). Regarding the identification of SB-LOCA phenomena, the accumulator penetration in the downcomer must be well simulated in order to predict the cold water flow. The condensation in the downcomer is also an important parameter for the temperature evaluation. This includes direct contact condensation at the free surface and below the swell level, where bubbles can condense and affect the liquid temperature.

- Phenomena involved in the downcomer liquid velocity: this parameter, combined with the temperature difference between vessel wall and liquid temperature, is involved in the calculation of the heat transfer coefficient. The parameter is driven by gravitational effects, and accordingly the temperature must be accurately predicted. Other parameters influencing the liquid velocity are the interfacial friction, the wall friction, transverse flow fluctuations and bubble entrainment.
- Phenomena involved in the liquid/vessel wall heat transfer: Closure laws for all heat transfer regimes that can occur during a PTS transient at the downcomer location are extremely important (both natural and forced convection for both laminar and turbulent flows).

The main identified parameters for the PTS simulation at a 3D system-scale approach, at least for the downcomer, are:

- turbulence modelling (diffusion, dispersion for energy and momentum);
- transverse flow in the downcomer;
- accumulator penetration in the downcomer;
- direct contact condensation at the free surface and below the surface in case of bubble presence;
- interfacial friction;
- wall friction;
- liquid/wall heat transfer closure laws.

2.2.5.4. 3D applications

The pressure vessel or downcomer 3D modelling produces highly representative results for the liquid temperature distribution in the pressure vessel, but few results have been published that are dedicated to the PTS. The references [2.2.5-3] and [2.2.5-4] should nevertheless be mentioned, which illustrate 3D modelling with system codes for the mixing phenomenon in the downcomer. The reference [2.2.5-5] presents comparisons of temperature fields in a downcomer, obtained using SYSTH code and CFD for several representative PTS cases in VVER reactors.

Some advice regarding improvements to be made to the 3D modelling with system code can be provided. Non-conform junctions are not yet possible in most codes and therefore the downcomer azimuthal meshing is usually a function of the number of loops. Every junction between the downcomer and the cold leg must be affected to only one mesh cell and consequently the downcomer azimuthal mesh size is at least equal to the cold leg's diameter. This constrain means that the downcomer is often modelled by an azimuthal nodalisation equal to the double the loop number. The non-conform meshing development will be a step forward for PTS applications by allowing a finer meshing in the downcomer.

Currently, when the porous 3D approach does not model the turbulent diffusion and dispersion in an open medium, usually only one mesh is used in radial direction. Physical model development would also be a major improvement for PTS modelling in the system code by allowing for the use of finer mesh. A fine mesh in the downcomer (3D meshing instead of 2D) would be a significant improvement and would simulate the relevant PTS mixing phenomenon in this area more precisely. Consequently, the turbulent diffusion and dispersion terms must be modelled and validated to prove their relevance for downcomer flow conditions. This approach would create the possibility of modelling a quasi-open medium with the system code 3D module.

2.2.6. Spent fuel pool loss-of-cooling and LOCA

This section describes the safety issues related to a spent fuel pool loss-of-cooling or loss-of-coolant accident (SFP-LOCA). The main safety-relevant T/H phenomena are then described, which will be shown to be mostly 3D by nature.

2.2.6.1. Description of the transient

The first phase of a SFP-LOCA, whatever the scenario, involves a loss of water from the SFP to the point that the top of the spent fuel assemblies is uncovered. As long as the fuel is immersed in water and effectively cooled, it will not be damaged or degraded so that it releases radioactive fission products, provided that subcriticality is maintained in the pool. Subcriticality could be lost during the spent fuel pre-uncovery phase due to decreasing neutron absorption, caused by an increase in coolant void fraction and/or a decrease in coolant soluble boron concentration. Criticality in the SFP would provide an additional source of heat and radiation and also generate an inventory of short-lived fission products in the fuel that could add to the release of radioactive material later on in the accident. Immediate fuel damage by the criticality excursion cannot be precluded, although very little is currently known about the likelihood of its occurrence.

Besides the risk posed to criticality, safety issues during the pre-uncovery phase are also linked to an increased release of hydrogen, tritium and radioactive contaminants from the pool water while it heats up. These safety issues moreover include an insufficient protection against radiation, should the pool water level drop to less than about 0.6 m above the spent fuel assemblies (FAs). These issues could obstruct access to the SFP building, thus hampering mitigation measures, surveillance and control. Furthermore, the increasing water temperature and decreasing water level in the SFP could prevent the recovery of the SFP cooling when the normal cooling system is restarted, e.g. by pump cavitation or the loss of suction to the strainers in the upper part of the pool.

Boiling in the SFP could have several potential consequences if it occurs during the accident. Firstly, boiling would increase the release of hydrogen and radionuclides from the pool water to the building. Hydrogen is produced in the pool mainly by the radiolysis of water, and the radiolytic yield of H₂ increases in boiling conditions. Moreover, the solubility of hydrogen and other gases in the pool water would decrease as the pool heats up, releasing pre-existing gaseous species in dissolution to the building. Radionuclides in the pool stem from activated corrosion products deposited on the spent fuel, leaking fuel rods (if any) and tritium. Tritium (³H) poses a particular problem because it cannot be removed from the pool water by the normal purification system. It is mainly formed by ¹⁰B neutron capture and is therefore a problem predominantly in PWR and VVER plants, where boric acid is used for reactivity control in both the reactor and the SFP. Tritium is formed in the SFP but is also carried over from the reactor to the pool during refuelling. Since it has a half-life of 12.4 years, the SFP tritium inventory builds up over time.

Secondly, spent fuel pools are not designed to operate at high temperature. If boiling occurs the normal pool cooling system may prove difficult to restart because of pump cavitation and/or loss of suction at the strainers. Damage to the steel-lined concrete structure also cannot be precluded if the pool is operated in boiling conditions for a significant length of time. The technical safety limit for the SFP water temperature typically ranges between 65 and 90°C. This limit ensures the proper operation of the pool cooling and purification system and an acceptable SFP building environment for its personnel.

Thirdly, boiling may lead to loss of subcriticality when the storage racks are of a low density design (i.e. a design with large pitch between the stored fuel assemblies that make no use of borated structural materials). In this case, the water between the FAs would provide the main neutron absorption and a reduction in the effective water density by boiling would reduce the subcriticality margin.

2.2.6.2. Key parameters to be calculated

The key parameters are the level of water in the pool, water temperature and rate of evaporation when boiling occurs in the pool.

As the pool water heats up, the evaporation rate at the pool surface increases. Evaporation of water from the pool surface is considered the dominant mechanism for heat removal from a SFP with an inoperable cooling system, and it increases dramatically alongside the temperature when the water temperature exceeds about 340 K. The evaporation rate is sensitive to the air velocity and humidity above the pool surface. The evaporation rate also depends on the 3D natural convection heat transfer from the lower part of the pool to the pool surface.

Boiling mechanisms - The contribution of boiling mechanisms to the overall SFP loss of mass (in addition to the free surface evaporation), depends on the possible vapour bubble nucleation within the pool and vapour bubble flow across the pool. Bubble nucleation can occur due to different physical processes, each corresponding to specific conditions. One of the most common processes, wall heterogeneous nucleation on heated structures, is likely to first occur in the upper part of high-power FAs. Bulk nucleation processes by homogeneous nucleation (sometimes referred to as bulk or surface boiling) or heterogeneous nucleation (either on suspended solid particles or on free-moving non-condensable gas bubbles) are unlikely to significantly contribute to the SFP loss of mass, since it would require very large liquid superheats and/or high concentrations of suspended particles or non-condensable gas bubbles. Bubble nucleation along unheated solid surfaces such as pool walls or immersed solid structures – namely “pool flashing” - must be considered as a possible mechanism of vapour formation when the local liquid temperature well exceeds the saturation temperature. This condition would be expected to arise near the pool surface. Generally, the occurrence of nucleate boiling in an SFP depends on the 3D liquid temperature distribution within the pool, thereby on convective thermal mixing and power distribution between the FAs. It also depends on local conditions (wall heat flux and wall temperature of heated structures, surface roughness, wettability for unheated walls), as well as the water content in non-condensable gases, and the pool water level. The hot water that exits from high-power FAs and initiates nucleation processes is mixed with colder water as the fluid rises and bubbles may condense when the pool water level is high above the fuel racks. The impact of steam generated by bubble nucleation processes on the SFP loss of mass could therefore be weakened. Notably, even though bubble nucleation processes do not directly contribute to the SFP loss of mass, they could significantly contribute to the overall heat transfer from FAs to the pool surface; bubbling is understood to powerfully enhance convective heat transfer in comparison to single natural convection.

Water supply as a mitigation measure - Mitigation measures for the pre-uncovery phase of a SFP-LOCA include SFP building ventilation, to evacuate steam and heat, and pool water injection to compensate for evaporation and leakage. However, an injection of unborated water into a SFP that normally uses boric acid for criticality control would possibly reduce the subcriticality margin. The distribution of un-borated water within the pool is a 3D phenomenon by nature. This fact should be taken into account during SFP safety evaluations.

2.2.6.3. Main 3D phenomena

A SFP-LOCA is dominated by 3D T/H phenomena by nature. Analyses using CFD show that natural convection loops develop in the pool. The most modern storage rack designs for spent light water reactor (LWR) fuel have a closed cell design, in which each fuel assembly is enclosed in a separate cell within walls made of stainless steel or aluminium, and sometimes combined with neutron absorbing materials containing boron. This closed cell design allows for lateral crossflow in only the regions below and above the racks. The overall shape of the natural convection flow pattern in the pool largely depends on the location of free paths for water to flow downwards and on the distribution of fuel assemblies with regard to their power generation. The power generation stems from the radioactive decay of unstable fission products and actinides.

Flow reversal is made possible in low-power FAs due to natural convection in a large number of parallel heated channels that are fed by the same downcomer. As a result, unstable natural circulation flow can occur. Furthermore, the flow could be reduced and the cooling of the FAs perturbed in some channels, leading to local nucleate boiling. Another possible reason for the occurrence of local boiling is the natural convection flow in some FAs being perturbed by the outflow of water through a nearby leak. This is also a 3D thermal-hydraulic process by nature.

2.2.6.4. Known applications and main drawbacks of these applications

Several SPF accident analyses were performed using CFD [2.2.6-1] or SYSTH codes such as RELAP [2.2.6-2] but with pseudo-3D simulations and a junction between several channels to stimulate crossflows. Detailed information is provided in a specific chapter of NEA/CSNI report [2.2.6-3].

2.2.7. Passive safety systems

2.2.7.1. Introduction

A passive safety system (PSS) is defined as “a system which is composed entirely of passive components and structures or a system which uses active components in a very limited way to initiate subsequent passive operation” [2.2.7-1].

In contrast to active safety systems, which are the basis of the safety concept of currently operated reactors, a passive safety system uses physical processes such as natural convection heat transfer, vapour condensation, liquid evaporation, pressure-driven coolant injection or gravity-driven coolant injection.

According to [2.2.7-2], PSSs can be classified into two different groups:

1. PSSs used for decay heat removal;
2. PSSs used for containment cooling and pressure suppression.

The PSSs considered for the removal of decay heat from the core after a reactor scram are:

- accumulator: pre-pressurised core flooding tanks;
- core make-up tanks: elevated tank natural circulation loop;
- gravity drain tanks;
- passively cooled steam generator natural circulation;
- passive residual heat removal heat exchangers;
- passively cooled core isolation condensers;
- sump natural circulation.

The PSSs used to remove heat from the containment and reduce pressure inside the containment following a loss-of-coolant accident are:

- containment pressure suppression pools;
- containment passive heat removal/pressure suppression systems;
- passive containment spray.

The application of PSSs has a wide spectrum of embodiment; plant design specific features and common T/H phenomena of natural forces, large advanced light water reactors (ALWRs) and innovative SMRs. The weak driving forces of passive safety systems based on natural circulation, careful design and analysis methods should be considered to assure their intended safety functions.

2.2.7.2. Phenomena involved in the PSS

The T/H characterisation for the same systems requires a consideration of certain phenomena, i.e. PSS phenomena.

The identification and characterisation of phenomena involved in the operation of passive systems are presented in Table 2.1 [2.2.7-2].

Table 2.1. PSS phenomena identification

Phenomena identification	Characterising thermal-hydraulic aspect
1) Behaviour in large pools of liquid (including surrounding SMR)	Thermal stratification
	Natural/forced convection and circulation
	Steam condensation (e.g. chugging, etc.)
	Heat and mass transfer at the upper interface (e.g. vapourisation)
	Liquid draining from small openings (steam and gas transport)
2) Effects of non-condensable gases on condensation heat transfer	Effect on mixture to wall heat transfer coefficient
	Mixing with liquid phase
	Mixing with steam phase
	Stratification in large volumes at very low velocities
3) Condensation on containment structures	Coupling with conduction in larger structures
4) Behaviour of containment emergency systems (PCCS, external air cooling, etc.)	Interaction with primary cooling loops
5) Thermo-fluid dynamics and pressure drops in various geometrical configurations	3D large flow paths, e.g. around open doors and stair wells, connection of big pipes with pools, etc.
	Gas liquid phase separation at low Re and in laminar flow
	Local pressure drops
6) Natural circulation	Interaction among parallel circulation loops inside and outside the vessel
	Influence of non-condensable gases
	Stability
	Reflux condensation

Source: IAEA, 2009.

Table 2.1. PSS phenomena identification (Continued)

Phenomena identification	Characterising thermal-hydraulic aspect
7) Steam liquid interaction	Direct condensation
	Pressure waves due to condensation
8) Gravity-driven cooling and accumulator behaviour	Core cooling and core flooding
9) Liquid temperature stratification	Lower plenum of vessel
	Downcomer of vessel
	Horizontal/vertical piping
10) Behaviour of emergency heat exchangers and isolation condensers	Low pressure phenomena
11) Stratification and mixing of boron	Interaction between chemical and thermo-hydraulic problems
	Time delay for the boron to become effective in the core
12) Core make-up tank	Thermal stratification
	Natural circulation

Source: IAEA, 2009.

The T/H performance of PSSs is characterised by no less than a dozen key phenomena, which were then characterised through specific descriptions, including multiple relevant T/H aspects as shown in Table 2.1.

Particular attention should be paid to the natural circulation phenomenon, which is an important aspect in a PSS's operation (see e.g. phenomena 1, 6 or 12 of Table 2.1).

The implementation of natural circulation as a central mechanism (e.g. for nuclear core heat removal, either directly or through the use of passive safety systems) appears to require a thorough understanding of local and integral system natural circulation phenomena, validated benchmark data, accurate predictive tools, as well as comprehensive and reliable analysis methods.

There are three important reasons for identifying the local and integral system phenomena that can impact the natural circulation behaviour of a PSS or nuclear plant design:

1. Some local and integral system phenomena could adversely affect the reliability of PSSs.
2. Some model developments may be needed to accurately model these phenomena using predictive tools.
3. All significant phenomena must be faithfully simulated in the test facilities when used to assess the safety and operation of an advanced plant design.

A predictive tool, such as a computer code, must be assessed against applicable experimental data before it can be used in the design or analysis of a reactor system. The uncertainty in the code's predictions of key safety parameters must be established and its ability to model system operation during normal and transient conditions demonstrated. These are the typical requirements for obtaining final design approval and plant certification. Although numerous natural circulation experiments have been conducted, it can be difficult to find a database that directly relates to new design. A new, properly scaled, test facility will likely need to be designed and operated to obtain a sufficiently broad range of data for the code to be fully exercised and assessed.

T/H aspects related to passive systems are studied in another Working Group for the Analysis and Management of Accidents (WGAMA) activity [2.2.7-3].

The principal local transport phenomena encountered in the natural circulation systems of an advanced water cooled reactor are detailed below:

- a) reactor core phenomena;
- b) interconnecting piping;
- c) heat sinks (steam generators);
- d) passive residual heat removal systems;
- e) containment shells (external air or water cooling);
- f) containment cooling condensers/heat exchangers;
- g) large cooling pools (for heat exchangers, spargers and as a source of coolant).

The integral system behaviour is complex due to the coupling of many local transport phenomena occurring in components and subsystems. The predictive tools used to describe integral system phenomena typically consist of systems' analysis computer codes. The system transport phenomena are detailed below:

1. working principles of a natural circulation loop.

The buoyancy force (that drives the fluid through the loop) produced by the density difference and acted on by gravity over the difference in elevation between the source and the sink is known as natural circulation.

2. instabilities in natural circulation systems.

The T/H instability is any periodic time oscillation of flow, flow pattern, temperature, fluid density, pressure or core power in a T/H system. Such oscillations can arise in multiple parameters simultaneously, may be in-phase or out-of-phase with each other, and can be present at multiple locations in the system.

The evident advantages of using natural circulation as a means of core heat removal have prompted the worldwide development of separate effects and integral system test facilities. The data from these facilities has been used to both identify a wide range of T/H phenomena that are important to natural circulation systems and also to assess the predictive capabilities of a variety of T/H analysis codes.

Passive heat removal using large water pools

Large pools of water at near atmospheric pressure have been incorporated into several advanced reactor designs. Some examples include:

- the pressure suppression pool (wet well) of the economic simplified boiling water reactor (ESBWR);
- the in-containment refuelling water storage tank (IRWST) of the advanced pressurised 1 000 (AP-1000) and advanced power reactor 1400 (APR1400);
- the flooding pool of the KERENA reactor (Siedewasserreaktor-1000 [SWR-1000]);
- the pool of the passive auxiliary feedwater system (PAFS) of the advanced power reactor plus (APR+);
- the gravity-driven water pool of the advanced heavy water reactor (AHWR);

- the flooded reactor pool of the NuScale modular reactor;
- the reactor water storage tank of the mPower.

These large pools provide a heat sink for either heat removal from the reactor or containment by means of natural circulation inside the pool and evaporation of the water inventory, as well as a source of water for core cooling. Heat exchangers consisting of vertical or almost horizontal tube bundles are used for the heat transfer. Due to the limited zone in terms of volume, a wide spectrum of geometric configurations in the large pools is possible, which results in an inhomogeneous distribution of pool temperature and thermal stratification. Depending on the considered reactor's design, the water reservoir (together with connected components, e.g. those used for heat transfer) is especially important to the control of many of the initiating events. The following paragraphs provide a description of the processes typically occurring inside the pool during operation.

Description of the operation method

Thermal stratification can occur during the heating of the water inside the pool by an immersed heat exchanger, with the lowest temperatures below and the highest within the heat exchanger. Temperature decreases above the heat exchanger due to mixing with unheated water at the top of the pool. The inhomogeneous temperature distribution causes natural circulation inside (parts of) the large water pool. Subcooled boiling can occur on the heat exchanger's surface, with the rest of the water inventory temperature below saturation. Pressure inside the containment only increases slowly during this state of the operation. Once all the water inside the pool is in saturation conditions, boiling strongly increases pressure within the containment. Additionally, injected steam may be released from the pool into the containment and further increase pressure. Unlike most large pools, the pool of PAFS of the APR+ is located outside the containment. However, temperature stratification is also important in the pool of PAFS because thermal stratification and natural circulation play a key role in heat transfer between the heat exchanger and the water pool.

If other passive systems with non-active (i.e. small) driving forces are implemented in the facility, the processes inside the pool would trigger these systems' activation. An example is the interaction of the emergency condenser and the containment cooling condenser of the KERENA SWR-1000 design. The containment cooling condenser is located above the flooding pool, which is heated up by the emergency condenser. After the steam evaporated from the flooding pool comes into contact with the containment condenser's tubes, heat removal is initiated. The heat transfer is affected by the local concentration of non-condensable gases within the containment. Ultimate heat sink of the containment cooling condenser also occurs in a large water pool.

Several advanced reactor designs implement core make-up tanks (CMTs) to provide natural circulation cooling to the core. CMTs are elevated tanks connected to the reactor vessel and primary loop at the top and bottom of the tank. Special lines connect the bottom of the tank with the reactor vessel, termed DVI. An important interaction occurs between the CMT, accumulator and IRWST in relation to DVI and the actuation signal for automatic depressurisation. The tanks are filled with cold borated water and can provide coolant injection at system pressure. The tanks are normally isolated from the reactor vessel by an isolation valve located at the bottom of the vessel. The fluid always senses the full system's pressure through the top connection line. In the event of an emergency, the bottom isolation valve opens to complete the natural circulation loop and permit cold borated water to flow to the core. The relative elevation of the core compared to the CMT, and the density difference between the hot primary system water and the cold CMT water creates a

buoyancy-driven natural circulation flow that eliminates the need for a pump. Decay heat is removed from the core by convective heat transfer from the fuel to the single-phase liquid in the reactor vessel. CMT behaviour includes natural circulation, liquid thermal stratification in the tank, and liquid flashing during plant depressurisation.

2.2.7.3. Key parameters

The most important parameter of a PSS using a large water pool for heat removal is the heat exchanger tube bundles' heat transfer capacity. The heat transfer depends on the single- or two-phase flow states on the tubes' inside and outside. Heat transfer capacity on the pool-side of the heat exchanger tube bundle, where pronounced 3D flows establish, is mainly influenced by the following parameters:

- single- and two-phase heat transfer in (almost) horizontal or vertical tube bundles, depending on the particular design;
- fluid temperature in the pool;
- fluid velocity in the pool and around the tubes;
- the degree of temperature mixing inside the pool;
- heat and mass transfer between the water inventory of the pool and the containment.

2.2.7.4. Main 3D phenomena

The parameters identified in the previous section are the most significant for the heat transfer capacity of a PSS and are mainly influenced by the flow state inside the pool. A 3D two-phase modelling of the macroscopic natural circulation processes inside the pool would capture flow behaviour and corresponding temperature distribution and evaporation in the pool.

The following most significant 3D phenomena that have to be simulated by a SYSTH code can be considered:

- 3D natural circulation: it determines the temperature distribution and fluid velocity inside the pool and in the region of the tube bundles.
- (Subcooled) nucleate boiling at the tube's surface and rising bubbles: both directly affect the degree of 3D mixing inside the pool due to increasing buoyancy effects and fluid velocity.
- The condensation of bubbles inside the water reservoir and release of vapour out of the pool into the containment: the strength of these interdependent processes influences the heat and mass release out of the pool and thereby the degree of subcooling inside the pool. A sufficiently exact description of the free water surface inside the pool must be provided by the employed simulation code in order to capture this phenomenon.
- The condensation and evaporation at the free surface of the water: these processes affect the water inventory of the pool. Their simulation requires a detailed resolution of the free water surface as well as a consideration of the effect of non-condensing gases in the atmosphere on the mass transfer rate across the water level. The fluid at the top of the pool can reach the saturation temperature while the bulk fluid is still subcooled, depending on the actual temperature distribution. Temperature stratification thus influences local evaporation. Condensation and evaporation also impact the pressure increase inside the containment.

Another important quantity that directly affects the heating and natural circulation in the pool is the two-phase heat and condensation transfer at the heat exchanger tubes' inner and the outer surfaces. Adequate heat transfer correlations for the prevailing flow regimes and fluid conditions must be implemented. The correlations need to account for the 3D bundle character of the horizontal or vertical tubes used. 3D flows and the 3D nature of the temperature stratification in all the above described phenomena require appropriate modelling. The simulation of a large pool with an acceptably fine grid to capture the relevant flow processes is generally also necessary. The turbulent diffusion and dispersion terms are significant for temperature mixing phenomena. The processes at the free water surface must also be considered for the simulation of two-phase flows, interfacial friction and heat and mass transfer.

Some rather coarse 3D nodalisations were used to model such passive systems with a porous region and open medium that captured the phenomena rather well. These situations usually have turbulence mixing effects over-shadowed by density gradients. However, other situations more sensitive to turbulence mixing may require a finer nodalisation of all zones with shear flows.

2.2.7.5. *Known applications*

In the past, several CFD codes have been employed to simulate (single-phase) natural circulation and temperature stratification inside a water pool, which was used as heat sink in a PSS [2.2.7-4]. Recently, the 3D model of Analysis of THERmal-hydraulics of LEaks and Transients (ATHLET) was employed to simulate the flooding pool of the INtegral Test Facility KARlstein (INKA) test facility, representing the KERENA SWR-1000 design. The T/H aspects that had to be captured with ATHLET were:

- heat transfer from the primary side to the pool's water inventory;
- single- and two-phase natural circulation inside the pool;
- tracking of 3D water level;
- boiling and vapour release to the containment across the free water surface.

The following tests were simulated [2.2.7-5]:

- separate effect tests;
- emergency condenser tests for the simulation of thermal stratification within the core flooding pool during heat-up by the EC;
- passive core flooding test, with focus on the mixture-level-tracking model of ATHLET to capture drainage of the flooding pool;
- IET;
- main steam line break (MSLB);
- additional calculations are intended for the future: feed water line break, RPV bottom leak and station blackout.

References

- [2.1-1] Kliem, S. and R. Franz (2012), “OECD PKL2 Project – Final Report on the ROCOM Tests”, HZD\FWO\2012\03, Forschungszentrum Rossendorf, Dresden.
- [2.1-2] NEA (2017), “Summary Report of the NEA ATLAS-2 Joint Project”, OECD Publishing, Paris, www.oecd-nea.org/jcms/pl_65730.
- [2.2.1-1] Dempster, W.M. and D.S. Abouhadra (1994), “Multidimensional two-phase flow regime distribution in a PWR downcomer during an LBLOCA refill phase”, *Nuclear Engineering and Design*, 149(1-3), pp. 153-166.
- [2.2.1-2] Yadigaroglu, G., R.A. Nelson, V. Teschendorff, Y. Murao, J. Kelly and D. Bestion (1993), “Modelling of Reflooding”, *Nuclear Engineering and Design*, 145(1-2), pp. 1-35.
- [2.2.1-3] Shaw, R.A., S.Z. Rouhani, T.K. Larson and R.A. Dimenna (1988), “Development of a phenomena identification and ranking table for thermal-hydraulic phenomena during a PWR Large-Break LOCA”, *NUREG/CR-5074*, EG&G Idaho, Inc.
- [2.2.1-4] Kraftwerk Union AG (1987), “Test No. 5 Downcomer Separate Effect Test”, 2D/3D Program Upper Plenum Test Facility Quick Look Report, U9 316/87/17, KWU, Erlangen, Germany.
- [2.2.1-5] Hochreiter, L.E., F.B. Cheung, T.F. Lin, C. Frepoli, A. Sridharan, D.R. Todd and E.R. Rosal (2010), “Rod bundle heat transfer test facility test plan and design”, *NUREG/CR-6975*, US Nuclear Regulatory Commission, Washington, DC.
- [2.2.1-6] Damerell, P.S. and J.W. Simons, editors (1993), *Reactor Safety Issues Resolved by the 2D/3D Program*, *NUREG/IA-0127*, US Nuclear Regulatory Commission, Washington, DC.
- [2.2.1-7] Frepoli, C., K. Ohkawa and R.M. Kemper (2004), “Realistic Large Break LOCA Analysis of AP1000 with ASTRUM”, *NUTHOS-6*, 4-8 October, Nara, Japan.
- [2.2.1-8] Sauvage, J.-Y. and M. Keldenich (2005), “ESM-3D: A fully-extended Statistical Method based on CATHARE 3D for LOCA transient analyses”, *ICONE13*, 16-20 May, Beijing.
- [2.2.1-9] Jang, H.W., S.Y. Lee, S.J. Oh and W.B. Kim (2017), “The sensitivity analysis for APR1400 nodalisation under large break LOCA condition based on MARS code”, *Nuclear Technology and Radiation Protection*, 32(1), pp. 10-17.
- [2.2.1-10] Clarno, K.T. and Y.A. Hassan (2003), “Development of a RELAP5-3D Multidimensional Model of a VVER-1000 NPP for Analysis of a Large-Break Loss-of-Coolant Accident”, *Nuclear Technology*, 141(2), pp. 142-156.
- [2.2.1-11] US NRC (1988), “Compendium of ECCS [Emergency Core Cooling Systems] research for realistic LOCA [loss-of-coolant accidents] analysis: Final report”, *NUREG 1230*, US Nuclear Regulatory Commission, Washington, DC.
- [2.2.1-12] Glaeser, H. and U.S. Rohatgi (2019), “Scaling ability of the counter-current flow limitation (CCFL) correlations for application to reactor thermal-hydraulics”, *Nuclear Engineering and Design*, 354.
- [2.2.1-13] Kwon, T.-S., C.-R. Choi and C.-H. Song (2003), “Three-dimensional analysis of flow characteristics on the reactor vessel downcomer during the late reflood phase of a postulated LBLOCA”, *Nuclear Engineering and Design*, 226(3).
- [2.2.1-14] Bestion, D. and L. Matteo (2015), “Scaling considerations about LWR core thermalhydraulics”, *NURETH-16*, 30 August-4 September, Chicago.

- [2.2.2-1] Aksan, N. (2008), “International Standard Problems and Small Break Loss-of-Coolant Accident (SBLOCA)”, *Science and Technology of Nuclear Installations*.
- [2.2.2-2] NEA (1997), “Lessons learned from OECD/CSNI ISP on small break LOCA”, OECD/GD(97)-10, OECD Publishing, Paris, www.oecd-nea.org/jcms/pl_16140.
- [2.2.2-3] Pr ea, R., V. Figerou, A. Mekkas and A. Ruby (2017), “CATHARE-3: A first computation of a 3-inch-break loss-of-coolant accident using both Cartesian and cylindrical 3d-meshes modelling of a PWR vessel”, *NURETH-17*, 3 September, Xi’an, China.
- [2.2.2-4] Mazgaj, P., J.-L. Vacher and S. Carnevali (2015), “Comparison of CATHARE results with the experimental results of cold leg IB-LOCA obtained during ROSA-2/LSTF Test 7”, *ICAPP ‘15*, 3-6 May, Nice, France.
- [2.2.3-1] Korea Atomic Energy Research Institute (2007), “Non-LOCA PIRT for PWR”, S06NX08-E1-RD-03, Korea Atomic Energy Research Institute.
- [2.2.3-2] NEA (2003), “PWR MSLB Benchmark: Volume 4: Results on Phase III on Coupled Core-Plant Transient Modelling”, OECD Publishing, Paris, www.oecd-nea.org/jcms/pl_13542.
- [2.2.3-3] Cho, N.Z (2005), “Fundamentals and recent developments of reactor physics methods”, *Nuclear Engineering and Technology*, 37(1), pp. 25–78.
- [2.2.3-4] Joo, H.G., J.J. Jeong, B.O. Cho, W.J. Lee and S.Q. Zee (2003), “Analysis of the OECD Main Steam Line Break Benchmark Problem using the Refined Core Thermal-Hydraulic Nodalisation Feature of the MARS/MASTER Code”, *Nuclear Technology*, 142(2), pp. 166-179.
- [2.2.4-1] Salah, A.B. and J. Vlassenbroeck (2014), “Analytical Assessment of Natural Circulation Interruption Phenomenon in a 2-loop NPP”, Belgium: Bel V.
- [2.2.5-1] Bessette, D.E., W. Arcieri, C.D. Fletcher and R. Beaton (2005), “Thermal-Hydraulic Evaluations of Pressurized Thermal Shock”, NUREG-1809, US Nuclear Regulatory Commission, Washington, DC.
- [2.2.5-2] Lucas, D. and D. Bestion (2007), “On the simulation of two-phase flow pressurized thermal shock (PTS)”, *NURETH 12*, 30 September- 3 October, Pittsburgh, United States.
- [2.2.5-3] Salah, A.B., and J. Vlassenbroeck (2017), “Unsteady single phase natural circulation flow mixing prediction using CATHARE three-dimensional capabilities”, *Nuclear engineering and Technology*, 49(3), pp. 466-475
- [2.2.5-4] Mukin, R., R. Puragliesi, S. Ceuca, H. Austregesilo and A.B. Salah (2017), “Thermal mixing assessment using 3D thermal-hydraulic and CFD codes”, *NURETH 17*, 3-9 September, Xi’an, China.
- [2.2.5-5] Kral, P. and L. Vyskocil (2018), “Thermal-Hydraulic Analyses for PTS Evaluation. Comparison of Temperature Fields at RPV Predicted by System Code and CFD Code”, *ICONE26*, 22-26 July, London.
- [2.2.6-1] Boyd, C.F. (2000), “Predictions of Spent Fuel. Heatup After a Complete Loss of Spent Fuel Pool Coolant”, NUREG-1726, US Nuclear Regulatory Commission, Washington, DC.
- [2.2.6-2] Zhang, Z.W., Y. Du and K.S. Liang (2017), “Advanced modelling techniques of a spent fuel pool with both RELAP5 and MELCOR and associated accident analysis”, *Annals of Nuclear Energy*, 110, pp. 160–170.
- [2.2.6-3] NEA (2015), “Status Report on Spent Fuel Pools under Loss-of-Cooling and Loss-of-Coolant Accident Conditions: Final report”, OECD Publishing, Paris, www.oecd-nea.org/jcms/pl_19596.
- [2.2.7-1] IAEA (1991), “Safety Related Terms for Advanced Nuclear Plants”, IAEA-TECDOC-626, IAEA, Vienna.

- [2.2.7-2] IAEA (2009), “Passive Safety Systems and Natural Circulation in Water Cooled Nuclear Power Plants”, IAEA-TECDOC-1624, IAEA, Vienna.
- [2.2.7-3] NEA (forthcoming), “Status Report on Reliability of Thermal-Hydraulic Passive Systems”, NEA/CSNI/R(2021)2, OECD Publishing, Paris.
- [2.2.7-4] Krepper, E. and M. Beyer (2010), “Experimental and numerical investigations of natural circulation phenomena in passive safety systems for decay heat removal in large pools”, *Nuclear Engineering and Design*, 240(10), pp. 3170–3177.
- [2.2.7-5] Buchholz, S., P. Schöffel and A. Schaffrath (2017), “Exemplification of the AC² Multidimensional Capabilities to the Application of Large Pools within the Frame of the German EASY Project”, *NURETH-17*, 3-8 September, Xi’an, China.

3. Physical models

3.1. Flow regime identification

Flow regime identification is highly important to the development of physically-based mechanistic closure laws. Interfacial transfers greatly depend on the interfacial structure, which can include bubbles and drops of various sizes, and large interfaces such as free or film surfaces. Wall heat and momentum transfers also depend on the flow regime. Flow regime maps exist on an experimental basis for two-phase flows in horizontal and vertical pipes and for pre- and post-critical heat flux (CHF) conditions in the context of wall heating. However, no such flow regime map exists for the various sub-components of a light water reactor (LWR) pressure vessel. This was a difficulty for the zero-dimensional (0D) and one-dimensional (1D) modelling of the annular downcomer, lower plenum, core rod bundle, upper plenum and upper-head. There is limited information available for flow regimes in the core, which is the most important component in safety analyses. Various system codes have implemented flow regime maps that depend to a certain extent on flow geometry. For example, the Code for Analysis of THERmalhydraulics during an Accident of Reactor and safety Evaluation (CATHARE) code developed in the 1D module gives specific interfacial friction correlations for tubes, rod bundles and annuli. This is almost the same case for Analysis of THERmal-hydraulics of LEaks and Transients (ATHLET), for which the geometry, tube or bundle is additionally considered for the wall heat transfer. However, all other closure laws do not depend on geometry. For example, in CATHARE, with a 3D modelling of a core, the rod bundle interfacial friction that was developed for 1D is used whatever the flow direction. Therefore, there is no consideration of the impact of the flow direction on the flow regime. A specific set of interfacial friction models is used in the annular downcomer, which was based on the upper plenum test facility (UPTF) tests' analysis. A keyword was necessary in the CATHARE code development for a 0D modelling of lower plenum and upper plenum. The keyword identified the component and activated specific closure laws controlling the lower plenum voiding, remaining mass at the end of a large break loss-of-coolant accident (LB-LOCA) blowdown and de-entrainment in the upper plenum during a LB-LOCA's reflooding phase.

Much more has to be done to achieve a complete and detailed modelling of the geometrical effects in a pressure vessel's sub-components in all situations of the domain of simulation. Only dominant phenomena in some LOCA situations have so far been considered and treated in some dedicated closure laws that model some geometry-dependent flow regimes.

3.2. Scale-dependent modelling and mesh convergence

All principal variables in 1D models of system codes are functions of abscissa and time solutions of the set of partial differential equations. The equations are discretised to be solved, and mesh convergence and time step convergence tests are necessary to minimise numerical error. The tolerance criteria depend on the situation of interest and required simulations' accuracy. In many cases, the use of rather coarse meshes is acceptable although the first-order upwind scheme induces rather high numerical diffusion. The axial evolutions of flow parameters are often dominated by convective and source terms due to wall and interfacial transfer. As a result, axial diffusion (molecular and turbulent) is negligible, as well as numerical diffusion.

What is often termed 1D flows are in fact 3D flows with a privileged direction, for example in a pipe or rod bundle, when the flow is parallel to the rods. However, strong gradients of

flow parameters (phase velocities, phase temperatures and void fraction) exist in the radial direction due to wall friction and wall heat transfers. Such gradients induce high molecular and turbulent diffusion terms, which are simply modelled as algebraic wall transfers (wall friction and wall heat fluxes).

The use of a time and space averaging, or the integration over the given space domains of a pressure vessel (PV) in a porous 3D model filters all mixing processes at the space filter scale. All turbulent time fluctuations are filtered. Some of the space gradients are also filtered. Both time and space filters can lead to mixing processes that affect the mean variables and require specific models. Time averaging can be assumed to cover the spectrum of turbulent time fluctuations – as in a single-phase Reynolds-averaged Navier-Stokes (RANS) approach – and requires turbulent diffusion models. However, the use of a space averaging or integration requires scale-dependent dispersion terms to model the mixing effects, which depends on the space filter scale. Dispersion terms can therefore be treated as a turbulent viscosity (conductivity) in single-phase large eddy simulation (LES) model.

Two slightly different approaches can be used in porous 3D SYSTH codes:

1. A homogenised space-filtering approach: all equations are filtered using convolution products. This results in a homogenised problem and the solution will produce continuous filtered flow variables in time and space. In this approach, the required mesh size is smaller than (or at least equal to) the space filter.
2. A space integration approach: space integration is used for volumes linked to the solid structures. For example, there is the subchannel analysis approach in a core, with integration over the volume of each subchannel in the radial direction. There may be other more macroscopic approaches with an integration over the assembly or part of the assembly, or even a volume containing several assemblies. The result is a discretised problem with a juxtaposition of 0D interconnected control volumes. In this approach, the mesh size is equal to the space integration scale.

The former is a rather theoretical approach, which can help for the general derivation of equations. However, using it results in the link to the physical reality being partly lost and the second approach might make physical modelling easier, which is preferable for engineering applications.

The homogenised filtered approach requires time and space convergence in the same way as the 1D models, with the difference that there are greater chances of having gradients in three directions than in the axial direction of the flow.

For the space integration approach, the models for all diffusive processes must depend on the mesh size. The validation should also be made dependent on the mesh size and determination of the uncertainty of each closure law. No mesh convergence is required, but only a time step convergence. However, determining the model accuracy or uncertainty as a function of the space scale is a similar exercise to doing mesh convergence study in a homogenised space filtered model.

The mesh size in the code application to reactor transients should be similar to the one used for the validation, and the uncertainty should account for the mesh size dependence.

3.3. Wall friction and singular pressure losses

Wall friction terms in gas and liquid momentum equations in a standard 1D two-fluid model are usually derived from old correlations that were developed for 1D three-equation models [3-1] and [3-2]. Such models were developed from tube data, and therefore not flow regime

dependent, but covered the whole domain of void fraction in a continuous way. A phase repartition of the total friction term for the two-phase mixture is necessary, which requires further result interpretation from data analysis because it is impossible to measure wall-to-vapour and wall-to-liquid friction separately. This repartition can result from physical assumptions about the flow regimes. Successive modifications of the old models were found necessary in the CATHARE code after the comparison of a large data base and two flow regime transitions in the final modelling. The stratification criterion and the onset of droplet entrainment are used in the wall friction model, which now considers three possible situations¹:

- stratified flow regime;
- non-stratified bubbly-slug-churn-annular flow regimes;
- non-stratified annular-mist flow regime.

The general formulation of the wall-to-phase k friction term τ_{wk} in 1D models is:

$$\tau_{wk} = -\chi C_k C f_k \rho_k \frac{|V_k| V_k}{2}$$

χ is the friction perimeter (m)

$C f_k$ is the single-phase wall friction coefficient

C_k is a two-phase multiplier that depends on the flow regime

In a portion of duct of length L, the friction pressure loss is therefore:

$$\Delta P_{fr} = -\frac{4L}{D_h} \left[C_g C f_g \rho_g \frac{|V_g| V_g}{2} + C_l C f_l \rho_l \frac{|V_l| V_l}{2} \right]$$

with:

$$D_h = -\frac{4A}{\chi}$$

The models for C_k and $C f_k$ are validated for tubes and have been extrapolated to annuli and rods, or tube bundles, due to the lack of experimental data in all geometries.

The same friction terms can be used in 3D models with two possible extrapolations:

$$\tau_{wk,j} = -\chi_j C_{k,j}(|V_{k,j}|) C f_{k,j}(|V_{k,j}|) \rho_k \frac{|V_{k,j}| V_{k,j}}{2}$$

or

$$\tau_{wk,j} = -\chi_j C_{k,j}(\|\vec{V}_k\|) C f_{k,j}(\|\vec{V}_k\|) \rho_k \frac{\|\vec{V}_k\| V_{k,j}}{2}$$

χ_j is the friction perimeter for a flow along the j direction (m)

$V_{k,j}$ is the j-component of the velocity vector for phase k (m/s)

$\tau_{wk,j}$ is the j-component of the friction for phase k (N/m)

¹ As implemented in CATHARE.

The second formulation is supposed to be more physically based (the friction vector is collinear to the velocity vector) but the first formulation may be preferable when large meshes are used for numerical reasons.

The pressure repartition along walls in singular geometries induces some pressure losses that are expressed in the following way in 1D one-phase models:

$$\Delta P_{sing} = -K \rho \frac{|V|V}{2}$$

The form loss coefficient can only be a constant dependent on geometry, or a function of the Reynolds number. A repartition of the singular pressure loss term is necessary in two-phase flow. A simple repartition is implemented in the CATHARE code:

$$\Delta P_{sing,k} = -K \alpha_k \rho_k \frac{|V_k|V_k}{2}$$

However, this repartition induces a rather strong perturbation of the void fraction and slip ratio. Since no experimental data can provide sufficient information for this repartition, the total singular pressure loss term is usually modelled and a repartition may be chosen which does not influence the slip ratio. It must satisfy the following conditions:

$$\begin{aligned} \Delta P_{sing,v} + \Delta P_{sing,l} &= \Delta P_{sing} \\ (1 - \alpha)\Delta P_{sing,v} - \alpha\Delta P_{sing,l} &= 0 \end{aligned}$$

This is obtained with the following repartition

$$\begin{aligned} \Delta P_{sing,v} &= \alpha\Delta P_{sing} \\ \Delta P_{sing,l} &= (1 - \alpha)\Delta P_{sing} \end{aligned}$$

The total singular pressure, loss may be expressed as follows:

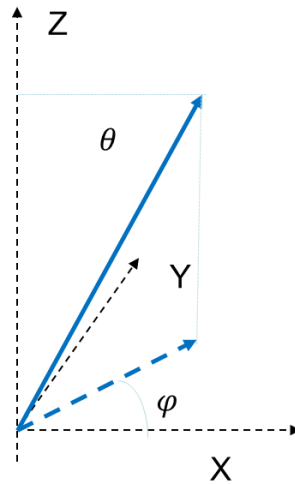
$$\Delta P_{sing} = -K \frac{|J|G}{2} \text{ or } \Delta P_{sing} = -K \frac{|G|G}{2\rho_m}$$

In a 3D module, the simplest extrapolation of wall friction and singular pressure losses was first implemented:

$$\begin{aligned} \Delta P_{kx} &= - \left[\frac{4L_x C_{kx} C_{f_{kx}}}{Dh_x} + K \alpha_k \right] \rho_k \frac{\|\vec{V}_k\| V_{kx}}{2} \\ \Delta P_{ky} &= - \left[\frac{4L_y C_{ky} C_{f_{ky}}}{Dh_y} + K \alpha_k \right] \rho_k \frac{\|\vec{V}_k\| V_{ky}}{2} \\ \Delta P_{kz} &= - \left[\frac{4L_z C_{kz} C_{f_{kz}}}{Dh_z} + K \alpha_k \right] \rho_k \frac{\|\vec{V}_k\| V_{kz}}{2} \end{aligned}$$

However, more complex formulations can be proposed where each component of the ΔP_k vector depends on the two angles θ and φ between the velocity vector and the axis (see the figure below) such as the following expressions:

$$\begin{aligned} \Delta P_{kx} &= - \left[\frac{4L_x C_{kx} C_{f_{kx}}}{Dh_x} + K \alpha_k \right] F_x(\theta, \varphi) \rho_k \frac{\|\vec{V}_k\| V_{kx}}{2} \\ \Delta P_{ky} &= - \left[\frac{4L_y C_{ky} C_{f_{ky}}}{Dh_y} + K \alpha_k \right] F_y(\theta, \varphi) \rho_k \frac{\|\vec{V}_k\| V_{ky}}{2} \\ \Delta P_{kz} &= - \left[\frac{4L_z C_{kz} C_{f_{kz}}}{Dh_z} + K \alpha_k \right] F_z(\theta, \varphi) \rho_k \frac{\|\vec{V}_k\| V_{kz}}{2} \end{aligned}$$



No experimental data are currently available to determine the functions $F_j(\theta, \varphi)$ in the reactor core where friction can play a significant role.

3.4. Interfacial friction

In 1D models, the interfacial friction is expressed as:

$$\tau_i = A_i C_i \rho |\Delta V| \Delta V$$

A_i interfacial area density (m^{-1})

C_i interfacial friction coefficient

ρ gas or liquid density (depending on the flow regime)

ΔV velocity difference between phases (m/s)

A_i , C_i , and ρ depend on the flow regime that is determined in the codes on the basis of flow regime maps.

In a 3D module, the simplest extrapolation of interfacial friction was first implemented with the assumption of isotropic behaviour:

$$\tau_i = A_i C_i \rho \overline{\|\Delta V\|} \overline{\Delta V}$$

However, more complex non-isotropic formulations can be made, where each component of the interfacial friction vector depends on two angles, θ and φ , for example in the following expression:

$$\begin{aligned} \tau_{ix} &= A_i C_{ix} \rho G_x(\theta, \varphi) \overline{\|\Delta V\|} \overline{\Delta V_x} \\ \tau_{iy} &= A_i C_{iy} \rho G_y(\theta, \varphi) \overline{\|\Delta V\|} \overline{\Delta V_y} \\ \tau_{iz} &= A_i C_{iz} \rho G_z(\theta, \varphi) \overline{\|\Delta V\|} \overline{\Delta V_z} \end{aligned}$$

A tensor formulation of the friction coefficient can also be made:

$$\tau_i = A_i \begin{bmatrix} C_{ixx} & C_{ixy} & C_{ixz} \\ C_{iyx} & C_{iyy} & C_{iyz} \\ C_{izx} & C_{izy} & C_{izz} \end{bmatrix} \rho \overline{\|\Delta V\|} \overline{\Delta V}$$

No experimental data are available to determine the functions $G_j(\theta, \varphi)$ or the tensor components in the reactor core where the geometry is non-isotropic.

3.5. Wall heat transfer

Wall heat transfers were first established and validated in 1D models. Heat transfer coefficients only depend on one geometrical scale (the hydraulic diameter) and the two phasic velocities. The simplest extrapolations just replaced the two phasic velocities with the modulus of the two velocities. No other geometrical effects were taken into account, even in the presence of singular geometry such as spacer grids. However, a bundle geometry (horizontal or vertical) might have a significant impact on heat transfer.

A more complete modelling would account for the possible effects of the flow velocity direction (e.g. on angles θ, ϕ) in a core and geometrical parameters other than the hydraulic diameter. Some work has focused on the effects of spacer grids in a core, but no experimental data are available to determine the functions of θ and ϕ .

3.6. Interfacial heat transfer

Interfacial heat transfers were first established and validated in 1D models. Heat transfer coefficients depend on only one geometrical scale (the hydraulic diameter) and the two phasic velocities. In 3D models the simplest extrapolations simply replaced the two phasic velocities by the modulus of the two velocities. No other geometrical effects were taken into account, even in presence of singular geometry such as spacer grids. One exception is the splitting of drops on spacer grids in reflooding, which increases the steam-to-droplet heat transfers and the wall-to-droplets radiative heat transfer.

A more complete modelling would include the possible effects of the phase velocity directions (e.g. on angles θ, ϕ in a core) and geometrical parameters other than the hydraulic diameter on all possible interfacial transfers, but no experimental data are currently available.

3.7. Turbulence and dispersion

The time averaging of momentum convection terms causes momentum turbulent diffusion (the first right-hand side term of the below equation). Space averaging or integration of momentum convection terms causes momentum dispersion terms. Both terms can be modelled as diffusion terms. The dispersion term can become significantly larger than turbulent diffusion terms in components consisting of many internal structures, for example a reactor core. The components are highly sensitive to geometry details and in particular to mixing vanes of spacer grids in core that are designed to promote radial transfers between subchannels. Some component codes have modelled the effects of spacer grids as a non-isotropic wall friction tensor in a subchannel model to better account for the specific arrangement of various mixing vanes' orientations.

$$\alpha_k \rho_k \frac{\partial \overline{V}_k}{\partial t} + \alpha_k \rho_k \overline{V}_k \cdot \nabla \overline{V}_k = \frac{1}{\phi} \nabla \cdot \left(\phi \alpha_k \rho_k \overline{T}_d \right) - \alpha_k \nabla P + F_{ik} + F_{pk} + \alpha_k \rho_k g$$

Turbulent dispersion of the void fraction results from the time and space averaging of viscous and pressure interfacial forces. It is included in the interfacial momentum transfers F_{ik} and represents the transport of a dispersed phase (bubbles or drops) by the turbulent eddies of the continuous phase.

Turbulent diffusion of heat (the third right-hand side term of the below equation) results from the time averaging of enthalpy convection terms. Heat dispersion terms result from the space averaging or integration of enthalpy convection terms. Both terms can be modelled as diffusion terms. The dispersion terms can become significantly larger than turbulent diffusion terms in components consisting of many internal structures, for example

a reactor core. The components are highly sensitive to details of the geometry, in particular to the mixing vanes of spacer grids in a core.

$$\begin{aligned} & \frac{\partial}{\partial t} \left[\phi \alpha_k \rho_k \left(H_k + \frac{V_k^2}{2} \right) - P \right] + \nabla \cdot \left[\phi \alpha_k \rho_k \vec{V} \left(H_k + \frac{V_k^2}{2} \right) \right] \\ & = \phi \alpha_k \rho_k \vec{g} \cdot \vec{V}_k + \phi \Gamma_k \left(H_k + \frac{V_k^2}{2} \right) - \nabla \cdot \alpha_k q_k + \phi q_{ki} + S q_{pk} \end{aligned}$$

Momentum and heat diffusion and dispersion coefficients are coupled and may be related through a diffusion-dispersion Prandtl number.

Diffusion and dispersion terms also exist for a scalar transport (e.g. boron concentration), which can be coupled to momentum diffusion-dispersion terms through a diffusion-dispersion Schmidt number.

There is some information available from small rod bundle experiments (cf. Chapter 5) about such diffusion-dispersion terms in rod bundles such as a pressurised water reactor (PWR) Subchannel and Bundle Test (PSBT), boiling water reactor (BWR) Full-size Fine-Mesh Bundle Test (BFBT), AGATE (cf. 5.1.13.4), GRAZIELLA (cf. 5.1.13.3), OMEGA (cf. 5.1.13.2), PERICLES-rectangular (cf. 5.1.5), cylindrical core test facility (CCTF) and slab core test facility (SCTF). These terms are usually neglected in system thermal-hydraulic (T/H) codes and some explanations for these simplifications are as follows:

- It can be reasonably assumed that the turbulent void dispersion of momentum plays a minor role when crossflows arise due to radial power profiles that induce void radial gradients and buoyant recirculation (below a swell level in a core uncover).
- It can be reasonably assumed that the turbulent void dispersion of momentum plays a minor role when crossflows arise due to radial power profiles that induce temperature and density radial gradients.
- It can be reasonably assumed that the turbulent void dispersion of momentum plays a minor role when wall heat transfers and interfacial heat transfer are high (core during core reflooding or core uncover).

However, it would be better to quantify such terms than qualitatively neglecting them. The modelling of such diffusion-dispersion terms is also important, as is the fact that the effects of crossflows depend on the space integration scale and mesh size.

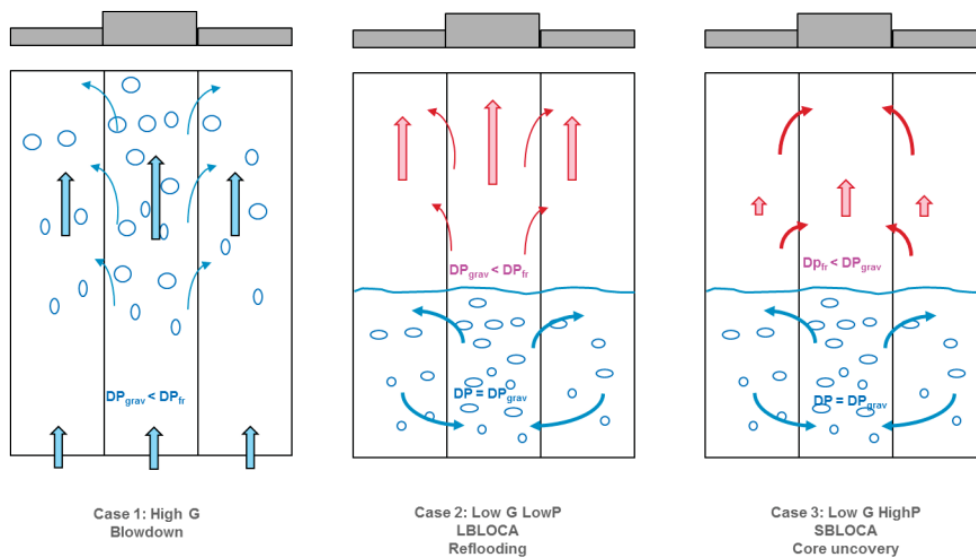
3.8. Modelling of the chimney effect and other crossflows

Core uncovering phases are expected during loss-of-coolant accident (LOCA) transients. A lack of water cooling can result in a two-phase mixture up until the swell level and a pure vapour flow in the core's upper part. Such configuration takes place after the scram when the power decay is below 5% nominal power (NP) [3-3].

Water is generally at the saturation temperature under the swell level and boiling occurs due to power decay. Hot assemblies with high-power regions produce more vapour than others, and gravity-driven natural circulation creates a radial flow from high-power regions to low-power regions. This phenomenon tends to homogenise the void fraction. This radial homogenisation means that swell level is almost uniform. The phenomenon has been observed in experiments [3-4] and [3-5]. The vapour mass flux leaving the swell level also tends to be homogenised due to radial flows. The prediction of these crossflows is controlled by the wall and interfacial friction models for non-axial two-phase flow.

In the dry zone, where cladding temperature excursion occurs, the vapour flow is mainly axial. There can be a higher cladding temperature in the highest power assembly. Then, crossflow can occur between assemblies according to the radial power profile. Two situations could arise: the “chimney” effect, where crossflows come from the lowest power assemblies to the higher power ones, and the “diverging” effect, where crossflows come from the highest power assemblies to the lower power ones. The cladding temperature is linked to the local vapour mass flux: higher cladding temperatures are expected with lower mass flux. Crossflows therefore impact the peak clad temperature (PCT): the “chimney” effect tends to decrease the PCT, while the “diverging” effect tends to increase the PCT by providing or removing cooling to the highest power assemblies. Figure 3.1 presents both situations. The prediction of these crossflows is controlled by the axial and radial wall friction and singular pressure losses models in non-axial vapour flows.

Figure 3.1. Chimney (right) and diverging (centre) effect phenomena (radial power profiles appear in grey)



Source: Bestion and Matteo, 2015.

References

- [3-1] Choi, C.-J., J.-H. Yang, H.-K. Cho, D.-J. Euh and G.-C. Park (2017), “Validation of Wall Friction Model in Multidimensional Component of Mars with Two-Phase Flow Experiments Describing ECC Behaviour in Downcomer”, *PBNC 2016*, 5-9 April, Singapore.
- [3-2] Yang, J.H., C.-J. Choi, H.-K. Cho, D.J. Euh and G.-C. Park (2017), “Assessment of wall friction model in multi-dimensional component of MARS with air–water cross-flow experiment”, *Nuclear Engineering and Design*, 312, pp. 106-120.
- [3-3] Pr ea, R. and C. Rabe (2019), “Chimney and Diverging Effects in Core PWR: Analysis and Experimental Characterization for Predictive Behaviour During Loss of Coolant Accident”, *NURETH-18*, 18-22 Aug, Portland, United States.
- [3-4] Morel, C. and D. Bestion (1999), “Validation of the CATHARE code against PERICLES 2D BOIL-UP Tests”, *NURETH-9*, 3-8 October, San Francisco.
- [3-5] R. Pr ea (2019), “Validation of CATHARE 3D module on LSTF Core”, *NURETH-18*, 18-22 August, Portland.
- [3-6] Bestion, D. and L. Matteo (2015), “Scaling considerations about LWR core thermalhydraulics”, *NURETH-16*, 30 August-4 September, Chicago.

4. Implementation of 3D capabilities in 3D system-scale T/H Codes

Engineering design and safety analyses of nuclear installations often require modelling the entire power plant coolant system. Some general information, not specific to three-dimensional (3D) modelling, on features implemented in system thermal-hydraulics (SYSTH) codes can be found in [4-1] and [4-2].

The current simulation tools still have limitations that industries and regulatory bodies would like to address. Some limitations are related to the simplifications and assumptions behind the models of the system-scale codes describing physical phenomena.

The field equations are averaged in time and in space in system-scale codes. Flow systems of a nuclear power plant are mainly built of pipes and therefore one-dimensional (1D) flow equations are usually sufficient. However, all flows are 3D by nature and 3D phenomena predictions are nowadays quite essential for correctly reproducing the system behaviour pertaining to recent nuclear power plants' generation. The development of 3D capabilities in thermal-hydraulic (T/H) system codes was followed by a simple extrapolation of 1D closure laws to 3D models. There is no guarantee that these simplifications are relevant to all situations. The growing role of 3D modelling of reactor cores and pressure vessels requires additional experimental data for a proper validation of at least transients that the 2D-3D experimental programme did not address.

Some information related to some of the present 3D SYSTH codes is summarised in Table 4.1.

Table 4.1. Overview of main features of 3D modules in SYSTH codes

CODE	Models and correlations (3D related)	Numerics (Time)					Equation discretisation		Numerics (Advective terms)			Solution Algorithm	Notes
		E	SI	NI	FI	O	FV	FD	U	HO	O		
ATHLET	Multidimensional flow model		X				X		X			Linear implicit Newton method	Extrapolation method to achieve higher order accuracy
CATHARE	Multidimensional flow model 3D diffusion terms		X				X	X	X			Full Newton iterative method	
MARS-KS	Multidimensional flow model 3D diffusion terms 3D conduction terms		X				X	X	X			1. Solve for phasic velocities as function of pressure and substitute to mass and energy equations 2. Solve for linearised pressure equation 3. Back substitution for remaining variables	Linearise seven equations including non-condensable gas continuity equation

Table 4.1. Overview of main features of 3D modules in SYSTH codes (Continued)

CODE	Models and correlations (3D related)	Numerics (Time)					Equation discretisation		Numerics (Advective terms)			Solution Algorithm	Notes
		E	SI	NI	FI	O	FV	FD	U	HO	O		
SPACE	Multidimensional flow model		X				X	X	X			1. Solve for phasic velocities as function of pressure and substitute to mass and energy equations 2. Solve for linearised pressure equation 3. Back substitution for remaining variables	Linearise ten equations including non-condensable gas continuity equation
RELAP	Multidimensional flow model		X	X			X	X	X			Border profile lower upper Backward-Euler (BPLU)	
TRACE	Multidimensional flow model no models for turbulent diffusion and shear between fluid cells		X			SETS	X	X	X		CD		Stability-enhancing two-steps (SETS)

FV: finite-volume

FD: finite difference

E: explicit

SI: semi-implicit

NI: nearly implicit

FI: fully implicit

U: upward difference

HO: higher order upward difference

CD: central difference

O: other

The existing 3D T/H system codes are too numerous to be presented in this report. However, the ones presented hereafter (Multi-dimensional Analysis of Reactor Safety [MARS], Safety and Performance Analysis Code [SPACE], Analysis of Thermal-hydraulics of LEaks and Transients [ATHLET] and Code for Analysis of Thermalhydraulics during an Accident of Reactor and safety Evaluation [CATHARE]), which are based on the contributions received from the task group members, are sufficiently representative of the current status to cover most 3D capabilities' features.

General considerations are followed by specific code descriptions. The main characteristics of these codes are summarised, and propositions given for the codes' capabilities and limitations, aiming to clarify what the conditions are for a correct application of the codes for safety analysis.

4.1. Approaches

4.1.1. Field equations

The derivation of the field equations used in SYSTH codes starts from the fundamental physical principle of mass, momentum and energy conservation. The time-behaviour of each field considered in the system-scale codes model is described using field equations

that are averaged in time and in space. The spatial and temporal averaging means that additional models are needed to compensate for the loss of information.

Further simplifications would reduce the number of solved field equations in system-scale analyses. Different simplifications produce different flow models and several field equations:

- homogeneous equilibrium model (HEM);
- drift-flux model;
- the two-fluid model;
- multi-field models.

Fewer assumptions are associated with a larger number of field equations and therefore the predictions are more accurate. However, using more field equations also demands more constitutive equations and thus greater quantities that must be measured.

One or more types of multidimensional components or modules have been implemented in current SYSTH codes from the equations of 1D components that have been modified and extended to 3D components, such as the Multi-dimensional Analysis of Reactor Safety - Korea Institute of Nuclear Safety (MARS-KS) code, which has two kinds of multidimensional components. Furthermore, specific options for 3D modules exist in the codes TRACE, reactor excursion and leak analysis programme 5 (RELAP5) and CATHARE for modelling the reactor pressure vessel.

Nearly all current two-phase flow models used in present SYSTH codes are based on the “two-fluid model”. Phases are treated as interpenetrating media and “macroscopic” separate balance equations for each phase are obtained by a space and/or time, or ensemble averaging of the local instantaneous basic flow equations. For the ensemble averaging, source terms represent the wall and interfacial transfers for mass, momentum and energy. Generally, the non-equilibrium two-phase three-field (of continuous liquid, gas/vapour and droplets) governing equations are implemented into the codes’ 3D module in Cartesian and cylindrical co-ordinates. The droplet field is sometimes considered separately, but only in the mass and momentum equations. The field equations and assumptions are occasionally component- or geometry-specific.

The porous media approach has been widely adopted, with the aim of including the geometric features of the system part in the modelling while also enabling a coarse mesh nodalisation of the reactor vessel. Non-condensable gas and a boron transport equation have also been considered.

4.1.2. Numerical scheme and solution algorithms

The field equations have to be discretised in time and in space for numerical solutions. The temporal discretisation is inherently connected to the (implicit or semi-implicit) solution method used. Fully-implicit algorithms are more demanding of central processing unit (CPU) time to solve but may have some advantages (they bring about neither material Courant–Friedrichs–Lewy condition [CFL] nor diffusion time step limitation) [4.2-2].

The first-order upwind scheme is most commonly used for the convection terms in spatial discretisation. This produces a stable and robust solution scheme, which is also associated with a high level of numerical diffusion.

The system code’s user carries out the actual spatial discretisation while building the simulation model. Guidance is usually provided by code developers and should be followed.

Practically all system-scale codes use the so-called staggered-grid discretisation. In this scheme, the momentum equations are discretised at different points than the other (scalar) field equations:

- pressures, enthalpies and void fractions are solved in a calculation cell's centre;
- velocities are solved at the cells' boundaries.

Solving all the field equations with fully-implicit discretisation at the same time is possible when the general approach is used with non-linear partial derivative equations' (PDEs') generalised Newton method. This solution method is used in the CATHARE or ATHLET codes, among others. The drawback to this approach is that the matrix that has to be inverted (the Jacobian of the coefficient matrix) becomes relatively large, resulting in the inversion requiring a large CPU. This is especially the case in 3D situations, where the coefficient matrix is far denser than in 1D situations. Efficient methods for calculation and storage of the Jacobian are therefore required. The drawback can be bypassed by a numerical estimation of the Jacobian, or the use of a Jacobian-free Newton-Krylov method.

The other option is to use non-iterative semi-implicit methods, which produce a rapid calculation speed (low computational cost of a single time step). However, the time steps sizes are limited by the material CFL condition. Non-iterative semi-implicit methods are used in the following computer codes: RELAP5, TRAC, TRACE, MARS and SPACE.

High-order numerical methods with flux-limiters or other low diffusivity methods have also been considered during recent development of SYSTH codes [4.1-1] and [4.1-2].

4.2. Simplifications and limitations

The system-scale codes use simplified approaches and methods to achieve their goal. The following limitations must be kept in mind when system codes are used [4.2-1]:

- Many physical phenomena highly depend on geometry and the models therefore may only be valid for specific geometry.
- There can be significant uncertainty associated with closure laws due to the simplification of physics used or the presence of non-modelled phenomena, and a better and more accurate model therefore might be required.
- Correlations are derived for fully-developed flow, which is certainly not the case for nuclear technology.
- Computed quantities are time and space averaged, providing a limited time and space resolution of time and space variations.

Another important limitation of present system codes concerns the coarse nodalisation of the reactor circuit due to CPU cost. The geometrical complexity is highly simplified for this case and specific effects cannot be predicted.

Information about local flow processes, such as turbulence and transfers at the interface separating the two phases or at the region near the walls, is lost due to the averaging. This lost information must be compensated for by additional modelling for specific phenomena, which leads to errors due to the closure laws' imperfections and numerical issues.

Closure laws are empirical correlations based on measurements in different geometries (circular pipe, rod bundle or tube bundle, annuli) that do not cover all pressure vessel (PV) sub-components and situations:

- The correlations are always based on steady-state measurements.
- The parameter ranges used for deriving the correlations are often limited.
- The correlations are usually tuned during the validation process of a code.

Their intrinsic origin as an extension of the 1D component equations has resulted in the 3D model showing some limitations, which are mainly related to the typically-employed coarse numerical grids and the closure relations used for the physical modelling. Models and correlations that were developed for 1D flow (the condition of a fully-developed 1D flow and simple geometry) have also been extended to the 3D module code in a simplified way.

The coarse meshes limit the spatial resolution of flow phenomena to large-scale effects, while the adoption of models and correlations developed specifically for 1D situations means that there is now a great need for the development of a specialised set of experiments to validate the 3D modules (e.g. in the bundle region, downcomer) in more 3D flow situations. Confidence in the simulation results obtained from system-scale tools has to be established through an extensive verification and validation effort.

The 3D diffusion terms (the viscous and turbulent stress terms in the momentum equation, the fluid molecular and turbulent energy diffusion and the dispersion terms due to space averaging) are sometimes not present in the 3D model. This can impair the modelling of natural circulation at low flow or quasi-stagnant flow in large tanks (e.g. passive cooling tank). The MARS-KS codes apply a simple Prandtl's mixing length model to the implementation of the turbulent diffusion terms. However, this application of such a simplified model is only suitable for relatively fine grids. Models for turbulent and diffusion phenomena are also implemented as options in some 3D modules.

The relative importance of the diffusion terms strongly depends on the porosity and hydraulic diameters. The transfers with walls (friction and heat transfers) in a fairly low porosity small-hydraulic-diameter component such as a light water reactor (LWR) core can play a dominant role compared to diffusion terms. Natural circulation phenomena are then controlled by a balance between wall friction and buoyancy forces, instead of a balance between diffusion and buoyancy forces as in an open medium. The objective is to clearly identify the sub-component and physical situations in which diffusive terms should be used and validated.

Additional effort is also likely required to identify the flow regime in complex geometry multidimensional components and develop suitable theoretical physical models for 3D applications, such as transport equations for an interfacial area or turbulent scales, or multi-field modelling.

4.3. Review of 3D system-scale analysis codes

The development of the present generation of system codes was initiated in the years from 1970 to 1980. The main objective of developing these codes was to replace evaluation models that used conservative assumptions in a best estimate approach with more realistic predictions of the accidental transients of a pressurised water reactor (PWR) or boiling water reactor (BWR).

SYSTH codes have a wide range of applications, from research to safety and design purposes. Examples of its applications are listed below [4.2-1]:

- Safety analysis;
- The quantification of the conservative analyses' margin;
- The investigation of plant operating procedures and accident management (AM);
- The definition and verification of emergency operating procedures (EOPs);
- Investigations for new types of fuel management;

- The preparation and interpretation of experimental programmes with scaling analyses;
- Licensing when used in a best estimate plus uncertainty (BEPU) approach;
- The design of new reactors and systems, including the passive features for the third and fourth generations of nuclear power plants.
- The implementation in a full scope plant simulator.

The system code application has often been extended to the field of severe accidents. They are coupled with other codes that model core degradation and fission product release.

3D modules were implemented into SYSTH codes with the main objective of modelling large-scale 3D phenomena in a nuclear power plant pressure vessel during large break loss-of-coolant accidents (LB-LOCAs), for example emergency core cooling systems (ECCS) water downcomer penetration or reflooding of the core with transverse power profile effects. The range of application of the 3D module code usually relate to the reactor pressure vessel (RPV) and core. A 3D component is rarely used to model the water pools of passive safety systems, moderator tanks in pressurised heavy water reactor (PHWR) and the spent fuel pool, where multidimensional flow processes are expected to occur.

Other applications could be developed relating to research reactors, pool-type liquid metal cooled reactors and steam generators, or other heat exchangers. There are few applications to cold leg and hot leg: CATHARE 3 used the 3D module for some pressurised thermal shock (PTS) analyses.

The transient application is mainly relevant to:

- LOCAs (LB-LOCA and intermediate break [IB-]LOCA);
- Steam line breaks (SLBs);
- Boron dilution transients.

Other transients could benefit from 3D simulations, but only a few applications have been performed so far. These include the departure of nucleate boiling ratio (DNBR) analysis for transient accidents, control rod (CR) ejection, protected loss of flow, BWR reactivity insertion accidents (RIAs), design extension conditions (DEC), PTS, station blackout (SBO) and steam generator tube rupture (SGTR).

The heavy computational effort required has led to 3D modules being mainly used for fast (short) transients such as large break LOCA. Rather coarse nodalisation schemes are applied in most applications and consequently the advantage of a 3D modelling of the flow processes can be offset to a certain extent. However, large-scale 3D effects can be better modelled with 3D models than with 1D models.

The applications of 3D models that have been briefly introduced above originate from the experiences of the project's partners. A questionnaire about the use of 3D SYSTH codes was filled-out by them, whose main content is summarised in Appendix A.

4.4. MARS-KS code

MARS-KS is the code for simulating the T/H behaviour of a reactor system during transient conditions. The backbones of MARS-KS are the RELAP5/MOD3.2.1.2 [4.4-1] and the COBRA-TF codes [4.4-2] and [4.4-3]. The RELAP5 code is a versatile and robust code based on a 1D two-fluid model for two-phase flows. The COBRA-TF code's specific purpose is to predict nuclear fuel channel behaviour during a LOCA and it employs a 3D,

two-fluid, three-field model on rectangular Cartesian or subchannel co-ordinates. In order to fully exploit the features of each code, these two codes have been consolidated into a single code in the form of system analysis module (RELAP5) and 3D vessel analysis module (COBRA-TF) through the integration of a hydrodynamic solution scheme and the unification of various T/H models, equation-of-state and I/O features. The codes' sources were entirely restructured using the modular data structure and a new dynamic memory allocation scheme of FORTRAN 90.

The system analysis module employs a two-fluid model for two-phase flows. The two-fluid equations consist of (a) two phasic continuity equations, (b) two phasic momentum equations, (c) two phasic energy equations, and (d) several additional continuity equations. The 3D vessel analysis module adopts a two-fluid, three-field model on rectangular Cartesian or subchannel co-ordinates. The adopted field equations are (a) four continuity equations for vapour, continuous liquid, and entrained liquid droplets, (b) three momentum equations for continuous liquid, entrained liquid, and the mixture of vapour and non-condensable gases, and (c) two energy equations for the mixture of vapour and non-condensable gases and mixture of continuous and entrained liquid.

The MARS-KS code runs on a Windows platform and is currently used as a multidimensional T/H tool to analyse reactor transients, to experiment facility simulations and for various safety research purposes. The code can also be connected through dynamic linkage using DLLs to other codes such as the 3D kinetics code, containment analysis codes and severe accident codes. The MARS-KS code has been updated with several features such as a Canada Deuterium Uranium (CANDU) Channel component, new reflood model, interfaces for uncertainty analysis, and more [4.4-4]. The first version of the MARS-KS code was developed by Korea Atomic Energy Research Institute (KAERI) and released in early 1997. The Korean Institute of Nuclear Safety (KINS) has used and maintained the MARS-KS code for regulatory purposes since 2007. The latest code version is MARS-KS V1.4, which was released in 2016.

4.4.1. Description

The MARS-KS has two kinds of multidimensional components:

- the VESSEL component of the 3D vessel analysis module;
- the MULTID component of the system analysis module.

Two multidimensional components can be solved independently or together in the same hydrodynamic scheme, while each multidimensional component adopts distinct field equations and assumptions.

4.4.2. Field equations of MULTID component

The field equations of one-dimensional mass, momentum and energy equations have been modified and extended to the 3D form to develop the MULTID component. The control volume is assumed to be porous media and therefore an area fraction factor or volume fraction factor are multiplied to appropriate terms. The mass equations implemented the 3D convection term, while the momentum equations implemented the full 3D convection and diffusion terms. The energy equations implemented the 3D convection and conduction and diffusion term for turbulent mixing. The dissipation term in energy equations is proportional to the square of volume velocity, while other dissipation effects due to

interface mass transfer, interface friction and virtual mass are neglected. The field equations of MULTID components are given by:

$$\gamma_v \frac{\partial}{\partial t} (\alpha_k \rho_k) + \nabla \cdot (\gamma_a \alpha_k \rho_k \vec{V}_k) = \gamma_v \Gamma_k \quad (4.4.2-1)$$

$$\gamma_v \frac{\partial}{\partial t} (\alpha_k \rho_k \vec{V}_k) + \nabla \cdot (\gamma_a \alpha_k \rho_k \vec{V}_k \vec{V}_k) + \gamma_v \alpha_k \nabla P = \gamma_v \alpha_k \rho_k \vec{g} + \nabla (\gamma_a \alpha_k \vec{\tau}') - \gamma_v F_i - \gamma_v F_w \quad (4.4.2-2)$$

$$\begin{aligned} (\alpha_k \rho_k U_k) + \frac{1}{\gamma_v} \nabla \cdot (\gamma_a \alpha_k \rho_k U_k \vec{V}_k) = & -P_k \left[\frac{\partial \alpha_k}{\partial t} + \frac{1}{\gamma_v} \nabla \cdot (\gamma_a \alpha_k \vec{V}_k) \right] + \Gamma_k \left(U_k + \frac{P_k}{\rho_k} \right) \\ & - \frac{1}{\gamma_v} \nabla \cdot (\gamma_a \alpha_k (\vec{q}_k + \vec{q}_k^T)) + \vec{q}_{ik} \cdot \vec{A}_i + \vec{q}_{wk} \cdot \vec{A}_{wk} + \alpha_k Q_k + DISS \end{aligned} \quad (4.4.2-3)$$

k is a subscript as phase indicator, γ_a is an area porosity, γ_v is a volume porosity, i is a subscript for phase interface, w is a subscript for a wall, α_k is a volume fraction of k phase and *DISS* is an energy dissipation term.

4.4.3. Field equations of the VESSEL component

The VESSEL component employs field equations for three fields without porosity factors, with the 3D effect terms implemented in similar way as for the MULTID component. The mass equations implemented the 3D convection term, while the momentum equations implemented the full 3D convection and diffusion terms. The energy equations implemented the 3D convection, conduction and diffusion term for turbulent mixing.

$$\frac{\partial}{\partial t} (\alpha_k \rho_k) + \nabla \cdot (\alpha_k \rho_k \vec{V}_k) = \Gamma_k \quad (4.4.3-1)$$

k=l, v, e or n for continuous liquid, vapour, entrained liquid and non-condensable gases respectively.

$$\frac{\partial}{\partial t} (\alpha_k \rho_k \vec{V}_k) + \nabla \cdot (\alpha_k \rho_k \vec{V}_k \vec{V}_k) + \alpha_k \nabla P = \alpha_k \rho_k \vec{g} + \nabla \cdot (\alpha_k \vec{\tau}') + \vec{M}_k^\Gamma + \vec{M}_k^d \quad (4.4.3-2)$$

k=l, v+n, or e for continuous liquid, gaseous phase, entrained liquid respectively.

The \vec{M}_k^Γ and \vec{M}_k^d stand for the average supply of momentum to phase k due to mass transfer to phase k and the average drag force on phase k by other phases.

$$\begin{aligned} \frac{\partial}{\partial t} (\alpha_k \rho_k U_k) + \nabla \cdot (\alpha_k \rho_k U_k \vec{V}_k) = & -P_k \left[\frac{\partial \alpha_k}{\partial t} + \nabla \cdot (\alpha_k \vec{V}_k) \right] + \Gamma_k \left(U_k + \frac{P_k}{\rho_k} \right) - \nabla \cdot \left(\alpha_k (\vec{q}_k + \vec{q}_k^T) \right) \\ & + \vec{q}_{ik} \cdot \vec{A}_i + \vec{q}_{wk} \cdot \vec{A}_{wk} + \alpha_k Q_k \end{aligned} \quad (4.4.3-3)$$

k=l+e, or v+n for liquid and gaseous phase respectively.

4.4.4. Simplifications and limitations

Although the 3D VESSEL analysis module can handle the multi-channel flow, there are limitations in the application of shear terms and the cylindrical co-ordinate system. Overcoming these limitations required the development of a new multidimensional (indicated by MULTID in the input cards) component, which has been installed as a new component of the system analysis module. The MULTID component also provides more flexible 3D capabilities in the system code and allows the user to more accurately model the multidimensional hydrodynamic features of reactor applications, primarily in the vessel (i.e. the core and downcomer) and steam generator.

The MULTID component defines a one-, two- or three-dimensional array of volumes and the internal junctions connecting these volumes. The geometry can be either Cartesian (x,y,z) or cylindrical (r,θ,z). Full 3D convection and diffusion terms are implemented in the momentum equation. A simple Prandtl's mixing length model is applied for the implementation of turbulent viscosity. The 3D turbulent thermal mixing terms are also implemented in the energy equation. The flow regime map of MULTID component is identical to that of the one-dimensional component of the system analysis module, except for the fact that the horizontal stratified flow is removed from the horizontal flow regime map.

3D diffusion term

The viscous stress gradient term as a 3D diffusion term in the second term of the right-hand side (RHS) of momentum equations contains two terms, which are the viscous diffusion term ($\underline{\tau}^l$) and the turbulent diffusion term ($\underline{\tau}^T$).

$$\overline{\tau}^i = \overline{\tau}^l + \overline{\tau}^T \quad (4.4.4-1)$$

For the Cartesian co-ordinate, the viscous diffusion term is given by:

$$\overline{\tau}^l = \left[\mu \left(\frac{\partial^2 u}{\partial y^2} + \frac{\partial^2 u}{\partial z^2} \right), \mu \left(\frac{\partial^2 v}{\partial x^2} + \frac{\partial^2 v}{\partial z^2} \right), \mu \left(\frac{\partial^2 w}{\partial x^2} + \frac{\partial^2 w}{\partial y^2} \right) \right] \quad (4.4.4-2)$$

For the cylindrical co-ordinate, this viscous diffusion term is given by:

$$\overline{\tau}^l = \left[\mu \left(\frac{\partial}{r\partial\theta} \left(\frac{\partial u}{r\partial\theta} \right) + \frac{\partial}{\partial z} \left(\frac{\partial u}{\partial z} \right) \right), \mu \left(\frac{\partial}{r^2\partial r} r^2 \left(\frac{\partial v}{\partial r} - \frac{v}{r} \right) + \frac{\partial}{\partial z} \left(\frac{\partial v}{\partial z} \right) \right), \mu \left(\frac{\partial}{r\partial r} \left(r \frac{\partial w}{\partial r} \right) + \frac{\partial}{r\partial\theta} \left(\frac{\partial w}{r\partial\theta} \right) \right) \right] \quad (4.4.4-3)$$

The Prandtl's mixing length model is applied for the turbulent diffusion term and the momentum mixing length and the energy mixing length must therefore be defined. MARS-KS allows users to define the lengths based on the experience and Table 4.2 provides reference. As MARS-KS does not adopt the wall function, the recommended range of mixing length is also suggested. The turbulent diffusion term is defined by:

$$\overline{\tau}^T = 2\mu_T \underline{D}_{KB}^* \quad (4.4.4-4)$$

where \underline{D}_{KB}^* is the deleted bulk deformation tensor and μ_T is the turbulent or eddy viscosity.

For the Cartesian co-ordinate, the deleted bulk deformation tensor is given by:

$$\underline{D}_{KB}^* = 0.5 \times \begin{pmatrix} 0 & \frac{\partial u}{\partial y} + \frac{\partial v}{\partial x} & \frac{\partial u}{\partial z} + \frac{\partial w}{\partial x} \\ \frac{\partial u}{\partial y} + \frac{\partial v}{\partial x} & 0 & \frac{\partial v}{\partial z} + \frac{\partial w}{\partial y} \\ \frac{\partial u}{\partial z} + \frac{\partial w}{\partial x} & \frac{\partial v}{\partial z} + \frac{\partial w}{\partial y} & 0 \end{pmatrix} \quad (4.4.4-5)$$

For the cylindrical co-ordinate, the deleted bulk deformation tensor is given by:

$$\underline{D}_{KB}^* = 0.5 \times \begin{pmatrix} 0 & \frac{\partial v}{\partial r} + \frac{\partial u}{r\partial\theta} - \frac{v}{r} & \frac{\partial w}{\partial r} + \frac{\partial u}{\partial z} \\ \frac{\partial v}{\partial r} + \frac{\partial u}{r\partial\theta} - \frac{v}{r} & 0 & \frac{\partial v}{\partial z} + \frac{\partial w}{r\partial\theta} \\ \frac{\partial w}{\partial r} + \frac{\partial u}{\partial z} & \frac{\partial v}{\partial z} + \frac{\partial w}{r\partial\theta} & 0 \end{pmatrix} \quad (4.4.4-6)$$

The turbulent viscosity is given by:

$$\mu_T = \rho_k l_m^2 \left(\frac{\partial u}{\partial y} \right) = \rho_k l_m^2 \sqrt{2 \underline{D}_{KB}^* : \underline{D}_{KB}^*} \quad (4.4.4-7)$$

For the Cartesian co-ordinate, the product of deleted bulk deformation tensor is given by:

$$\sqrt{2 \underline{D}_{KB}^* : \underline{D}_{KB}^*} = \sqrt{\left(\frac{\partial u}{\partial y} + \frac{\partial v}{\partial x} \right)^2 + \left(\frac{\partial u}{\partial z} + \frac{\partial w}{\partial x} \right)^2 + \left(\frac{\partial v}{\partial z} + \frac{\partial w}{\partial y} \right)^2} \quad (4.4.4-8)$$

For the cylindrical co-ordinate, the product of deleted bulk deformation tensor is given by:

$$\sqrt{2 \underline{D}_{KB}^* : \underline{D}_{KB}^*} = \sqrt{\left(\frac{\partial v}{\partial r} + \frac{\partial u}{r \partial \theta} - \frac{v}{r} \right)^2 + \left(\frac{\partial w}{\partial r} + \frac{\partial u}{\partial z} \right)^2 + \left(\frac{\partial v}{\partial z} + \frac{\partial w}{r \partial \theta} \right)^2} \quad (4.4.4-9)$$

The mixing length range is recommended as:

$$\frac{\Delta x}{5} \leq l_m \leq \Delta x \quad (4.4.4-10)$$

Table 4.2. Turbulent length

Flow	Turbulent length scale (l_m)	Length scale, L
Mixing layer	0.07L	Layer width
Jet	0.09L	Jet half width
Wake	0.16L	Wake half width
Axisymmetric jet	0.076L	Jet half width
Boundary layer	0.09L	Boundary layer thickness
Viscous sub-layer		
Log-law layer		
Outer layer		
Channel	$L[0.14-0.081-yL2-0.061-y/LA]$	Channel half width

3D heat diffusion terms

The 3D heat diffusion is the third term of the RHS of the energy equation, consisting of the viscous conduction term (\vec{q}_k) and turbulent thermal mixing term (\vec{q}_k^T), which are given by:

$$\vec{q}_k + \vec{q}_k^T = -(k_k + k_k^T) \nabla T_k \quad (4.4.4-11)$$

where k_k is the thermal conductivity and k_k^T the turbulent thermal conductivity.

The turbulent thermal mixing term is similarly treated with the turbulent viscosity term. The turbulent thermal diffusivity of the mixing term for the mass cell centre is computed from the double dot product of the deformation tensor, in the same manner that the turbulent viscosity was obtained.

Turbulent thermal mixing term is given by:

$$\vec{q}_k^T = -k_k^T \nabla T_k \quad (4.4.4-12)$$

$$k_k^T = \rho_k C_p \varepsilon_k^T = \rho_k C_p l_h l_m \sqrt{2 \underline{D}_{KB}^* : \underline{D}_{KB}^*} \quad (4.4.4-13)$$

where l_m is the momentum mixing length and l_h the energy mixing length. The momentum and energy mixing length is defined by user input.

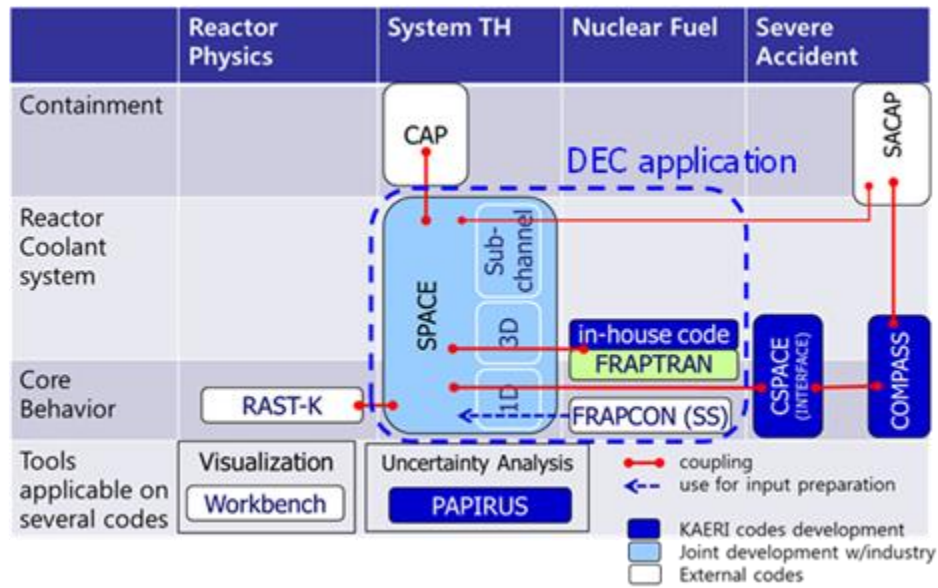
4.5. SPACE code

The Korean nuclear industry launched the Safety and Performance Analysis Code (SPACE) for nuclear power plants code development project in 2006. The project aims to develop a new T/H system analysis code by adopting advanced physical modelling of two-phase flows, mainly using multi-field models and with a multidimensional simulation capability by the use of structured and/or unstructured meshes. The code development and validation process was completed in early 2013. After this, the licensing work for plant application was started in mid-2013 and accomplished in March 2017.

SPACE includes multidimensional non-equilibrium two-phase flow models, heat transfer models, nuclear fuel kinetics models and a reflood models, based on a two-phase (liquid and gas phase) three-field (continuous liquid, gas, and droplets field) governing equations which is a nine-equation model. SPACE also offers a six-equation model similar to RELAP5 [4.4-1], which neglects the droplet field in the nine-equation model. SPACE was programmed in an object-oriented manner using C++ programming language. SPACE can simulate the loss-of-coolant accidents, main steam line break, main feed water pipe rupture, and main steam generator tube rupture accidents, which are necessary for pressurised water reactor safety analyses. SPACE can also stimulate the transient phenomena, such as the loss of offsite power (LOOP), turbine trip and nuclear reactor shutdowns. This use of SPACE could be applied to establish strategies for mitigating accidents, developing operating guides and planning T/H tests and analyses. SPACE was developed to simulate transient phenomena in nuclear power plant reactor cooling systems. However, because it is a general purpose T/H system code, it can be also used in the non-nuclear-power fields where a steam-water-non-condensable gas mixture is included. SPACE has various interfaces with other codes for the multiphysics analysis. Figure 4.1 shows the summary of major code interfaces of SPACE.

The SPACE includes, among other items, input and output packages, a hydrodynamic model package, heat structure model, control system model and reactor kinetic model. The input and output packages read the input and restart-files and inspect input errors, memory allocation and variable initialisation, generating output files that include restart-files. It also transfers data between different modules such as the input module and hydraulic solver. The hydrodynamic model package consists of a hydraulic solver, constitutive models, special process models and component models. The hydraulic solver offers a numerical solution scheme for the multidimensional two-phase three-field governing equations as well as the 1D flow model. The governing equations (including the mass, energy and momentum equation) deal with the three fields comprised of water, steam and droplets. The governing equations require porosity to account for the structural material impact on the fluid flow. A mass conservation equation of non-condensable gas and boron transport equation are also considered. The finite-volume method (FVM) was applied to establish the discretised governing equations. The non-linear temporal and source terms are linearised by using Taylor expansion. The SPACE code's primitive variables are non-condensable gas pressure, phasic temperatures, phasic volume fractions, total pressure and phasic velocities. The non-primitive variables, such as the density and internal energy, are therefore linearised with respect to the primitive variables, by applying the first-order Taylor expansion. The mesh system uses a structured or unstructured mesh system. It is also possible to use a combination of the two mesh systems. Such a combined mesh system could not only depict a 1D pipe flow network, but also describe more complex 3D geometry by using the structured mesh Cartesian, or cylindrical co-ordinate system, and the unstructured mesh system.

Figure 4.1. SPACE code interfaces [4.5-4]



Source: Lee et al., 2016.

A semi-implicit scheme is implemented into SPACE as the basic numerical time advancement scheme, similar to the RELAP5 solution scheme, and developed so that a simultaneous solution could be obtained with structured or unstructured mesh schemes. The constitutive models include the flow regime map, interfacial heat transfer models, wall and interfacial friction models, droplet entrainment and de-entrainment models and wall-to-fluid heat transfer models. The SPACE code also contains component models, 1D and 2D heat structure models, and reactor kinetics models that are based on the point-kinetics model. The component models include a pump, pressuriser, valve, steam separator, safety injection tank and turbine. Finally, a special process model contains the critical flow model, countercurrent flow limitation model, abrupt area change model, offtake model (liquid entrainment by vapour) and water level tracking models, which can simulate the nuclear power plant's special T/H phenomena. Furthermore, for the code user's convenience, SPACE also provides the functions of steady-state run and restart run.

4.5.1. Governing equations

The multidimensional component of SPACE, whose component name is "3D", can handle one, two and three-dimensional flow in Cartesian and cylindrical co-ordinates [4.5-1]. The governing equations used in the SPACE code are derived, applying the time-volume averaging scheme to the local instantaneous conservation equations. This is described in detail in the reference [4.5-2]. The resulting two-fluid, three-field formulation uses a separate set of conservation equations for each field. The three fields include vapour, continuous liquid and entrained liquid. The method of dividing the liquid phase into two fields is a convenient and physically reasonable way of handling flows where the liquid appears in both continuous liquid and droplet form, because the thermal and hydraulic behaviours of the droplets can differ significantly from those of the continuous liquid. The governing equations of SPACE are described as follows:

Continuity equation for vapour phase

$$\varepsilon \frac{\partial}{\partial t} (\alpha_g \rho_v) + \nabla \cdot (\varepsilon \alpha_g \rho_v \mathbf{U}_g) = \varepsilon (\Gamma_l + \Gamma_d + \Gamma_l^w + \Gamma_d^w) \quad (4.5.2-1)$$

Continuity equation for continuous liquid phase

$$\varepsilon \frac{\partial}{\partial t} (\alpha_l \rho_l) + \nabla \cdot (\varepsilon \alpha_l \rho_l \mathbf{U}_l) = \varepsilon (-\Gamma_l - S_E + S_D - \Gamma_l^w) \quad (4.5.2-2)$$

Continuity equation for entrained liquid phase

$$\varepsilon \frac{\partial}{\partial t} (\alpha_d \rho_d) + \nabla \cdot (\varepsilon \alpha_d \rho_d \mathbf{U}_d) = \varepsilon (-\Gamma_d + S_E - S_D - \Gamma_d^w) \quad (4.5.2-3)$$

where the subscript v, l, d and g refer to the vapour, continuous liquid, droplet and vapour/non-condensable gas mixture respectively. The mass transfer due to phase change, denoted by Γ_l, Γ_d , occurs at continuous liquid-vapour and droplet-vapour interfaces. The two liquid fields can also exchange mass by entrainment or de-entrainment, which is denoted by S_E, S_D respectively, and ε refers to the cell's fluid porosity.

The energy conservation equation is set up for each of the vapour/gas mixture, continuous liquid, droplet fields with the assumption that all fields are at thermal non-equilibrium.

Internal energy equation for vapour-gas mixture

$$\begin{aligned} & \varepsilon \frac{\partial (\alpha_g (\rho_v e_v + \rho_n e_n))}{\partial t} + \nabla \cdot (\varepsilon \alpha_g (\rho_v e_v + \rho_n e_n) \mathbf{U}_g) \\ &= -\varepsilon P \frac{\partial \alpha_g}{\partial t} - P \nabla \cdot (\varepsilon \alpha_g \mathbf{U}_g) + \varepsilon (Q_{iv-l} + \Gamma_l h_{vl}^* + \Gamma_d h_{vd}^* + Q_{iv-d} + Q_{l-n} + Q_{d-n}) \\ & \quad + \varepsilon (Q_g^w + \Gamma_l^w h_{vl}' + Q_{iv-l}^w + \Gamma_d^w h_{vd}' + Q_{iv-d}^w) \end{aligned} \quad (4.5.2-4)$$

Internal energy equation for liquid phase

$$\begin{aligned} & \varepsilon \frac{\partial (\alpha_l \rho_l e_l)}{\partial t} + \nabla \cdot (\varepsilon \alpha_l \rho_l e_l \mathbf{U}_l) \\ &= -\varepsilon P \frac{\partial \alpha_l}{\partial t} - P \nabla \cdot (\varepsilon \alpha_l \mathbf{U}_l) + \varepsilon (Q_{il} - \Gamma_l h_l^* - S_E h_l + S_D h_d - Q_{l-n}) + \varepsilon (Q_l^w - \Gamma_l^w h_l' + Q_{il}^w) \end{aligned} \quad (4.5.2-5)$$

Internal energy equation for droplet phase

$$\begin{aligned} & \varepsilon \frac{\partial (\alpha_d \rho_d e_d)}{\partial t} + \nabla \cdot (\varepsilon \alpha_d \rho_d e_d \mathbf{U}_d) \\ &= -\varepsilon P \frac{\partial \alpha_d}{\partial t} - P \nabla \cdot (\varepsilon \alpha_d \mathbf{U}_d) + \varepsilon (Q_{id} - \Gamma_d h_d^* + S_E h_l - S_D h_d - Q_{d-n}) + \varepsilon (Q_d^w - \Gamma_d^w h_d' + Q_{id}^w) \end{aligned} \quad (4.5.2-6)$$

In the above phasic energy conservation equations, the interfacial heat transfer rate per volume and the associated mass transfer rate are denoted by Q and Γ respectively.

Each field's momentum conservation equations have been derived using semi-conservative momentum flux term and phasic intensive form, in which the governing equation is divided by phasic volume fraction and phasic density, as follows:

Momentum equation for vapour phase

$$\begin{aligned}
& \varepsilon \frac{\partial \mathbf{U}_g}{\partial t} + \nabla \cdot (\varepsilon \mathbf{U}_g \mathbf{U}_g) - \mathbf{U}_g \nabla \cdot (\varepsilon \mathbf{U}_g) \\
&= -\frac{\varepsilon}{\rho_g} \nabla P - \frac{\varepsilon F_{wg}}{\alpha_g \rho_g} \mathbf{U}_g - \frac{\varepsilon F_{gd}}{\alpha_g \rho_g} (\mathbf{U}_g - \mathbf{U}_d) - \frac{\varepsilon F_{gl}}{\alpha_g \rho_g} (\mathbf{U}_g - \mathbf{U}_l) + \varepsilon \mathbf{B} \\
&+ \frac{\varepsilon}{\alpha_g \rho_g} (\Gamma_{l,E} \mathbf{U}_l + \Gamma_{d,E} \mathbf{U}_d - \Gamma_{l,E} \mathbf{U}_g - \Gamma_{d,E} \mathbf{U}_g) \\
&+ \frac{\varepsilon}{\alpha_g \rho_g} (\Gamma_{l,E}^w \mathbf{U}_l + \Gamma_{d,E}^w \mathbf{U}_d - \Gamma_{l,E}^w \mathbf{U}_g - \Gamma_{d,E}^w \mathbf{U}_g) \\
&- \frac{\varepsilon}{\alpha_g \rho_g} \left\{ C_{g,gd} \alpha_g \alpha_d \rho_{m,gd} \frac{\partial (\mathbf{U}_g - \mathbf{U}_d)}{\partial t} + C_{g,gl} \alpha_g \alpha_l \rho_{m,gl} \frac{\partial (\mathbf{U}_g - \mathbf{U}_l)}{\partial t} \right\}
\end{aligned} \tag{4.5.2-7}$$

where $C_{g,gl}$ and $C_{g,gd}$ are coefficients of virtual mass and \mathbf{B} is body force.

Momentum equation for continuous liquid phase

$$\begin{aligned}
& \varepsilon \frac{\partial \mathbf{U}_l}{\partial t} + \nabla \cdot (\varepsilon \mathbf{U}_l \mathbf{U}_l) - \mathbf{U}_l \nabla \cdot (\varepsilon \mathbf{U}_l) \\
&= -\frac{\varepsilon}{\rho_l} \nabla P - \frac{\varepsilon F_{wl}}{\alpha_l \rho_l} \mathbf{U}_l - \frac{\varepsilon F_{lg}}{\alpha_l \rho_l} (\mathbf{U}_l - \mathbf{U}_g) + \varepsilon \mathbf{B} + \frac{\varepsilon}{\alpha_l \rho_l} (-\Gamma_{l,C} \mathbf{U}_l + \Gamma_{l,C} \mathbf{U}_g + S_D \mathbf{U}_d - \mathbf{U}_l S_D) \\
&+ \frac{\varepsilon}{\alpha_l \rho_l} (-\Gamma_{l,C}^w \mathbf{U}_l + \Gamma_{l,C}^w \mathbf{U}_g) - \frac{\varepsilon}{\alpha_l \rho_l} C_{g,lg} \alpha_l \alpha_g \rho_{m,lg} \frac{\partial (\mathbf{U}_l - \mathbf{U}_g)}{\partial t}
\end{aligned} \tag{4.5.2-8}$$

where $\Gamma_l = \Gamma_{l,E} - \Gamma_{l,C}$.

Momentum equation for droplet phase

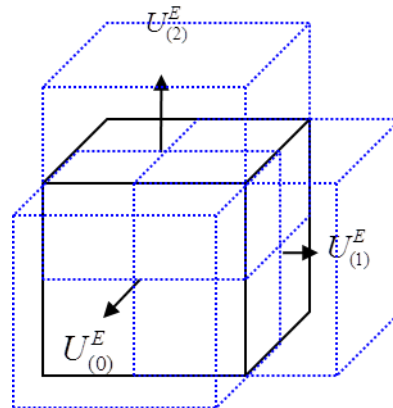
$$\begin{aligned}
& \varepsilon \frac{\partial \mathbf{U}_d}{\partial t} + \nabla \cdot (\varepsilon \mathbf{U}_d \mathbf{U}_d) - \mathbf{U}_d \nabla \cdot (\varepsilon \mathbf{U}_d) \\
&= -\frac{\varepsilon}{\rho_d} \nabla P - \frac{\varepsilon F_{wd}}{\alpha_d \rho_d} \mathbf{U}_d - \frac{\varepsilon F_{dg}}{\alpha_d \rho_d} (\mathbf{U}_d - \mathbf{U}_g) + \varepsilon \mathbf{B} + \frac{\varepsilon}{\alpha_d \rho_d} (-\Gamma_{d,C} \mathbf{U}_d + \Gamma_{d,C} \mathbf{U}_g + S_E \mathbf{U}_l - S_E \mathbf{U}_d) \\
&+ \frac{\varepsilon}{\alpha_d \rho_d} (-\Gamma_{d,C}^w \mathbf{U}_d + \Gamma_{d,C}^w \mathbf{U}_g) - \frac{\varepsilon}{\alpha_d \rho_d} C_{g,dg} \alpha_d \alpha_g \rho_{m,dg} \frac{\partial (\mathbf{U}_d - \mathbf{U}_g)}{\partial t}
\end{aligned} \tag{4.5.2-9}$$

where $\Gamma_d = \Gamma_{d,E} - \Gamma_{d,C}$.

As shown in the equations above, there are no 3D diffusion terms that are the viscous stress term in the momentum equation, and the fluid conduction term in the energy equation. However, the momentum flux terms in the governing equations and convection terms in the mass/energy equation consider the full-3D flow model.

SPACE's staggered mesh system is based on the orthogonal hexahedral shape of a cell and its surrounding faces. All the geometric quantities are described in terms of cell volume, centroid, face area and face centre, so that Cartesian and cylindrical mesh systems can be expressed in same manner. Each scalar cell normally has six faces in three-dimensional Cartesian or cylindrical mesh blocks. But two-dimensional Cartesian meshes or one-dimensional pipes can be also represented by simply reducing the numbers of the surrounding faces. Each momentum cell is shifted by the half size of scalar cell, so that it consists of the front half-part of the owner scalar cell and the back half-part of the neighbour scalar cell, as shown in Figure 4.2.

Figure 4.2. Momentum cells in the SPACE staggered mesh system



4.5.2. Simplifications and limitations

As mentioned in the section above, SPACE's multidimensional flow model does not have 3D diffusion terms such as viscous stress terms and viscous/turbulent heat conduction terms in the governing equations. SPACE therefore cannot be used for an analysis where 3D diffusion effects are dominant, for example to analyse natural circulation in the large tank or almost stagnant flow. However, the multidimensional component used in the safety analyses of nuclear power plants is related to bundle geometries such as a reactor core and U-tubes in the steam generator. As a result, a multidimensional component of SPACE can be applied to all major nuclear reactor components, with the exception of large tanks such as a passive cooling tank and in-containment refuelling water storage tank (IRWST).

The constitutive models (including the flow regime map, wall and interfacial drag models, interfacial and wall heat transfer models and droplet entrainment and de-entrainment models) are based on the correlations that were established with fully-developed 1D flow and simple geometry such as pipe and bundle. For example, the wall drag model of SPACE is based on the Churchill (1977) [4.5-3] correlation, which was developed in pipe flow conditions. The same correlation is applied to all directions with different hydraulic diameters and velocities, depending on flow direction.

4.6. ATHLET code

4.6.1. Description

The T/H system code ATHLET is being developed by Gesellschaft für Anlagen- und Reaktorsicherheit (GRS) for the analysis of the whole spectrum of operational conditions, design basis accidents and beyond design-basis accidents without core degradation for nuclear energy facilities. The code provides specific models and methods for the simulation of nuclear power plants covering all common LWR designs, advanced Generation III, III+ and IV reactors as well as small modular reactors. The latest code version is ATHLET 3.2,

which was released in June 2019 [4.6-1] as part of the GRS code package AC²-2019 (including ATHLET, ATHLET-CD [core degradation], COCOSYS and complemented by the interactive simulator software ATLAS) [4.6-2].

ATHLET consists of several basic modules used for the simulation of the fundamental, multi-physical phenomena involved in the operation of a nuclear reactor, including thermal fluid dynamics (TFDs), heat transfer and heat conduction, neutron kinetics and the control and balance-of-plant. Dedicated interfaces for other independent modules are available, such as 3D neutron kinetic codes, computational fluid dynamics (CFD) codes or the GRS containment simulator COCOSYS. The extended code ATHLET-CD is applicable for the analysis of beyond design-basis accidents with core degradation. Figure 4.3 gives an overview of the most important code interfaces implemented in ATHLET.

The TFD-module of ATHLET offers two different sets of model equations for the simulation of the fluid-dynamic behaviour: (i) the two-fluid model with fully phase-separated conservation equations for liquid and vapour mass, momentum and energy; and (ii) the five-equation model with separate conservation equations for liquid, vapour mass and energy, supplemented by a mixture momentum equation. Both models account for thermal and mechanical non-equilibrium. The five-equation model includes a mixture-level-tracking capability, designed to capture the dynamic motion of and two-phase processes at a horizontal phase interface. A full-range drift-flux model is available for the calculation of the relative velocity between the fluid phases and considers different geometries such as horizontal and vertical pipes, annuli or bundles. The solution variables are the pressure, vapour temperature, liquid temperature and vapour mass quality, as well as the mass flow rate (five-eq. model) or the phase velocities (six-eq. model) respectively.

The range of working fluids covers light and heavy water and takes the transition between subcritical and supercritical fluid states into consideration. Helium, liquid sodium, lead and lead-bismuth eutectic (LBE) can be selected as the coolant. These extensions aim to simulate future Generation IV reactor designs. All liquid metal working fluids have thus far been treated as single-phase liquid. Code extensions towards evaporation and two-phase sodium flows are currently under development.

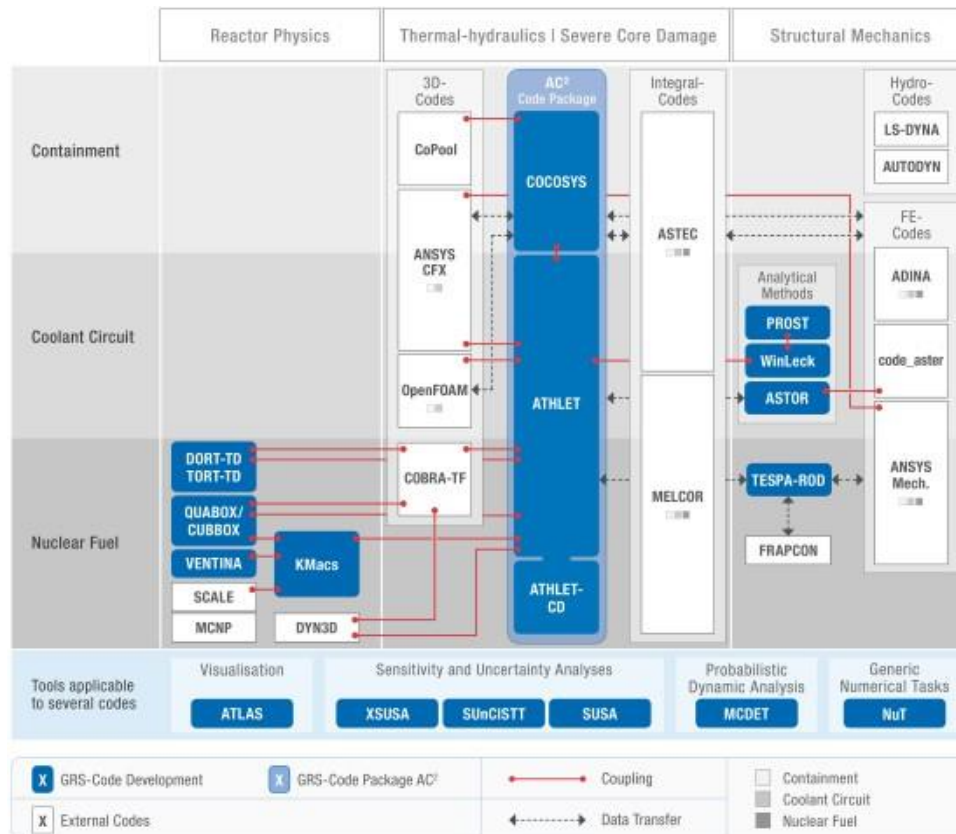
ATHLET also allows for the simulation of non-condensable gases. This applies to water as well as to liquid metal working fluids. Fluid properties are provided for hydrogen, nitrogen, oxygen, air, helium and argon. Additional mass conservation equations can be included for the description of boric acid or zinc-borate transport within the coolant system, as well as of the transport and release of nitrogen dissolved in the coolant's liquid phase.

The heat transfer package covers a wide range of single-phase and two-phase flow conditions of water. Correlations for critical heat flux and minimum film boiling temperature are included. The influence of spacer grids on the post-critical heat flux (CHF) can be considered. Evaporation and condensation occurring directly at heating or cooling surfaces can be calculated. A quench front model for bottom and top reflooding is available. Special heat transfer correlations are also available for supercritical water, liquid metal working fluids and helium, which accounts for specific geometries such as rod bundles or pebble beds. ATHLET enables the simulation of two-dimensional heat conduction in structural components, for which in-built or user-provided material properties can be used.

The time-dependent behaviour of the nuclear power generation is calculated by either a point-kinetics model or a 1D neutron kinetics model. The point-kinetics model is based on the application of the kinetics equations to one group of prompt and six groups of delayed neutrons. The reactivity changes due to control rod movement and reactivity feedback effects for the fuel temperature, moderator density, moderator temperature and boron concentration are considered. The 1D kinetics model solves the time-dependent neutron

diffusion equations with two energy groups of prompt neutrons and six groups of delayed neutrons. ATHLET also offers a general interface for the coupling of 3D neutron kinetic models. Several 3D codes for rectangular and hexagonal geometries have been successfully coupled, as referenced in Figure 4.3.

Figure 4.3. ATHLET code interfaces



Source: Lerchl et al., 2019.

Specific models are provided for the simulation of valves, pumps, accumulators, heat exchangers, steam separators, steam and gas turbines, compressors, steam condensers, single and double-ended breaks, fills and leaks. Critical flow – e.g. discharge flow – is calculated by a dedicated 1D thermal non-equilibrium model with consideration of the given flow geometry.

The time integration of the thermo-fluid dynamic model is performed with a standard ordinary differential equation (ODE) solver. The model provides the implicit solution of a first-order ODE linear system. The linearisation of the underlying conservation equation system is done numerically by calculating the Jacobian matrix. A block sparse matrix package can be used to efficiently handle the repeated evaluations of the Jacobian matrix and calculate the solution of the resulting system of linear equations. A rigorous error control is carried out by a higher order scheme for the time integration, obtained by an extrapolation analysis.

4.6.2. 3D model description

In the current release version 3.2, the TFD-module of ATHLET provides (i) a standard one-dimensional flow model, (ii) a well-established and often-used pseudo-multidimensional method, where the one-dimensional momentum equations are applied separately to each

co-ordinate direction of a multidimensional numerical grid, and (iii) an enhanced model with a genuine multidimensional set of thermal-hydraulic conservation equations. The latter is available only together with the six-equation two-fluid model. As a key element, this approach includes the phase-separated three-dimensional momentum equations presented in conservative form in equation (4.6.2-1), where μ stands for the phase index, liquid or vapour, α for void fraction, ρ for density, \vec{w} for velocity, p for pressure and RHS summarises further contributions such as gravitation, wall and interfacial shear or phase momentum change due to mass transfer.

$$\frac{\partial}{\partial t} (\alpha_\mu \rho_\mu \vec{w}_\mu) + \nabla (\alpha_\mu \rho_\mu \vec{w}_\mu \otimes \vec{w}_\mu) + \alpha_\mu grad(p) = RHS \tag{4.6.2-1}$$

By substituting the continuity equation into equation (4.6.2-1), the well-known primitive form of the momentum equation in terms of the phase velocity is obtained:

$$\alpha_\mu \rho_\mu \frac{\partial}{\partial t} (\vec{w}_\mu) + \alpha_\mu \rho_\mu \vec{w}_\mu \cdot \nabla \vec{w}_\mu + \alpha_\mu grad(p) = RHS \tag{4.6.2-2}$$

A simplified description of the three ATHLET flow models can be given in terms of the convective part of the momentum balance (4.6.2-2). As illustrated for Cartesian co-ordinates in Table 4.3, only the fully multidimensional flow model accounts for the mixed momentum flux contributions originating from the underlying vectorial character of the momentum equation.

Table 4.3. ATHLET flow models

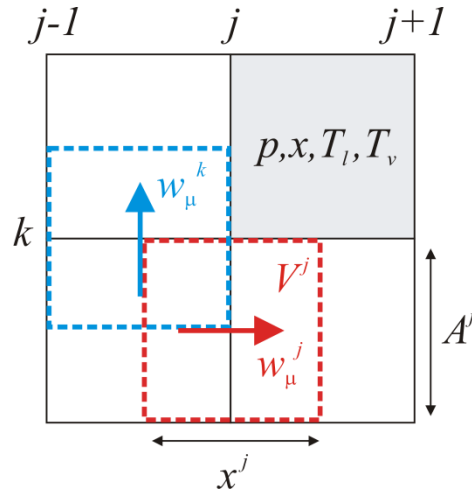
1D flow model	$\vec{w} \cdot \nabla \vec{w} = w_x \frac{\partial w_x}{\partial x}$
Pseudo 3D flow model	$\vec{w} \cdot \nabla \vec{w} = \begin{pmatrix} w_x \frac{\partial w_x}{\partial x} \\ w_y \frac{\partial w_y}{\partial y} \\ w_z \frac{\partial w_z}{\partial z} \end{pmatrix}$
3D flow model	$\vec{w} \cdot \nabla \vec{w} = \begin{pmatrix} w_x \frac{\partial w_x}{\partial x} + w_y \frac{\partial w_x}{\partial y} + w_z \frac{\partial w_x}{\partial z} \\ w_x \frac{\partial w_y}{\partial x} + w_y \frac{\partial w_y}{\partial y} + w_z \frac{\partial w_y}{\partial z} \\ w_x \frac{\partial w_z}{\partial x} + w_y \frac{\partial w_z}{\partial y} + w_z \frac{\partial w_z}{\partial z} \end{pmatrix}$

Source: Lerchl et al., 2019.

The implementation of the set of balance equations is performed on the basis of a finite-volume staggered-grid approach. The equations for the scalar solution variables include pressure p , mass quality x and phase temperatures T_l and T_v , which are derived from mass and energy conservation [4.6-1]. These are solved within control volumes, whereas the

momentum equations are integrated over so-called junctions connecting the centres of adjacent control volumes (see Figure 4.4).

Figure 4.4. Staggered-grid approach of ATHLET



The implemented momentum balance of the multidimensional flow model is not derived directly from equation 4.6.2-2, but from an expanded formulation:

$$\alpha_{\mu}\rho_{\mu}\frac{\partial}{\partial t}(\vec{w}_{\mu}) + \nabla(\alpha_{\mu}\rho_{\mu}\vec{w}_{\mu} \otimes \vec{w}_{\mu}) - \vec{w}_{\mu} \cdot \nabla(\alpha_{\mu}\rho_{\mu}\vec{w}_{\mu}) + \alpha_{\mu}grad(p) = RHS \quad (4.6.2-3)$$

As illustrated by Figure 4.4, the adopted finite-volume scheme integrates equation 4.6.2-3 across a junction-associated control volume V^j . The discretisation of the integral form of equation 4.6.2-3 is accomplished through use of the Gauss theorem and a first-order upwind scheme for the convective terms.

The multidimensional flow model that is implemented in Cartesian and cylindrical coordinates applies to 2D and 3D numerical grids. This application enables a numerically efficient solution of axis-symmetric problems, which can be simulated using a wedge-shaped 2D grid of arbitrary angle. The 3D model is generally used with structured grids. Multi-block grids can be used to geometrically approximate complex geometries like the RPV. The grid can also include gaps and consider internal structures.

Regarding software engineering, the multidimensional flow model is integrated in ATHLET as an extension of the phase-separated 1D balance equations of the two-fluid model. The multidimensional equations therefore directly benefit from the model basis that is already available in ATHLET, such as the comprehensive two-phase modelling or the coupling with other code modules for heat transfer, etc. Moreover, since 1D and 3D equations are based on same discretisation schemes, a close coupling of them using one common Jacobian can be easily achieved, which ensures improved numerical stability and efficient calculation with large time step sizes. Provided that a particular 3D grid is given, the required CPU times are comparable for the pseudo-3D and fully 3D flow model. This is the case due to the semi-implicit implementation of the multidimensional contributions, which keeps the structure and sparseness of the Jacobian matrix of the ODE system to be solved unchanged.

The main objective of the 3D T/H model is to enable complete system analyses at low numerical cost with a consideration of the impact of 3D flow phenomena on overall system behaviour. The low CPU time demand is especially important for the code's intended scope of application, which covers long-term analyses of nuclear facilities and safety assessment using numerically challenging uncertainty analyses. Coarse numerical grids are usually

employed for the discretisation of the TFD domain, which is adequate for the modelling basis of a system code approach and ensures reasonable computing power demands. The range of potential applications of the 3D model typically concerns vessels such as (parts of) the RPV, or huge water pools of passive safety systems where multidimensional flow processes are anticipated. There are currently no intrinsic restrictions and therefore the 3D model can also be applied to other components or geometries.

4.6.3. Simplifications and limitations

The multidimensional flow ATHLET model aims for a better and a more realistic representation of the complex flow phenomena occurring at macroscopic scales in large geometries such as the RPV. Its origin as an extension of the 1D TFD model means the 3D model currently has some limitations that are mainly related to the rather vague geometry representation by coarse grids and the closure relations used for the physical modelling.

The typically-employed coarse numerical grids limit the spatial resolution of flow phenomena to large-scale effects because only processes above grid scale can be captured. If the characteristic cell length is equal or even larger than the hydraulic diameter, the grid does not exactly resolve internals and details of the structure's geometry, which structure-aligned grids with nodes placed on the structure surface would do. Small-scale components can therefore only be considered in a simplified way by adapting the control volume geometry parameters (a kind of porosity influencing flow area and volume) and/or by using form losses that are often imprecise. The numerical schemes were used in addition to the coarse numerical grid (such as the first-order upwind scheme), which suffer from a rather high numerical diffusion that limits the exact treatment of steep gradients of the physical quantities. Dedicated models, such as those for boron transport, are implemented in ATHLET to attenuate this effect.

The closure laws, for example for wall and interfacial transfer, are based on algebraic equations that were originally derived from fully established 1D flows in specific geometries (e.g. pipe or bundle). The suitability of applying these models to general and more complex geometries is contested. If the fluidic domain is discretised by a multidimensional grid with a characteristic cell length that is smaller than the hydraulic diameter (e.g. in an open medium), wall-distant control volumes appear. Friction cannot be captured by source terms such as wall transfer for these internal volumes but must be modelled as transfer between adjacent fluid volumes. The multidimensional flow model in ATHLET optionally allows for the consideration of stresses due to fluid viscosity and turbulence-induced momentum diffusivity. The Reynolds stresses are calculated using an algebraic turbulence model, the Prandtl mixing length model, to close the equation system. The application of a turbulence model is only reasonable for relatively fine grids. A zero-equation turbulence model is also limited in its predictive capability.

4.7. CATHARE code

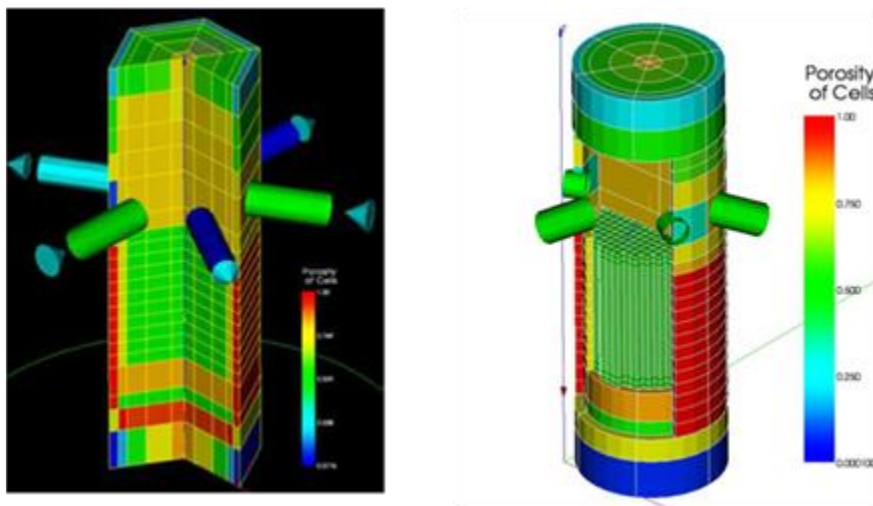
System codes like RELAP and ATHLET first developed “crossflow junctions” between 1D modules as a way of representing multidimensional flow features. Following TRAC, the CATHARE team developed an explicit 3D module for the reactor pressure vessel. It was a simple extension of the 1D module to 3D in porous medium using cylindrical and/or Cartesian co-ordinates. The main objective of such 3D modules was to model large-scale 3D effects in a pressure vessel during LB-LOCA, for example the downcomer penetration of ECCS water and reflooding of the core with transverse power profile effects. The heavy computational effort required resulted in the 3D module being mainly used for fast (short) transients such as large break LOCAs. With the increasing computer power, the

CATHARE 3D module is now used for SB- and IB-LOCAs. The rather coarse nodalisation schemes (about 1 000 nodes for a CATHARE pressure vessel 3D nodalisation) are usually applied and consequently the advantage of a 3D modelling of the flow processes can be offset to a certain extent. However, large-scale 3D effects could be better modelled than using 1D models.

The use of coarse nodalisation is not converged in space. These 3D modules must validate the physical model, numerical scheme and reference vessel nodalisation using full-scale experiments such as upper plenum test facility (UPTF) tests for the downcomer refill and PERICLES-2D and slab core test facility (SCTF) for the core reflooding (see Chapter five for the description of these experiments). This does not prevent compensating errors from arising. However, the large scale of the validation tests means that these compensations are expected to be similar in the reactor and the validation.

Figure 4.5 shows a nodalisation of a PWR pressure vessel using a CATHARE 3 3D module. The figure on the left shows an old nodalisation of a three-loop reactor, which has a cylindrical co-ordinate and five meshes in the radius, six meshes in the azimuthal direction and 21 meshes in the vertical direction for a total of only 630 meshes (198 meshes in the core). The figure on the right shows the reactor vessel in cylindrical co-ordinates, except for the core that is Cartesian [4.7-1] and described by one column of meshes per assembly. There is one only mesh in the downcomer in the radial direction, one for the core baffle, and five radial meshes in lower plenum, upper plenum and upper-head. This nodalisation makes the core better described, with about 6 000 meshes. This type of representation is new for CATHARE 3 [4.7-2] and not possible with CATHARE 2.

Figure 4.5. Illustration of the nodalisation of a PWR pressure vessel using a 3D module. On the left an old coarse nodalisation; on the right a recent finer nodalisation particularly in the core



Source: Pr ea et al., 2017.

The continuous progress of computer power will make it possible to combine various sub-components using Cartesian, cylindrical or elliptical frames of reference, depending on the local geometry as in Figure 4.6. Local mesh refinements in one or a few fuels assemblies are also likely to become possible, which would be treated by a subchannel analysis model, i.e. with one row mesh for each subchannel.

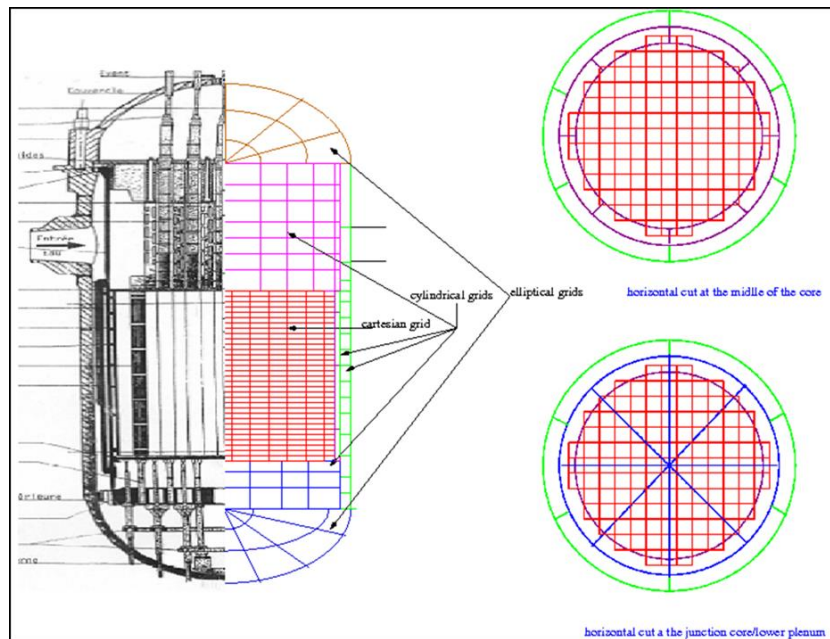
A 3D pressure vessel will be extended to applications such as:

- LOCAs: including SB-LOCAs, IB-LOCAs and LB-LOCAs;
- main steam line break (MSLB): in low flow, low power and high flow, high power conditions;
- boron dilution transients;
- loss of residual heat removal (LORHR);
- any other transient that might benefit from 3D simulations.

Other applications for research reactors, steam generators or other heat exchangers may be developed.

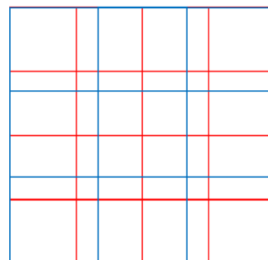
CATHARE 3 enables connections between 3D modules that do not have the same meshes to couple different types of 3D modules, which are non-conformal junctions. A third mesh is created when two different meshes are merged: the intersection mesh. Figure 4.7 illustrates a merge between two Cartesian regular meshes (3*3 in blue and 4*4 in red). A velocity is calculated by CATHARE 3 for each elementary exchange face belonging to the two meshes (in the example, there are 36 elementary faces). Non-conformal junctions are also available for Cartesian-cylindrical connections.

Figure 4.6. Illustration of a CATHARE advanced pressure vessel 3D modelling [4.7-1]



Source: Pr ea et al., 2017.

Figure 4.7. Scheme for non-conformal junctions



4.7.1. Description

The standard 3D description of two-phase flows used in CATHARE is a “porous” version of the two-fluid six-equation model. This model has been obtained from the local instantaneous two-phase balance equations using a double averaging. First, a time averaging to filter the pseudo-random variations of the flow variables due to turbulence and two-phase intermittence. Then, a space averaging accounting for the presence of complex and relatively small solid structures within the flow, such as in the case of the core, rod bundles, grids and guide tubes (referenced by [4.7-3] and [4.7-4]). These internal structures are homogenised and accounted for via a porous medium approach, which is similar to the one used in component scale codes. This approach allows for the nodalisation of the reactor vessel with coarse meshes.

Base 3D model in CATHARE 2 and CATHARE 3

CATHARE 2 and CATHARE 3 include a base 3D model used for reactor vessel applications. The porous approach’s mass, momentum and energy balance equations are written for each phase k (liquid or gas):

$$\frac{\partial \phi \alpha_k \rho_k}{\partial t} + \nabla \cdot (\phi \alpha_k \rho_k \mathbf{V}_k) = \phi \Gamma_k \quad (4.7.2-1)$$

$$\phi \alpha_k \rho_k \left(\frac{\partial \mathbf{V}_k}{\partial t} + \mathbf{V}_k \cdot \nabla \mathbf{V}_k \right) = -\phi \alpha_k \nabla p + \phi p_i \nabla \alpha_k + \phi (-1)^k \boldsymbol{\tau}_i + \phi \boldsymbol{\tau}_{pk} + \phi \alpha_k \rho_k \mathbf{g} \quad (4.7.2-2)$$

$$\frac{\partial \phi \alpha_k \rho_k e_k}{\partial t} + \nabla \cdot (\phi \alpha_k \rho_k e_k \mathbf{V}_k) = \phi \Gamma_k H_{ki} + \phi q_{ke} + \phi q_{pk} - p \left[\frac{\partial \phi \alpha_k}{\partial t} + \nabla \cdot (\phi \alpha_k \mathbf{V}_k) \right] \quad (4.7.2-3)$$

In these equations α_k , ρ_k , \mathbf{V}_k , e_k and H_k are the void fraction, density, velocity, internal energy and enthalpy of the phase k respectively, while ϕ is porosity (defined as the ratio of the fluid volume over the total volume including the structures), p pressure, Γ interfacial mass exchange, p_i interfacial pressure, τ_i interfacial friction, τ_{pk} wall friction and g gravity. q_{ki} and q_{pk} denote the interfacial and the wall-to-phase k heat transfer.

The mass (4.7.2-1) and energy (4.7.2-3) balance equations are written in a conservative form, whereas the momentum (4.7.2-2) balance equation is written in a non-conservative form. As a result, the porosity term ϕ can be eliminated from the momentum balance equation and from the convective term, whereas it must be taken into account in the convective term of both the mass and energy balance equations. The system of equations (4.7.2-1)-(4.7.2-2)-(4.7.2-3) models neither the turbulent diffusion nor the dispersion terms. The system is suitable for simulating LOCAs with a coarse mesh, where the interfacial and wall transfer terms have the most influence, but less suitable for mixing problems such as MSLB or boron dilution.

CATHARE 3 3D models

The CATHARE 3 3D module for core applications also includes extended capabilities to improve the accuracy of simulations of light water reactor accidents. This option features models for turbulent and diffusion phenomena that can affect the temperature map in a rod bundle. Moreover, in the case of an occurrence of two-phase crossflows between adjacent subchannels, the void dispersion phenomena are accounted for by a mixing term in the

momentum balance equations. Equations (4.7.2-2) and (4.7.2-3) have been accordingly modified in the following ways in [4.7-3] and [4.7-5]:

$$\phi \alpha_k \rho_k \left(\frac{\partial \mathbf{V}_k}{\partial t} + \mathbf{V}_k \cdot \nabla \mathbf{V}_k \right) = -\phi \alpha_k \nabla p + \phi (p_i + p_i^T) \nabla \alpha_k + \phi (-1)^k \boldsymbol{\tau}_i + \phi \boldsymbol{\tau}_{pk} + \phi \alpha_k \rho_k \mathbf{g} + \nabla \cdot (\alpha_k \rho_k \underline{\underline{\boldsymbol{\tau}_k^T}}) \quad (4.7.2-4)$$

$$\frac{\partial \phi \alpha_k \rho_k e_k}{\partial t} + \nabla \cdot (\phi \alpha_k \rho_k e_k \mathbf{V}_k) = \phi \Gamma_k H_{ki} + \phi q_{ke} + \phi q_{pk} - p \left[\frac{\partial \phi \alpha_k}{\partial t} + \nabla \cdot (\phi \alpha_k \mathbf{V}_k) \right] + \nabla \cdot (\alpha_k \mathbf{q}_k^T) \quad (4.7.2-5)$$

The three different mixing terms implemented are represented by the void dispersion term $p_i^T \nabla \alpha_k$, stress tensor $\underline{\underline{\boldsymbol{\tau}_k^T}}$ that accounts for turbulent and dispersive effects in the momentum equation and the turbulent, and dispersive heat flux \mathbf{q}_k^T .

CATHARE 3 also includes a three-field model (continuous gas, continuous liquid and droplets) in the 3D module. It is intended to calculate 3D components where the behaviour of the droplets can be significant, for example in the core or upper plenum.

4.7.2. Simplifications and limitations

For the interfacial and wall transfers, in the base 3D model, the mass, energy and momentum balance equations are directly extrapolated from the 1D models, in which the code includes two flow patterns: the stratification limit and the onset of entrainment (see [4.7-6] for an overview of the 1D models). The 3D model of CATHARE also assumes no stratification. Only the onset of droplet entrainment criterion is therefore explicitly written. Finally, no added mass term is considered in the 3D model equation system.

Specific laws in the downcomer

The 3D module assessment against the downcomer refill tests (UPTF tests six and seven) [4.7-7] and [4.7-8] and end of reflood phase tests (tests UPTF 25 and Japan Atomic Energy Research Institute [JAERI]-SUDO refill tests) [4.7-9] and [4.7-10] have led to a specific set of suggested correlations compared to those dedicated to the 1D approach that better describe the annular refill phase during a LB-LOCA and the end of reflood phase. These correlations concern the liquid-to-interface heat flux condensation coefficient, entrainment fraction used in the interfacial friction models and interfacial friction in bubbly/slug/churn flow regimes [4.7-4]. The entrainment fraction E (ratio of the droplet flow rate over the total liquid flow rate) is adapted for such calculations in the downcomer by the modification of the inception entrainment velocity used for 1D calculations, i.e. the critical gas velocity V_0^{1D} allowing entrainment phenomena:

$$V_0^{1D} = 2.1 \times 10^{-4} \frac{\sigma}{\mu_G} \sqrt{\frac{\rho_L}{\rho_G}} \quad (4.7.3-1)$$

The critical velocity V_0^{1D} is based on the Steen-Wallis correlation. The adapted correlation for the downcomer is:

$$V_0^{DC} = 3 \times V_0^{1D} \quad (4.7.3-2)$$

The entrainment rate is thus computed as:

$$E = \left[1 - \text{Min} \left(1, \frac{V_0^{DC}}{\alpha |V_G|} \right) \right]^{-2} f_\alpha \quad (4.7.3-3)$$

where f_α is a function of the void fraction.

The liquid-to-interface heat flux condensation is also modified in the downcomer:

$$q_{le}^{DC} = 5.0 \times q_{le}^{1D} \quad (4.7.3-4)$$

where q_{le}^{1D} is the liquid-to-interface heat flux condensation for the 1D module, based on the Shah and Chen correlations, and taking into account the condensation on droplets.

The interfacial friction term needed to be decreased in the simulation of UPTF test 25 and JAERI-SUDO experiments in the case of bubbly-slug-churn flow for the 3D module/annular downcomer, with respect to the one used in the 1D module:

$$\tau_{il}^{DC} = 0.3 \times \tau_{il}^{1D} \quad (4.7.3-5)$$

Mixing terms for rod bundle calculations

The momentum and energy turbulent and dispersive diffusive terms came out during the double (time and space) averaging process of the local convection terms. Further details can be found in [4.7-3].

The turbulent diffusion and dispersion tensor $\underline{\underline{\tau}}_k^T$ in equation (4.7.2-4) is modelled following the microscopic eddy-diffusivity concept:

$$\underline{\underline{\tau}}_k^T = (v_{ik}^\phi + v_{dk}^\phi) \left[\nabla(\phi \mathbf{V}_k) + \nabla^T(\phi \mathbf{V}_k) - \frac{2}{3} \nabla \cdot (\phi \mathbf{V}_k) \mathbf{I} \right] \quad (4.7.3-6)$$

The macroscopic turbulent viscosity v_{ik}^ϕ can be modelled using a macroscopic k- ϵ model. The sum of the dispersive momentum coefficient and the macroscopic turbulent viscosity comes from a correlation developed by Teruel [4.7-11], which averages microscopic results obtained from numerical computations of flows in arrays of cubes and is dependent on the hydraulic diameter D_h :

$$\frac{(v_{ik}^\phi + v_{dk}^\phi)}{D_h |\mathbf{V}_k|} = C_\mu \left[\left(\frac{120}{C_D} \frac{\sqrt{1-\phi} + \phi - 1}{\phi^4} \left(\frac{\sqrt{1-\phi}}{\text{Re}} + \frac{1}{60} \right) \right)^{4/3} \frac{\phi^4}{120 \sqrt{1-\phi}} \left(\frac{\sqrt{1-\phi}}{\text{Re}} + \frac{1}{60} \right)^{-1} \right] \quad (4.7.3-7)$$

where $C_\mu=0.09$, $C_D=1.4$ and Re is the Reynolds number based on the hydraulic diameter.

The turbulent and dispersive heat flux \mathbf{q}_k^T is given by:

$$\mathbf{q}_k^T = \left(\alpha_{ik}^\phi \mathbf{I} + \underline{\underline{D_{dk}^\phi}} \right) \phi \nabla e_k \quad (4.7.3-8)$$

The macroscopic turbulent thermal conductivity α_{ik}^ϕ is related to the macroscopic turbulent viscosity ν_{ik}^ϕ via a macroscopic turbulent Prandtl number, $\alpha_{ik}^\phi = \nu_{ik}^\phi / \text{Pr}_{ik}^\phi$. This term is usually dominant over the macroscopic turbulent heat flux in rod bundle calculations by two or three orders of magnitude. The transverse component of the thermal dispersive tensor is correlated as:

$$D_{dk}^{\phi,trans} = \frac{A \sqrt{\langle k_f \rangle} D_h}{\text{Pr}_{ik}^\phi} \quad (4.7.3-9)$$

where A is a parameter adjusted to 0.5 for the PWR Subchannel and Bundle Tests (PSBT) benchmark (see Chapter 5 for the description of the experiment) and the macroscopic turbulent Prandtl number is equal to 1. The spatial averaged turbulent kinetic energy $\langle k_f \rangle$ is given by a correlation established for a single-phase flow in tubes or subchannels, far from spacer grid:

$$\langle k_f \rangle = 0.0367 |\mathbf{V}_L|^2 \text{Re}^{-1/6} \quad (4.7.3-10)$$

The turbulent interfacial pressure in the void dispersion term $p_i^T \nabla \alpha_k$ has the following expression:

$$p_i^T = B \rho_L \sqrt{\langle k_f \rangle} \mathbf{V}_L \quad (4.7.3-11)$$

where B is a parameter adjusted to 0.2 for the PSBT benchmark and $\langle k_f \rangle$ is given by equation (4.7.3-10).

References

- [4-1] Roth, G.A. and F. Aydogan (2014), “Theory and implementation of nuclear safety system codes”, *Progress in Nuclear Energy*, Volume 76, pp. 160-182.
- [4.2] Bestion, D. (2008), “System Code Models and Capabilities”, In Vitanza, C. (Ed.). Thicket-2008, Italy, p. 486.
- [4.1-1] Rafael, M.-J. and J.H. Mahaffy (1998), “Numerical diffusion and the tracking of solute fields in system codes: Part II. Multi-dimensional flows”, *Nuclear Engineering and Design*, 179(3), pp. 321-344.
- [4.1-2] Wang, D., J.H. Mahaffy, J. Staudenmeier and C.G. Thurston (2013), “Implementation and assessment of high resolution numerical methods in TRACE”, *Nuclear Engineering and Design*, 263 (4), pp. 327-341.
- [4.2-1] Bestion, D. (2017), “System thermalhydraulics for design basis accident analysis and simulation: Status of tools and methods and direction for future R&D”, *Nuclear Engineering and Design*, 312, pp. 12–29.
- [4.2-2] Calleja, M. (2014), “X-TREAM project: Task 1a. Survey of the different numerical algorithms used in present computer codes”, *Chalmers University of Technology*, CTH-NT-288, Gothenburg, Sweden.
- [4.4-1] Kaeri, M. (1998), *Code Manual Volume I: Code Structure, System Models, and Solution Methods*, NUREG/CR-5535, US Nuclear Regulatory Commission, Washington, DC.
- [4.4-2] Thurgood, M.J., J.M. Kelly, T.E. Guidotti, R.J. Kohrt and K.R. Crowell (1983), “COBRA/TRAC - A Thermal-Hydraulics Code for Transient Analysis of Nuclear Reactor Vessels and Primary Coolant Systems”, NUREG/CR-3046 PNL-4385, US Nuclear Regulatory Commission, Washington, DC.
- [4.4-3] Paik, C.Y., L.E. Hochreiter, J.M. Kelly and R.J. Kohrt (1986), “Analysis of FLECHT SEASET 163-Rod Unblocked Bundle Data Using COBRA-TF”, NUREG/CR-4166, Electric Power Research Institute, Pittsburgh.
- [4.4-4] Chung, B.D., K.D. Kim, S.W. Bae, J.J. Jeong, S.W. Lee, M.K. Hwang and C. Yoon (2010), “Code Manual Volume I: Code Structure, System Models and Solution Methods”, KAERI/TR-2812/2004, Korea Atomic Energy Research Institute.
- [4.5-1] Ha, S.J., C.E. Park, K.D. Kim and C.H. Ban (2011), “Development of the SPACE Code for Nuclear Power Plants”, *Nuclear Engineering and Technology*, 43(1), pp. 45-62.
- [4.5-2] Lee, S.Y. (2008), “Governing equations for SPACE code”, S06NX08-N-1-TR-01, KOPEC/NED TR/07-006 Rev. 1, Korea Power Engineering Company, Daejeon, Korea.
- [4.5-3] Churchill, S.W. (1977), “Friction-Factor Equation Spans All Fluid Flow Regimes”, *Chemical Engineering*, Volume 84, pp. 91-92.
- [4.5-4] Lee, S.W. et al. (2016), “Current Development Status and Future Plan of SPACE”, the 9th National Congress on Fluids Engineering (9NCFE), 10-12 August, Daegu, Korea.
- [4.6-1] Lerchl, G., H. Austregesilo, A. Langenfeld, P. Schoffel, D. von der Cron and F. Weyermann (2019), “ATHLET 3.2 User’s Manual”, *Gesellschaft fuer Anlagen- und Reaktorsicherheit (GRS) gmbH*, 1, Rev. 8.
- [4.6-2] Wielenberg, A., L. Lovasz, P. Pandazis, A. Papukchiev, L. Tiborcz, P.J. Schöffel, C. Spengler, M. Sonnenkalb and A. Schaffrath (2019), “Recent improvements in the system code package AC² 2019 for the safety analysis of nuclear reactors”, *Nuclear Engineering and Design*, 354.

- [4.7-1] Pr ea, R., V. Figerou, A. Mekkas and A. Ruby (2017), “CATHARE-3: A first computation of a 3-inch-break loss-of-coolant accident using both Cartesian and cylindrical 3d-meshes modelling of a PWR vessel”, NURETH-17, 4-9 September, Xi’an, China.
- [4.7-2] Emonot, P., A. Souyri, J.L. Gandrille and F. Barr e (2009), “CATHARE-3: A new system code for thermal-hydraulics in the context of the NEPTUNE project”, NURETH-13, 27 September-2 October, Kanazawa City, Japan.
- [4.7-3] Chandesris, M., M. Mazoyer, G. Serre and M. Valette (2013), “Rod bundle thermalhydraulics mixing phenomena: 3D analysis with CATHARE 3 of various experiments”, NURETH-15, 12-17 May, Pisa, Italy.
- [4.7-4] Dor, I., M. Chandesris, P. Germain and A. Ruby (2013), “CATHARE 3D module from CATHARE 2 V2.5_3 to CATHARE 3 V1.0”, NURETH-15, 12-17 May, Pisa, Italy.
- [4.7-5] Valette, M. (2012), “Analysis of Subchannel and Rod Bundle PSBT Experiments with CATHARE 3”, *Science and Technology of Nuclear Installations*.
- [4.7-6] Bestion, D. (1990), “The physical closure laws in the CATHARTE code”, *Nuclear Engineering and Design*, 124 (3), pp. 229-245.
- [4.7-7] Dor, I. (1993), “Analysis of UPTF downcomer tests with the CATHARE multi-dimensional model”, NURETH-6, Grenoble, France, 5-8 October.
- [4.7-8] Jeong, J.J., I. Dor and D. Bestion (1997), “Improvement and assessment of the CATHARE 2 three-dimensional module compared with the UPTF downcomer test 7”, *Nuclear Technology*, 117(3), pp. 267-280.
- [4.7-9] Dor, I., G. Lavialle, P. Germain and T. Mieusset (2007), “Investigation of downcomer level evolution during late reflooding with CATHARE 3D module”, NURETH-12, 30 September-4 October, Pittsburgh, Pennsylvania, United States.
- [4.7-10] Sudo, Y. and H. Akimoto (1982), “Downcomer Effective Water Head during Reflood in Postulated PWR LOCA”, *Journal of Nuclear Science and Technology*, 19(1), pp. 34-45.
- [4.7-11] Teruel, F.E. (2007). *Macroscopic turbulence modelling and simulation for flow through porous media*, PhD thesis, University of Illinois, United States.

5. Experimental support with 3D capabilities

5.1. Separate effects tests

5.1.1. ROCOM

5.1.1.1 Objective of the experiment

The ROCOM (Rossendorf Coolant Mixing Model) test facility was built at the German research centre HZDR (Helmholtz Centre Dresden Rossendorf) for the investigation of coolant mixing in the reactor pressure vessel of pressurised water reactors (PWRs). ROCOM was a 1:5 model of a four loops German PWR.

The test facility was designed for the investigation of a wide spectrum of mixing scenarios [5.1.1-1]. Experiments were carried out to measure the time-dependent distribution of the transport variables such as the coolant temperature and boron concentration inside the reactor pressure vessel. The leading input variables were the time history of the flow rates in the four loops of the primary circuit and the coolant temperature, or boron concentration at the inlet nozzles. The differences in either boron concentration or coolant temperature were modelled using salt, sugar or ethanol tracer solutions, which influence electrical conductivity.

The test facility was equipped with wire mesh sensors, which enabled a high resolution measurement of the transient tracer concentration in time and space.

5.1.1.2 Description of the test loop

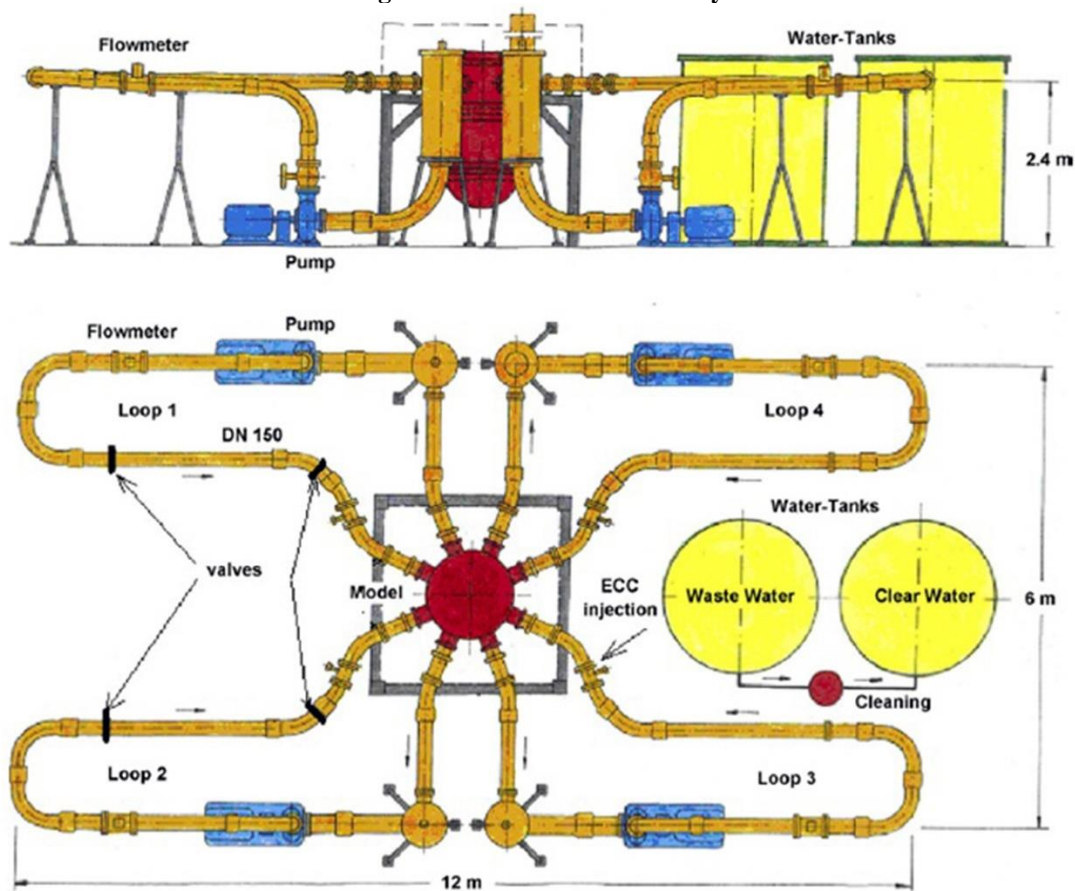
The reactor pressure vessel manufactured from acrylic glass is the main part of the test facility (Figure 5.1). The model matches the original reactor's geometrical similarity, of the scale 1:5, from the bends in the cold leg that are closest to the reactor inlet until the core inlet. The inlet nozzles' geometry, with their diffuser segments and the curvature radius of the inner wall at the junction with the pressure vessel, was closely replicated in the model. Similarity was also taken into account for the perforated sieve drum and core support plate with the orifices for the coolant. The entry into each fuel assembly was an orifice with a diameter of 30 mm, containing one measurement position of the integrated core inlet wire mesh sensor. Furthermore, all inlet nozzles of the reactor pressure vessel were equipped with sensors. Two different types of sensors were installed in the test facility's downcomer. The first type measures tracer concentration in one radial plane. One sensor of this type was installed at the inlet (just below the nozzle plane) and at the outlet of the downcomer, and 64 measurement positions along the circumference were distributed in a distance of 5.625° . The conductivity was measured at each of these positions at four measuring points over the width of the downcomer (pitch: 13 mm). A second type of sensor was developed and installed for an improved visualisation and quantification of the mixing processes in the downcomer. This type consists of two measuring grids of 64 azimuthal positions and 29 positions over the height of the downcomer, which were arranged in a formation of two concentric cylinders. Additional sensors could be installed at additional positions along the

flow path, for example in the outlet nozzles or by the emergency core cooling (ECC) water injection.

The vessel core itself was only represented by a hydraulic resistance of the fuel elements. A core basket was inserted as a hydraulic short circuit between the core inlet and outlet. The pressure vessel's model was equipped with a plane vessel head. The upper plenum did not contain any internals.

ROCOM was equipped with four speed-controllable circulation pumps in each loop. These circulation pumps were controlled by individual frequency transformers that enable any desired combination of flow rates to be set in each loop. The corresponding pumps were operated at reduced rotation speed for natural circulation conditions. The volume ratio of vessel to loop was the same for both test facility and original reactor, ensuring identical coolant travelling times.

Figure 5.1. The ROCOM facility



Source: Grunwald et al., 2002.

5.1.1.3 Tests performed

The experiments performed in the ROCOM facility with coolant mixing include the following.

Coolant mixing in stationary flow regimes

For this flow regime, a constant mass flow rate over time is present at the inlet nozzles of all loops or in part of the loops, while the coolant temperature or boron concentration in one of the running loops changes. Such scenarios become possible during forced

convection (main coolant pumps in operation) as well as natural circulation in the primary circuit of a nuclear reactor. A typical cause of temperature perturbation is a leak in one of the main steam lines, which causes overcooling of the coolant in one loop. This overcooled water can reach the reactor before the main coolant pumps are switched off.

Start-up of a reactor coolant pump

The inadvertent start of the main coolant pump in a loop, where there is coolant with reduced boron concentration, is the main topic of investigations into flow scenarios using changing coolant flow rates in one or more loops of the reactor. Coolant with decreased boron concentration can build up, for example due to a malfunction of the make-up system of a switched-off reactor, or during a steam generator tube rupture when a flow of de-borated water goes from the secondary to the primary circuit.

Buoyancy-related mixing experiments

Density differences between the injected coolant and primary loop inventory can play an important role during a loss-of-coolant accident; the injection of the relatively cold emergency core cooling water can induce buoyancy-driven stratification. This stratification can cause high-temperature gradients and increased thermal stresses in the reactor pressure vessel's wall. A boron dilution transient could be initiated in the case of inadvertent injection of emergency core cooling water with low boron concentration.

Coolant mixing under natural circulation conditions following a postulated small break loss-of-coolant accident

Under-borated coolant can accumulate in the loops and can be transported towards the reactor core during a loss-of-coolant accident. The mixing of weakly borated water inside the reactor pressure vessel was therefore investigated in experiments at the ROCOM test facility. The mixing in the downcomer was strongly focused on, which was observed with a measuring grid of 64 azimuthal and 32 vertical positions. The boundary conditions for these experiments were derived from thermal-hydraulic (T/H) experiments at the Primär-Kreislauf (PKL) test facility operated by AREVA in Erlangen [5.1.1-6].

The test facility's design parameters based on water at 20°C are presented in Table 5.1 together with the original reactor's data.

Table 5.1. Design parameters of the ROCOM facility

Parameter	Original PWR	ROCOM
Inner diameter of the pressure vessel (m)	5.0	1.0
Height of pressure vessel (m)	~12.0	~2.4
Inner diameter of the inlet nozzle (m)	0.75	0.15
Downcomer width (m)	0.315	0.063
Coolant flow rate per loop (m ³ /h)	23 000	350 (max) 185 (nom.)
Coolant inlet velocity (m/s)	14.5	5.5 (max.) 2.91 (nom.)
Velocity in the downcomer (m/s)	5.5	2.1 (max.) 1.1 (nom.)
Reynolds number in the inlet nozzle (-)	8.4x10 ⁷	8.3x10 ⁵ (max.) 4.4x10 ⁵ (nom.)
Reynolds number in the downcomer	2.7x10 ⁷	2.6x10 ⁵ (max.) 1.4x10 ⁵ (nom.)
Ratio Reynolds reactor/ROCOM	1	~100 (max.) ~190 (nom.)
Travelling time reactor/ROCOM (-)	1	1 (nom.)

Source: Grunwald et al., 2002.

5.1.1.4 Application for system code validation

The experiments with coolant mixing in the downcomer and core lower plenum under natural and forced circulation are particularly suitable for the validation of three-dimensional (3D) system codes. Several pre- and post-test calculations of a series of ROCOM tests matrix with 3D T/H system codes have been reported over the past few years [5.1.1-2 to 5.1.1-5]. The local tracer concentration measurements with a high resolution in time and space are suitable for assessing fluid mixing in the cold legs and downcomer and from the lower plenum to the core inlet. However, only mixing scalars were measured and there is no further information about other quantities, such as fluid velocities.

The ROCOM facility has now been dismantled. However, the experimental data and corresponding reports are available at HZDR and in the NEA Data Bank.

5.1.2. INKA

5.1.2.1 Objective of the experiment

The INtegral Test Facility KARlstein (INKA) test facility was designed and constructed in 2008 to test and demonstrate the performance of passive safety systems for an advanced boiling water reactor design, which was denominated KERENA™ [5.1.2-1]. It is operated by FRAMATOME (formerly AREVA). All passive safety features necessary to simulate accident scenarios (loss-of-coolant accidents [LOCAs] and non-LOCAs) are included in the facility's design.

The passive safety systems at INKA can be individually tested to analyse their performance and during integral tests to analyse the interaction between systems and therefore the capability of the KERENA™ passive systems to perform their design function. KERENA™ is the reference for INKA and therefore tests dealing with generic tasks for boiling water reactor (BWR) plants or other light water reactor designs can be performed.

5.1.2.2 Description of the test loop

The central component of the INKA facility is the water/steam accumulator vessel of the former large valve test facility Großarmaturen-Prüfstand (GAP), which simulates the reactor pressure vessel (RPV) at a volumetric scale of 1:6 (Figure 5.2). This vessel has a design pressure of 11 MPa, storage capacity of 125 m³ and is fed by a Benson boiler with a maximum power supply of 22 MW.

The INKA setup simulates the KERENA™ containment in a 1:24 scale. It includes three main passive safety systems:

- Emergency condenser (EC): a passive emergency core natural circulation flow cooling system. It includes a tubular heat exchanger. During normal plant operation, the heat exchanger tubes are filled with water and the EC is not in operation. If there is a drop in the reactor pressure vessel water level, for example following a reactor scram caused by a LOCA, steam fills the tubes and the EC starts to operate. The efficiency of the EC increases as reactor pressure increased and the RPV water level decreases. The temperature and pressure on the secondary side of the heat exchanger (flooding pool vessel) have only a small effect on the EC's efficiency.
- Containment cooling condenser (CCC): a passive long-term containment heat removal system that also uses natural convection. The system similarly includes tubular heat exchangers. Each CCC tube is filled with water from the shielding/storage pool located above the containment (Figure 5.2). Steam released

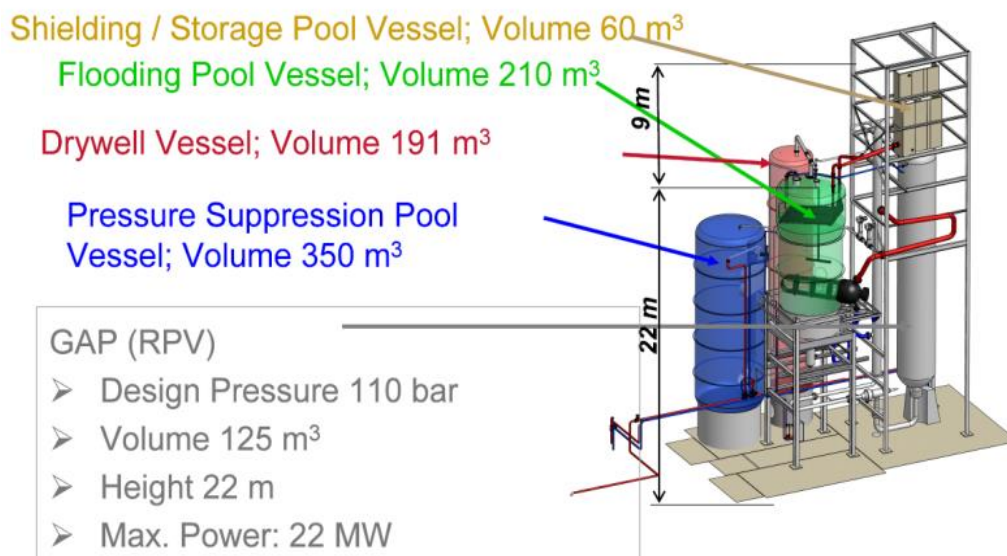
into the drywell, when an accident occurs, condenses on the external tube walls. The water inside the CCCs' tubes heats up, causing natural circulation. The system's efficiency increases as containment pressure increases. The EC and CCC together build the passive cooling chain connecting the heat source from the RPV with the heat sink to the shielding/storage pool.

- Passive core flooding system (PCFS): this refills the RPV when a LOCA occurs. A check valve opens as soon as the pressure difference between the RPV and the flooding pool vessel (FPV) reaches a defined value, ensuring long-term core cooling.

The containment is simulated by three vessels. The FPV contains the EC and CCC passive systems. The PCFS connects the FPV to the EC's return line. The drywell vessel (DWV) simulates the residual gas volume of the containment drywell. The pressure suppression pool is simulated by the third pressure suppression pool vessel (PSPV) (Figure 5.2).

All components of the test facility are located at their original height to ensure that the driving forces for all natural circulation processes are correctly modelled. Key components contributing to the passive safety features are implemented at a component scale of 1:1, but only one train is simulated, unlike the multi-train implementation in the reference plant.

Figure 5.2. The INKA Facility



Source: Leyer and Wich, 2011.

All INKA vessels and systems can be individually operated. The vessels are connected by pipes that can be opened and closed, as required. Each vessel can be independently heated by direct steam injection. The vessels' water levels can also be independently set. Usually only the FPV is needed for tests of the individual passive components. All vessels and components are used for the integral transient and LOCA experiments.

INKA has over 300 available sensors. Most are conventional instrumentation, such as temperatures, mass flow, pressures and differential pressure sensors. In addition to these, there are two-phase flow sensors (thermo-needle probes and gamma densitometers) installed. The gas mixture in the vessels is measured using a mass spectrometer with a probe sampling system. The pressures, water levels and temperatures in the water and gas volumes are essentially measured in all vessels. Mass flow rates are measured in the main pipes, such as the break line, EC inlet line and steam safety/relief line.

The scaled INKA flooding pool only provides a relatively small water volume compared with the original plant design. The pool's limited dimensions mean that inhomogeneous 3D temperature distribution inside it may not be as pronounced as in the original plant. EC heat transfer and temperature stratification inside the flooding pool were still measured. Thermocouples were installed within the flooding pool to carry this out in several layers of different heights.

5.1.2.3 Tests performed

Different single effect tests for the different passive safety systems have been performed in the past for EC (steady-state and transient cases), containment cooling condenser with and without non-condensable gases, and passive core flooding systems.

The experimental programme plans the following integral tests in the test facility:

- main steam line break within the containment;
- small break at RPV bottom;
- feedwater line break within the containment;
- loss of the ultimate heat sink (comparable to a station blackout).

A key boundary condition for all four proposed scenarios is an extended loss of AC power (ELAP), where no active pump, active control system actions or operator actions are possible.

Experimental data can be obtained from FRAMATOME.

5.1.2.4 Application for system code validation

The FPV has the highest sensor density (mainly temperature measurements) because this vessel contains the EC and CCC passive systems. Thermal stratification can be observed within the vessel during the heating up of the FPV by the EC. A 3D approach used for the simulation of the FPV can be validated by comparing the calculated results with the experimental temperature data gathered from the EC separate effect tests. A mixture-level-tracking model can also be verified, for example by using data from experiments for the passive flooding system (continuously falling mixture level within the FPV during drainage).

5.1.3. Upper plenum test facility

5.1.3.1 Objective of the experiment

The upper plenum test facility (UPTF) was a full-scale mock-up of the primary system of a four-loop 1 300 MWe Siemens/KWU pressurised water reactor. Both the separate effect tests and integral effect tests were carried out using the UPTF facility.

The test vessel upper plenum internals, downcomer and primary coolant piping were replicas of those from the reference plant. However, some important PWR components – such as the core, coolant pumps, steam generators and containment – were replaced by devices that simulated the T/H behaviour of these components during end-of-blowdown, refill and reflooding phases of a LB-LOCA. UPTF simulated hot and cold leg breaks of various sizes. The ECC injection systems at the UPTF were configured to simulate the various ECC systems of German, Japanese and US PWRs within the framework of the international UPTF 2D/3D research programme [5.1.3-1].

Figure 5.3 shows how the UPTF primary system was divided into investigation and simulation areas. The investigation areas, which were exact replicas of a German PWR,

consisted of the following: core/upper plenum interface, upper plenum, hot legs, cold legs, downcomer, lower plenum and downcomer lower plenum interface. An understanding of the physical phenomena occurring in these two areas during a LOCA is important for reactor safety analysis.

Realistic T/H behaviour in the investigation areas was ensured by the establishment of appropriate initial and boundary conditions. The boundary conditions were established using simulators. The simulators' setup and operation were based on small-scale data and mathematical modelling.

The simulation areas included the core simulator, steam generator, pump simulators and containment simulator.

5.1.3.2 Description of the test loop

The main components of the UPTF are described below.

Test vessel and internals

The dimensions of the UPTF test vessel (Figure 5.3) were identical to the reactor vessel of the reference PWR, with the exception of the wall thickness. The entire inner surface was clad with stainless steel. Penetrations were provided for instrumentation. The vessel internals consisted of lower plenum internals, core simulator, dummy fuel assemblies and upper plenum internals. The lower plenum had identical dimensions to the reference PWR. The core region contained the core simulator and 193 quarter-length dummy fuel assemblies with end boxes.

The core simulator consisted of 17 pipes for steam and water injection. These injection pipes subdivided into a total of 193 steam/water injection nozzles, one below each dummy fuel assembly. The core simulator was divided into 17 zones, each of which had separate injection control valves, so that lateral distribution of steam and water flow rates could be obtained to simulate core radial peaking, for example. The total flow capacities were 360 kg/s for steam and 2 000 kg/s for water.

The upper plenum matched the reactor's dimensions and contained 61 control rod guide tubes (CRGTs) and 16 support columns. Eight vent valves were mounted in the core barrel above the hot leg nozzle elevation to simulate ABB and Babcock & Wilcox (B&W) PWRs. The vent valves could be locked or unlocked, depending on the type of test.

Steam generator simulators

Each of the three intact loops contained a steam generator simulator (SG) for the simulation of a PWR SG. The loops were designed to measure water carried into the simulators and simulate the SG's response to carryover, while preserving the flow resistance of the reference SGs. Water carryover was measured by separating the water from the steam flow using a set of 31 two-stage cyclone separators. A steam mass flow equivalent to the measured water entrainment was injected into the simulator to simulate the thermal response of a PWR SG.

Steam/water separators

Steam/water separators were located in the hot and cold legs of the broken loop. Their configurations were similar to the SG simulators that have been described, except for the dimensions and number of cyclones that were adjusted to account for the larger mass flows expected in the broken loop.

Emergency core cooling system (ECCS)

The ECC injection systems commonly used in US and Japanese PWRs and SG PWRs were simulated at UPTF using accumulators. There were four accumulators in total: two with a capacity of 150 m³ and two with a capacity of 125 m³ each. Two of them could be alternatively used as nitrogen accumulators for the simulation of accumulator nitrogen release in US and Japanese PWRs.

Pump simulators

UPTF simulated the flow resistance and key internal heights of a reactor pump with manually-adjustable valves installed in each intact loop, between the pump seal and the cold leg injection port.

Containment simulator

The containment simulator was designed to simulate the containment pressure history following a LOCA in the PWR. It was divided into an upper dry well of about 500 m³ and a wet well of about 1 000 m³. Vent pipes routed steam from the dry well into the wet well's water pool, where it condensed.

Process instrumentation and control

The scope of the process instrumentation included 414 measurements in total. The measurements were of fluid temperatures, single-phase mass flows, water levels, absolute pressures, differential pressures and valve positions. These instruments monitored test boundary conditions and supported the operation of the facility's auxiliary systems. The signals from 265 process instrumentation channels were also directed towards the main test data acquisition system for test evaluation.

The UPTF core simulator steam and water injection rates and steam generator simulator steam injection rates could be either pre-programmed or controlled by feedback systems. These feedback systems simulated the T/H responses of the PWR active core and steam generators to water penetration.

The instrumentation and data acquisition system provided T/H data from both the investigation and simulation areas and the supply and disposal subsystems of the test facility. In all, 36 flow modules and 94 breakthrough detectors (BTDs) were installed in the test vessel at the core/upper plenum interface. These detected the steam and water mass flows and water breakthrough at the tie plate. The flow modules included three individual measurement systems for measuring the fluid momentum flux at the tie plate, as well as the local fluid velocity and water level above the tie plate. Numerous flow temperature and pressure measurements were located in the upper plenum and downcomer. An array of 705 optical sensors was also installed throughout the upper plenum and downcomer to sense the presence or absence of water.

Conventional T/H measurements were primarily used outside the test vessel to monitor the test's boundary conditions. Five pipe flowmeter systems, including drag rakes and gamma densitometers, measured the mass flow rates in the hot legs and broken cold leg. Seventy-one conventional mass flow measurements were also used.

5.1.3.3 Tests performed

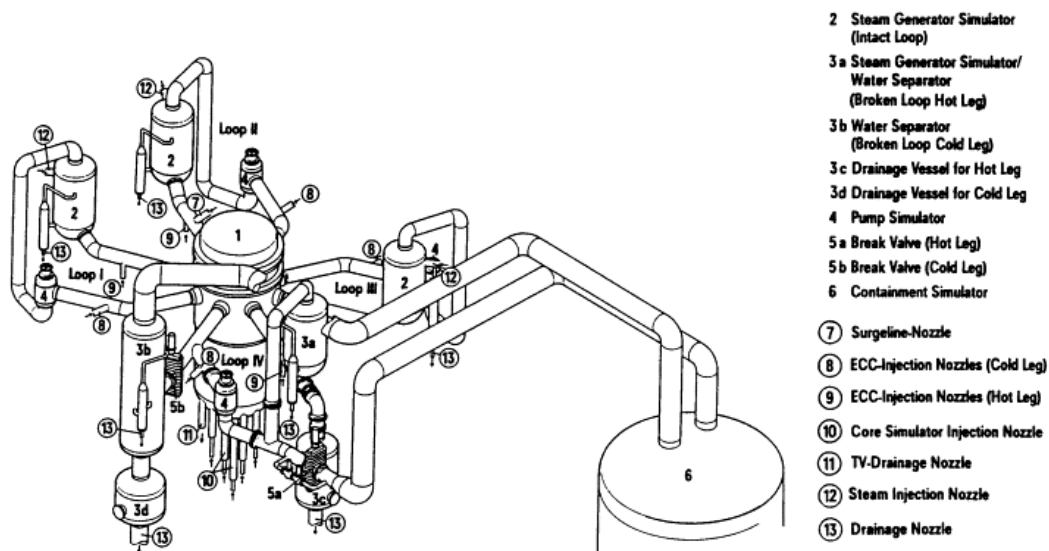
Tests performed in the UPTF 2D/3D program

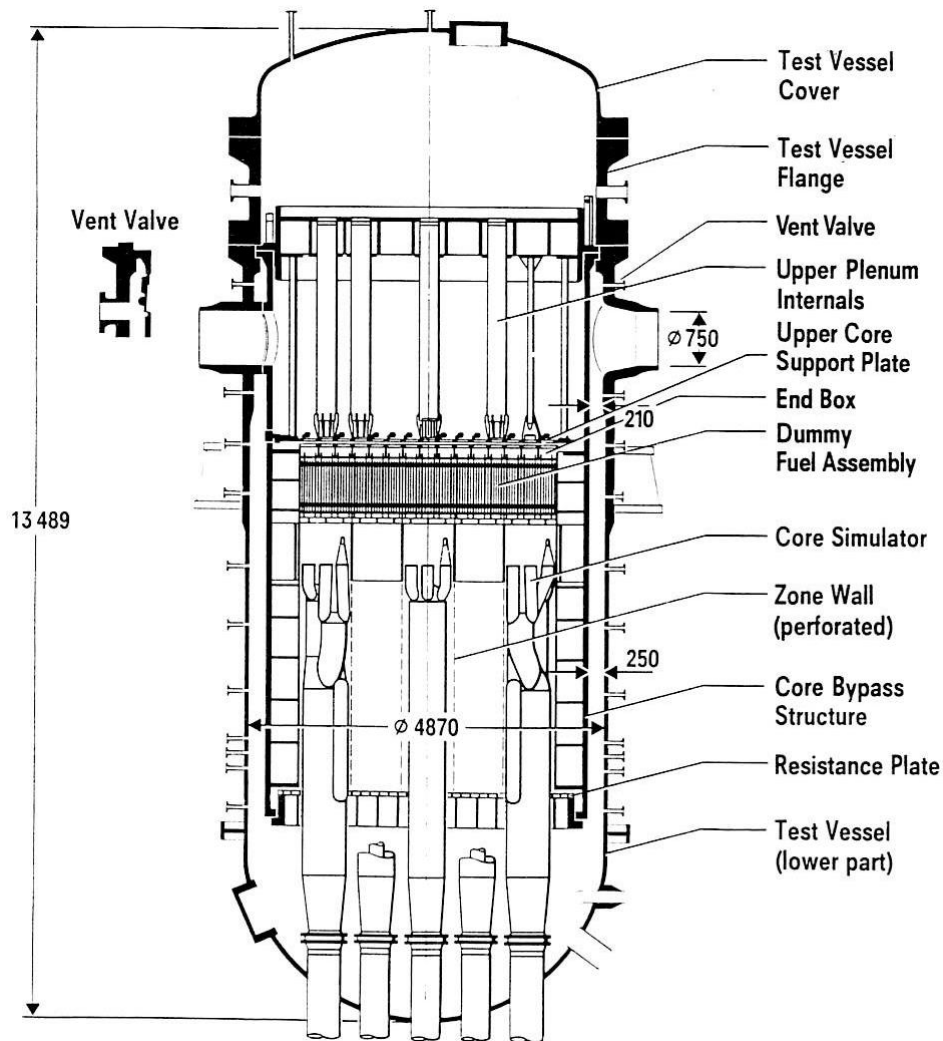
The UPTF test program consisted of 30 tests and consisted of 80 test runs [5.1.3-3]. There were two basic types of tests performed within this program:

- twenty separate effects tests that emphasised “transparent” boundary conditions to quantify controlling phenomena in the primary system during LOCA and support code improvement [5.1.3-4 and 5.1.3-5];
- ten integral tests that focused on system-wide behaviour during a simulated transient to identify controlling phenomena in the primary system during a LOCA transient.

Figure 5.3. The UPTF Test Facility

Primary system (top) and test vessel (bottom)





Source: Damerell and Simons, editors, 1993.

The separate effects tests were grouped according to the primary system's region and the T/H phenomena of interest:

- countercurrent flow phenomena in the downcomer for cold leg ECC injection during end-of-blowdown and refill phases of a LB-LOCA;
- entrainment in the downcomer during reflood for cold ECC injection;
- T/H phenomena in the upper core, tie plate and upper plenum;
- de-entrainment along the flow path from the core to the steam generators for cold leg ECC injection;
- steam/ECC interactions in the hot and cold legs;
- the impact of vent valves on the steam/water flow in the upper plenum and the downcomer of ABB and B&W PWRs;
- temperature distribution in the downcomer for ECC injection in the cold legs when the primary system is filled with warm water;
- steam/water countercurrent flow in the hot legs under the boundary conditions of small and intermediate-sized breaks;
- ECC delivery to the core for high pressure injection in the hot legs.

The integral tests covered the end-of-blowdown, refill and reflood phases of a LB-LOCA. They can be subdivided into the following groups based on the ECCS type, configuration and break location:

- four tests simulated a cold leg break with ECC injection into the cold legs (US and Japan type PWR);
- five tests simulated a hot or cold leg break with combined ECC injection into the hot and cold legs (Siemens/KWU PWR);
- one test simulated a cold leg break with ECC injection into a cold leg of an intact loop, the downcomer and the vent valves free-to-open.

Tests performed in the UPTF-TRAM program

The UPTF 2D/3D Program was followed by a national experimental project called UPTF transient and accident management program (TRAM). This experimental program focused on incidents that have been assigned by different risk monitoring studies and significantly contribute to the overall risk, mainly beyond design small leak transients and accident management (AM) procedures. Transients that could provoke a pressurised thermal shock have also been considered within this program [5.1.3-2].

Large-scale T/H phenomena have been investigated in 15 tests, essentially separate effect test facilities (SETs), concluding with 111 test runs. The experimental program has been divided in four groups:

- test group A: tests related to small break transients;
- test group B: AM tests;
- test group C: mixing tests in the cold leg and downcomer, which are related to thermal shock and recriticality;
- test group D: hot gas convection inside the pressure vessel and the reactor coolant system components.

The following phenomena have been investigated, among others:

- the flow regimes in the hot legs during two-phase natural circulation;
- the transportation of ECC water by single- and two-phase natural circulation;
- loop seal clearing;
- steam flow and liquid entrainment from the upper plenum towards the pressuriser during relief valve actuation;
- coolant mixing during the ECCS injection.

5.1.3.4 Application for system code validation

The UPTF tests, which were performed in the international 2D/3D program and the UPTF-TRAM program, have been extensively used for system code validation because of their exclusive “full-scale” feature [5.1.3-6]. In particular, the separate effect tests such as the downcomer tests, upper plenum tests and Test group C of the UPTF-TRAM program, have been used for the validation of the 3D SYS T/H modules [5.1.3-7, 5.1.3-8 and 5.1.3-9]. Some of the UPTF tests also have been adopted for the validation of computational fluid dynamics (CFD) codes [5.1.3-10 and 5.1.3-11].

5.1.4. CCTF and SCTF

5.1.4.1 Objective of the experiment

The T/H response of a PWR primary coolant system to a LOCA and the performance of the ECCS have been areas of strong research interest. The 5.1.4. cylindrical core test facility (CCTF) and slab core test facility (SCTF) tests were performed [5.1.4-1] by the Japan Atomic Energy Research Institute (JAERI) (formerly JAEA) in the 2D/3D program, which focused on the following phenomena that are strongly influenced by multidimensional (2D and 3D) effects during the end-of-blowdown, refill and reflood with of several types of ECC systems. The experimental program was divided in three groups:

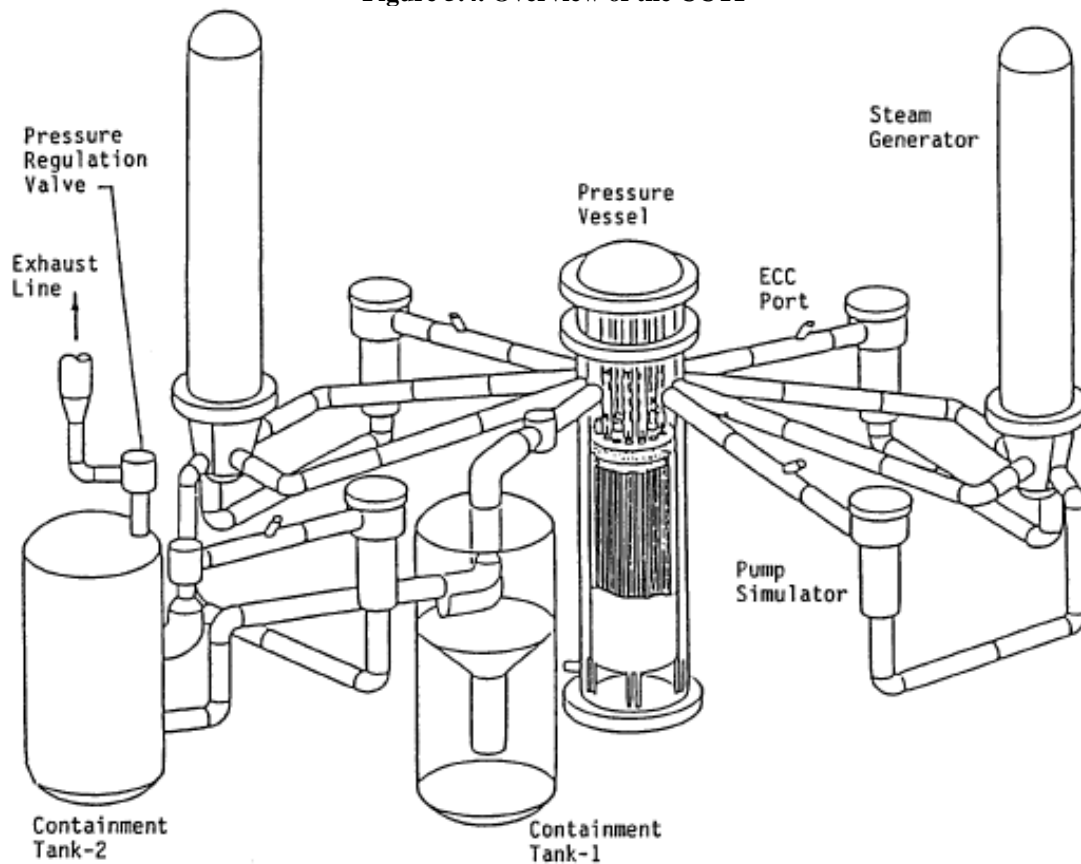
- Phenomena during the end-of-blowdown and refill phases of an LB-LOCA; penetration of ECC to the lower plenum; condensation of steam by ECC including the effect of dissolved nitrogen, and flow pattern through the core and resultant core cooling.
- Phenomena during the reflood phase of a LB-LOCA; entrainment, storage and transport of water; steam/ECC interaction and flow patterns; heat transfer in the core; and influence of nitrogen discharge from accumulators.
- Phenomena from other transients; for example, hot leg steam/water countercurrent flow during a small break LOCA (SB-LOCA); fluid/fluid mixing during a pressurised thermal shock event; and high pressure ECC injection into the hot legs during an SB-LOCA.

5.1.4.2 Description of the test loop

Description of the CCTF

CCTF was a full-height, 1/21-scale model of the primary coolant system of a 1 100MWe four-loop PWR. The facility simulated the overall primary system response, as well as the in-core behaviour, during the refill and reflood phases of a large cold LB-LOCA. Figure 5.4 depicts the facility's major components. They included a pressure vessel, four primary piping loops, two steam generators, four pumps and two tanks attached to the ends of the broken loop to simulate containment. The vertical dimensions and locations of the system components were closely replicated to those of the reference reactor.

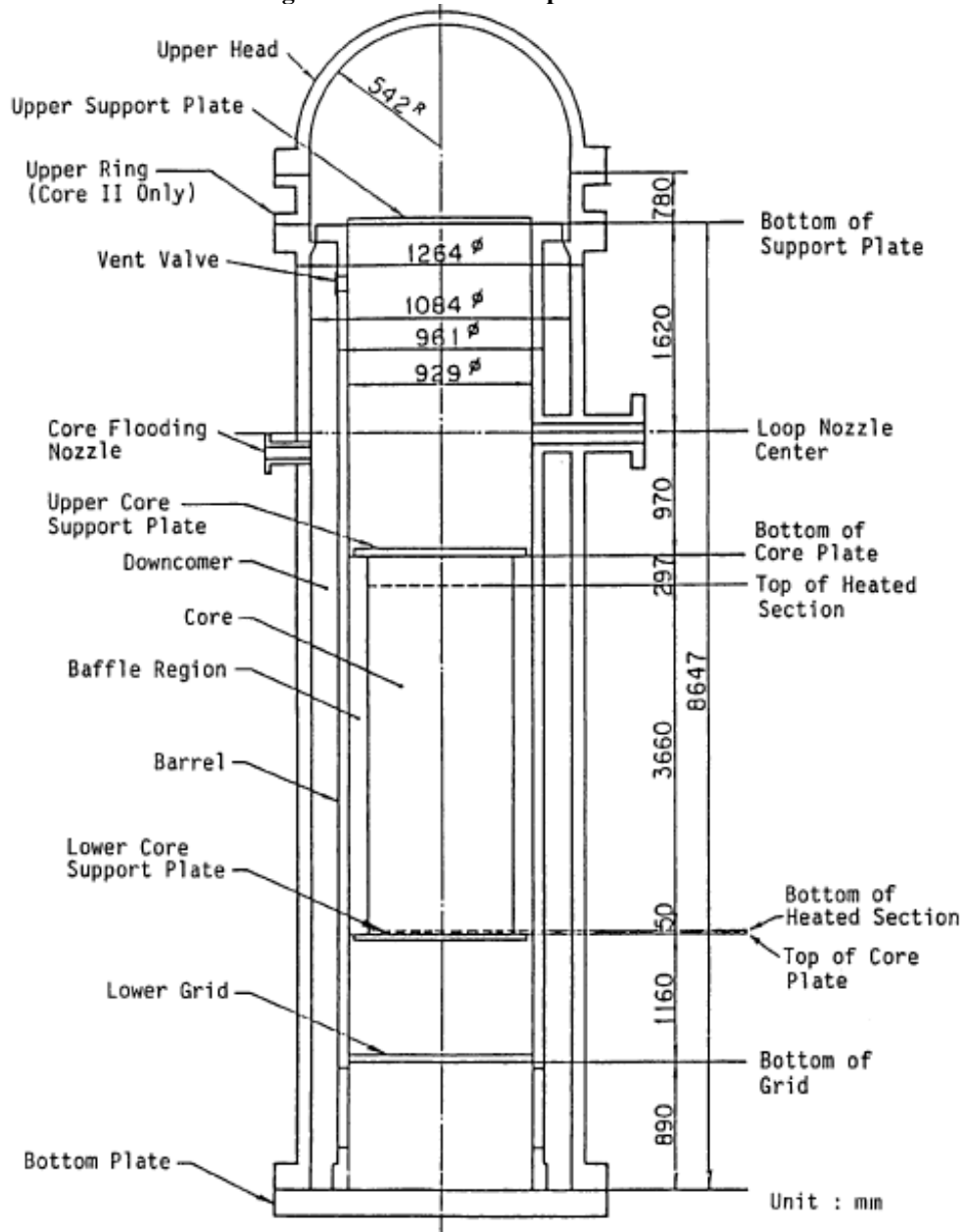
Figure 5.4. Overview of the CCTF



Source: Ichikawa, 1995.

Figure 5.5 shows the CCTF pressure vessel housing a downcomer, lower plenum, core and upper plenum. The CCTF core contained 32 bundles (Figure 5.6), each containing 57 electrically heated rods and seven non-heated rods (1 824 heated rods and 224 non-heated rods in total). The non-heated rods simulated the guide thimble tubes and instrument thimble tubes in PWR fuel assemblies. Figure 5.6 shows the three (high, medium and low) power zones of the electrically heated core. The radial power distribution of the core was controlled by setting the power supplied to each zone. The axial power profile in all rods was a chopped cosine.

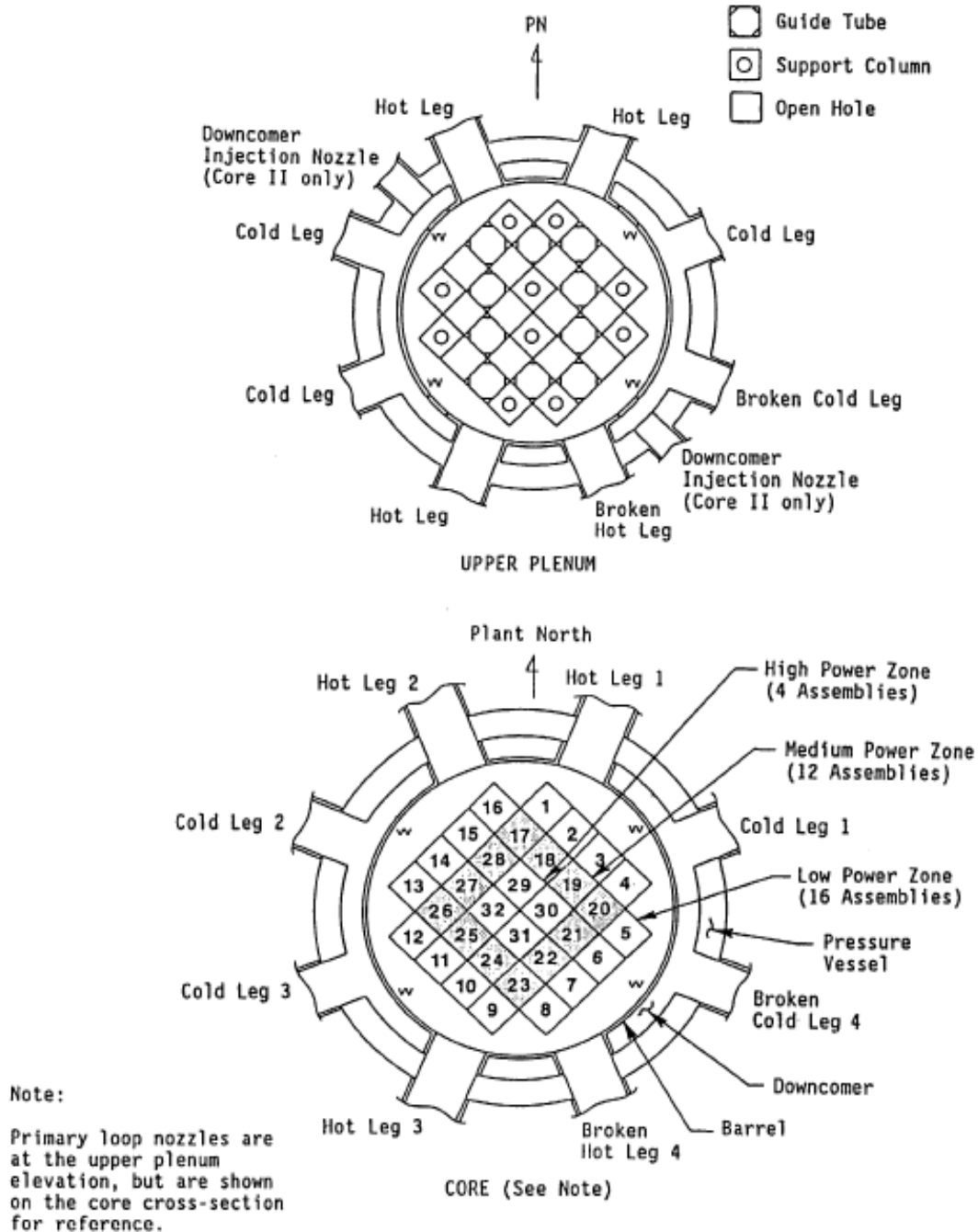
Figure 5.5. CCTF core-II pressure vessel



Source: Ichikawa, 1995.

Four full-length primary loops were connected to the central pressure vessel (Figure 5.4). Three of the loops were intact, meaning that they sent the flow from the reactor vessel upper plenum, through the hot leg, steam generator, pump simulator and cold leg to the reactor vessel downcomer. The fourth loop simulated a full-size, double-ended, offset cold leg break set at about two m from the vessel wall. Quick-opening break valves were located at the two ends of the cold leg break. The pipe area was scaled from the PWR by the ratio of core flow areas. The steam generator simulators were vertical, U-tube and shell type heat exchangers. Two interconnected tanks, one attached to each of the two ends of the cold leg break, simulated the PWR containment. An internal steam/water separator and a liquid level metre on the tank connected to the vessel side of the break together enabled the measurement of broken cold leg phase flow rates.

Figure 5.6. CCTF pressure vessel cross sections



In CCTF-I test run, the ECCS included two water supply tanks. The pressurised accumulator (ACC) tank, capable of providing water at a high flow rate for a short duration, and the low pressure coolant injection (LPCI) tank, which provided water at a lower flow rate for a longer duration. Each tank could supply water to either the lower plenum or cold legs. A second pressurised tank was added in the CCTF-II test run, with ECCS piping running to the upper plenum injection header, the downcomer and the hot legs.

Description of the SCTF

SCTF was a full-height, full-radius 1/21-scale model of a sector of a 1 100 MWe, four loops PWR. While the pressure vessel was simulated in detail, only a crude loop simulation was used (Figure 5.7). The most significant feature of SCTF was that it contained a full-height heated core with realistic rod diameters and spacing and a core lateral extent of over 1.8m (the core radius of the largest PWRs). This large core lateral extent allowed the model to examine multidimensional effects. Figure 5.7 depicts the facility's major components.

Figure 5.8 shows the SCTF pressure vessel, which housed a downcomer, lower plenum, core and upper plenum. The vessel simulated the radial slice of a PWR from the centre (bundle one in Figure 5.8) to the periphery (downcomer). The core consisted of eight simulated fuel bundles arranged in a row (i.e. a slab geometry). Each bundle contained 234 electrically heated rods and 22 non-heated rods arranged in a 16×16 array. Power to each bundle was individually adjustable to simulate radial power distribution.

The primary flow loops were simulated using a simplified system consisting of a single hot leg, steam/water separator, intact cold leg and broken cold leg. The hot leg connected the upper plenum with the steam/water separator. A steam/water separator located in the hot leg measured the amount of water entrained in the steam flow out of the upper plenum and through the hot leg. Although the separator did not simulate an actual steam generator, it was designed to obtain a realistic two-phase flow pattern at its inlet. The intact cold leg connected the steam/water separator with the downcomer's upper portion. The broken cold leg was simulated by two pipes. One pipe connected the downcomer with a containment tank and the second pipe connected the steam/water separator with the other containment tank. The two containment tanks were the same tanks as those used for CCTF.

The SCTF ECCS consisted of an accumulator and low pressure injection system. The injection ports for these systems were in the lower plenum, downcomer, broken cold leg, hot leg and intact cold leg, between the pump simulator and pressure vessel. The injection and extraction systems also provided and/or removed ECC using special nozzles located just above the upper core support plate.

5.1.4.3 Test performed

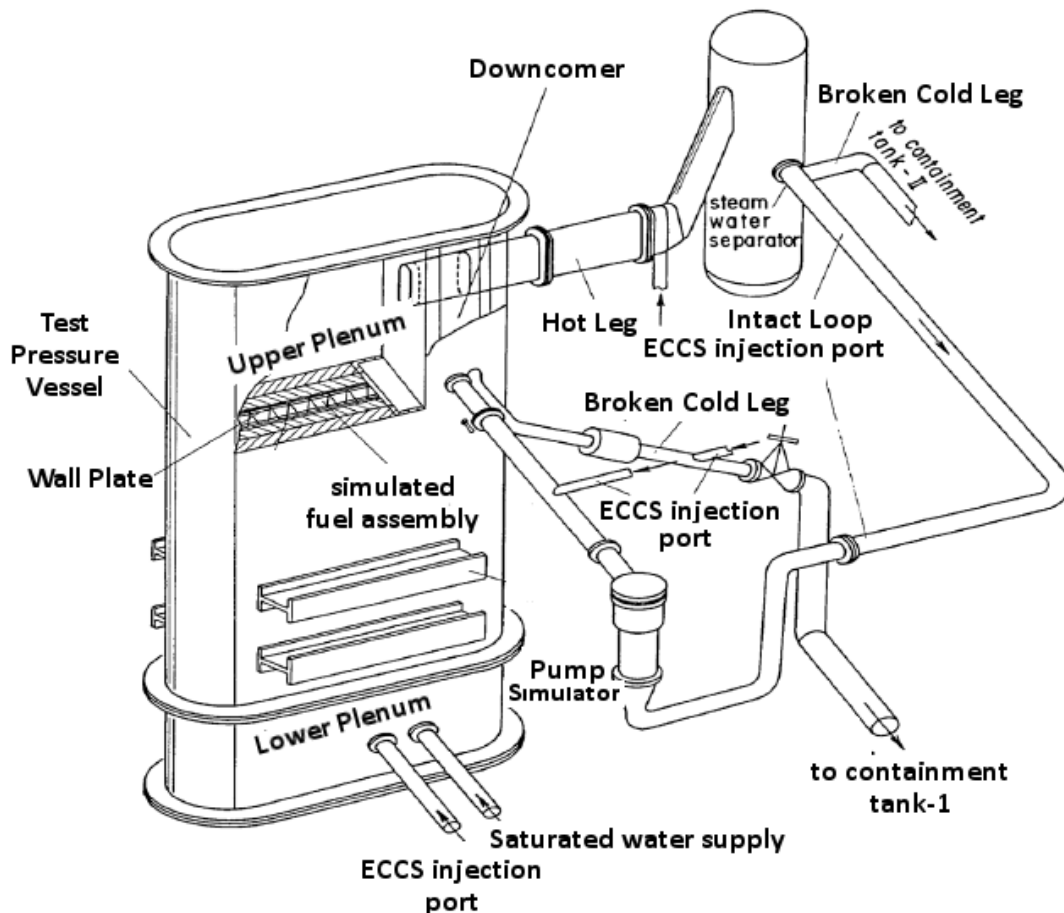
CCTF and SCTF tests are first classified by the injection configuration being simulated (cold leg injection, combined injection, downcomer injection, or upper plenum injection) and then further classified by the test objective (effects of pressure, core power, initial cladding temperature, ECC flow rates, etc.).

The ranges of experimental conditions in both types of tests are shown below. The values shown were determined from the results of safety evaluation analyses and engineering judgement.

- pressure in containment tanks 1 and 2: 0.1 - 0.42 MPa (base case: 0.2 MPa);
- maximum initial clad temperature: 653 –1 153 K (base case: 1 027 K);
- average linear power rate of heated rods: 1.06-1.40 kW/m (base case: 1.40 kW/m);
- initial total core power (1 824 heated rods): 7.1-9.4 MW (base case: 9.4 MW);
- initial ACC injection rate: 6.7×10^{-2} - 10.3×10^{-2} m³/s (base case: 9.1×10^{-2} m³/s);
- LPCI rate: 0.5×10^{-2} - 2.5×10^{-2} m³/s (base case: 1.1×10^{-2} m³/s);
- downcomer wall temperature: 400-476 K (base case: 476 K);
- loop seal water: Yes, No (base case: No);

- loop flow resistance: 25, 35 (base case: 25);
- nitrogen injection: Yes, No (base case: No);
- horizontal core power distribution: Uniform, Non-uniform (base case: Non-uniform);
- clad temperature distribution: Uniform, Non-uniform (base case Non-uniform);
- evaluation model (EM) condition/ best-estimate (BE) condition: EM, BE (base case: EM).

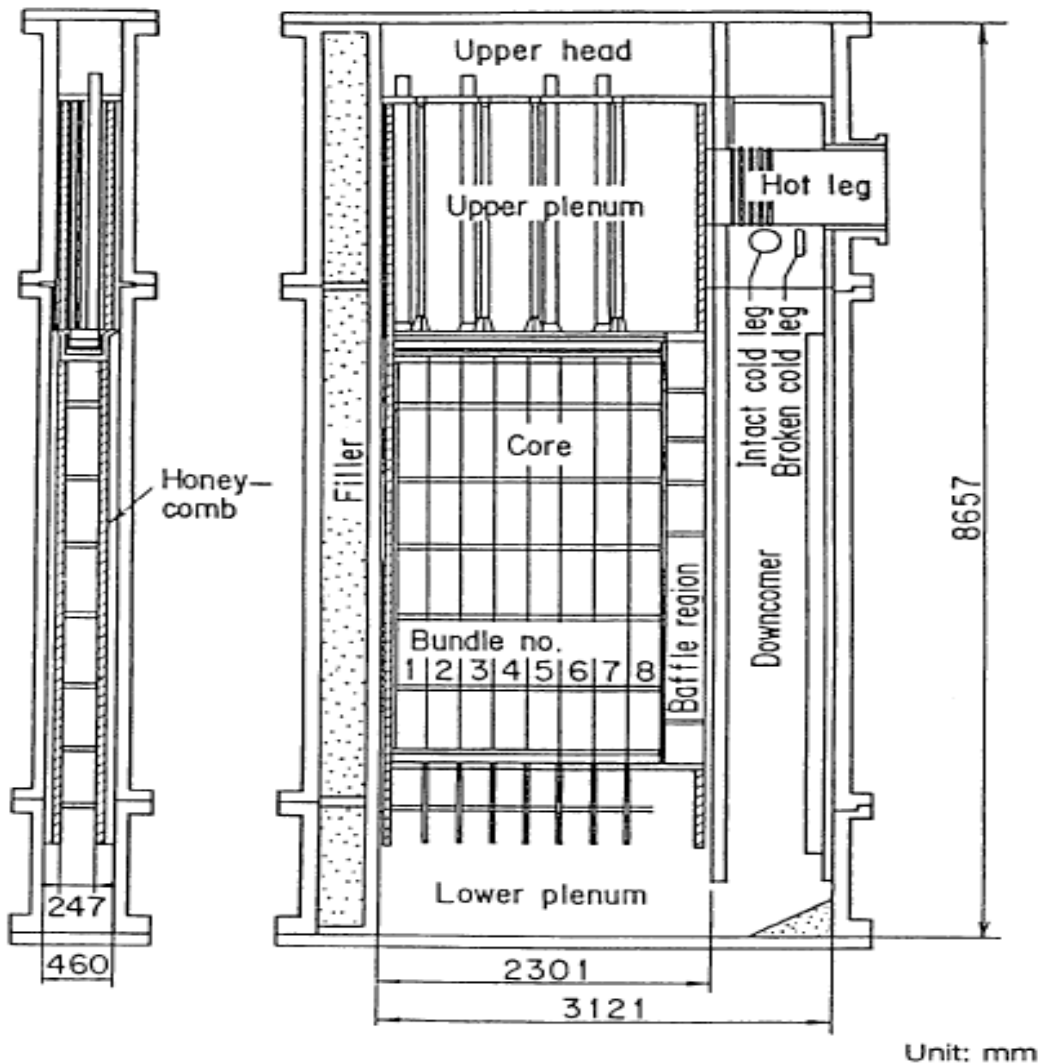
Figure 5.7. Overview of the SCTF



Source: Ichikawa, 1995.

The CCTF and SCTF tests clarified the thermal hydraulics in primary components (i.e. core, upper plenum, hot legs, steam generators, crossover legs, primary pumps, cold legs, downcomer, and lower plenum) in the refill and reflood phase [5.1.4-2]. Flow below the quench front in the core was from the low-power region to the high-power region. Yet flow above the quench front in the core was from the high-power region to low-power region. This three-dimensional flow circulation resulted in heat transfer being enhanced in the high-power region and degraded in the low-power region. Figure 5.9 shows the experimental results of the reflood phase in the CCTF C2-16 test, which was performed as one of the base cases.

Figure 5.8. Cross-section of SCTF core-II pressure vessel



Source: Ichikawa, 1995.

5.1.4.4 Application for system code validation

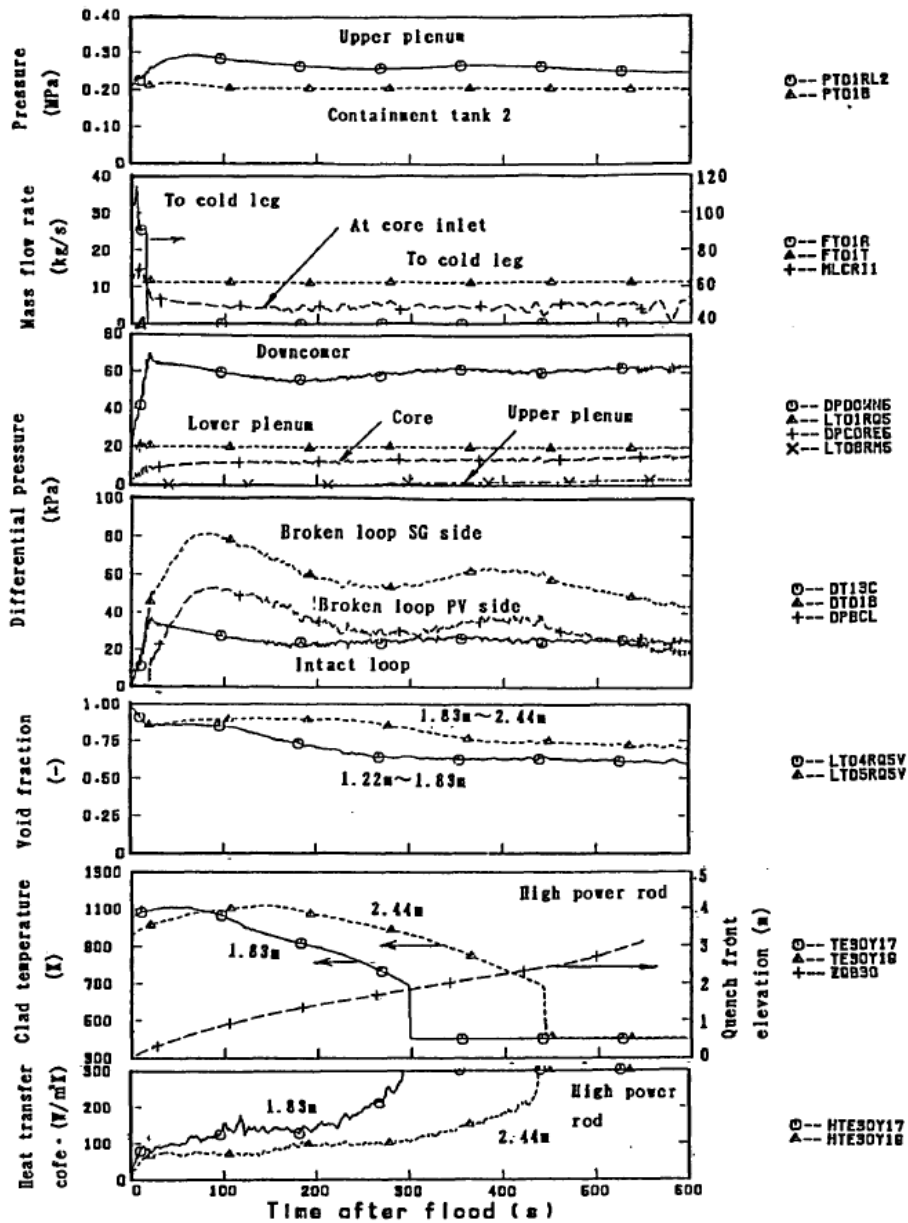
The results of CCTF tests are used to assess TRACE reflood thermal-hydraulics models [5.1.4-3]. TRACE has shown it is capable of calculating the data trends during core reflood for different variations in boundary and initial conditions. TRACE demonstrated its capability to correctly calculate reflood behaviour for variations in core power, radial power profile and system pressures. TRACE also exhibited its capability to predict reflood behaviour reasonably well under “best-estimate” conditions (run 71). However, TRACE was unsuccessful in the simulation of run 58; code failures prevented the simulation from advancing past the initial rod heat-up period when the system was stagnant.

The rod clad temperature in the upper core half was over-predicted and resulted in a longer quenching time. The upper third of the core is highly voided. The vapour temperature is almost as high as the rod surface temperature, while the liquid temperature is at saturation. The calculated liquid and vapour velocities in the upper core are on the order of 2.5 and 13 m/s respectively. It appears interfacial drag is under-predicted because small droplet sizes (two mm or less), liquid and vapour velocities should be closer together. The interfacial heat transfer also seems to be under-calculated.

5.1.4.5 Main advantages and drawbacks of the facility

Both CCTF and STCF have full-height pressure vessel. In addition, the CCTF simulates four full-length primary loops connected to the central pressure vessel. The SCTF has the core extent of over 1.8 m, which simulates the core radius of the largest PWRs. These are the advantages of predicting T/H behaviours in cores and primary loops without scaling distortion.

Figure 5.9. Reflood phase of CCTF C2-16 test



Source: Ichikawa, 1995 .

5.1.5. PERICLES 2D

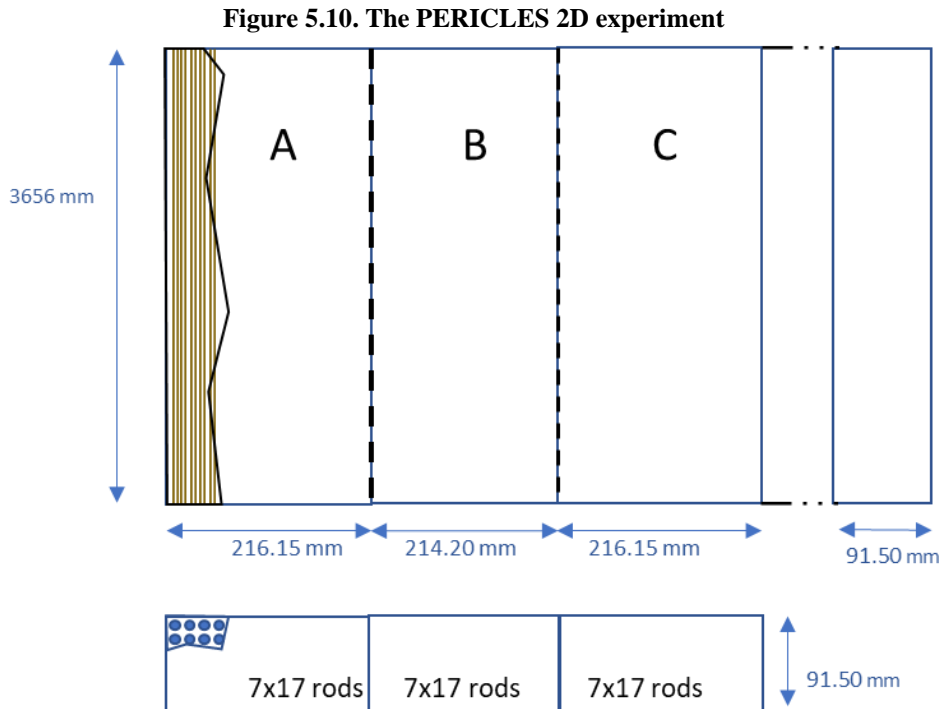
5.1.5.1 Objective of the experiment

The PERICLES 2D experimental programme was partly embedded in the shared cost action programme (SCA) of the European communities (CEC) on reactor safety, research area n°4, which involved analysing experimental data about loss-of-coolant accidents and emergency core cooling [5.1.5-1] and [5.1.5-2].

The PERICLES 2D experiment has been carried out to investigate the multidimensional effects that can occur in a PWR core where the heating power is not radially uniform, for specifically core uncover (relative to SB-LOCAs) and reflooding (relative to LB-LOCAs) cases.

5.1.5.2 Description of the test loop

The experiment consists of a vertical rectangular channel containing three different rod assemblies, denoted here by A, B and C. Each assembly contains $7 \times 17 = 119$ full-length heater rods. The dimensions of the assemblies are indicated in Figure 5.10.



The assemblies are heated by two independent electrical power sources, which makes it possible to heat the central assembly B (the “hot” assembly) more than the two lateral ones A and C (the “cold” assemblies). The rods’ heated length is 3 656 mm and the rod diameter is 9.5 mm.

The heating is not uniform and depends on the axial position (elevation) on the rod. All rods have the same axial heating shape and the highest flux density occurs at mid-length. The nominal heat flux densities ϕ in the lateral assemblies A and C are identical and that the ratio $\phi(B)/\phi(A,C)$ defines the radial peaking factor.

The cladding temperature and the fluid temperature are measured using thermocouples. The cladding temperature in each assembly is measured at 24 different elevations and the fluid temperature is measured at six different elevations.

The void fraction is obtained at six different elevations in each assembly using pressure drop measurements, which assumes that the pressure difference between two points located at two different elevations is approximately equal to the gravity head of the two-phase column. The inlet liquid flow rates in the three assemblies are measured in turbine flow meters and the outlet vapour flow rates are measured using calibrated orifices.

The controlling parameters were the nominal values of the wall-to-fluid heat flux densities in the three assemblies and inlet liquid flow rate, corresponding to a stationary position of the swell level ZG (Figure 5.11). The swell level positions in the different tests ranged from 2.20 m to 3.45 m and were approximately the same for the three assemblies.

5.1.5.3 Tests performed

Test conditions

The nominal values of the heat flux densities in the different tests investigated ranged from 24.5 kW/m² to 50 kW/m², with given values of the radial peaking factor between one and 1.85. The system's pressure was equal to three bar and the water's temperature entering into the assemblies was 60°C below saturation temperature (133.5°C).

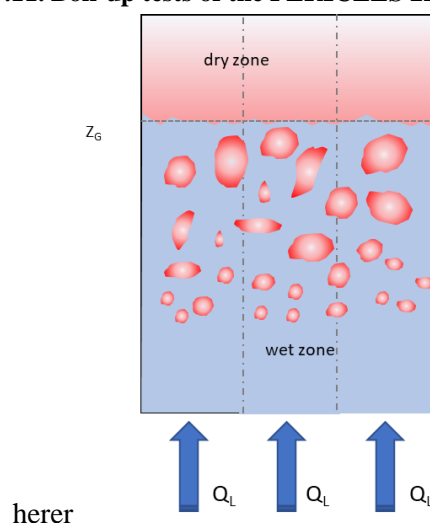
Reflooding tests

In the reflooding tests of the PERICLES 2D experiment, the three assemblies initially contain no water. During a first stage, the rods are electrically heated to bring the cladding temperatures to fixed initial values. When these values are reached, some water is injected through the bottom of the test section to reflood the three assemblies and the heating of the rods is maintained. During the reflooding stage, a quench front progresses in each assembly and the reflooding stage is terminated once the three quench fronts have reached the top of the assemblies.

Boil-up tests

In the boil-up tests of the PERICLES 2D experiment, some subcooled water enters the assemblies at the bottom of the system. The rods are electrically heated, and some vapourisation occurs along the channel. The flow is first a single-phase liquid, then a two-phase mixture and finally a single-phase vapour flow. The transition between the two-phase zone and the dry zone (single-phase vapour) occurs at the elevation of the swell level ZG (Figure 5.11).

Figure 5.11. Boil-up tests of the PERICLES 2D experiment



The liquid flow rate at the entrance is regulated so that a given stationary position of the swell level is obtained.

5.1.5.4 Application for system code validation

Reflooding tests

These tests investigate the reflooding phase in a LOCA scenario [5.1.5-3]. The observed experimental tendencies are the following:

- The progression of the quench front in the central hot assembly is slower than those in the lateral cold assemblies, but this effect is attenuated by the existing crossflows of water between the assemblies.
- The steam flow rates exiting from the three assemblies are identical.
- Water entrainment by the vapour flow up to the exit of the assemblies is sometimes more important in the hot assembly than in the cold assemblies, despite the higher heat flux density. This may be due to the water flowing from the cold assemblies above the hot assembly's quench front and the entrainment of this water by the upward vapour flow. This carryover provides a better cooling of the rods in the hot assembly.

Boil-up tests

These tests investigate the core uncover phase in a LOCA scenario [5.1.5-4]. The observed experimental tendencies are the following:

- The axial position of the swell level ZG is almost identical for the three assemblies, even if the radial peaking is not uniform.
- The void fraction profiles in the three assemblies are similar, showing the existence of crossflows in the wetted zone. The wetted zone is thus characterised by a perfect (or quasi-perfect) radial mixing.
- The wall-to-vapour heat transfer in the dry zone is close to that obtained by assuming a perfect radial mixing in the wetted zone, a uniform steam flux at the swell level and no radial mixing in the dry zone.

5.1.6. PRIUS

5.1.6.1 Objective of the experiment

The rod bundle is a fuel element geometry frequently used in nuclear reactors. The coolant flows axially through the subchannels formed between the rods. The mixing of cooling fluid in a rod bundle reduces the temperature differences in the coolant and along the perimeter of the rods. Flow inside the rod bundles is similar to flow in porous media. Detailed information of the heat transfer and turbulent mixing flow phenomena taking place within the subchannels is required to ensure thermal performance of a nuclear reactor. The subchannel analysis is one of the key T/H calculations for safety analysis of the nuclear reactor core. Subchannel computer codes are currently used to simulate fuel elements of nuclear reactor cores and predict the performance of cores under normal operating and hypothetical accident conditions. The ability of these subchannel codes to predict both the flow and enthalpy distribution in fuel assemblies is highly important for the design of nuclear reactors. A new component scale analysis code, named CUPID [5.1.6-1], has been

recently developed in KAERI. It has the capability of the multidimensional flow application with a component scale.

The in-PWR Rod bundle Investigation of Undeveloped mixing flow across Subchannel (PRIUS) test facility is being designed and constructed to generate an experimental database in a rod bundle geometry that addresses the modelling and validation of subchannel analysis [5.1.6-2]. The facility could also be useful for CFD in open medium validation.

5.1.6.2 Description of the test loop

Figure 5.12 shows a schematic of the PRIUS test facility. The fluid system consists of a test section, storage tank and two-inch (0.05 m) piping system for the water supply to the test section and back into the storage tank. The storage tank is installed at the top part of the facility. The water temperature in the system is controlled using a cooler and heater that is imbedded in the storage tank. The water flow is supplied by a centrifugal pump, with a 40 m head and 48 m³/h capacity, which is controlled by adjusting the impeller speed using an inverter. A bypass line is established at the upstream of the test section to enable efficient control of the water flow. Instrumentations for the flow rate, temperature and pressure are installed in the water injection line, which is divided into two branch lines. A honeycomb is installed inside the inlet chamber to maintain a straight flow at the inlet.

The test section of PRIUS-I has a rectangular geometry with a dimension of 84 mm×58 mm×1.5 m and is made of acryl with 15 mm thickness. The typical configuration for the rod bundle examined in this study consists of a 4×6 array of parallel rods, as shown in Figure 5.13. The unheated rods have almost the same size as those commonly used in pressurised water reactors, which have an outer diameter, D , of 10.0 mm and are separated on a pitch, P , of 13 mm. Table 5.2 shows the geometrical parameters of the PRIUS test facility.

The matching index of refraction (MIR) technique is adopted to remove the image distortion induced by the different refraction indexes of water and acryl rods. A transparent acrylic rod was chosen in combination with a solution of 62.5% sodium iodine (NaI) in 37.5% deionised water. The viscosity of the solution is low enough to enable Reynolds number identity with a feasible mass flow. However, the NaI-solution is highly corrosive to ferrous metals, even to stainless steels, and therefore piping with Teflon coating was installed to prevent corrosion. The circular pump's internals are made from FRP (fibre-reinforced plastic). The valves and storage tank are also made of PVC (polyvinyl chloride) or PE (polyethylene).

Table 5.2. Geometry parameters of 4x6 rod bundles

Subchannel type, i	Number	Flow area, A_i (mm ²)	Wetted perimeter, P_{wi} (mm)	Hydraulic diameter, D_h (mm)
Central	15	90.46	31.42	11.52
Wall	16	84.23	28.71	11.74
Corner	4	70.62	26.85	10.52
Total	35	2 987.04	1 037.98	11.51

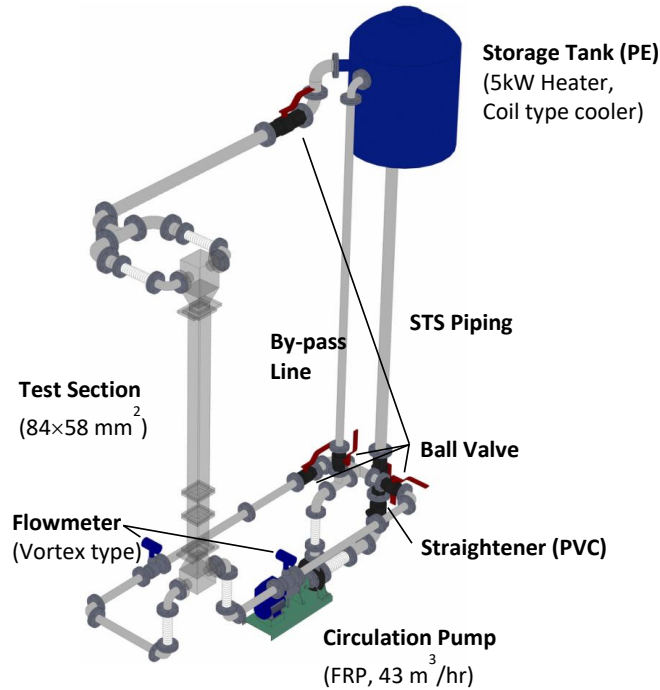
Source: Yoon et al., 2018.

Instruments

Several types of commercially available instruments have been installed for measuring the boundary conditions, as shown in Figure 5.14. The volumetric flow rate of the water is measured using a 2-inch (5 cm) vortex flow meter installed at each inlet water line. The estimated uncertainty for the measured mass flow was 0.80% of its read value. The system

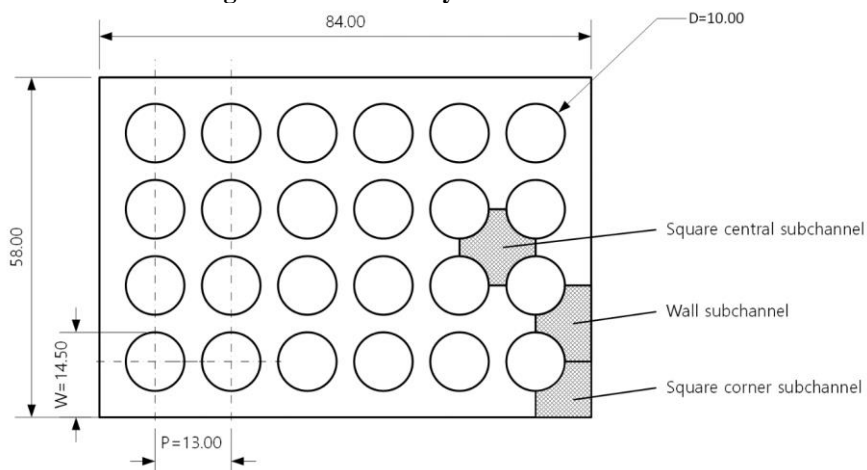
pressure is measured at the top of the test section and each inlet water line using two SMART-type pressure transmitters (PTs). The estimated uncertainty of each PT reading was 0.08% of the full scale, including the data acquisition system uncertainty. Four TCs are installed at the piping system to measure the temperature of the fluid. The system temperature was maintained at 30°C, which accounts for heat generation from the pump at the maximum flow condition and the cooling capability of the loop. The applied power of the heater inside the storage tank was controlled by a silicone controlled rectifier (SCR) by referring to the temperature at the water supply line.

Figure 5.12. Schematic of the test facility (PRIUS-I)



Source: Kim et al., 2017.

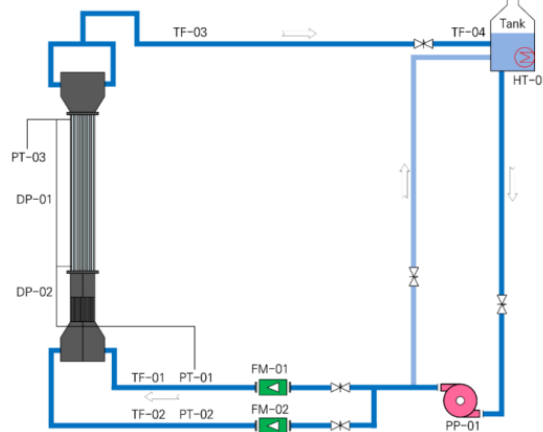
Figure 5.13. Geometry of 4x6 rod bundles



Source: Kim et al., 2017.

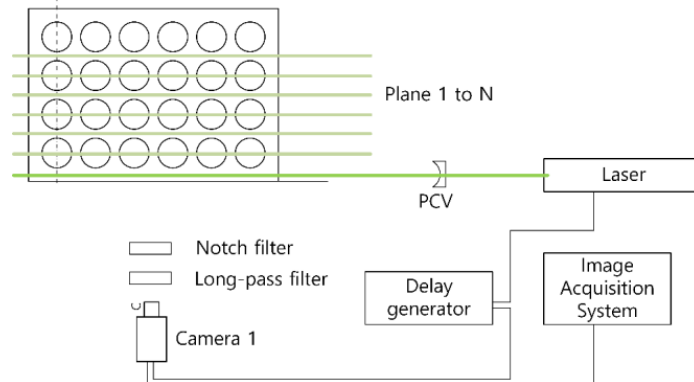
Figure 5.15 shows a schematic diagram of the optical setup for particle image velocimetry (PIV) velocity field measurements, which consists of a 65-mJ laser with an emission wavelength of 532 nm, 2K×2K charge-coupled device (CCD) camera and delay generator. The acquisition rate of the raw image is controlled by a delay generator. Eight frames per second is used. The laser light sheet illuminated the test flow through the right side. NaI-solution is used as the working fluid for the PIV measurements. Fluorescent (Rhodamine B) polymer beads with an average diameter of 10 μm and a specific gravity of 1.02 are used as the tracer particles. A long pass filter ($\lambda > 550$ nm) and notch filter are used to eliminate the scattered light, except for the fluorescence light, and block the 532 nm wavelength light, which are installed in front of the 2K×2K CCD camera. Statistical results, such as the mean velocity vector fields and turbulence intensity, are obtained by the ensemble average of 1 000 instantaneous velocity vector fields. The laser-induced fluorescence (LIF) technique is adopted to visualise and quantify the mixing characteristics between each rod bundle.

Figure 5.14. Schematic diagram of test facility



Source: Kim et al., 2017.

Figure 5.15. Experimental setup of PIV-MIR measurement system



Source: Kim et al., 2017.

5.1.6.3 Tests performed

There are various combinations set for the test matrix, consisting of a selection of inlet flow conditions and flow area sudden changes. Flow visualisation since the second half of 2016 has been performed by a high speed camera and using image analysis techniques, which quantify detailed information for the two-dimensional movement of single-phase flow. The

PIV technique is used in the present work to measure the velocity field of multidimensional flow that is driven by various combinations with inlet flow conditions and flow area changes.

Table 5.3 shows a test matrix for the visualisation experiment. Equal/unequal inlet velocity conditions will be simulated for the turbulent diffusion term or turbulent frictional term evaluation to create the crossflow between the assemblies. The range of Reynolds numbers that the PRIUS-I can simulate corresponds to the Reynolds number covering the SB-/IB-LOCA accident condition [5.1.6-3]. The simplest experimental conditions were set, and the boundary conditions were clarified in order to maximise the accuracy of the physical modelling. The inlet velocity distribution for each assembly can be provided as inlet conditions.

Table 5.3. Indicative PRIUS-I test matrix

$V_{left}:V_{right} \frac{V_{left}}{V_{right}}$	10 000	20 000	30 000
	1:1	⊕	⊕
7:3	⊕	⊕	⊕

Source: Kim et al., 2017.

5.1.6.4 Application for system code validation

Application and drawbacks for 2D/3D application

SB-LOCA and IB-LOCA encounter significant 3D effects in the core due to the radial power profile, with crossflows and diffusion-dispersion. A more precise validation of each of the mixing processes is required. Unfortunately, only a CFD in porous body approach is practically applicable and a simulation of the whole core is not possible with the CFD in open medium. The PRIUS mainly addresses the subchannel codes. It also provides validation data for the CFD in open medium and, to a lower extent, for system codes.

Availability of the data

Current data were generated from the project supported by the Korean government's Ministry of Science and Technology (MOST), in which several companies and institutes formed a consortium for the work and to share the product. The current data could be made available with their mutual agreement.

Future plan

The PRIUS-II test programme will be conducted with the aim of building the experimental database for the nuclear fuel assembly scale. The typical configuration for the rod bundle will consist of 6×12 unheated rods, representing two scaled PWR fuel assemblies.

5.1.7. ACOP

5.1.7.1 Objective of the experiment

The core thermal margin is evaluated based on the minimum core inlet flow rate and core outlet pressure at each fuel assembly. The core inlet flow distribution also plays an important role in structural problems, for example the damage caused by the lift force to the fuel assembly or shear at the core edge region. The core inlet flow distribution should therefore be investigated for each fuel assembly's local maximum and minimum flow rates.

There are four principal parameters for a test model representing the hydraulics of a prototype nuclear reactor. These are: the geometry (flow path), relative roughness, Reynolds number, and Euler number ($Eu = \Delta P / \rho v^2$, ratio of the pressure forces to the inertial forces, perfect frictionless flow corresponds to a Euler number of one). The Euler number and aspect ratio on the flow path should be preserved in the test model. The effect of the Reynolds number in a sufficiently high turbulent region is rather small because the dependency of the form and frictional loss coefficients on the Reynolds number is considered small where the condition of the ratio of the total pressure drop is conserved.

A 1/5-scale test facility named Advanced COre flow and Pressure distribution test facility (ACOP) was constructed to test the core inlet flow distribution and reactor pressure drop through fuel assemblies in the APR+ reactor [5.1.7-1]. The APR+ reactor has been designed with an electric power of 1 500 MW and 257 fuel assemblies. The reactor adopts advanced safety system concepts, such as an emergency core barrel duct for a direct vessel injection of the emergency core cooling water and a passive auxiliary feed water system. The ACOP test facility focuses on the flow distribution of the reactor and core and is therefore operated at low pressure (<ten bar) and low temperature (<80°C) conditions. All internal structures were linearly reduced at a scaling ratio of 1/5 in the ACOP test facility to preserve the characteristics of the APR+'s reactor flow distribution. The Euler number is considered an essential dimensionless parameter for the similitude of the flow characteristics. The Euler number was preserved by maintaining the Reynolds number in the ACOP at a sufficiently high turbulent region and under the same flow path geometry as the reference plant. The fuel assembly of the APR+ reactor has a 17x17 square lattice array geometry.

The purposes of the APR+ core flow distribution test can be summarised as follows: (1) to provide a measurement of the core inlet flow distribution and core outlet pressure distribution, and (2) to provide a measurement of the downcomer and reactor pressure losses along the main coolant flow paths, from the cold to the hot leg.

5.1.7.2 Description of the test loop

The reactor vessel and internal structures of the ACOP facility were linearly scaled down from the APR+ reactor design by a 1/5 scaling ratio (factor). The ACOP test facility is focused on the hydraulics in a reactor vessel and consequently steam generators in the loop were not considered. All of the flow paths and internal geometries have their original shapes conserved, with the exception of the core. The diameters of cold leg nozzles, downcomer, lower head, lower plenum, upper plenum and hot leg nozzles of the APR+ have been scaled down by a 1/5 scaling ratio in the ACOP test facility's design. The Euler number of the APR+ reactor has been preserved in the ACOP test facility and the turbulent flow condition is preserved by operating at a sufficiently high Reynolds number condition. Table 5.4 summarises the scaling ratio of the major design parameters applied to the ACOP facilities. The scaling ratios of the ACOP test parameters are expressed for normal (balanced) four RCP running conditions and postulated three RCP running conditions of the APR+ respectively. The Reynolds numbers in the ACOP test facility for balanced four RCP running condition are, respectively, around 4.0×10^5 , 2.6×10^6 and 3.7×10^6 at the downcomer, cold leg and hot leg, which are in a fully turbulent regime. The ratios of expected Reynolds numbers in the ACOP downcomer for the APR+ reactor were 1/41 for a balanced flow condition and 1/47.7 for the three RCP running cases, respectively.

The upper-head region of the reactor vessel was not considered in the reactor model because the ratio of reactor bypass flow is less than 1.2% in the APR+. The core bypass of baffle zone was not considered in the ACOP facility's design. The wall thickness of the

internal structures has been linearly reduced in the test facility's design so that the ratios of the internal volume and flow areas were preserved.

Figure 5.16 shows a schematic of the ACOP test facility. The four independent pumps were installed for the individual cold leg flow. The 257 fuel assemblies of the APR+ core were represented by the same number of core simulators. The core simulator has a venturi pipe at the inlet part to measure the inlet water flow rate and a pressure tap to measure the differential pressure over a core simulator. The core outlet static pressure can be calculated using this pressure difference and core inlet pressure. Figure 5.17 shows the core simulator of the ACOP test facility. The axial pressure drops of the core simulators were calibrated to the scaled value by controlling the flow area of the orifices, which were located at four different downstream elevations. The flow discharge coefficients of the core simulator venturi pipe were calibrated for 40~130% flow rates of the reference scaled flow rate at the Calibration Loop for Internal Pressure drop (CALIP) calibration loop.

A cold leg CL-1B pump was isolated and the simulated failed cold leg was connected to a hot leg to simulate the postulated single pump failure condition. Within this configuration, part of the water from cold legs bypasses the core and is delivered to the failed cold leg. This water should flow to the hot leg HL-1, via pump CL-1B and the steam generator in the APR+. The estimated flow through this reversed flow path, via a pump and steam generator, can be obtained from the plant's design data. The reversed flow rate is controlled in the test by throttling a valve located at the bypass line. The rate is measured by a vortex flow meter in the ACOP facility. The actual piping configuration is shown in Figure 5.18.

Table 5.4. Scaling parameters

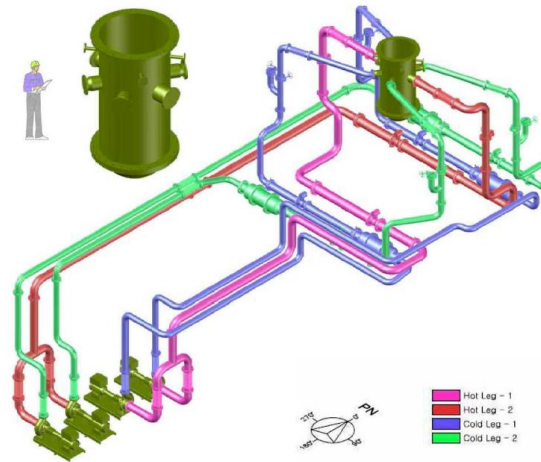
Parameters	APR+	Scaling Ratio	ACOP	
			4P-A	3P
Temperature, °C	310	-	60	
Pressure, MPa	15	-	0.2	
Length ratio	1	LR	1/5	
Height ratio	1	LR	1/5	
Diameter or width ratio	1	LR	1/5	
Area ratio	1	LR ²	1/25	
Volume ratio	1	LR ³	1/125	
Aspect ratio	1	1	1.0	
Velocity ratio	1	VR	1/2.17	1/2.53
Mass flow rate ratio	1	$\rho_R V_R L_R^2$	1/39.0	1/45.3
Density, kg/m ³	705.8	ρ_R	983.2	
Density ratio	1	ρ_R	1.39	
Viscosity, Ns/m ²	8.88e-5	μ_R	4.66e-04	
Viscosity ratio	1	μ_R	5.26	
Ex-core re ratio	1	$\frac{\rho_R V_R D_R}{\mu_R}$	1/41.0	1/47.7
DP ratio	1	$\rho_R V_R^2$	1/3.39	1/4.58

Measurements

The major parameters that should be measured are as follows:

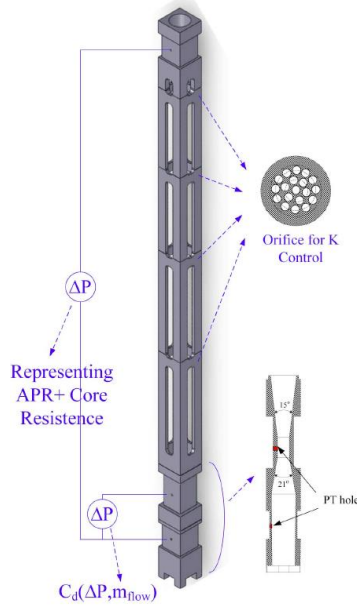
- four cold leg flow rates (inlet boundary);
- two hot leg flow rates (outlet boundary);
- 257 core simulator inlet flow rates (core inlet flow distribution);
- 257 core simulator outlet pressures (core outlet pressure distribution);
- sectional pressure drops between the cold leg nozzle and hot leg nozzles;
- upper plenum pressure distribution.

Figure 5.16. Bird's eye view of ACOP test facility

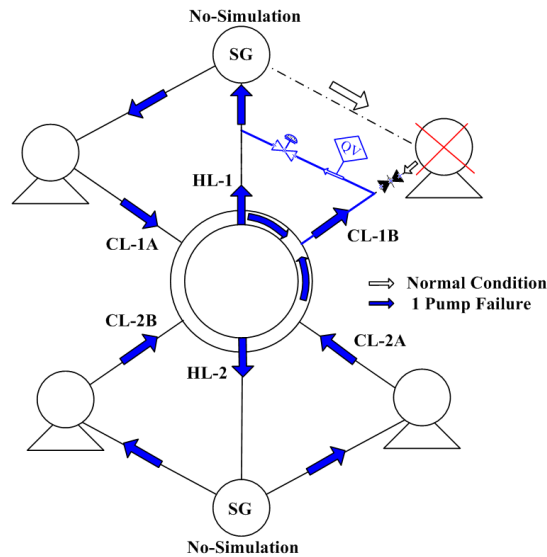


Source: Kim et al., 2013.

Figure 5.17. Core simulator



Source: Kim et al., 2013.

Figure 5.18. Single pump failed condition flow diagram

Source: Kim et al., 2013.

The cold leg and hot leg flows are measured by vortex flow meters installed at each leg. The desired flow rate can be achieved by controlling the pump speed with inverters. The system pressure is controlled by valves connected to a pressuriser.

Figure 5.19 shows the instrumentation applied to the ACOP test section that corresponds to the APR+ reactor vessel. Seven total sectional pressure drops of the reactor were measured:

- cold leg to upper downcomer;
- upper to lower downcomer;
- lower downcomer to lower head;
- lower head to core inlet;
- core inlet to outlet;
- core outlet to upper plenum;
- upper plenum to hot leg.

Twelve points (each 30° apart) were selected for the downcomer to obtain the distribution of pressure drop in azimuthal angles at one elevation plane. The average core pressure drop was identified by 12 selected points. Thirteen measuring points were selected at a quadrant at the core upper plenum. This region's pressure distribution can be obtained using a static pressure along with 12 differential pressures between the selected point and each of the remaining points.

The core inlet flow distribution can be obtained using the core inlet flow rates, measured at the inlet regions of the 257 core simulators. Venturi installed at the inlet of a core simulator measure the pressure differential through the venturi, which when used with the discharge coefficient of corresponding venturi can calculate the mass flow rate through a core simulator. The core outlet pressure distribution can be obtained by measuring 12 differential pressures in the core outlet region and a static pressure at a reference point at the core outlet. The loop flow rate, pressure and temperature can be measured using vortex flow meters, smart-type pressure transmitters and resistance temperature detectors (RTDs)

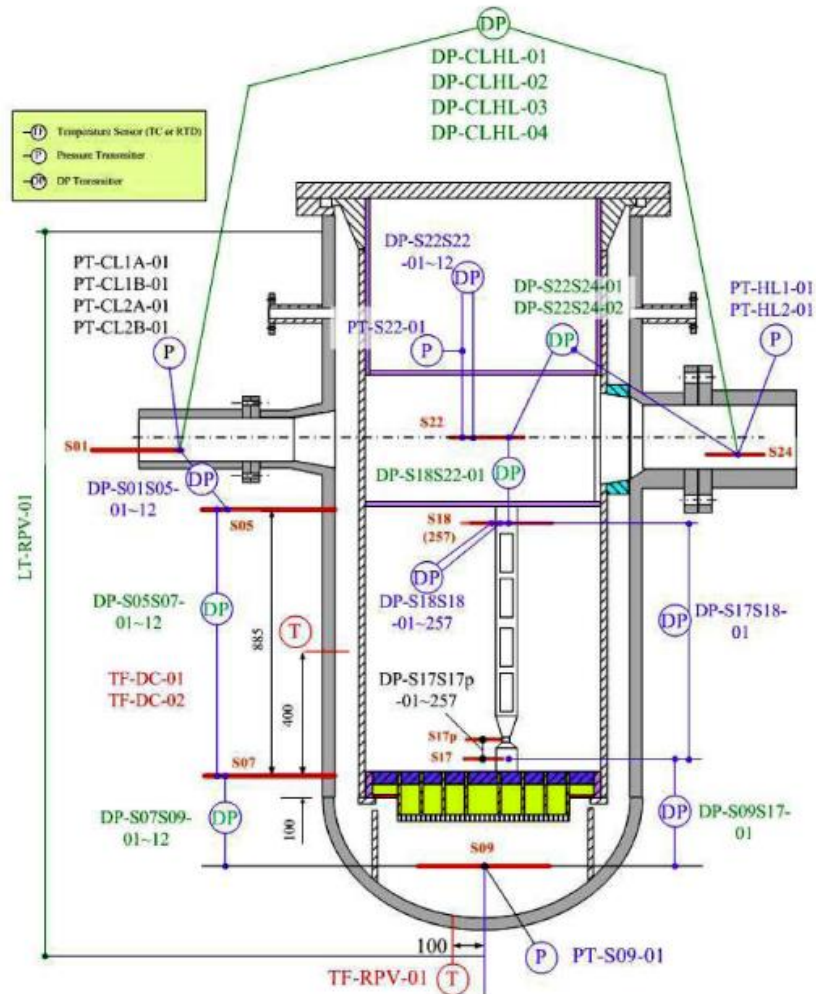
respectively. Nine static pressures, 327 differential pressures for the pressure distributions, and 257 differential pressures for the core inlet flow rates were measured in total.

5.1.7.3 Tests performed

For the test matrix, the following three conditions were selected: (1) balanced four cold leg flow condition (four RCP running conditions) [5.1.7-1], (2) 5% unbalanced four cold leg flow condition (four RCP running conditions with 5% mass flow rate deviation) and (3) three RCP flow conditions (one RCP failure).

The test matrix consists of (1) 15 balanced 4 cold leg flow (4 RCP running) conditions, (2) 5 unbalanced 4 cold leg flow conditions (4 RCP running with 5% mass flow rate deviation) and (3) 9 unbalanced 3 RCP running operation conditions representing a single pump failure. The major test conditions are summarised in Table 5.5 and they are the ensemble-averaged value of independent test results. The static pressures were measured at four cold legs, two hot legs, the lower head, the core shroud and the upper plenum. They have a standard deviation of 0.25% to 0.57% for all test cases. The temperatures were measured at a similar location as the pressure, and have 0.05 to 0.14% of standard deviations for all test cases. The loop flow rates were very accurately controlled and the data scattering based on the standard deviation of the cold leg, hot leg and core bypass flow rate of the one pump's failure was less than 0.0015%, 0.035%, and 0.012% respectively.

Figure 5.19. Pressure drop instrumentation network at downcomer and core



Source: Kim et al., 2013.

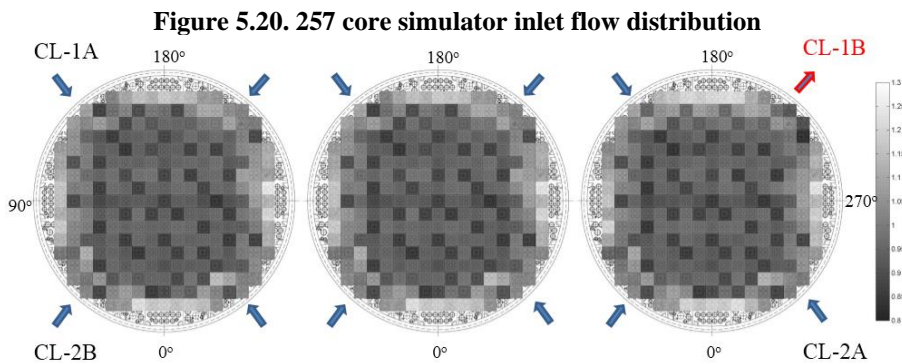
Table 5.5. Test conditions

Parameter	Test Conditions					
	4-Pump Running		4-Pump Running with 5% deviation		3-Pump Running	
	Mean	St. deviation	Mean	St. deviation	Mean	St. deviation
Cold Leg Pressure, kPa	375.3	0.35%	377.2	0.27%	379.4	0.25%
Total Core Flow, kg/s	540.0	0.00075%	540.0	0.00082%	347.8	0.0026%
Cold Leg 01, kg/s	135.0	0.00087%	136.1	0.00070%	160.0	0.0009%
Cold Leg 02, kg/s	135.0	0.00065%	136.1	0.00096%	-62.6	0.012%
Cold Leg 03, kg/s	135.0	0.0010%	130.7	0.00056%	125.2	0.0010%
Cold Leg 04, kg/s	135.0	0.0015%	137.1	0.0010%	125.2	0.0011%
Hot Leg 01 kg/s	269.2	0.024%	271.2	0.030%	159.7	0.036%
Hot Leg 02 kg/s	268.5	0.021%	266.4	0.015%	249.0	0.025%
Temperature, °C	59.9	0.11°C	60.0	0.07°C	60.1	0.09°C

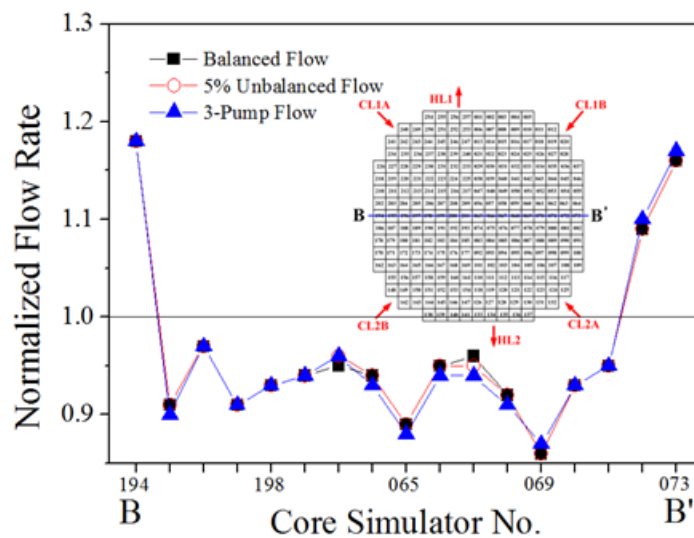
5.1.7.3 Application for system code validation

Results and discussions

The flow distribution at the core inlet is measured by 257 core simulators, and Figure 5.20 shows the measured flow distribution along the B-B' line of the ACOP core.



Note: (left) balanced flow case (centre) 5% unbalanced flow case (right) three pump flow case



Note: (d) Flow distribution along the B-B' line. Source: Kim et al., 2013.

Application and drawbacks for the 2D/3D application

There is available experimental data for the verification of the 2D and 3D analysis results of a reactor core and downcomer because 257 fuel assemblies' individual flowrates were measured.

Availability of the data

The current data was generated under the project supported by the Korean government's Ministry of Knowledge Economy (MOKE), in which several companies and institutes formed a consortium for the work and to share the product. The current data could be made available with their agreement.

Future plans

Further experimental work will be performed with new instruments such as wiremesh to evaluate the performance of the boron mixing at a lower plenum.

5.1.8. DYNAS

5.1.8.1 Objective of the experiment

The multidimensional behaviour of a two-phase flow is expected to occur at several regions in the reactor system, which significantly affects the key safety parameters. However, a very limited number of experiments offering a well-defined multidimensional flow have been found in the literature. A new experiment is hereafter presented, in which slab geometry that has a sufficiently large gap reduces the wall shear effect of individual cap/slug bubbles. A test facility in KAERI, called DYNamics of Air/water System (DYNAS), has been newly designed and constructed and aims to generate an experimental database for a multidimensional two-phase void distribution in 2D slab geometry [5.1.8-1]. Two separated test sections were prepared for the respective visualisation and impedance measurements. Various kinds of two-dimensional flow patterns were simulated using different opening combinations of the inlet and outlet nozzles. The major parameters measured were the two-dimensional void fraction profile in the slab-type test section and the T/H boundary conditions. The void fraction was converted from the impedance measured between two electrodes installed on the inner surfaces of the slab acrylic plates. Experiments were performed at a pressure lower than 0.2 MPa and at 35°C. Various flow rates of water and air were set in order to obtain data representing the dynamic multidimensional two-phase movement. The water flow ranged from 2 to 20 kg/s and the air flow rate ranged from 2.0 to 20 g/s for each selected inlet and outlet nozzle combination, which correspond to 0.4 to 4 m/s and 0.2 to 2.3 m/s of superficial liquid and gas velocities based on the inlet port area, respectively.

5.1.8.2 Description of the test loop

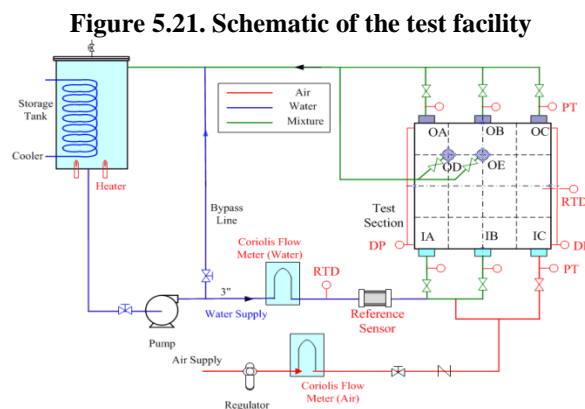
Figure 5.21 shows a schematic of the DYNAS experimental apparatus. The fluid system consists of a test section, storage tank and piping system, which allows the water and air supply to arrive at the test section and return back to the storage tank. The storage tank was installed at the top part of the facility, where the air in the returned two-phase mixture flow was separated. A cooler and heater imbedded in the storage tank controlled the water temperature in the system. A centrifugal pump supplied the water flow. A bypass line was established at the upstream of the test section to enable efficient control of the water flow. Instrumentations for the flow rate, temperature and pressure were installed in the water injection line. A reference impedance sensor was installed at the inlet of the test section in

the water supply system, of which the impedance value was utilised for compensation of the void fraction at each point in the test section. A compressor supplied air to the test section. A regulator controls the air injection pressure before the air is delivered to the test section.

Figure 5.22 shows the test section's design features and important components. The two-phase flow injected through the selected inlet valve was split into two streams and gathered at a common header. The flow goes downward in the annulus inside the common header and enters the test section through the inlet nozzle. A flow straightener and honey vane were installed inside the inlet pipe to maintain a straight flow at the inlet.

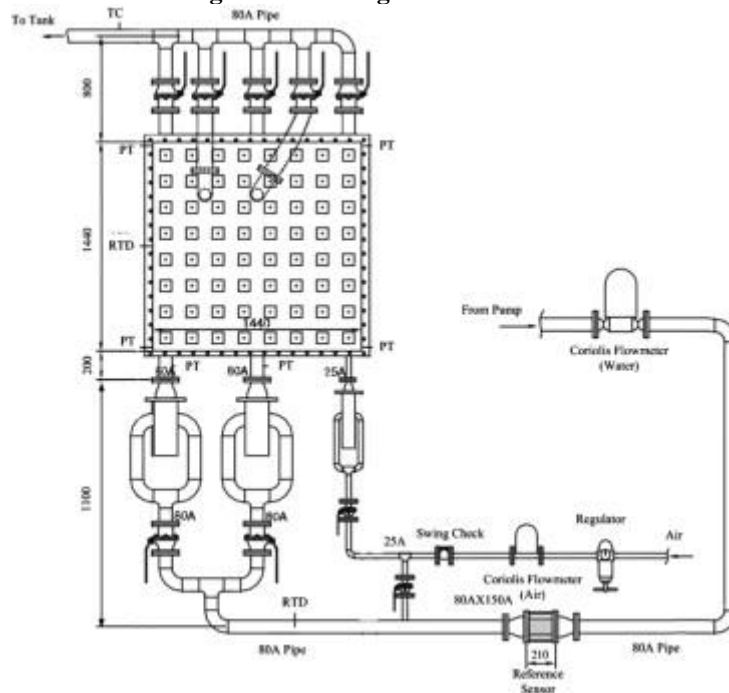
The present description focuses on the hydraulic behaviour of a reference nuclear reactor downcomer having a 0.25 m gap size. This relatively large channel prevents the formation of a slug bubble that would plug the channel. The small gap geometry of the test section can bear undesirable wall shear momentum loss induced by a slug bubble and therefore the test section was designed with a greater gap scale than the stable maximum bubble size.

Two test sections were manufactured to measure the impedance at the test section's local points and provide a visualisation of the overall flow characteristics of a 2D flow. Two independent tests for the same flow conditions were performed with different test sections corresponding to measurement methods. The visualisation test serves as a qualitative benchmark of the void profile results from the impedance measurement method. The local void fractions in the test section were obtained by measuring the impedance between two electrodes installed face-to-face on each inner surface of an independently manufactured test section. The size of the test section is 1.44 m x 1.44 m x 0.11 m. The test section has three inlet and five outlet nozzles. Each nozzle's inner diameter is 83 mm, except for the air inlet nozzle, where it is 28 mm. A single-phase water flow or two-phase mixture flow can be supplied through the other two inlet nozzles. Three outlet nozzles were installed on the top face of the steel structure, while two outlet nozzles were installed on the large rear face of an acrylic plate. A conceptual flow pattern in a downcomer near a postulated broken cold leg during a loss-of-coolant accident can be simulated using the latter two nozzles. Various types of multidimensional flow behaviours can be simulated by selecting a combination of inlet and outlet nozzles.



Source: Euh et al., 2013.

Figure 5.22. Design of test section



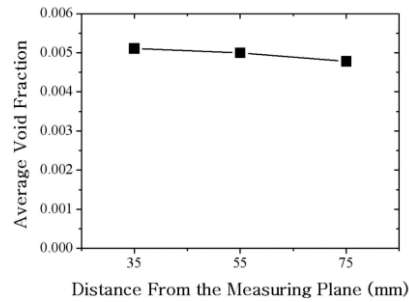
Source: Euh et al., 2013.

Instrumentation

Instrumentation of the DYNAS system can be classified into two categories: (1) the instrumentation for boundary parameters, such as pressure, temperature, and flow rates of both phases, and (2) the local measurement of impedance used to obtain a 2D void fraction.

Several types of commercially available instruments were installed for measuring the boundary conditions. The mass flow rate of the injected water was measured using a mass flow meter installed at the water supply line. A mass flow meter was also used to measure the air flow at the air supply line. The system pressure was measured at the top and bottom of the test section. Two RTDs were installed to measure the temperature of the fluid, one at the water supply line and the other by the test section. The system temperature was maintained at around 35°C, which accounts for the pump's heat generation at the maximum flow condition and the loop's cooling capability. The applied power of the heater inside the storage tank was controlled by an SCR by referring to the temperature at the water supply line.

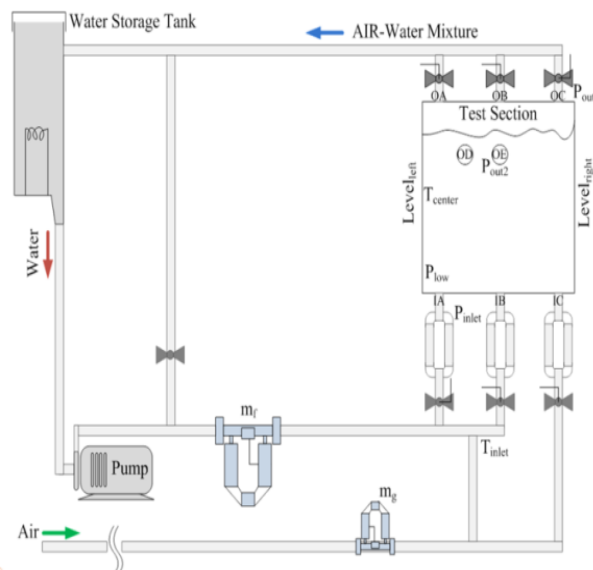
The test section has 15x15 measuring points for a local measurement in order to obtain a void fraction profile with a sufficiently high resolution. Each electrode has a dimension of 4x4 cm. Figure 5.23 shows a typical measurement result for average void fraction at measuring planes.

Figure 5.23. Effect of the gap void distribution

Source: Euh et al., 2013.

5.1.8.3 Tests performed

Figure 5.24 shows the measured parameters and definition of the inlet and outlet nozzles. Each test condition was achieved by selecting an inlet and an outlet nozzle among the three inlet nozzles (IA, IB and IC) and five outlet nozzles (OA, OB, OC, OD and OE). The water flow ranged from two to 20 kg/s, and the air flow rate from 2.0 to 20 g/s for each selected inlet and outlet nozzle combination, which corresponds to 0.4 to four m/s and 0.2 to 2.3 m/s based on the inlet port of superficial liquid and gas velocities area, respectively.

Figure 5.24. Measured parameters and nozzle definition

Source: Euh et al., 2013.

5.1.8.4 Application for system code validation

Each test case uses 200 data numbers for statistical analysis for the visualisation test. The visualisation test results revealed that the mixture flows in a rather 1D way for low air and water condition, whereas high air or water flow cases show a strong multidimensional pattern. Additionally, coalescence occurred in low air and water flow condition and there was sufficient contact time among the air bubbles for a large air region to form.

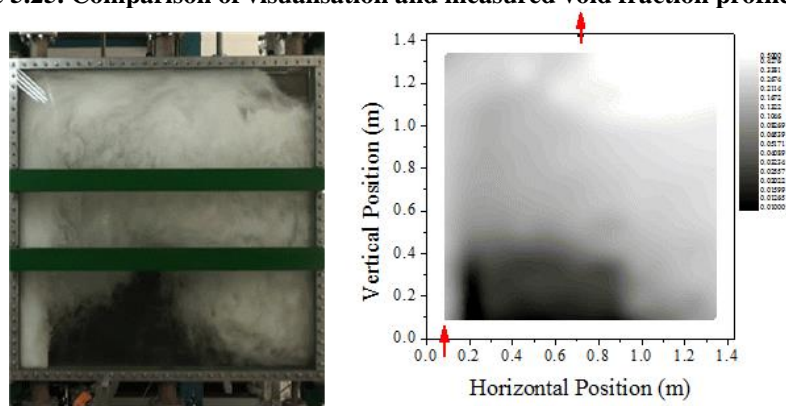
Twenty tests were performed for the impedance measurement, for which six sets of a combination of inlet and outlet ports were selected. Hundreds of data points were acquired at each local point with a 100 Hz/channel sampling speed in these applications. The instantaneous measured data was processed for the statistical results. All the impedances

measured at 225 electrodes were converted to void fraction data by using calibration curves and plotted into a 2D contour form, which was directly compared with the visualisation results. One of the comparisons of measured void profiles with the visualisation test results is shown in Figure 5.25. Although the visualisation cannot clarify the void profile in-depth direction, it does imply the relevance of the measured void profiles. In general, the measured void profile matches the visualisation results.

The liquid levels near the two side walls measured from the differential pressure transmitters were compared with those from the impedance measurements to check the accuracy of the measured data another way. A comparison of both measurements reveals a 5% deviation between the two measured average void fractions for three data points.

This experiment was performed under government supports that are intended to be used for Safety and Performance Analysis Code (SPACE) code validation.

Figure 5.25. Comparison of visualisation and measured void fraction profile (AB04)



Source: Euh et al., 2013.

Availability of the data

The current data was generated under the project supported by the Korean government's Ministry of Trade, Industry and Energy (MOTIE), in which several companies and institutes formed a consortium for the work and to share the product. The test data are not available to the public. It might be made available under a separate agreement between organisations.

5.1.9. DOBO

5.1.9.1 Objective of the experiment

Direct vessel injection (DVI), during which the ECC water of an ECCS is directly injected into the reactor vessel's downcomer, is employed in some advanced reactors such as APR+, APR1400, AP600. The analysis results for an APR1440 show that a DVI type safety injection system induced a late heating during the late reflood phase of a LB-LOCA at an earlier stage. However, since the existing safety analysis code was developed to be suitable for a safety analysis in a cold leg injection type, there remain some unanswered questions about its applicability to a reactor employing DVI.

The core reflood rate following the injection of ECC water during a LB-LOCA is determined by the pressure difference between the core and downcomer, which is the static head difference by the collapsed water level [5.1.9-1] and [5.1.9-2]. As shown in Figure 5.26, when the ECC water of an APR1400 is injected into the core through a DVI, it is mixed with the steam generated from the residual heat in the reactor inside the downcomer, and its penetration into the core is partially disturbed. The subcooled degree of the coolant

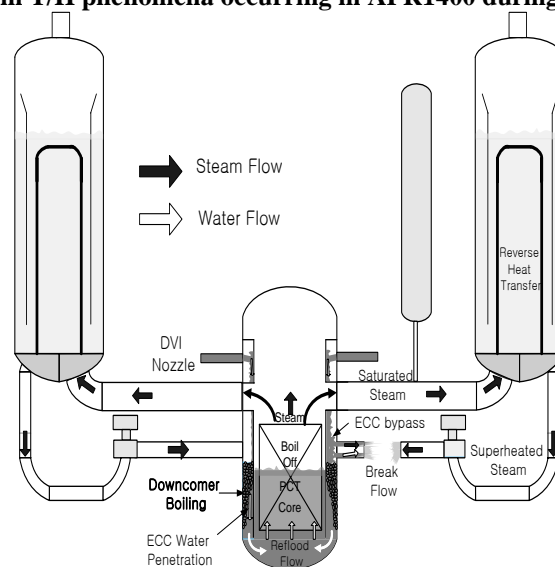
heated by the steam also affects the core cooling and peak cladding temperature of nuclear fuel. In the results of a calculation using the RELAP5 code, the ECC water injected into the reactor vessel abruptly boils inside the downcomer from the thermal energy transferred from the high-temperature reactor vessel structure, which results in a rapid increase in the void fraction. This leads to a reheating of the core by reducing the head in the downcomer part and decreasing the reflood rate in the core, which seriously threatens the nuclear fuel rod's integrity. Analysis results using Multi-dimensional Analysis of Reactor Safety (MARS) and TRAC also show that the boiling in the downcomer can cause the temperature the nuclear fuel rod in the core to increase.

There are therefore concerns that must be addressed regarding whether the boiling of the coolant accumulated at the bottom of the downcomer occurs due to a wall heating effect of the reactor vessel, which decreases the core cooling ability. A review of the technical validity of the related T/H model of the safety analysis code is required. A T/H test with adequate boundary conditions of reflood downcomer setup is essential for this.

5.1.9.2 Description of the test loop

The test facility was designed following the volumetric scaling method. The volumetric scaling method has the temperature, pressure and height set to match the model and reference plant. However, the lateral length is reduced to follow to this methodology, as well as the downcomer gap in the DOwncomer BOiling (DOBO) test facility. The reduced downcomer gap size changes the ratio of the downcomer gap to the bubbly boundary layer thickness, and the DOBO value is distorted compared to the APR1400's. Ultimately, this distorts the interface friction force between water and void in the downcomer. A modified volumetric scaling method was employed to correct the drawback of the original volumetric scaling method in the DOBO test facility, which preserved one of the two lateral direction length scales. Although a 1D assumption about which axial direction is dominant was introduced in the conventional volumetric scaling methodology, only one out of two lateral direction flows was ignored in the modified methodology. The velocity, heat flux and gravity can still be preserved by introducing the scaling analysis method in this way because the advantage of the existing volumetric scaling method can be preserved, as well as the multidimensional flow phenomena in one direction out of the multidimensional flow phenomena occurring in two lateral directions.

Figure 5.26. Main T/H phenomena occurring in APR1400 during LB-LOCA reflood



Source: Euh et al., 2008.

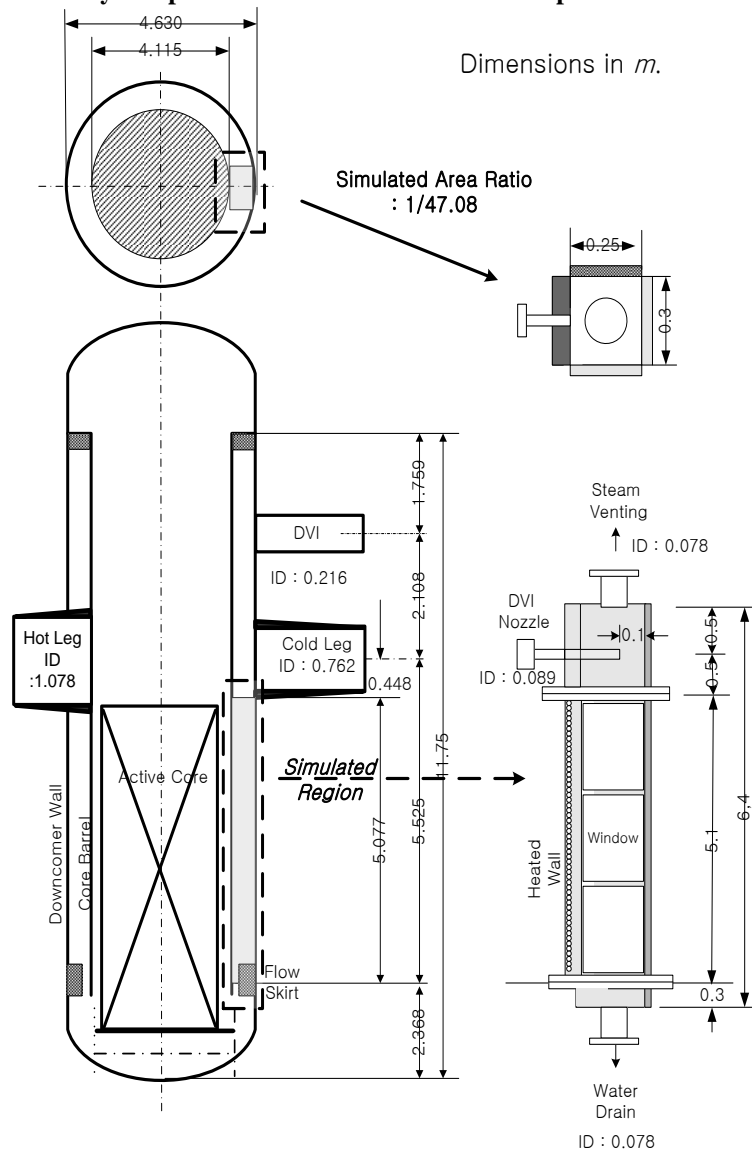
The height of the test facility and the downcomer gap were preserved to 1:1 in the DOBO test facility by introducing the modified volumetric scaling method. This enabled the preservation of key two-phase flow phenomena, for example the bubbly boundary layer thickness and void fraction distribution produced in the downcomer. Figure 5.27 shows the downcomer simulation part of the DOBO facility and APR1400 downcomer.

As shown in Figure 5.28, the test facility consists of a downcomer simulation part (test section), pre-heater, water/steam separator, steam condenser, circulation pump, heat exchanger, accumulator and mixing tank. The test facility can be operated at 0.5 MPa at the most, and the design pressure was set up as one MPa in mind of safety considerations.

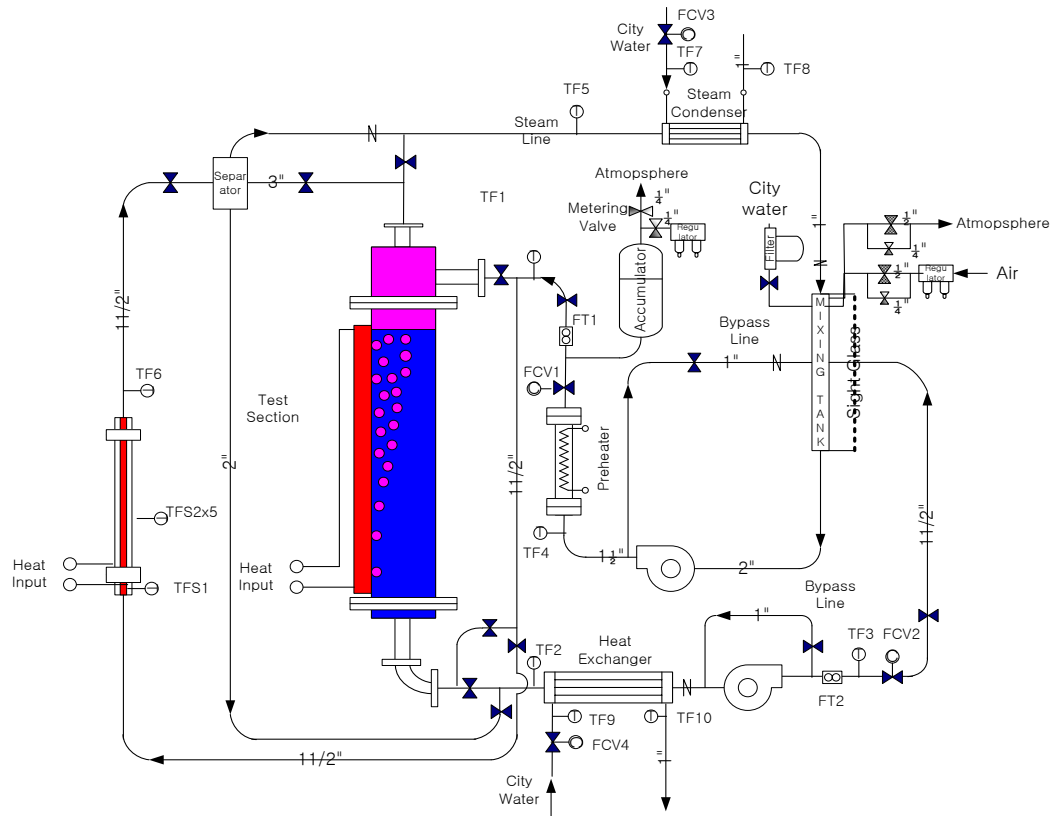
The downcomer of the reactor is simulated by a slab-type flow channel. One wall of the slab is heated by an electric heater and reinforced glass is installed on three side walls to enable visualisation. Over 200 cartridge electric heaters were installed on the heated wall. The heat flux of the heating part was obtained from the analysis result of RELAP5 and TRAC-M.

A pre-heater controls the temperature of ECC water injected into the downcomer. The pre-heater of the test facility can increase the temperature by 7.3°C in the maximum operable flow condition and by 20°C in a reflood condition. The water/steam separator separates water and steam when the two-phase flow of water and steam is injected into the top of the test section. The water/steam separator is used to make a moisture separation using the cyclone principle. A steam condenser is a plate-type heat exchanger that condenses the steam released at the top of the main test section to make the condensed water flow into the mixing tank. The capacity is designed for the removal of 150 kW of latent heat. The amount of steam condensation is controlled by a flow adjustment of the coolant on the secondary system. The heat exchanger is a plate-type heat exchanger of the same type as a steam condenser, which removes heat from the coolant leaked to the bottom of the downcomer. This facilitates the operation of a pump by maintaining the low temperature of the coolant flowing to the pump. The heat exchanger has a heat removal capacity of 100 kW, which is the same capacity as the pre-heater's. Like a steam condenser, heat removal is controlled by a flow adjustment of the coolant in the secondary system. Circulation pumps are installed on the bottom of the test section and mixing tank to coping with the drain in the lower part of the test section and the injection of ECC water respectively. In the test, the circulation pump is operated at the maximum output condition of the pump, and the flow injected or drained is controlled by the control valve and bypass pipeline installed at the pump's downstream. The pump heads are 40 and 30 m respectively and can make a maximum of 3.23 kg/s of flow. Steam generated by boiling in the test section passes the condenser and is collected in the mixing tank. Meanwhile, subcooled water released to the lower part also passes through the recirculation pump, heat exchanger and flow meter, before being collected in the mixing tank.

Figure 5.27. Geometry comparison of downcomer: simulated part of APR1400 and test facility



Source: Euh et al., 2008.

Figure 5.28. Schematic diagram of DOBO test facility

Source: Euh et al., 2008.

Measurements and instrumentation

The DOBO test facility was designed to apply 1) a macroscopic parameter measurement system that measures the mass and energy transfer in the downcomer, and 2) a special two-phase flow measurement system that measures a local two-phase flow parameter. The macroscopic parameters (the temperature, pressure and heating surface average heat flux) were measured and provided as boundary conditions to be used for a safety analysis code evaluation. The flow and energy at the boundary surface in the test, such as the temperature, pressure and injection flow of the fluid, are measured at the entrance and exit of the test section. The two-phase flow basic parameters such as temperature, pressure, void fraction, void velocity and water velocity are measured at the cross-section of the test section. The measured parameters can then be processed and converted into flow parameters, as needed for analysis on an interface area concentration (IAC) and interface friction coefficient. Key measurement parameters and measurement instruments are summarised in Table 5.6.

Figure 5.28 shows the fluid system of the DOBO test facility and measurement device installation locations. As shown by the figures, the temperature and pressure of the fluid, and the injection mass flow are measured at the entrance and exit pipelines of the downcomer simulation part. The energy transfer at the boundary surface is then calculated and the mass flow and energy change in the downcomer simulation part measured. Eight differential pressure transmitters are installed in the downcomer simulation part to measure the average void fraction distribution in the axial direction or to measure the water level. The five-conductance probes used to measure the local two-phase flow parameter measurement and the local bi-direction flow tube are described in detail in the next section. The average heat flux applied to the heating wall of downcomer simulation is calculated

by dividing the total electric power that is applied to the heater installed on the wall by the section area of the heated wall.

Table 5.6. Measurement parameter and measuring instrument summary

Measurement parameter	Instrumentation
Heat flux	Power metre, wall temperature
Average void fraction	Differential pressure transmitter
Local void fraction	Conductance probe
Fluid temperature	TC
Bubble velocity interfacial drag	5-conductance probe
Degree of subcooling	TC, pressure transmitter
Pressure	Pressure transmitter
Water level	Differential pressure transmitter
Liquid velocity	Bidirectional flow tube
Mass flow rate	Coriolis mass flow meter

A five-probe electric conductivity method, consisting of five probes specially developed by a KAERI research team, is applied in order to obtain the local void fraction distribution and local void velocity distribution under a multidimensional two-phase flow condition. In this method, probes that are electrically insulated (with the exception of the tip) are used to measure the difference in electric conductivity. The difference varies depending on the fluid, such as water and air or water and steam. The probes measure the interface between the gas phase and liquid phase and calculate the local two-phase flow parameter. A five-probe electric conductivity method consisting of a total of five probes was used to measure the multidimensional flow phenomena in the downcomer.

A precise 2D traverse of the probe at a given height is required to measure the distribution of each local parameter on the cross-section and section average. A traversing device was newly invented for these tests and applied to fulfil this function. A rotating axis and bellows are on the fixed part of the main test section wall (into which the probe is inserted) and transfer the probe sensor part to the desired location by adjusting the radius and rotating angle. A probe traversing device will be installed at five locations based on the test section's height, which will measure the multidimensional distribution of the local parameters by height.

A local bidirectional flow tube (BDFT), which is available in a high void fraction air-water or steam-water two-phase flow, was applied during these tests for the liquid velocity. The operational principle of a BDFT is similar to a Pitot tube. The difference is that in a BDFT the absolute pressure is measured by the absolute pressure tube located at the back of the flow tube and the measured absolute pressure becomes smaller than the absolute pressure in the flow channel due to the suction effect produced by wake flow. The differential pressure measured at the front and back ends of the flow tube is higher than the dynamic pressure produced by the flow of the fluid in the flow field. This characteristic of the differential pressure measurement value results in the flow velocity measurement being easier in a low velocity region. In addition, the geometry of a bidirectional flow tube is the same in both directions and therefore the tube can measure the bidirectional flow velocity in a flow whose direction changes.

5.1.9.3 Tests performed

The major boundary conditions are summarised in Table 5.7, which was divided into the top and bottom water injections. The test cases R1 to R4 inject water from the top, considering the accident whereby ECC water injects from the top of the downcomer via the direct vessel injection nozzle. The conditions focus on the boundary value for the

postulated LB-LOCA scenario in consideration of safety concerns. There was a free surface at the upper part of the downcomer and the local parameters were not measured.

The second part of the C-series injects the water from the bottom. The global water and steam directions are the same and a relatively simple two-phase flow condition is expected. The C-series does not have a free surface and the two-phase mixture goes through the top exit of the test section. Local bubble parameters and liquid velocity were measured in the C-series of test by using a local conductance probe and bidirectional flow tube (BDFT). C2-1a and C2-1b have the same T/H conditions. The former refers to the experiment using the conductance probe and the latter the experiment using BDFT.

Table 5.7. Test matrix

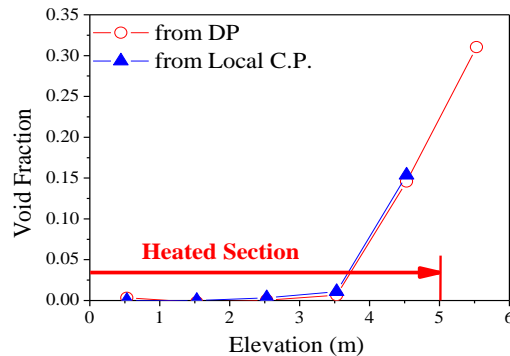
ID	T _{ECC} (°C)	P _{Top} (kPa)	W _{ECC} (kg/s)	Heat Flux (kW/m ²)	Water level (m)	ECC injection type	Local parameter
R1	110.14	162.8	1.22	50.2	5.4	Top	X
R2		161.42	1.16	69.7	5.4	Top	X
R3	109.64	166.47	1.2	82.1	5.4	Top	X
R4	109.52	170.78	1.2	91.1	5.4	Top	X
C2-1a	112.9	160.6	1.29	72.2	N/A	Bottom	O
C2-1b	112.6	159.2	1.31	71.6	N/A	Bottom	O

5.1.9.4. Application for system code validation

The pressure difference between the top and bottom of the test section was mainly contributed by the hydrostatic head, which could be converted to the average void fraction in the test section. For the C-series, the test shows a resultant average void fraction of 7.2% for the overall test section and 3.1% for the heated section. As the subcooled liquid flowed upward, the temperature of the liquid increased and nucleate boiling started at the heated wall, which is called “the onset of nucleated boiling”. The nucleated bubble started to slide along the heated wall and was lifted off the wall. The bubble which entered the bulk region was immediately condensed because the bulk liquid was maintained at the subcooled state. This phenomenon formed a bubbly boundary layer near the heated wall. The thickness of the bubbly boundary layer gradually increased as the liquid temperature increased. The distinct bubble boundary layer is a typical characteristic of subcooled boiling flow, which occurs in the lower and middle regions. In the upper region, there was well-mixed bulk boiling, while the bubbly boundary layer expanded to the opposite wall. The liquid reached a saturated temperature at the bulk boiling region, causing an expected flashing phenomenon in the upper section as the nearly saturated liquid flowed upward.

The channel size was large enough for the pressure drop between each pressure tab to mainly come from the hydrostatic head, which could then easily be converted into the void fraction. The average void fraction measured from the pressure drop (DP) transmitter was compared to the data from the local conductivity probe, as shown in Figure 5.29. The two void fractions agreed within 5.6% of the discrepancy at 4.5 m from the initiation of the heated section.

The unheated section starts at 5.1 m from the bottom of the heated section. Even when the heated section finished at 5.0 m elevation, the void fraction still increased. As a result, the liquid reached a saturated condition. A flashing was expected as the flow went upward with this saturated condition, which increased the amount of steam and was reflected by the increased void fraction, as shown by Figure 5.30.

Figure 5.29. Profile of the channel area averaged void fraction

Source: Yun et al., 2008.

The local parameters measured in this study were void fraction and steam velocity. Local conductivity probes were installed at five elevations that were selected for the local measurements along the heated test section. Each measuring plane was located at a midpoint between each DP tab. Five measured lines with 24 points were selected at each measure plane, as shown in Figure 5.30. The distance between each point line was 1.0 cm and between each measuring line 35 mm. The data acquiring time of the five-conductance probe was 30 s with a 20 kHz sampling rate at each point.

Figure 5.30 shows the propagation of the local void fraction along the test section. At the lower elevation, where boiling was initiated, the steam concentrated near the heated wall. As the generated steam flowed upward, the void profile widened and a distinct bubbly boundary layer formed. At the upper part of the heated section, a peaking of the void profile moved to the central region of a measuring plane. This trend reflected the visual observation well because the bubbly boundary layer thickness increased rapidly as the elevation became higher.

The current programme also generated local 3D bubble velocities, which were obtained from the five-conductance probe and liquid velocity using BDFT. However, these are undergoing the data quality enhancement process, which includes reducing the data fluctuation, etc.

Application and drawback for 2D/3D application

Current data include multidimensional two-phase flow behaviour in respect of void fraction. The resolution of the data is around one cm in the form of a 2D contour at five elevations inside downcomer, which is a sufficient scale for the validation of the system-scale codes. The data will soon be used for the validation of the 3D system code, SPACE.

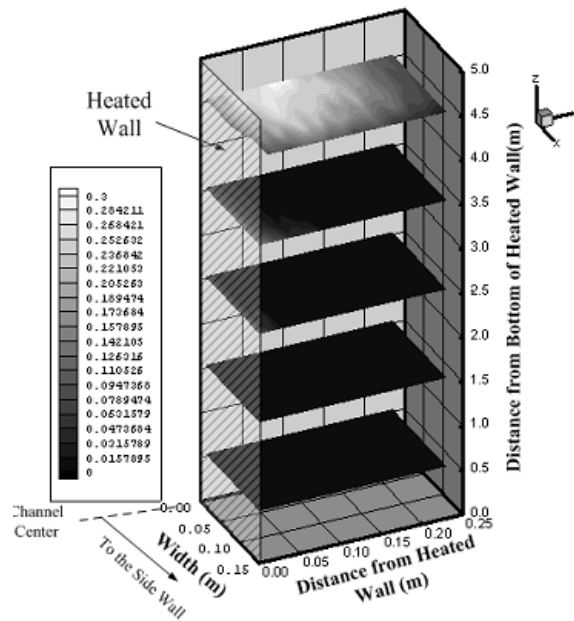
Availability of the data

Current data were generated under the project supported by the Korean government's MOTIE, in which several companies and institutes formed a consortium for the work and to share the product. The current data could be made available with their agreement.

Future plans

Currently there are no plans for the test facilities. The infrastructures have been significantly dismantled.

Figure 5.30. Typical local void fraction in the test section



Source: Yun et al., 2008.

5.1.10. MIDAS

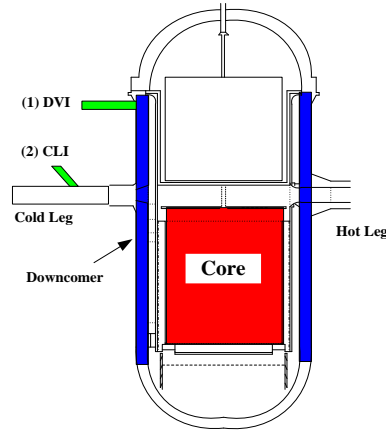
5.1.10.1. Objective of the experiment

The APR1400 reactor adopted DVI for an ECC water system. Figure 5.31 shows a location of ECC water injection nozzles in the cold leg injection (CLI) and DVI systems. Multidimensional thermal-hydraulic phenomena were induced during a late reflood period of a LB-LOCA of the APR1400 by a crossflow of the steam in the transverse direction and ECC water flow in the axial direction, which can occur in the downcomer, as shown in Figure 5.32. Green arrows in the figure refer to the water warmed by steam and the water interactions.

The Multi-dimensional Investigation in Downcomer Annulus Simulation (MIDAS) test facility, which is a separate effect test facility for investigating T/H phenomena in the downcomer, was designed by a modified linear scaling method (scale factor of 1/4.93) of the APR1400 [5.1.10-1]. Two test series (direct ECC bypass tests and void height tests) have been performed in this facility. The direct ECC bypass tests were performed under two DVI injection modes: a single DVI nozzle injection through one of four DVI nozzles and two DVI nozzle injections through a combination of DVI-1 and -4, DVI-2 and -4, and DVI-3 and -4 nozzles. An ECC bypass fraction, a steam condensation fraction and a temperature distribution in the downcomer were precisely measured in these tests. However, the sweep-out phenomenon was excluded and only direct bypass of the ECC water to the broken cold leg was considered. The initial water level in the downcomer was therefore maintained at sufficiently lower level than the water level for the onset of entrainment in order to exclude the ECC water bypass via a sweep-out. In the void height tests, the collapsed water level of the downcomer and the subcooling of ECC water were measured under a constant reflood flow rate condition in the core and both direct ECC bypass and sweep-out phenomena were considered.

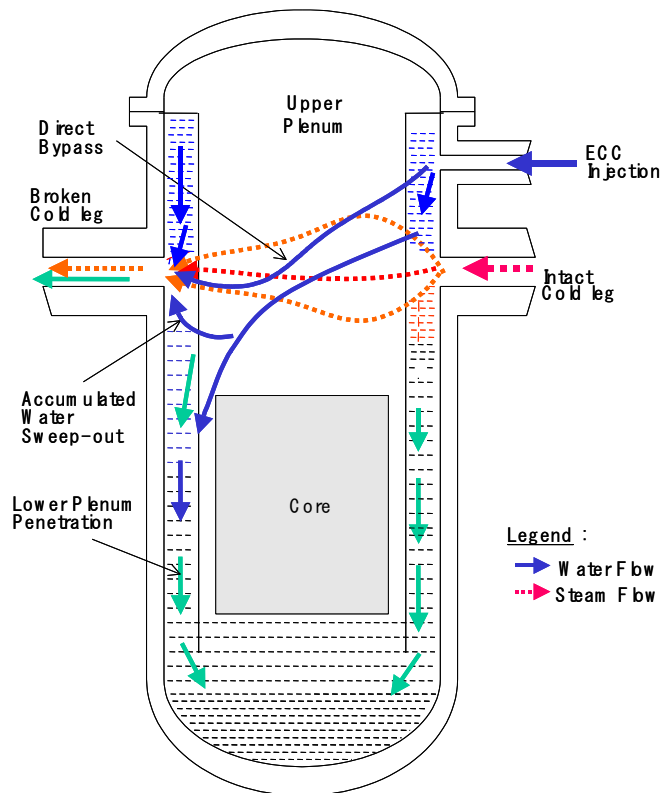
The MIDAS test results can identify any code deficiency for a LB-LOCA simulation during a late phase reflood period, especially for DVI-adopted nuclear power plants.

Figure 5.31. DVI mode versus standard CLI mode



Source: Yun et al., 2001.

Figure 5.32. T/H phenomena during a reflood period of LB-LOCA in the APR1400



Note: the green arrows refer to warmed water and interactions with steam.
Source: Yun et al., 2001.

5.1.10.2. Description of the test loop

A modified linear scaling method was applied to the MIDAS test facility’s design. This scaling method preserves the prototype’s gravity and aspect ratio scale. This scaling method thereby can simulate the multidimensional flow phenomena in the downcomer.

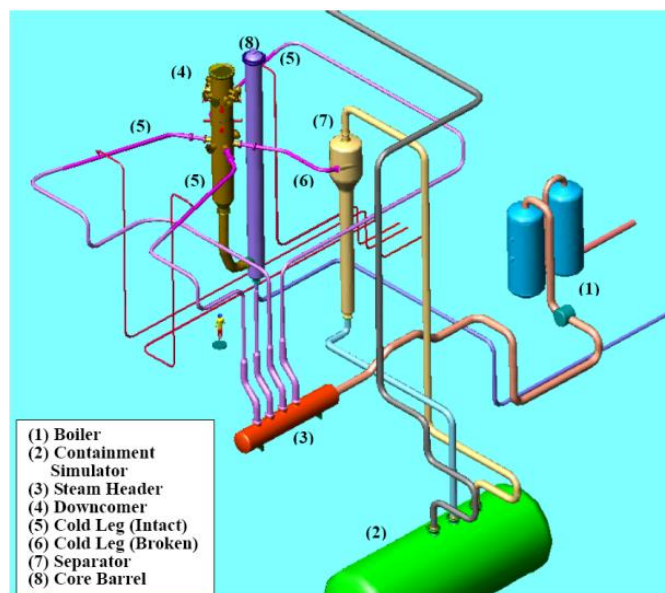
The MIDAS test facility consists of downcomer and core barrel simulators, a primary piping system, an ECC water supply system for SIS simulation, a superheated steam supply system, a containment system and a measurement system, as shown in Figure 5.33.

Figure 5.34 shows a schematic diagram of the primary piping system. The downcomer annulus and core region were separated in the test facility to preserve the multidimensional flow phenomena in the upper section of the downcomer and enhance the accessibility of instrumentation to the downcomer's inside and outside walls. The lower part of the downcomer was designed as a single pipe with a simple flow path connecting to the inlet plenum of the reactor core.

The upper downcomer's annulus' gap width in the APR1400 ranges from 25.41 cm to 25.71 cm, depending on the vertical height. The gap width chosen in the MIDAS test facility was 25.71 cm.

The region between the downcomer and the core barrel corresponding to the core bottom elevation was simulated by a single inclined pipe. The connecting region between the downcomer annulus and single pipe was designed as a wedged-shaped shape to establish uniform flow.

Figure 5.33. Schematic diagram of MIDAS test facility



Source: Yun et al., 2001.

The downcomer simulator was connected to various nozzles, such as cold leg nozzles, hot legs nozzles and DVI nozzles. Four DVI nozzles were installed in the upper part of the downcomer simulator at a scale-downed height by the volume scaling method. Another four DIV nozzles were installed at the upper location of 0.427 m from the cold leg's centre line, following the modified linear scaling methodology for tests.

In the MIDAS test facility, the nozzle simulating the hot legs was installed to preserve the effect of the hot leg on the flow behaviour in the downcomer. The inner diameter of the cold leg was determined by the length scale and safety injection nozzles were installed at each cold leg to simulate the CLI mode.

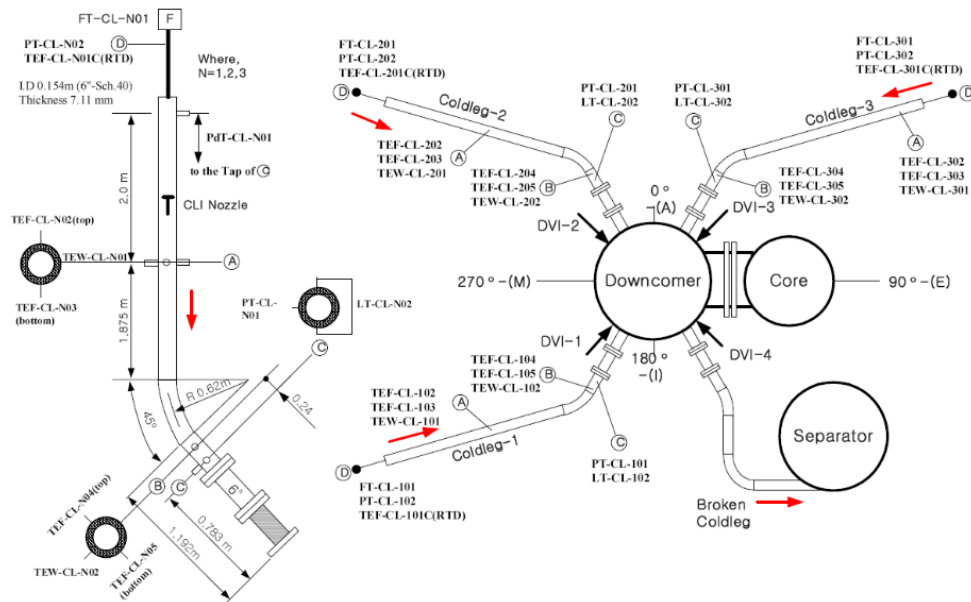
The safety injection system of the APR1400 reactor consists of DVI nozzles, safety injection tanks (SITs) and high pressure safety injection (HPSI) pumps. The safety

injections from the SITs and the HPSIs are simulated in the MIDAS test facility by the separate pump systems.

A superheated steam boiler was installed to simulate the steam discharged from the reactor core to the cold legs. The superheated steam boiler simulates the decay heat and phase change energy for droplets in the upper core, in order to convert the superheated steam through a steam generator.

The containment simulating system consists of a water-steam separator and large storage tank. This system stores the discharged fluid from the broken cold leg and controls the system pressure. The discharged fluid from the broken cold leg is separated in the water-steam separator and the water is then discharged into the storage tank through the connecting pipes. The water discharged into the storage tank is collected and the steam condensed. Some steam is discharged into the atmosphere to control the containment pressure. The containment pressure is controlled by adjusting the steam discharge rate into the atmosphere during the MIDAS test. The water-steam separator is also used to measure the break flow rate.

Figure 5.34. Schematic diagram of primary piping system



Source: Yun et al., 2001.

Instruments

Six hundred instrumentations were installed in the MIDAS test facility to measure the major T/H parameters, which including the ECC water and superheated steam’s mass flow rates and the break flow rate. Many devices were installed in the reactor downcomer to measure the multidimensional flow phenomena from a quantitative point of view. Major instrumentations included thermocouples, pressure transmitters and differential pressure transmitters.

5.1.10.3. Tests performed

The MIDAS tests have been classified into direct ECC bypass tests and void height tests. The direct ECC bypass tests were performed under two DVI injection modes: a single DVI line injection through one of four DVI nozzles and two DVI line injections through a

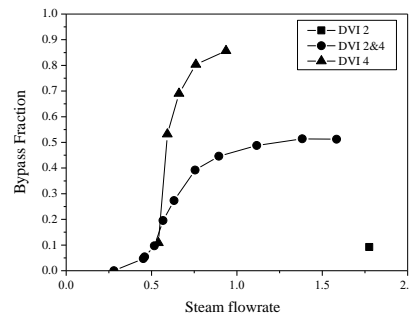
combination of DVI-1 and -4, DVI-2 and -4, and DVI-3 and -4 nozzles. In the direct ECC bypass tests, the sweep-out phenomenon was excluded and the direct bypass of the ECC water to the broken cold leg was considered. The initial water level in the downcomer was therefore maintained at a sufficiently lower level than the water level for the onset of entrainment to exclude the ECC water bypass via a sweep-out.

In the void height tests, the collapsed water level of the downcomer and the subcooling of ECC water were measured under a constant reflood flow rate condition in the core and both the direct ECC bypass and the sweep-out phenomena were considered.

5.1.10.4. Application for system code validation

Figure 5.35 shows the ECC bypass fraction in the steam-water test through DVI nozzles. The direct ECC bypass fraction was calculated from the ECC injection flow rate, steam condensation rate and drain flow rate at a reactor downcomer annulus.

Figure 5.35. ECC bypass fraction



Source: Yun et al. 2001.

Application and drawbacks for 2D/3D application

The experimental data are available for the verification of 2D downcomer thermal distribution and direct ECC bypass fraction.

Availability of the data

The current data were generated under the project supported by the Korean government's MOKE, in which several companies and institutes formed a consortium for the work and to share the product. The current data could be made available with their agreement.

5.1.11. PSBT

5.1.11.1. Objective of the experiment

Void generation in the fuel assemblies provides a redistribution of coolant flow throughout the core under transient and accident conditions and reduces the fission power due to void reactivity feedback mechanism. The void behaviour affects not only T/H but also neutronics. 3D void behaviour in fuel assemblies is thus one of the most important factors in reactor safety. The needs should not be limited to the currently available macroscopic methods, but should be extended to next-generation analysis techniques that focus on more microscopic processes.

The Nuclear Power Engineering Corporation (NUPEC) performed a series of void measurement tests from 1987 to 1995 in Japan using full-size mock-up tests, where void fraction distribution and departure nucleate boiling (DNB) were measured under steady-

state and transient conditions. Part of the experimental data obtained in the NUPEC tests were used in the international OECD/NRC PWR Subchannel and Bundle Tests (PSBT) benchmark [5.1.11-1], [5.1.11-2] and [5.1.11-3] and are now provided by NEA's Data Bank. The following data could support the validation for 3D T/H codes including subchannel analysis codes:

- steady-state bundle void distribution;
- transient bundle void distribution;
- steady-state fluid temperature distribution;
- steady-state DNB;
- transient DNB.

5.1.11.2. Description of the test loop

The NUPEC test facility shown in Figure 5.36 consists of a high pressure and high-temperature recirculation loop, cooling loop, instrumentation and data recording systems. The recirculation loop consists of a test section, circulation pump, pre-heater, steam drum (acting as a pressuriser) and water mixer. The range of operating conditions for the facility is given in Table 5.8 and the operating range for the four transient tests are given in Table 5.9.

In the test section, three different test assemblies were used to model void distribution in a rod bundle. The bundles represented by these assemblies are described in Table 5.10. An electrically heated rod bundle was used to simulate a partial section and full-length of a PWR fuel assembly. Figure 5.37 shows the test section used for the rod bundle void measurements. The effective heated length is 3 658 mm. The measurements were performed at three axial elevations: upper 3 177 mm, middle 2 669 mm and lower 2 216 mm from the bottom of the heating section respectively. Two different radial power distributions, named A and B, were used in the void distribution measurement. An axial power distribution based on uniform or cosine shapes was used in the bundle tests.

The test assemblies used for the fluid temperature distribution and DNB measurement are described from Table 5.11 to Table 5.13. The DNB measurements were performed for full-length partial 5×5 and 6×6 array rod bundles, which simulate 17×17 PWR fuel assemblies. The heater rods used in these bundles the same type as those used in the bundles in the void distribution measurements. The four types of different radial power distributions, A to D, are used in the DNB measurement.

There were three types of spacer instruments used along the axial length in bundle test assemblies: simple spacer (SS), spacer with non-mixing vanes (NMVs) and spacer with mixing vanes (MVs). The simple spacer only has dimples, while NMV and MV have dimples and springs. The grids straps are made out of Inconel 600 alloy. Figure 5.38 provides 3D views of the simple spacer, non-mixing vane and mixing vane grids. These dimples provide a gap (0.1 mm) around each heating rod, which prevents bowing of these rods when they linearly expand at high temperatures. The insulator and the heater are made of Inconel and alumina respectively, and the gap between the heater and insulator could be assumed to be zero contact. The rod is a single-ended, grounded electrical heater rod, which simulates the heat generation from a fuel rod. Figure 5.39 provides a cross-sectional view of the heater rods with their dimensions.

Table 5.8. Range of NUPEC PWR test facility operating conditions

Quantity	Range
Pressure	4.9 – 16.6 MPa
Mass velocity	550 – 4150 kg/m ² s
Inlet coolant temperature	140 – 345°C

Table 5.9. Transient parameters of NUPEC PWR test facility

Transient scenario	Transient change
Depressurisation	-0.03 MPa/s
Temperature increase	1 °C/s
Flow reduction	-25 %/s
Power increase	15 %/s

Table 5.10. Test assembly in void distribution measurement

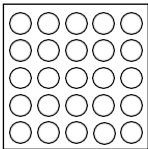
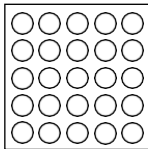
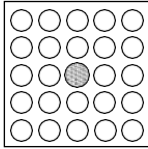
Item	Data		
Assembly			
	B5	B6	B7
Rods array	5×5	5×5	5×5
Number of heated rods	25	25	24
Number of thimble rods	0	0	1
Heated rod outer diameter (mm)	9.50	9.50	9.50
Thimble rod outer diameter (mm)	-	-	12.24
Heated rods pitch (mm)	12.60	12.60	12.60
Axial heated length (mm)	3 658	3 658	3 658
Flow channel inner width (mm)	64.9	64.9	64.9
Radial power shape	A	A	B
Axial power shape	Uniform	Cosine	Cosine
Number of MV spacers	7	7	7
Number of NMV spacers	2	2	2
Number of simple spacers	8	8	8
MV spacer location (mm)	471, 925, 1 378, 1 832, 2 285, 2 739, 3 247		
NMV spacer location (mm)	2.5, 3 755		
Simple spacer location (mm)	237, 698, 1 151, 1 605, 2 059, 2 512, 2 993, 3 501		

Table 5.11. Test assembly in liquid temperature distribution and DNB measurement - Assembly A0

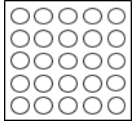
Item	Data
Assembly	
	A0
Rods array	5×5
Number of heated rods	25
Number of thimble rods	0
Heated rod outer diameter (mm)	9.50
Thimble rod outer diameter (mm)	-
Heated rods pitch (mm)	12.60
Axial heated length (mm)	3 658
Flow channel inner width (mm)	64.9
Radial power shape	A
Axial power shape	Uniform
Number of MV spacers	5
Number of NMV spacers	2
Number of simple spacers	6
MV spacer location (mm)	610, 1 219, 1 829, 2 438, 3 048
NMV spacer location (mm)	0, 3 658
Simple spacer location (mm)	305, 914, 1 524, 2 134, 2 743, 3 353

Table 5.12. Test assembly in liquid temperature distribution and DNB measurement - Assembly A1, A2 and A3

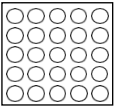
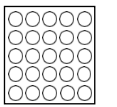
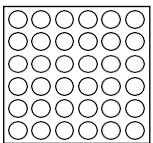
Item	Data		
Assembly			
	A1	A2	A3
Rods array	5×5	5×5	6×6
Number of heated rods	25	25	36
Number of thimble rods	0	0	0
Heated rod outer diameter (mm)	9.50	9.50	9.50
Thimble rod outer diameter (mm)	-	-	-
Heated rods pitch (mm)	12.60	12.60	12.60
Axial heated length (mm)	3 658	3 658	3 658
Flow channel inner width (mm)	64.9	64.9	77.5
Radial power shape	C	A	D
Axial power shape	Uniform	Uniform	Uniform
Number of MV spacers	7	7	7
Number of NMV spacer	2	2	2
Number of simple spacers	8	8	8
MV spacer location (mm)	457, 914, 1 372, 1 829, 2 286, 2 743, 3 200		
NMV spacer location (mm)	0, 3 658		
Simple spacer location (mm)	229, 686, 1 143, 1 600, 2 057, 2 515, 2 972, 3 429		

Table 5.13. Test assembly in liquid temperature distribution and DNB measurement - Assembly A4, A8, A11 and A12

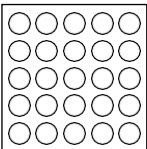
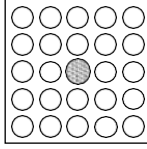
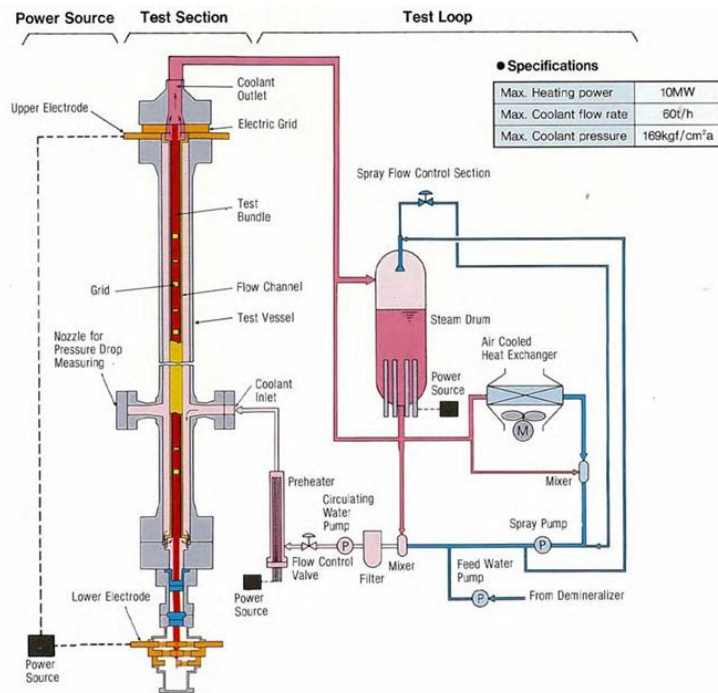
Item	Data	
Assembly		
	A4, A11	A8, A12
Rods array	5×5	5×5
Number of heated rods	25	24
Number of thimble rods	0	1
Heated rod outer diameter (mm)	9.50	9.50
Thimble rod outer diameter (mm)	-	12.24
Heated rods pitch (mm)	12.60	12.60
Axial heated length (mm)	3 658	3 658
Flow channel inner width (mm)	64.9	64.9
Radial power shape	A	B
Axial power shape	Cosine	Cosine
Number of MV spacers	7	7
Number of NMV spacer	2	2
Number of simple spacers	8	8
MV spacer location (mm)	471, 925, 1 378, 1 832, 2 285, 2 739, 3 247	
NMV spacer location (mm)	2.5, 3 755	
Simple spacer location (mm)	237, 698, 1 151, 1 605, 2 059, 2 512, 2 993, 3 501	

Figure 5.36. System diagram of NUPEC PWR test



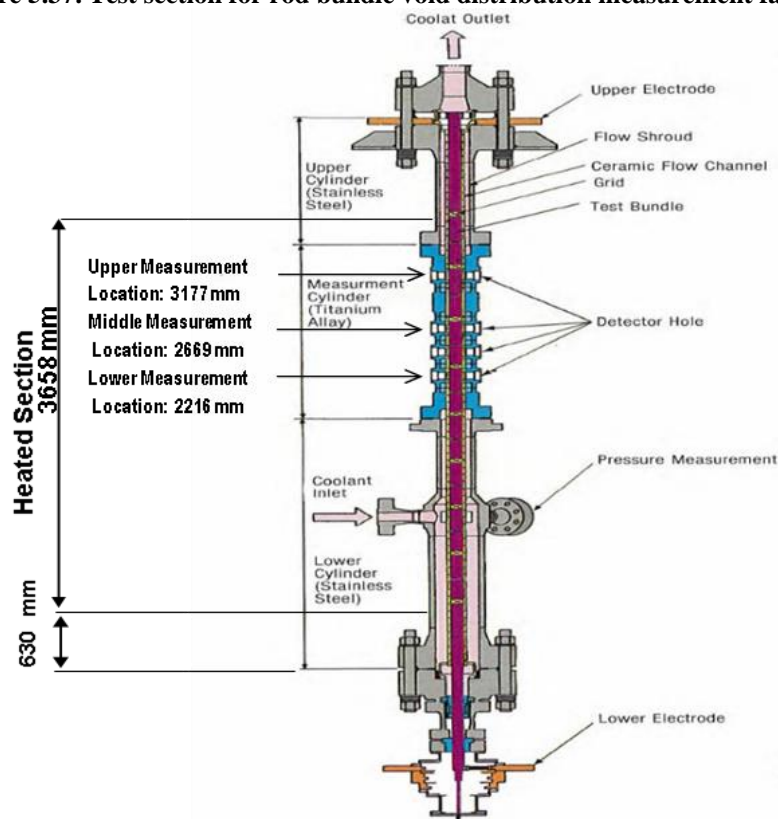
Source: NEA, 2012.

Instrumentation and measurements

The detailed explanation for the void fraction measurement procedure is provided in references [5.1.11-4] and [5.1.11-5]. Figure 5.40 shows the procedure used to perform the void fraction measurements. The void measurement systems consist of gamma-ray sources, detectors, collimators and signal processing units. The attenuation of the gamma-rays, which depends on the void fraction, was determined by the count rate of the signal processing. As shown in the bottom half of Figure 5.40, a multi-beam system was used to measure each chordal averaged subchannel void fraction of the rod bundle. Six transmission data of x -direction and six transmission data of y -direction between the rod and rod/channel wall were used to reconstruct the void fraction of the 36 subchannels by an iterative method. The subchannel averaged void fractions in the rod bundle tests, which were determined based on the relationships between subchannel averaged void fraction and chordal averaged void fraction that was obtained in the single subchannel tests. The CT scanner system operated by translate/rotate method was used to define the subchannel averaged void fraction in the single subchannel tests. The measurements were performed simultaneously at three axial elevations. Table 5.14 describes the sources of error in the void measurement process (these values correspond to one standard deviation, one σ). Table 5.15 shows the time required to perform the void fraction measurements.

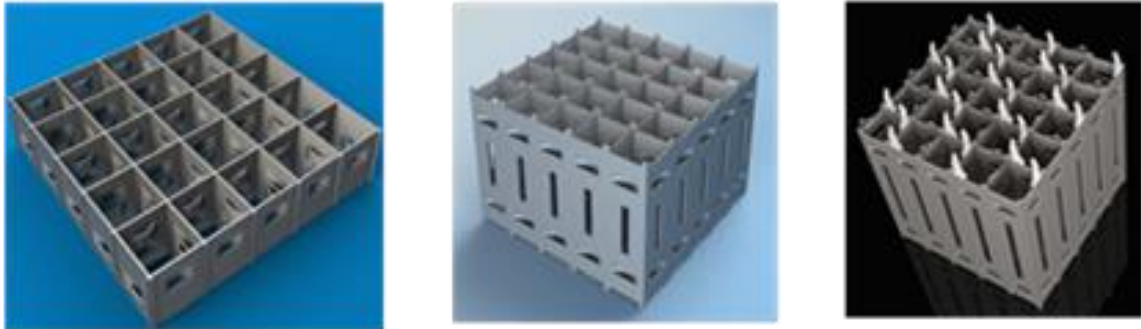
The exit fluid temperatures were measured by the thermocouples at each subchannel of 457 mm from the top of heating section. Ten pressure taps inserted into the rod bundle measured the pressure.

Figure 5.37. Test section for rod bundle void distribution measurement facility



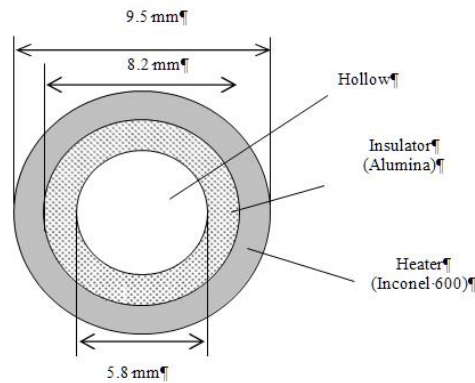
Source: NEA, 2012.

Figure 5.38. View of simple spacer grid (left), non-mixing vane spacer grid (centre) and mixing vane spacer grid (right)



Source: NEA, 2012.

Figure 5.39. Cross-sectional view heater rod



Source: NEA, 2012.

The bundle power was gradually increased in fine steps for the steady-state and transient DNB measurement to the expected vicinity of DNB, which was based on previous analysis operator experience. The onset of DNB was confirmed by a rod temperature rise that was greater than 11°C , as measured by the thermocouples whose location is shown in Figure 5.41. The DNB power is defined as the power corresponding to the step immediately preceding the step during which this temperature rise is seen. Table 5.16 shows the estimated accuracies of different process parameters for the DNB measurements.

Table 5.14. Error sources for void measurements

Error source		Chordal averaged		CT averaged
		Steady-state	Transient	
γ -ray measurement	Effect of surrounding condition (magnetic-field and temperature) on measurement system	0.1%	0.1%	0.1%
	Randomness of γ -ray source decay	0.02%	0.2%	0.1%
	Correction error due to background	0.0%	0.0%	0.0%
	Correction error due to counting loss	<0.5%	<0.5%	<0.1%
	Calibration error	0.1%	0.1%	0.1%
	Correction error due to attenuation by surrounding water	0.0%	0.0%	-
	Correction error due to scattering from multi γ -rays	<0.2%	<0.2%	-
	Total	<0.55%	<0.6%	<0.2%
Subchannel density	Transfer to density	<9 kg/m ³	<10 kg/m ³	<15 kg/m ³
	Distribution error to Subchannel	<5 kg/m ³	<5 kg/m ³	-
Correlation error from Chordal averaged to CT averaged		<6 kg/m ³	<6 kg/m ³	-
Subchannel density		<20 kg/m ³	<21 kg/m ³	<15 kg/m ³
Subchannel void*		0.040	0.042	0.030
Uncertainty (1s)		4 %	5 %	3 %

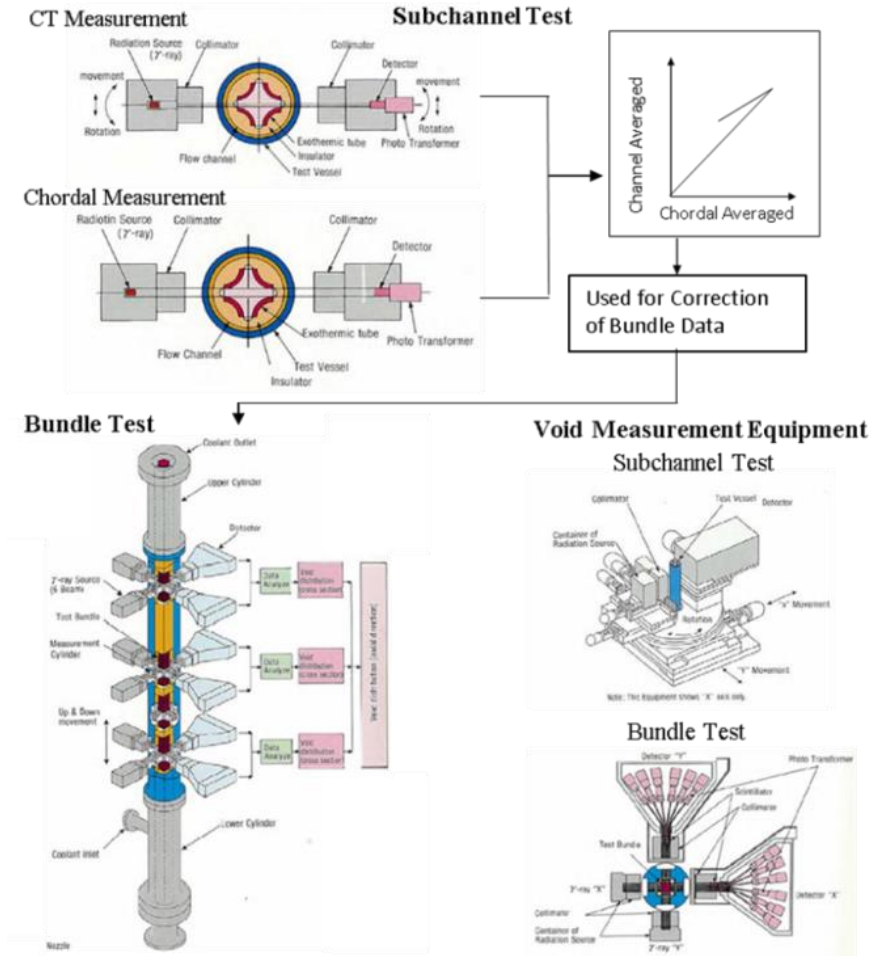
Table 5.15. Time required to perform void fraction measurements

Item		CT measurement	Chordal measurement
Steady-state	Time needed	5 s/step × T ₃₃ × R ₁₇ step (it takes 2 h)	100 s sampling cycle 0.1 s
	Measurement	2 times	3 times
Transient	Time needed	-	200 s
	Measurement	-	1 time

Table 5.16. Estimated accuracy for DNB measurements

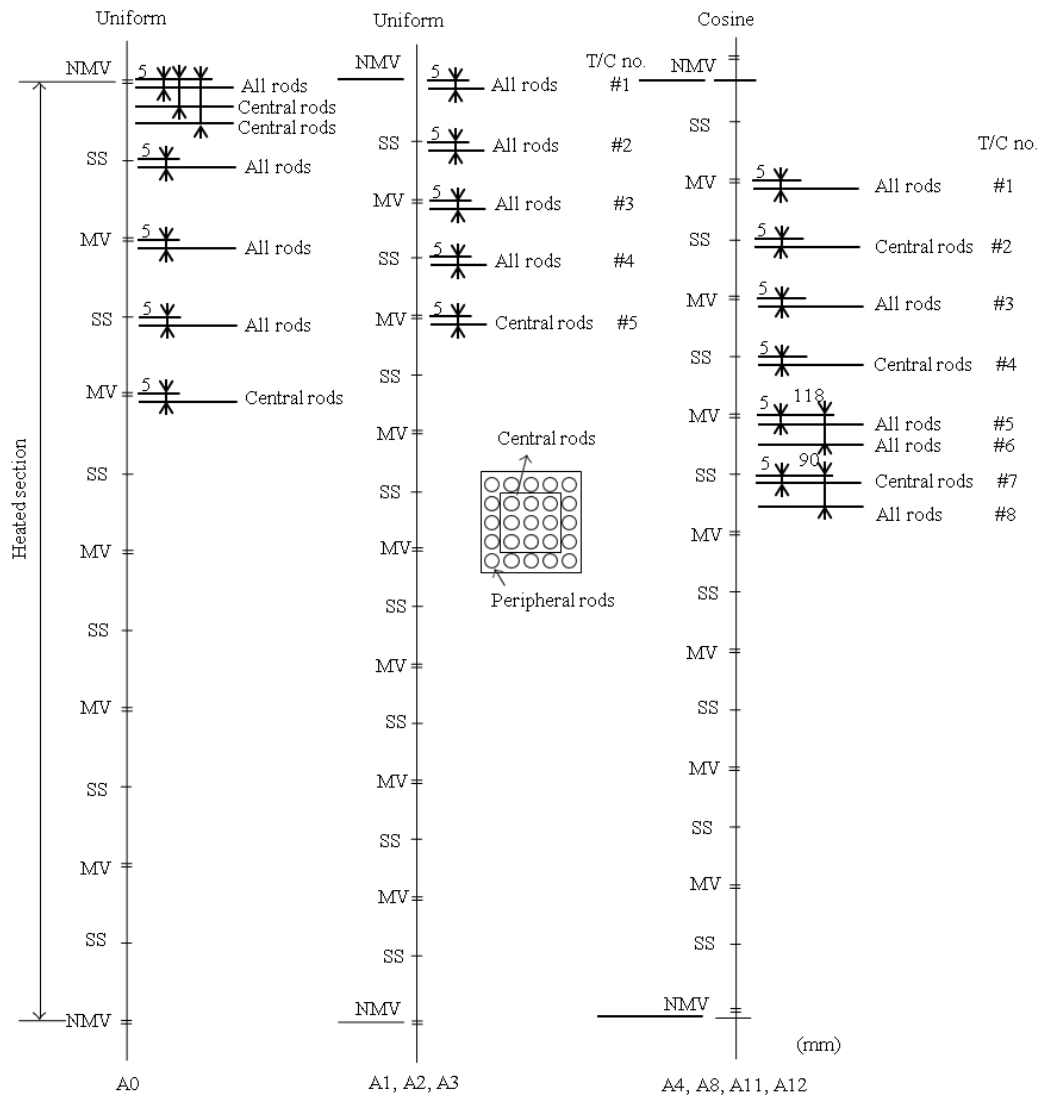
Quantity	Accuracy
Pressure	1 %
Flow	1.5%
Power	1 %
Fluid temperature	1 Celsius

Figure 5.40. Void fraction measurement procedure



Source: NEA, 2012.

Figure 5.41. Location of thermocouples for test assemblies



Source: NEA, 2012.

5.1.11.3. Tests performed

The available data for steady-state bundle void distribution include void fraction (chordal averaged) at three axial elevations by a X-ray densitometer. The averaging is over the four central subchannels of the bundle. There are four test series (test series 5, 6, 7 and 8) providing data. Test assemblies B5, B6 and B7 shown in Table 5.11 were used in test series 5, 6 and 7 respectively. The same assembly type was used in test series 5 and test series 8. Test cases performed at similar conditions can therefore be used to assess the repeatability of the measurements. The test condition's range is shown in Table 5.17.

The available data for transient bundle void fraction distribution include the void fraction (chordal averaged) at three axial elevations by X-ray densitometer. The averaging is over the four central subchannels of the bundle. There are three test series (test series 5T, 6T and 7T) providing data. Test assemblies B5, B6 and B7 were used in test series 5T, 6T and 7T respectively. Four transient scenarios (temperature increase, power increase, depressurisation and flow reduction) were simulated in each test series, yielding 12 total

test cases. The pressure, mass flux, power and inlet temperature were varied in each test case to simulate each transient scenario. The initial condition is shown in Table 5.18.

The available data for steady-state fluid temperature distribution were taken by the thermocouples for each subchannel in the bundle assembly at the exit of the test section. Test assembly A1 was used for this measurement. The test condition's range is shown in Table 5.19.

The available data for steady-state DNB include the axial and radial locations of DNB in the bundle, as well as the power at which DNB first occurred. There are six test series (test series 0, 2, 3, 4, 8 and 13) performed for the available data. Test assemblies A0, A2, A3, A4, A8 and A13 were used in test series 0, 2, 3, 4, 8 and 13 respectively. The test condition's range is shown in Table 5.19.

The available data for transient DNB include the transient time at which DNB was first detected in the rod bundle. There are two test series (test series 11T and 12T) providing these type of data. Test assemblies A11 and A12 were used in test series 11T and 12T, respectively. Four transient scenarios (temperature increase, power increase, depressurisation and flow reduction) were simulated in each test series, yielding eight total test cases. The pressure, mass flux, power and inlet temperature were varied in each test case to simulate each transient scenario. The initial condition is shown in Table 5.18-21.

Table 5.17. Range of test conditions for steady-state bundle void distribution measurement

Quantity	Test condition
Pressure (MPa)	4.90, 7.36, 9.81, 12.26, 14.71, 16.67 (Range: 4.791 – 16.59)
Mass flux (kg/m2s)	556, 1 389, 2 222, 3 056, 4 167 (Range: 556 – 4 256)
Inlet coolant temperature (°C)	Range: 143.4 – 322
Power (MW)	1, 1.5, 2, 2.5, 3, 3.3, 3.5, 3.8, 4 (Range: 0.957 – 4.032)

Table 5.18. Range of initial test condition for transient bundle void distribution measurement

Test series	Assembly	Initial conditions				Simulated transients
		Pressure (kg/cm2a)	Mass flux (106kg/m2h)	Power (MW)	Inlet temperature (°C)	
5T	B5	15.12	3 319	2.282	300.4	Power increase
		15.08	3 314	2.244	301.2	Flow reduction
		15.00	3 311	2.236	300.4	Depressurisation
		14.96	3 317	2.230	301.7	Temperature increase
6T	B6	15.51	3 208	2.621	288.1	Power increase
		15.53	3 342	2.574	288.8	Flow reduction
		15.16	3 339	2.556	288.2	Depressurisation
		15.42	3 311	2.603	288.8	Temperature increase
7T	B7	15.51	3 339	2.500	291.9	Power increase
		15.50	3 344	2.405	292.0	Flow reduction
		15.20	3 331	2.577	291.8	Depressurisation
		15.57	3 331	2.496	290.2	Temperature increase

Table 5.19. Range of test condition for steady-state fluid temperature distribution measurement

Quantity	Test condition
Pressure (MPa)	4.90, 9.81, 14.71, 16.67 (Range: 4.90 – 16.59)
Mass flux (kg/m ² s)	138.9, 194.4, 277.8, 555.6, 1 388.9, 3 055.6 (Range: 122.2 – 4744)
Inlet Coolant Temperature (°C)	Range: 84.5 – 289.2
Power (MW)	0.1, 0.25, 0.4, 0.5, 0.7, 1, 1.25, 1.5, 2.1, 2.7, 3.4 (Range: 0.11 – 3.44)

Table 5.20. Range of test condition for steady-state DNB measurement

Quantity	Range
Pressure (MPa)	4.903, 7.355, 9.807, 12.26, 13.73, 14.71, 15.69, 16.67 (Range: 4.844 – 16.80)
Mass flux (kg/m ² s)	277.8, 555.6, 1 389, 2 222, 3 056, 3 333, 3 889, 4 722 (Range: 316.7 – 4 944)
Inlet coolant temperature (°C)	Range: 122.6 – 334.5

Table 5.21. Range of initial test condition for transient DNB measurement

Test series	Assembly	Initial conditions				Transients
		Power (MW)	Mass flux (kg/m ² s)	Pressure (MPa)	Inlet temperature (°C)	
11T	A4	2.50	3 106	15.32	291.0	Power increase
		2.50	3 108	15.31	293.1	Flow reduction
		2.52	3 133	15.33	291.7	Depressurisation
		2.48	3 067	15.16	291.6	Temperature increase
12T	A8	2.51	3 167	15.31	291.3	Power increase
		2.51	3 253	15.33	292.5	Flow reduction
		2.50	3 172	15.32	290.6	Depressurisation
		2.50	3 161	15.28	291.2	Temperature increase

5.1.11.4. Application for system code validation

Several exercises for the prediction of participant's analysis codes were performed in the PSBT benchmark [5.1.11-1]. Ten participants used subchannel analysis codes in the steady-state bundle void distribution exercise, while one participant used a porous media code and six participants used system analysis codes. It was noted that the codes consistently over-predicted the void fraction at the lower elevation in the bundle. However, the results were generally improved at higher elevations, although there was some under-prediction. The majority of the codes also consistently predicted the correct thermal equilibrium quality at the lower elevations, with only a few exceptions that over-predicted the quality. All codes tended to under-predict the quality at the upper bundle elevations.

In the transient bundle void distribution exercise, nine participants used subchannel analysis codes, while one participant used a porous media code and six participants used system analysis codes. A slight time shift can be seen in the void fraction results when they are compared to the experimental data for the cases of temperature increase. It has been suggested that the structure between the downcomer and test section was not truly adiabatic and consequently there was some heat transfer between these regions that produced this shift. Otherwise, the codes generally predicting the void fraction throughout the different transients well, yielding the best results at the highest elevation in the bundle and the worst at the lowest elevation. Some codes consistently underestimated the void fraction, especially at higher elevations. There was also consistent under-prediction of void fraction at higher elevations for the depressurisation cases.

In the fluid temperature distribution exercise, six participants used subchannel analysis codes, while one participant used a porous media code and one participant used a system analysis code. The codes could not accurately model the fluid temperature at the right side of the bundle and over- or under-predicted, in several cases significantly. These conditions,

coupled with the strong power gradient across the bundle, create an environment that is difficult for the codes to model accurately.

In the steady-state DNB exercise, six participants used subchannel analysis codes, while one participant used a porous media code and two participants used system analysis codes. The various DNB modelling approaches, such as Groeneveld look-up tables and the Shah correlation, were used in the code for this exercise. The codes were generally able to calculate the DNB power satisfactorily and there was no observable bias across the test series. There was considerable variation in the predictions of axial elevation for first detected DNB. The measured data represent the first thermocouple at which DNB was detected. It is therefore the latest (axially speaking) point at which the onset of DNB would have occurred and is not an exact value because DNB could have occurred lower on the bundle.

In the transient DNB exercise, six participants used subchannel analysis codes, while one participant used a porous media code and one participant used a system analysis code. The codes could not predict the time of DNB during the simulated transients. Most of the codes calculated earlier DNB occurrence for both bundle types (with a thimble rod in the central region in test series 11 and without it in test series 12).

Main advantages and drawbacks of the facility

Bundle void distributions in the steady-state and transient condition were measured in PSBT. However, the void fraction averaged over the four central subchannels of the bundle was included in the data provided in the PSBT benchmark.

5.1.12. BFBT

5.1.12.1. Objective of the experiment

There have been significant efforts made in the past decades to achieve a realistic simulation of BWR fuel bundles' boiling transition (BT). The detailed void distribution inside the fuel bundle and crossflow through the subchannel gap has been considered an important factor of the BT. Subchannel analysis codes can predict the detailed void distribution and dryout process (disappearance of the liquid film on the fuel rod surface) by considering entrainment, deposition and evaporation. Subchannel analysis codes should be validated using experimental data on a subchannel basis.

NUPEC performed a series of void measurement tests from 1987 to 1995 using full-size mock-up tests [5.1.12-1]. They visualised the void distribution at the mesh size as much smaller than the subchannel under actual plant conditions. Steady-state and transient critical power were also measured. Some of the experimental data obtained by the NUPEC tests were used in the international OECD/NRC BWR Full-size Fine-Mesh Bundle Test (BFBT) benchmark [5.1.12-1] and are now in NEA's Data Bank. The following data could support validation for 3D T/H codes, including subchannel analysis codes:

- steady-state bundle void distribution;
- transient bundle averaged void fraction;
- steady-state critical power;
- transient critical power.

5.1.12.2. Description of the test loop

Figure 5.43 shows a diagram of the test loop. The maximum operating conditions for the facility are 10.3 MPa in pressure, 315°C in temperature, 12 MW in test power and 75 t/h in flow rate. The test facility has the capability for a full range of steady-state testing over BWR operating conditions and can also simulate time-dependent characteristics of complicated BWR operational transients. The test section, as shown in Figure 5.44, consists of a pressure vessel, simulated flow channel and electrodes. The simulated full-scale BWR fuel assembly was installed within the vessel.

Figure 5.45 shows the cross-sectional view of the heated rod. The rod is a single-ended, grounded electrical heater rod and represents the nuclear fuel rod. This geometry treatment does not affect the steady-state calculation. The thermal time constant for the transient may affect the results. Therefore, in addition to the demonstrated geometrical data, a thermal time constant of about five s is specified as a reference value. The heater rod structure is shown in Table 5.22.

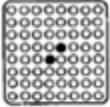
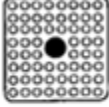
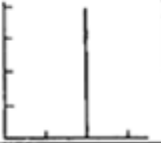
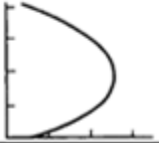
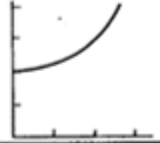
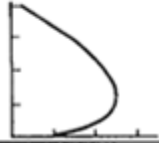
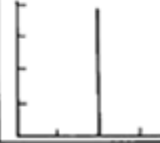
In the void distribution measurements, two types of BWR assemblies are simulated in a full-length test facility: an early 8×8 fuel bundle and a 8×8 high burn-up bundle, as shown in Figure 5.42. Three sub-types of test bundle 0, namely 0-1, 0-2 and 0-3, were used to examine the effects of radial power distribution on the void fraction distribution. The radial arrangements of heated and unheated rods are shown in Figure 5.46. Test assembly 0-1 simulates a current BWR fuel assembly and has two unheated rods. Test assemblies 0-2 and 0-3 have four and nine unheated rods respectively. Test assembly types 1, 2 and 3 are like assembly type 0-1 with two unheated rods, but with a different axial heated length and different axial power shapes. Three combinations of high burn-up assemblies with different radial and axial power shapes, namely C2A, C2B and C3, were utilised for the critical power measurements shown in Table 5.23.

Spacers generally have a beneficial effect on critical power in typical BWR assemblies. There are two types of spacers used in the experiments: a ferrule type and a grid type. The grid type of spacers is applied to the early 8×8 assemblies (assembly types 0, 1, 2 and 3). The ferrule type is applied to the high burn-up 8×8 assemblies (assembly types 4, C2A, C2B and C3). Figure 5.47 shows a different view of grid spacer design. It is not a design drawing and therefore there may be some disparity from the symmetry on the rod arrangement. Figure 5.47 also shows different views of the ferrule spacer, which was used for the high burn-up fuel assembly design.

Table 5.22. Heater rod structure

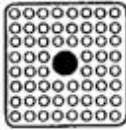
Item	Data	
Heater	Outer diameter (mm)	7.3
	Material	Nichrome
Insulator	Outer diameter (mm)	9.7
	Material	Boron Nitride
Cladding	Thickness (mm)	1.3
	Material	Inconel 600/Beryllium

Figure 5.42. Test assembly and radial power distribution for void distribution measurements

Test assembly No.	0	1	2	3	4
Fuel Type		Current use 8x8 			High burnup 8x8 
Planar power profile	Uniform	Simulated design profile	Simulated design profile	Simulated design profile	Simulated design profile
Axial power profile	Uniform	Cosine	Half-cosine	Inlet peak	Uniform
Heated length	Full	Full	Half	Full	Full
Axial power distribution Axial Power					

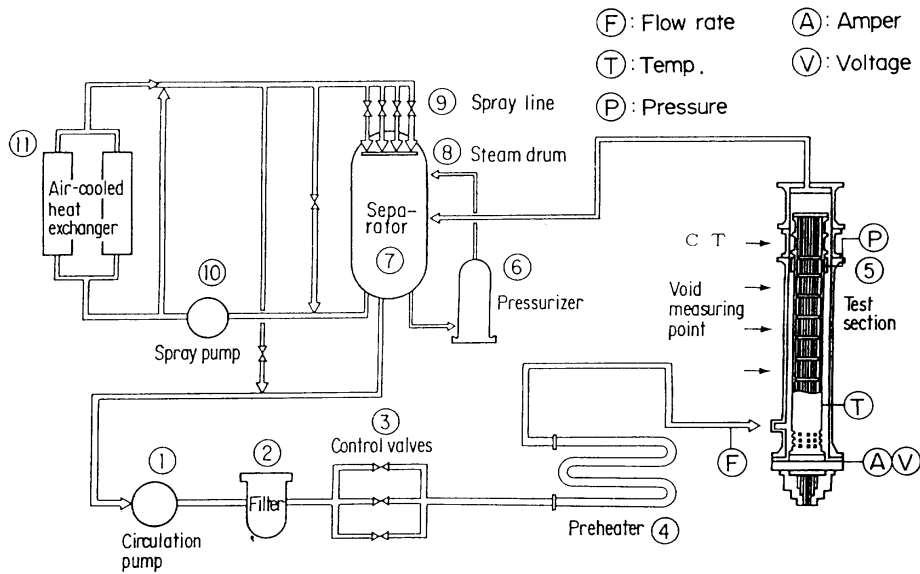
Source: NEA, 2005.

Table 5.23. Test assembly types for critical power measurements

Test item	Critical power test		
	C2A	C2B	C3
Fuel type	High burn-up 8 × 8		
Axial power shape	Cosine	Cosine	Inlet peak
Radial power shape	A	B	A

A – Simulation pattern for beginning of operation.

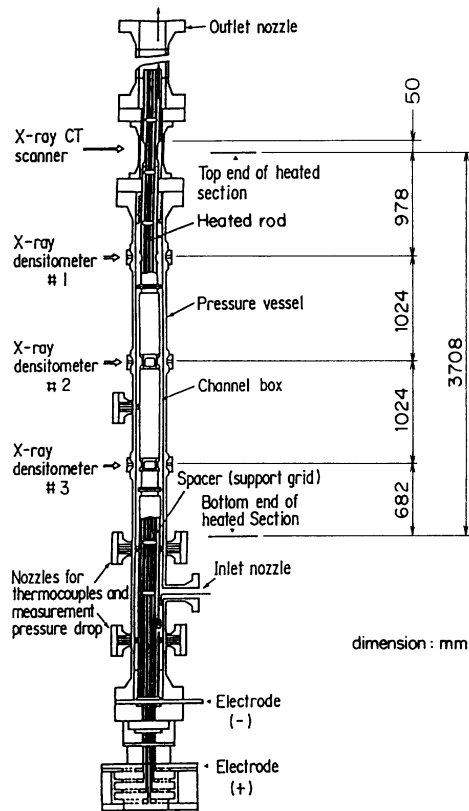
B – Simulation pattern for middle of operation

Figure 5.43. System diagram of test facility for NUPEC rod bundle test series

Source: NEA, 2005.

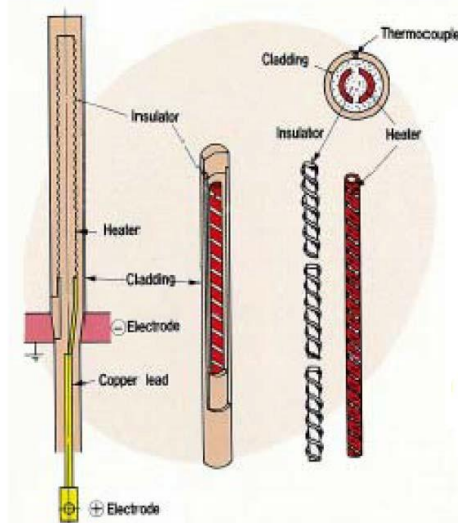
As shown in Figure 5.48 (a), two types of void distribution measurement systems were employed: an X-ray CT scanner and an X-ray densitometer. Fine-mesh void distributions were measured under steady-state conditions using the X-ray CT scanner, which was located 50 mm above the heated length. The system consisted of an X-ray tube and 512 detectors. Figure 5.48 (b) shows the void fraction measuring section, where the pressure vessel was made of titanium (Ti). The X-ray CT scanner was also used for transient void measurements called chordal averaged void fraction measurements [5.1.12-2]. During the transient, the X-ray CT scanner is not rotated but fixed. The X-ray densitometer measurements were performed at several axial elevations with relatively large uncertainty. Table 5.25 shows the X-ray CT scanner's basic specifications. Table 5.26 shows the X-ray densitometer's basic specifications. The void fraction measurement methods are shown in Figure 5.49. The cross-sectional averaged transient void distributions were measured with the X-ray densitometer. During the transient void measurements, the X-ray densitometer was fixed (not rotated) at a given axial position (Figure 5.48). The measurement was repeated nine times while changing the axial location of the densitometer along the heated length.

Figure 5.44. Cross-sectional view of test section



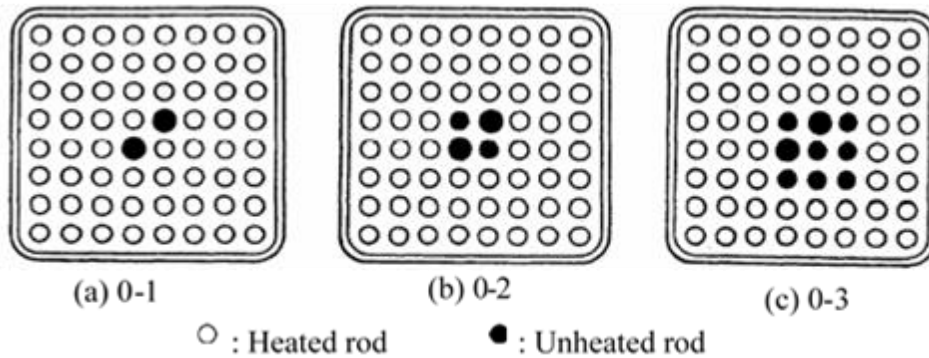
Source: NEA, 2005.

Figure 5.45. Cross-sectional view of heater rod



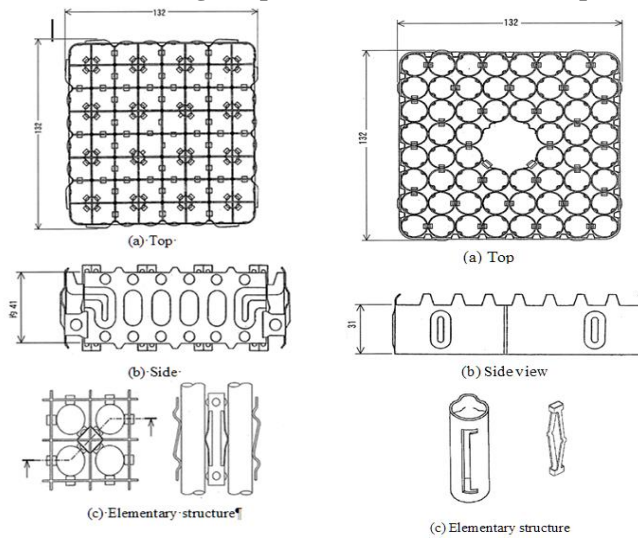
Source: NEA, 2005.

Figure 5.46. Unheated rods arrangements in test assembly type 0



Source: NEA, 2005.

Figure 5.47. Schematic of the grid spacer (left) and the ferrule spacer design (right)



Source: NEA, 2005.

Table 5.26 shows the estimated measurement accuracy. Three types of void fraction measurements were carried out: a local void fraction on a 0.3 mm×0.3 mm square pixel element; a subchannel averaged void fraction, which is averaged over more than 400 pixel elements; and a cross-sectional averaged void fraction, which is averaged over more than 105 pixel elements. The accuracy of these void fraction measurements depended on the X-ray source’s photon statistics, detector non-linearity and accuracy of the known fluid condition (temperature and pressure) measurements.

The heater rods’ surface temperatures were monitored at positions just upstream of the spacers by chromel-alumel thermocouples, which were located on the outer surface of the heater rod cladding. The thermocouples have a diameter of 0.5 mm. The rod surface temperature was also monitored at several locations, as depicted in Figure 5.50 (C2A assembly being the example). The critical power was measured while slowly increasing the bundle power and monitoring the individual heater rod thermocouple signals. The critical power was defined when the peak rod surface temperature became 14°C higher than the steady-state temperature level, before the dryout occurred.

Table 5.24. Specification of X-ray CT scanner

Item	Specification
Method of scanning	360 ⁰ rotation with pulse X-rays
Type of X-ray beam	Fan-shaped X-ray beam of 34 ⁰ radiation angle
Voltage of X-ray tube	Max. 120 kV
Current	Max 400 mA
Scanning time	15 s
Scanning region	D='300' mm
Dimensions of reconstruction element	0.3 mm × 0.3 mm

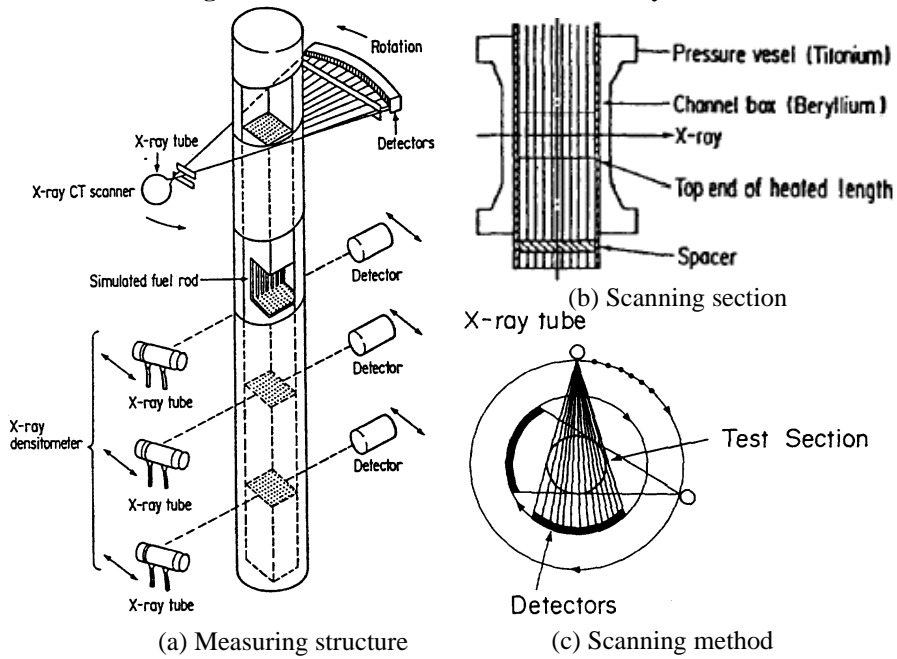
Table 5.25. Specification of X-ray densitometer

Item	Specification
Method of measurement	Continuous X-ray at fixed position
Type of X-ray beam	Pencil type beam
Voltage of X-ray tube	Max. 160 kV
Current	Approx. 19 mA at 160 kV
Sampling time	Max. 60 s (Variable)
Synchronisation	3 X-ray densitometers synchronise with X-ray CT scanner for data gathering

Table 5.26. Estimated accuracy of main process parameters for void distribution measurements

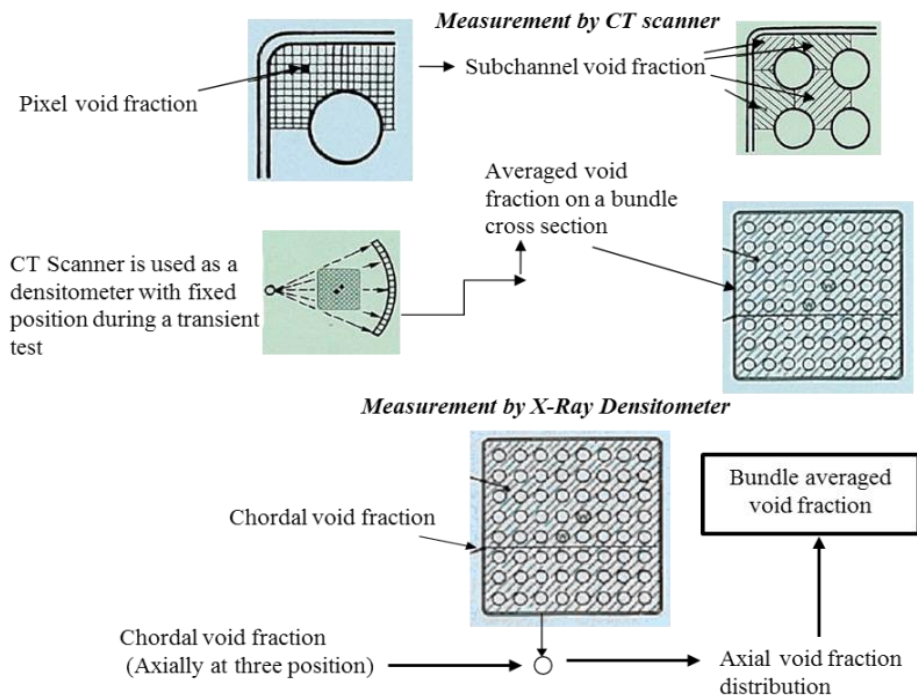
Quantity	Accuracy
Pressure	1%
Flow	1%
Power	1.5%
Inlet fluid temperature	1.5°C
X-ray CT scanner	
Local void fraction	8%
Subchannel void fraction	3%
Cross-sectional void fraction	2%
Nominal spatial resolution	0.3 mm×0.3 mm
Scanning time	15 seconds
X-ray densitometer	
Sampling time	Max. 60 seconds

Figure 5.48. Void fraction measurement system

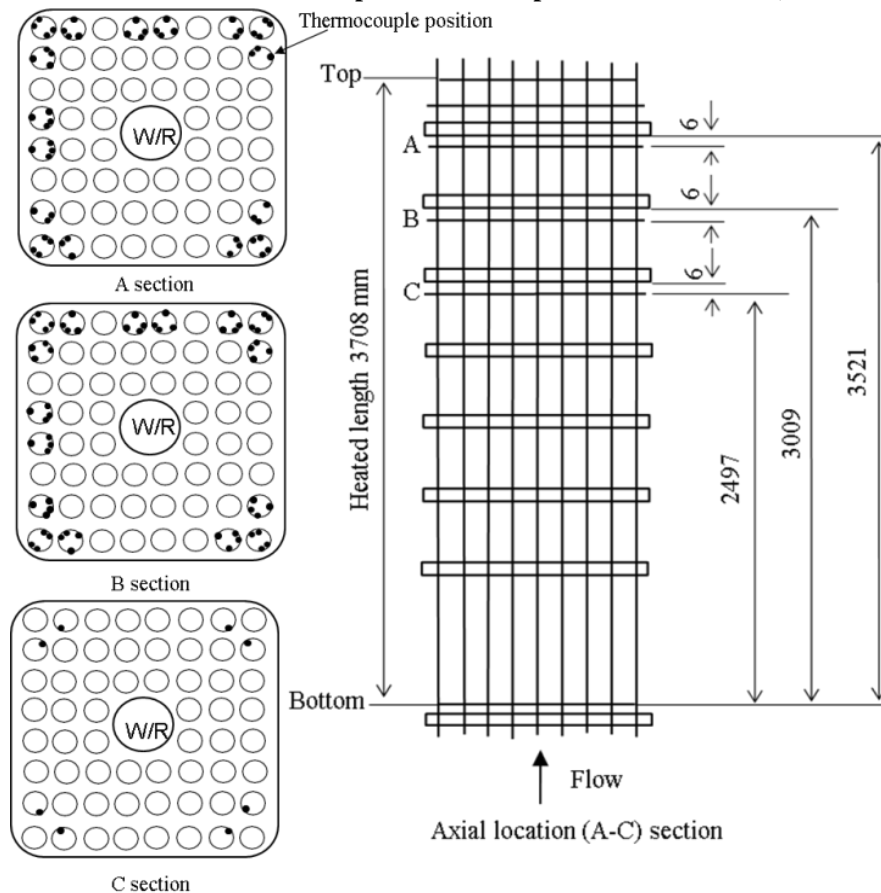


Source: NEA, 2005.

Figure 5.49. Void fraction measurement methods



Source: NEA, 2005.

Figure 5.50. Location of thermocouples for critical power measurement (C2A assembly)

Source: NEA, 2005.

5.1.12.3. Tests performed

The available data for steady-state void distribution include time and space averaged void distribution matrix in subchannel mesh size and raw image data (which has a resolution as small as $0.3\text{ mm} \times 0.3\text{ mm}$) of void fraction. Test assemblies 0, 1, 2, 3 and 4 were used for the steady-state void distribution measurement. The test condition is shown in Table 5.27.

The available data for transient bundle averaged void fraction include time histories of cross-sectional averaged void fraction in each axial level during transient. Two tests were performed to simulate turbine trip without bypass and recirculation pump trip, respectively. Test assembly 4 was used for the test. The pressure, power, flow rate and inlet temperature were varied in each test case to simulate each transient scenario. The initial condition is shown in Table 5.28.

The available data for steady-state critical power include critical power and the elevation of the BT. Test assemblies C2A, C2B and C3 were used for the steady-state critical power measurement. The test condition is shown in Table 5.29.

The available data for transient critical power include the time histories of cladding temperature where the BT occurred, BT timing, timing of rewetting and peak cladding temperature during transient. Test assemblies C2A and C3 were used for the test. Two transient scenarios (turbine trip without bypass and recirculation pump trip) were simulated in each test series, yielding 12 total 4 test cases. The pressure, power, flow rate and inlet temperature were varied in each test case to simulate each transient scenario. The initial condition is shown in Table 5.30.

Table 5.27. Range of test condition for steady-state bundle void distribution measurement

Quantity	Test condition
Pressure (MPa)	1.0, 3.9, 7.2, 8.6,
Flow rate (t/h)	10, 20, 30, 45, 55, 70,
Inlet subcooling (kJ/kg)	20.9, 50.2, 126
Exit quality (%)	2, 5, 8, 12, 18, 25

Table 5.28. Range of test condition for steady-state bundle void distribution measurement

Assembly		Initial conditions				Transients	
		Pressure (MPa)	Power (MW)	Flow rate (t/h)	Inlet temp. (Celsius)		Outlet quality %
4	7.16	4.5	55	279	18	Turbine trip without bypass	
4	7.2	4.5	55	279	18	Recirculation pump trip	

Table 5.29. Range of test condition for steady-state bundle void distribution measurement

Quantity	Test condition
Pressure (MPa)	5.5, 7.2, 8.6
Flow rate (t/h)	10, 20, 30, 45, 55, 60, 65
Inlet subcooling (kJ/kg)	25, 50, 84, 104, 126

Table 5.30. Range of test condition for steady-state bundle void distribution measurement

Assembly		Initial conditions/experimental conditions				Transients
		Pressure (MPa)	Power (MW)	Flow rate (t/h)	Inlet enthalpy (kJ/kg)	
C2A	7.2/7.136	6.2~8.5	45/42	1 217~1 227	Turbine bypass trip without bypass	
C2A	7.2/7.274	6.2~8.5	45/46.2	1 217~1 227	Recirculation pump trip	
C3	7.2/7.136	6.2~8.5	45/42	1 217~1 227	Turbine bypass trip without bypass	
					without	
C3	7.2/7.274	6.2~8.5	45/46.2	1 217~1 227	Recirculation pump trip	

5.1.12.4. Application for system code validation

Several exercises for the prediction of participant's analysis codes were performed in the BFBT benchmark. CFD codes and 1D system analysis codes were used in the exercise of steady-state bundle void distribution, subchannel analysis codes to predict subchannel void fractions and bundle average void fraction. Scatters were observed in calculations of the lower void fraction, where bubbly to large bubble/slug flow were expected. The codes have difficulties predicting the void distribution near unheated structures (housing and water rods). It was shown that a crossflow model of subchannel analysis codes affected the measured data prediction.

In the exercise of transient bundle averaged void fraction, subchannel analysis codes and 1D system analysis codes were used to predict transient void fraction in scenarios of a turbine trip without bypass and a recirculation pump trip. The codes demonstrated capabilities for reproducing the transient behaviours of the bundle average void fraction for

both transient scenarios. Code-to-code comparisons were performed to provide snapshots of the predicted void fraction at a subchannel basis in the exercise.

In the exercise of steady-state critical power, subchannel analysis codes and 1D system analysis codes were used to predict critical power and BT elevations in the tests. The accuracy of the critical power predictions on critical power was affected by liquid film thickness modelling, onset of annular-mist flow criteria, droplet entrainment and deposition models, spacer grid effects and crossflow.

In the exercise of transient critical power, 1D system analysis codes were used to predict the time histories of cladding temperature in scenarios of a turbine trip without bypass and a recirculation pump trip. The codes could reproduce the transient behaviours of overall rod surface temperature at thermocouples in both scenarios.

The validation for subchannel analysis code is presented in [5.1.12-3].

Main advantages and drawbacks of the facility

In the BFBT, local void fractions on a 0.3 mm×0.3 mm square pixel element were measured by the X-ray CT scanner. While the X-ray densimeter could measure cross-sectional averaged void distributions in the steady-state and transient condition, the scanner had some systematic error. When the vapour bubbles had a higher concentration near the walls than the subchannel centre (low void fraction), the average void fraction was underestimated. When vapour concentration in the subchannel centre was higher than near the walls (high void fraction, slug and churn flow regime), the average void fraction was overestimated.

5.1.13. Other test facilities

5.1.13.1. PIERO

The PIERO experiment studied lower plenum voiding, which occurs at the end of a large break LOCA depressurisation phase in a PWR, when the steam generated in the reactor core flows out of the bottom of the core through the lower plenum towards the downcomer and the broken leg. If the steam velocity is high enough, it can drag water from the lower plenum and partially empty it.

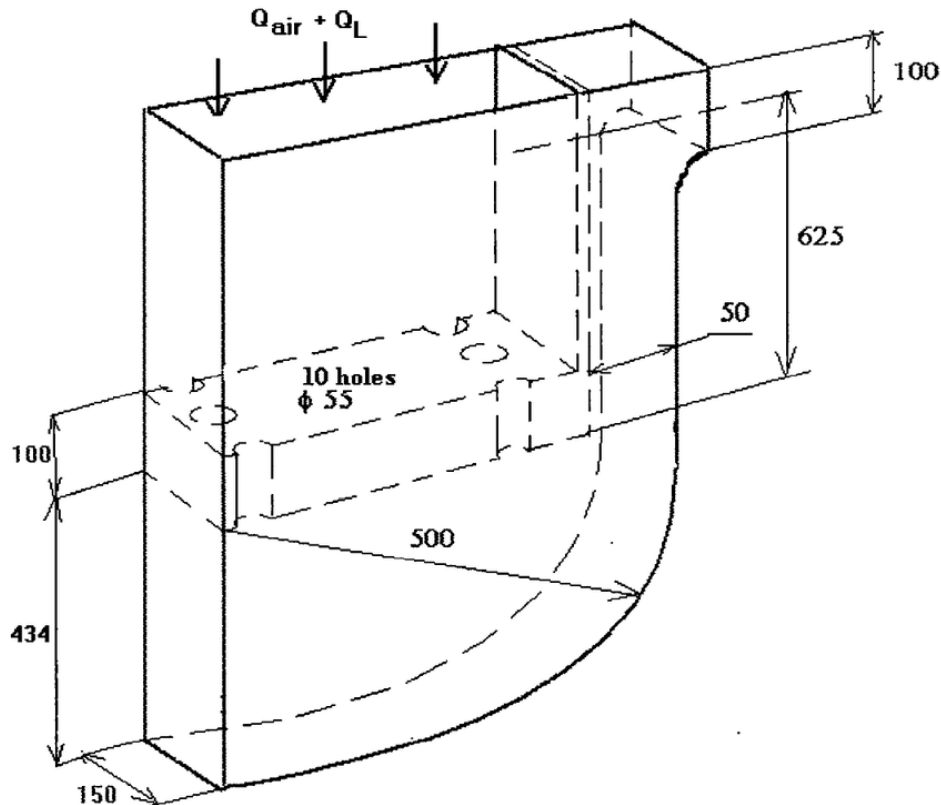
The PIERO test section, developed at CEA-Grenoble and now dismantled, is a half slab of a 1/4 scale vessel representing the lower plenum and the downcomer of a French PWR-type reactor. The test section represents a 2D cross-section of the lower plenum and downcomer. The width of the test section is 150 mm. The core lower plate is 100 mm thick with ten holes (55 mm inner diameter). The lower face of the lower core plate is 434 mm from the bottom of the lower plenum. The downcomer is 150 mm wide, 50 mm deep and 695 mm high. The bottom of the downcomer 625 mm under the exit of lower plenum (see Figure 5.51).

The gas flow or mist flow expelled from the core towards the lower plenum at the end of the blowdown phase is simulated by an air-water mixture flow rate under atmospheric pressure. The air and water are injected at the top of the test section above the core lower plate. The air or air-water mixture flowrate varies from 50 to 3 500 m³/h. Liquid is entrained (or not, depending on the conditions of the run) from the lower plenum to the downcomer.

For each run, experimental data are composed of:

- The inlet air flowrate (measured with less than 5% error).
- The liquid fraction, deduced from the water flowrate (the error of the liquid fraction is less than 1%).
- The level in the lower plenum after stabilisation. The level is measured by visualisation through a transparent front plate of the experiment.

Figure 5.51. Sketch of the PIERO test section



Source: Freitas and Pasquale, 2015.

The PIERO experiment is included in the separate effect tests matrix of Code for Analysis of THERmalhydraulics during an Accident of Reactor and safety Evaluation (CATHARE) and used to validate the 3D module of the code [5.1.13-1] and [5.1.13-2].

5.1.13.2. OMEGA

The OMEGA facility, built at CEA-Grenoble, was first dedicated to the characterisation of the heat transfer behaviour during the decompression phase of a LOCA and the characterisation of the critical heat flux (CHF) in PWR-type rod bundles. Several campaigns of CHF measurements were carried out at different T/H conditions (for example, see [5.1.13-3]).

The OMEGA-2 loop, is dedicated to study single-phase and two-phase flows in a rod bundle at high pressure. The test section features a 5x5 bundle of electrically heated rods of 9.5 mm outer diameter, arranged in a square array with a 12.6 mm pitch, simulating those in a PWR core. Simple support grids or mixing vane grids are used to maintain the

rod bundle. A uniform power is applied on the total heated length of 3.658 m. Radial power is non-uniform: the nine central rods have a heat flux of greater than the 16 peripheral ones.

A series of runs with CHF measurements have been published that cover PWR conditions (pressure from 10.5 to 16.6 MPa, mass flow rate 2.6-12.7 kg/s, inlet temperature 86.7-324.6°C and power 3.2-6.8 MW) and show the capacity of the loop at providing reliable data [5.1.13-4].

As part of the NESTOR project (CEA/EDF/EPRI), several series of analytical runs were carried out, which were in typical PWR conditions (pressure from 10 to 15.5 MPa, mass flux 3 000-4 600 kg/m²/s, inlet temperature 185-305°C, power 0.57-1.4 MW/m²) and addressed the axial offset anomaly phenomenon. Single-phase tests aiming to provide measurements (of the wall and fluid temperatures) were dedicated for single-phase heat transfer modelling in a rod bundle. The onset of nucleate boiling (ONB) was one of the phenomena studied in the boiling tests. A series of such tests were performed, which allowed for the determination of the location of the ONB point [5.1.13-5] and [5.1.13-6].

5.1.13.3. GRAZIELLA

The GRAZIELLA facility was developed at CEA-Grenoble in collaboration with Electricité de France (EDF). The test section consists of a vertical channel with a square cross-section containing a 5x5 PWR-type rod bundle. The rod bundle is maintained by spacer grids with or without mixing vanes. The tests are performed with Freon, simulating high pressure conditions, covering the range of thermal-hydraulic parameters in the nominal operating conditions of a PWR core or two-phase conditions. Adiabatic and heated tests were carried out. For the last ones, rods are electrically heated, with a uniform 3.65 m heating length.

Some tests performed in the GRAZIELLA loop are devoted to studying the DNB in rod bundle, and the effect of mixing grid on the DNB [5.1.13-7] [5.1.13-8].

For some of the heated tests, the nine central rods are overheated by 33% compared to the 16 external ones, introducing mixing effects between the subchannels. The flowrate and quality of each subchannel are measured at the end of the test section [5.1.13-9] and [5.1.13-10].

Some GRAZIELLA adiabatic single-phase tests have been used for the assessment of the turbulent diffusion and the dispersion term in the momentum equation of the CATHARE 3 3D model [5.1.13-10].

5.1.13.4. AGATE

The AGATE facility was built at CEA-Grenoble. The test section consists of a square lattice of 5x5 unheated rods, 1.5 m high, inserted in a 66.1 mm square channel. The diameter of the rods of this PWR-type bundle is 9.5 mm, and the bundle pitch is 12.6 mm.

Transparent windows in the square channel allow for the measurement of the three velocity components, with their fluctuations, in the subchannels using a laser velocimetry technique [5.1.13-11].

AGATE tests have been intensively used for the validation of codes using a CFD approach (e.g. [5.1.13-12] and [5.1.13-13]) and the porous (subchannel) approach (e.g. [5.1.13-8]), for the effects of the mixing grids on the flow and the heat transfer. AGATE tests have been also used for the 1D modelling of the turbulence induced by the grid by CATHARE 3 [5.1.13-14].

5.1.13.5. MR-2/MR-2A atmospheric pressure water loop

MR 2/MR 2A is a pumped circulation, atmospheric pressure flow modelling loop with two discrete flow circuits. This loop is located in Chalk River (Canada). Water is the primary working fluid, but air can be injected into the water flow to simulate two-phase flows. The primary circuit (MR 2) has three test stations and a choice of three circulation pumps, which can provide water mass flows of up to 14 kg/s. Air can be injected at 0.02 kg/s. Testing is normally conducted at ambient temperature, but the water can be heated to a maximum of 70°C. The second circuit (MR 2A) is adjacent to MR 2 but physically separated, and has a dedicated circulation pump, which can provide as much as 1.4 kg/s water flow at ambient temperature, with air injection of 0.02 kg/s. These facilities are used to study flow distribution and pressure drop over a wide range of complex geometries. Transparent test sections permit flow visualisation and the use of optical instrumentation to measure fluid parameters. The loop can accommodate powers of up to 1.7 MW, which facilitates the capability of CHF tests for fuel bundles such as NRU driver fuel with water as coolant. Net heat rejection is provided by a plate-type heat exchanger; a second plate-type heat exchanger is used to pre-heat the inlet water with heat from the outlet water, thus allowing the pump to operate at a lower temperature.

5.1.13.6. MR-3

MR-3 is a large high-temperature, high-pressure, pumped circulation heat transfer loop utilising hydrofluorocarbons as the working fluid. This loop is located in Chalk River (Canada). The loop vessels and piping systems are constructed of carbon steel, limiting the loop to non-aqueous working fluids. The primary circuit circulates R 134a (Freon) through the test sections and controls the test section flows, inlet temperatures and outlet pressures. To be consistent with economic limitations, the loop equipment is designed to operate over as wide a range as possible in order to minimise the number of settings and manual adjustments needed during an experiment. For example, both three and four-inch diameter piping are used for connecting the vertical test section to the vapour drum. During experiments with high test section outlet quality and high flows (above 12.5 kg/s), a four-inch pipe is required to keep the velocity within acceptable parameters. Conversely, during low quality, low flow instability tests, a three-inch pipe is required to avoid slug flow. The piping is flanged and the circuits suitably valved to facilitate piping changes.

The loop design pressure is 6.2 MPa (g) at 121°C, but it normally operates at 1.0–3.0 MPa (g) at 60°C, and at fluid mass flows up to 38 kg/s. A typical CHF test would operate at ~1.9 MPa (g) pressure at 60°C and ~21 kg/s mass flow, with up to 1.7 MW test section power. The internal loop volume is ~7 m³, with a normal working fluid inventory of ~4 500 kg of liquid hydrofluorocarbon. There is a 6 m vertical test station that can accommodate a full-scale PHWR fuel string simulator, and a horizontal test location that can accommodate either of pair of interchangeable test stations for full-scale (6 m) PHWR fuel string simulators, or full diameter half length (3 m) simulators. At present, the working fluid is R 134a, which permits full-scale fuel simulations at lower temperatures, pressures and power than would be the case in water. The loop was originally designed to operate with CFC 11, or CFC 12, but the conversion to R 134a has reduced the environmental ozone depletion impact of fluid leaks to zero.

The primary function of this facility is to investigate CHF enhancement and other heat transfer parameters of various existing PHWR fuel geometries, or experimental geometries. The MR-3 loop has a unique capability of performing T/H tests for a bundle string simulator with various radial power profiles by using a particular resistance. The loop also has a facility for conducting pressure drop tests and post dryout (PDO) heat transfer tests on full-scale PHWR bundles.

5.1.13.7. Header test facility

The header test facility is an approximately 1:3 scaled model of a typical PHWR header/feeder system, consisting of two headers and 72 feeders, operating at near atmospheric conditions with air and water as the working fluids. This facility is located in Chalk River (Canada). The header's multi-channel behaviour is one of the important phenomena influencing fuel sheath peak temperature of PHWR fuel under certain postulated accident conditions, into which further research is needed. The header test facility is used to investigate two-phase flow characteristics in the headers and their impact on flow and phase distribution in feeders during postulated accidents. A maximum water flow of 88 L/s and a maximum air flow of 0.5 m³/s are designed in this facility. This facility is instrumented with a sophisticated wire mesh sensor multiplexing system and a complex pressure drop measurement system to measure constitutive parameters of two-phase flow in headers and feeders. Experimental information obtained from this facility can be used to examine the void distribution along headers and among feeders and the mass flow rate distribution among feeders under various simulated hypothetical PHWR accident

5.1.13.8. MTF

The Moderator Test Facility (MTF) consists of a ¼ linear scale generic PHWR calandria vessel, complete with correctly scaled inlet and outlet piping and all necessary pumps, flow control valves, heat exchangers, process controls and instrumentation to permit a controlled simulation of virtually all PHWR moderator cooling circuits. This facility is located in Chalk River. Included within the moderator vessel are 480 electrically heated calandria tube simulators, which provide an axial heat flux profile representing a typical PHWR. DC power is delivered to the calandria tubes from the T/H laboratory of a 1.7 MW power supply. Through the use of easily removable blank ports and easily relocated piping, the vessel is configured to provide for up to 12 properly scaled and located inlet flow nozzles, as well as all current PHWR outlet flow port configurations. The MTF can simulate moderator flows in Canada Deuterium Uranium (CANDU) 9, CANDU 6 and Pickering, Bruce and Darlington reactor configurations. The facility can conduct modelling tests at current PHWR moderator pressures and temperatures and, with minor changes, achieve temperatures and pressures up to 120°C and 10⁵ kPa (g) for experiments such as passive moderator cooling system (PMCS). The vessel is fitted with multiple access ports for temperature and fluid velocity measurement instrumentation and has an array of viewing windows for observing and recording colour dye flow path visualisation experiments. Process control and data acquisition is provided by a dedicated P/C based computer system, utilising PARAGON TNT, a sophisticated process control/data acquisition software package that permits fully automatic (unattended) operation of the facility process controls and temperature data gathering.

In order to accommodate the range of moderator circulation test conditions for the CANDU 9 programme and for existing CANDU variants, plus the future PMCS programme, the values for various system parameters dictated by this flexible design are:

- Power: up to 1.7 MW (PMCS tests only), with normal cosine axial power distribution and reactor typical radial power distribution.
- Flow: primary side flow from 0 to 30 kg/s, with variable flow capability at each inlet and outlet nozzle.
- Temperature: primary side water from room temperature to 95°C, ±0.5°C for moderator circulation tests and up to 120°C for PMCS tests.
- Pressure: up to 85 kPa (gauge) for PMCS tests.

A one-third-scale moderator test facility modelling the calandria of the ACR-700 was recently constructed and tested at CNL to obtain moderator circulation data for validating the moderator T/H analysis code.

5.1.13.9. CREARE

The first models for downcomer refill were based on CREARE experiments. This test facility was replaced by a scale one experiment (UPTF) [5.1.13-15].

5.1.13.10. METERO-V

Objective of the experiment

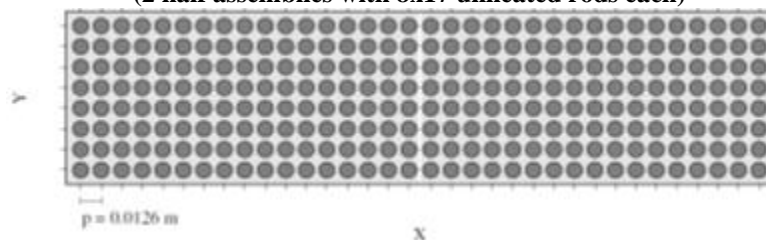
The analysis of LB-LOCAs required specific experimental programmes investigating large-scale 3D effects, particularly during downcomer refill and core reflooding. SB-LOCAs and IB-LOCAs also encounter significant 3D effects in the core due to the radial power profile, with crossflows and diffusion-dispersion. Similar situations exist at lower pressure for loss of residual heat removal (RHR) accidents. Other transients such as steam line break and boron dilution are sensitive to all mixing phenomena in the core. There is also a need for a precise validation of each mixing process.

The METERO-V (vertical) test facility, under construction at the CEA (Saclay), which has the commissioning of the first tests performed in 2022, intends to provide data for the validation phenomena in the core during these accidents, for both 3D systems and subchannel scales. As a side objective, it could also be useful for the validation of CFD in open medium.

Description of the test loop

The basic test section is a rod bundle with 8x34 unheated rods representing two half assemblies. In a first phase of experiments, the height of the test section is about 2m, although a full rod bundle length (3.6 to 4 m) would also be possible in future studies. The test section intends to be modular in order to adapt to various measurement techniques and geometries. The rods and rod arrays will be at scale one (rod outer diameter $d=9.5$ mm, pitch 12.6 mm), as shown by Figure 5.52.

Figure 5.52. Radial view of a sketch of METERO-V test section (2 half assemblies with 8x17 unheated rods each)

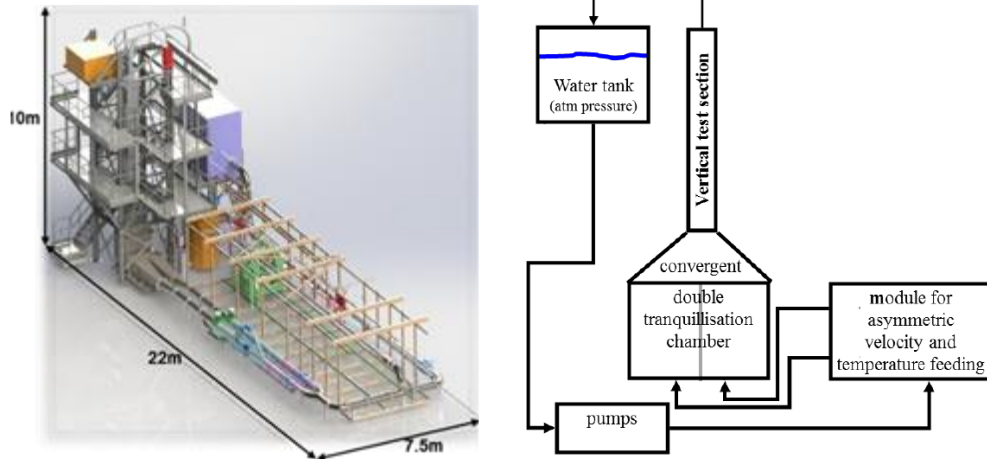


Source: Bestion et al., 2018.

A tranquillisation chamber has been designed in two separated parts to create a dissymmetry of the flow entering the vertical structure. Each part of the tranquillisation chamber is composed of a diverging pipe followed by a grid and then a straight larger pipe, honeycomb and grid. A set of parallel deflectors then change the flow's orientation to vertical. Another honeycomb is placed before a converging rectangular pipe downsizing the cross-section to fit the vertical structure inlet. A module for asymmetric distribution in

this double tranquillisation chamber creates differences of velocity, temperature, density or tracer concentration between the left and right half assemblies (Figure 5.53).

Figure 5.53. Left: 3D view of the METERO-V facility; Right: sketch of METERO-V loop with the vertical test section.



Source: Bestion et al., 2018.

METERO-V is designed to carry out single-phase and two-phase tests. The pressure is close to atmospheric at the top of the test section. The maximum water flowrate is 700 m³/h and the maximum air flowrate is 150 m³/h. The range of liquid Reynolds numbers that can be obtained with water flow is up to 100 000. The temperature of the fluid may be ambient (14 to 30°C) with possible heating to create a radial temperature difference of up to a maximum of 36°C, creating a radial density difference of about 1%.

Planned tests

Various test series are planned to address different processes in a separate way, with equal or unequal velocities, temperature or passive scalar concentration at the inlet of the assemblies

These tests series are summarised in Table 5.31.

Table 5.31. Test series planned in METERO-V experiment

Process	Test series
Wall friction	<ul style="list-style-type: none"> • Pressure losses in axial flow • Pressure losses in non-axial flow
Momentum turbulent diffusivity	<ul style="list-style-type: none"> • Pressure losses with transverse flow
Scalar turbulent diffusivity	<ul style="list-style-type: none"> • Mixing of a passive scalar in 1-phase flow
Scalar dispersive tensor	<ul style="list-style-type: none"> • Mixing of a passive scalar in 1-phase flow
Energy turbulent diffusivity	<ul style="list-style-type: none"> • Energy mixing in 1-phase flow
Energy dispersive tensor	<ul style="list-style-type: none"> • Energy mixing in 1-phase flow

Table 5.31. Test series planned in METERO-V experiment (Continued)

Process	Test series
Two-phase wall friction	<ul style="list-style-type: none"> • Pressure losses and interfacial friction in pure axial flow • Pressure losses and interfacial friction with transverse flows • Pressure losses and interfacial friction with buoyancy-driven crossflows
Interfacial friction	<ul style="list-style-type: none"> • Pressure losses and interfacial friction in pure axial flow • Pressure losses and interfacial friction with transverse flows • Pressure losses and interfacial friction with buoyancy-driven crossflows
Void dispersion	<ul style="list-style-type: none"> • Void dispersion tests

METERO will use the following instrumentation:

- PIV (single-phase tests) to measure profiles of axial and radial components of the velocity in the domain of subchannels visible through rod gaps. Measurements of the radial component may not be accurate if it is much smaller than the axial component.
- LIF (single-phase tests) will use to measure the variation of the luminescence of injected tracers with pH or with temperature. LIFs will be able to measure passive tracer radial concentration profiles at various elevations and temperature radial profiles at various elevations.
- Core wire (single-phase tests) to measure the fluid temperature at various positions.
- X-ray tomography (two-phase tests) will be used in two-phase air-water tests to measure linearly averaged void fraction.
- Pressure and pressure differences (1-phase and 2-phase tests) will be measured at several positions on lateral and front faces of the test section to measure all kinds of pressure losses.

The radial mixing of a passive scalar can be obtained by the unbalanced injection of a tracer and using the LIF technique. The radial temperature mixing can be studied using a homogeneous velocity and an unbalanced temperature measurable by LIF. Particles are injected, whose luminescence is sensitive to temperature. Crossflow is buoyancy-driven when gravitational axial pressure gradient dominates the friction axial pressure losses. The difference of temperature induces density differences that create different axial pressure gradients in the two assemblies. This creates radial pressure differences and crossflows from cold assembly to hot assembly. As soon as crossflows are significant, they may overpass diffusive radial mixing.

Application for system code validation

Some simulations using CATHARE 3 were performed to verify if the identified 3D phenomena might be reproduced in the METERO-V conditions. These simulations could also help build the test matrix and determine the range of the measured quantities (temperature, velocities, concentration, etc.) [5.1.13-16].

5.2. Integral effect tests

5.2.1. ATLAS

5.2.1.1. Objective of the experiment

KAERI has been operating the ATLAS integral effect test facility, Advanced Thermal-Hydraulic Test Loop for Accident Simulation, for transient and accident simulations of advanced PWRs [5.2.1-1]. The reference plant of ATLAS is a 1 400MWe-class evolutionary pressurised water reactor, APR1400. ATLAS has the same two-loop features as the APR1400 and is designed according to the scaling method suggested by Ishii and Kataoka [5.2.1-2] for simulating the various test scenarios as realistically as possible. ATLAS is a half-height and 1/288-volume scaled test facility compared to the APR1400. The fluid system of ATLAS consists of a primary system, secondary system, safety injection (SI) system, break simulating system, containment simulating system and auxiliary systems. The primary system includes an RPV, two hot legs, four cold legs, a pressuriser, four RCPs and two SGs. The secondary system of ATLAS is simplified to be of a circulating loop-type. Most of the safety injection features of the APR1400 and the optimised power reactor 1 000 (OPR1000) are incorporated into the ATLAS safety injection system. About 1 600 instrumentations have been installed in the ATLAS test facility to precisely investigate T/H behaviour in simulation of the various test scenarios.

The ATLAS has been used to provide the unique test data for the two (hot legs) x four (cold legs) reactor coolant system with a DVI of ECC; this will significantly expand the currently available data bases for code validation. The ATLAS has been operated in order to investigate major design and beyond design basis accidents and operational transients for advanced pressurised water reactors. The produced integral effect test data have been used to resolve the licensing issues of the APR1400 and to validate the safety analysis codes for the various accident sequences. The ATLAS test results will be used to evaluate the performance and thereby confirm the design concepts of new safety systems, validate the safety analysis code and related models, and understand the T/H phenomena occurring during the accident transients [5.2.1-3] and [5.2.1-4].

5.2.2.2. Description of the test loop

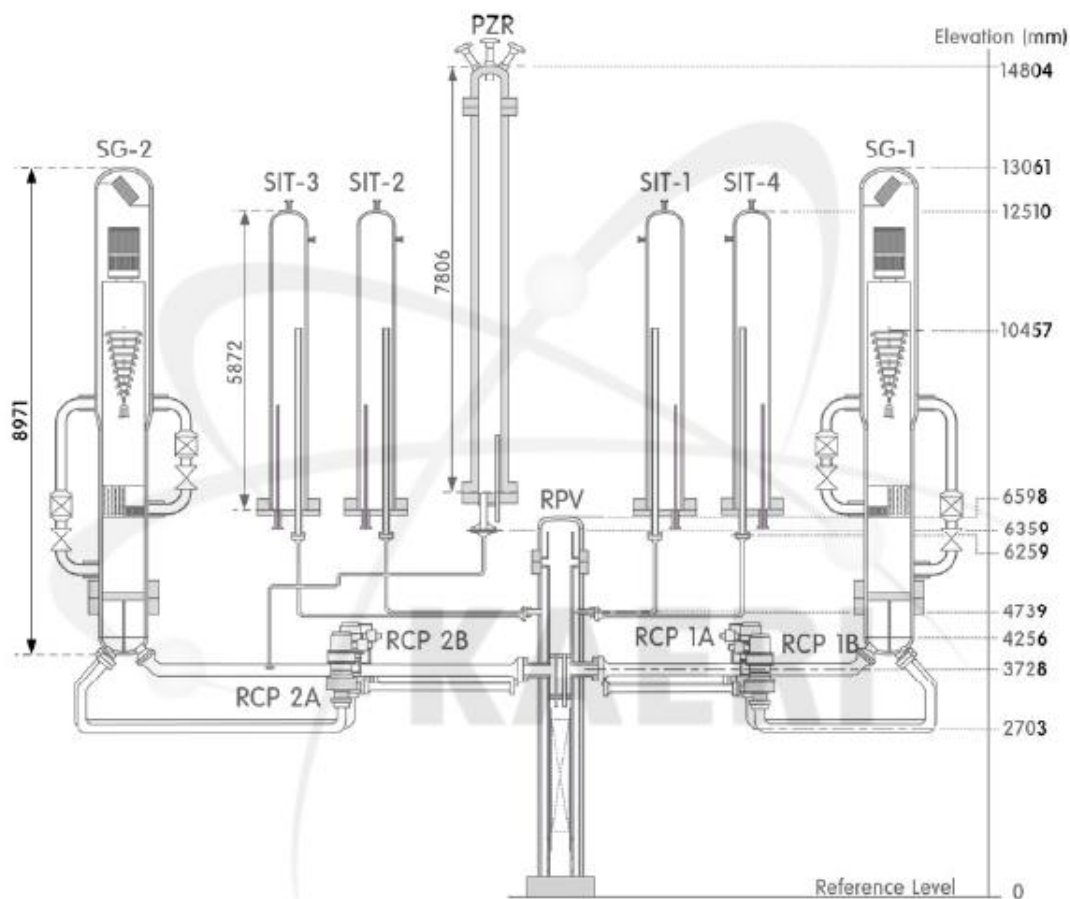
Figure 5.54 shows the schematic diagram of the loop connection, which shows the elevations of the major ATLAS components [5.2.1-5]. The elevations are based on the reference point of RPV bottom. The total height of the facility is about 30 m (10 m underground and 20 m above ground). All major components – such as the RPV, SGs, pressuriser and SITs – are above ground. The loop was designed to be operated at up to 18 MPa to simulate the high pressure scenarios. The total inventory of the ATLAS reactor coolant system is 1.6366 m³. A more realistic 3D view of ATLAS is shown in Figure 5.55.

The RPV and the core simulator are designed to preserve the distributions of the temperature, pressure, coolant volume, flow rate and flow area. They are also designed to preserve the hydraulic diameter and important local phenomena. The main focus in designing the reactor vessel downcomer was on the reproduction of the multidimensional phenomena related to a DVI as well as the preservation of the surface tension effect and the flow regime (especially for cap bubbles). Several parameters are considered during the local phenomena scaling analysis, including the void fraction, mixture level, transition criteria of a two-phase flow regime, flow reversal, ECC bypass, steam condensation, stored energy, pressure drop and more. Most of the design parameters are based on the integral scaling parameters. However, the gap size of the downcomer annulus is intentionally increased to simulate the multidimensional behaviour more realistically. The increased

downcomer volume is compensated for by reducing the lower plenum volume to maintain the total coolant volume ratio in the reactor vessel. Figure 5.56 shows a schematic diagram of the ATLAS reactor pressure vessel.

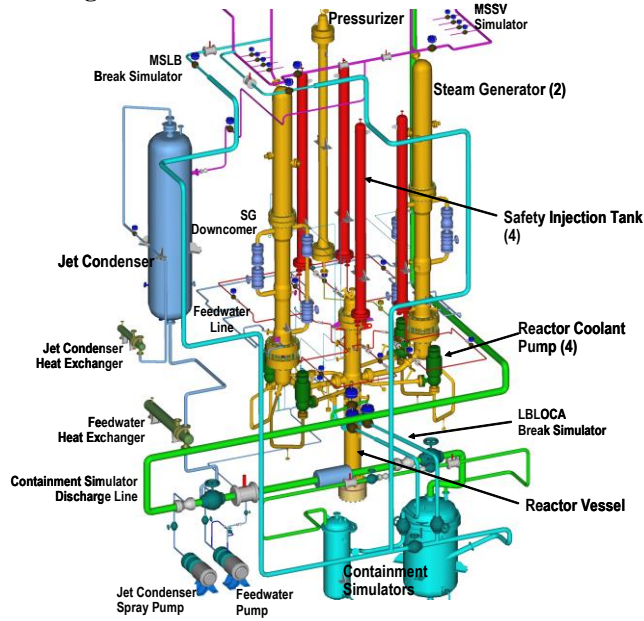
A total of 396 electrical heaters and unheated rods are used to simulate the fuel rods. Since the diameter is maintained to be identical to that of the APR1400, the temperature of the fuel rods reasonably represents the reference reactor during most accident conditions, if the initial stored energy can be reasonably treated. The maximum core power is 2 MW which corresponds to 10% of the scaled nominal power. A bundle of electric heaters has been installed to simulate the reactor core, which is in the lower part of a RPV. There are 390 electric heaters divided concentrically into three groups (group-1, group-2 and group-3). Group-1, -2 and -3 heaters are located in inner, middle and outer regions of the heater bundle respectively, and they have 102, 138 and 150 heaters respectively. The core heater bundle also has six unheated rods. The axial power profile of each heater rod is in the “chopped cosine” power shape. The simulated fuel assembly type is 16×16, and the prototypical spacer grid (PLUS-7) is used. The outer diameter of heater rod is 9.5 mm, which is the same as the prototypical rod diameter of APR1400.

Figure 5.54. Schematic diagram of loop connection of ATLAS



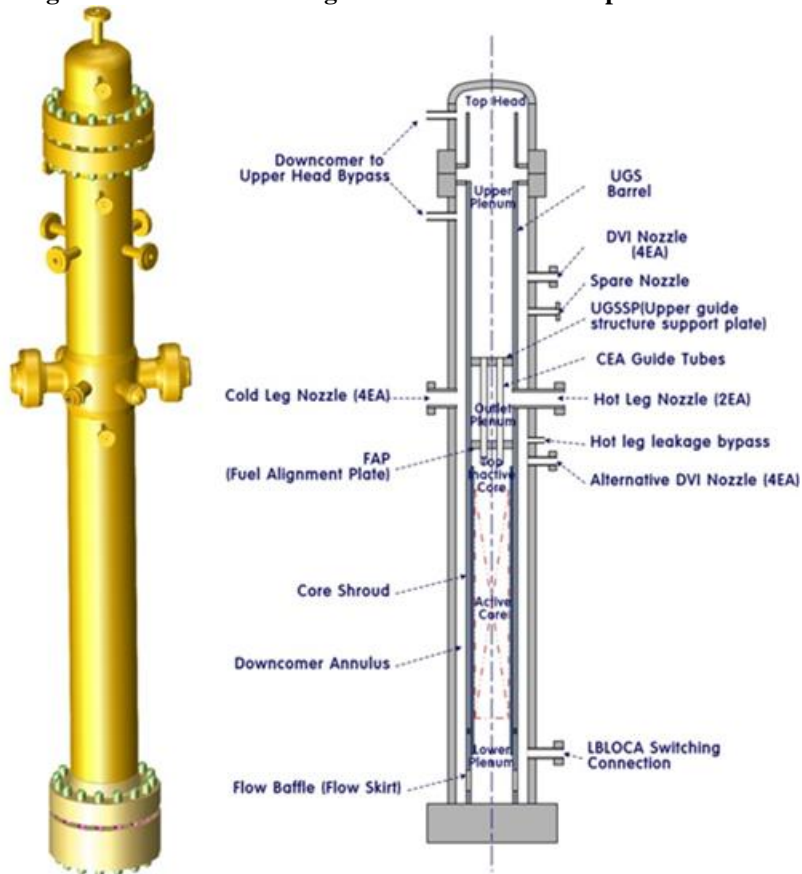
Source: Lee, 2018.

Figure 5.55. Three-dimensional view of ATLAS

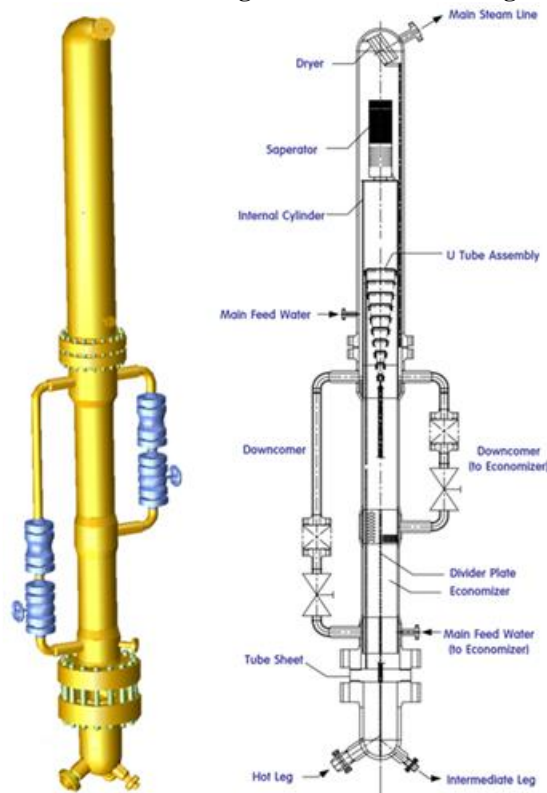


Source: Lee, 2018.

Figure 5.56. Schematic diagram of ATLAS reactor pressure vessel



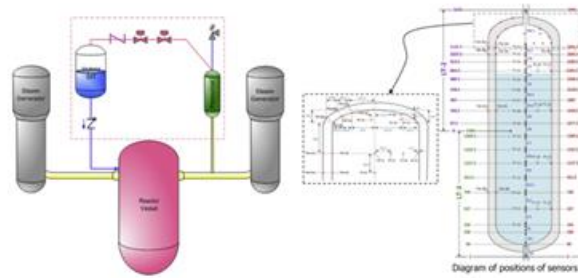
Source: Lee, 2018

Figure 5.57. Schematic diagram of ATLAS steam generator

Source: Lee, 2018.

ATLAS has two steam generators, which have the same designed specifications apart from a break unit to simulate U-tube rupture. The break unit is installed in SG-1. Each SG consists of a lower plenum, U-tube assembly, middle and upper SG vessels, two downcomer pipes and other internals, as shown in Figure 5.57. The ATLAS facility adopts a jet condenser for the heat removal from the secondary system to the component cooling water system. The break simulation system consists of several break simulating lines such as a large LB-LOCA, DVI LB-LOCA, SB-LOCA, SGTR, MSLB and FLB, etc. Each break simulating line consists of a quick-opening valve, break nozzle and other instruments. The line is precisely manufactured to have a scaled break flow through it for LOCA tests. The containment simulating system of the ATLAS has a function of collecting the break flow rate and maintaining a specified backpressure to simulate containment.

The ATLAS facility was revamped in the second half of 2016 with the aim of enhancing its utilisation. The first change was the integration of the reactor coolant system of ATLAS and a containment building. A properly scale-downed containment building was constructed to investigate the multidimensional T/H phenomena occurring inside the containment building of a nuclear power plant. The second change is the installation of a new heater rod bundle. A new heater rod bundle was manufactured and ready to be installed inside a new reactor pressure vessel. The location of the thermocouple was shuffled in this new heater rod bundle and given additional capability to capture the core exit temperature (CET) behaviour. The fourth change was the adoption of a hybrid safety injection tank (SIT) concept. The hybrid SIT replaces the existing SITs in order to enhance the emergency core cooling capability for a high-pressure accident sequence such as a station blackout (SBO). The hybrid SIT is connected not only to the pressuriser, but also to the cold leg. Various instrumentations will be installed to investigate the multidimensional T/H phenomena inside the hybrid SIT, as shown in Figure 5.58.

Figure 5.58. Schematic diagram of hybrid SIT of ATLAS

Source: Ryu et al., 2018.

Instrumentation

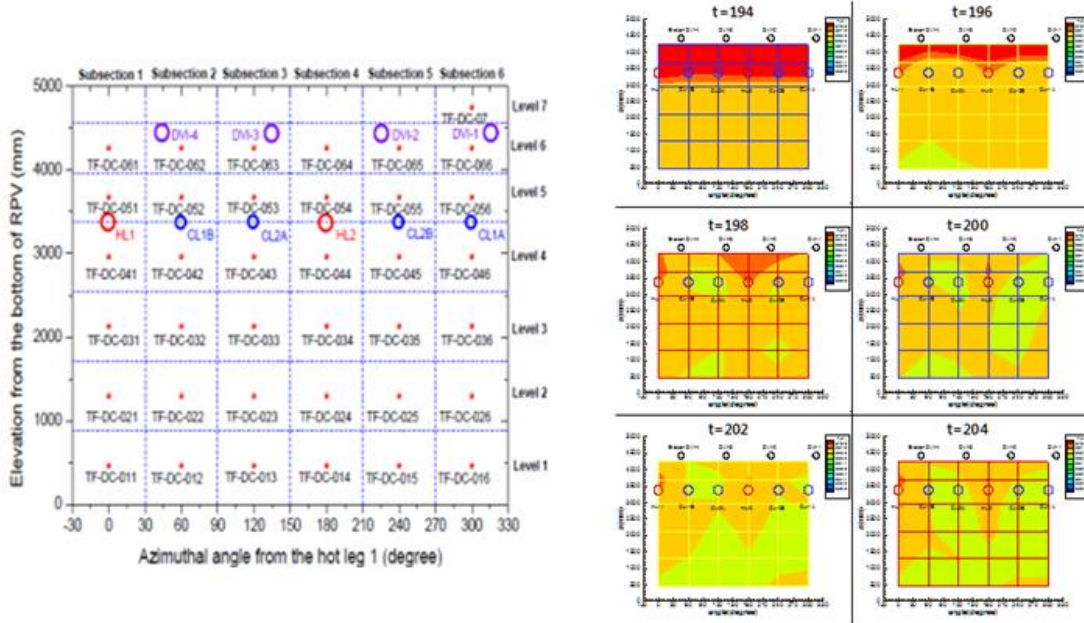
About 1 600 instrumentations have been installed in the ATLAS test facility to precisely investigate the T/H behaviour in simulations of the various test scenarios. Measuring parameters include the temperature, pressure, level, power, flow rate and mass. All instruments were calibrated by the manufacturers prior to installation in the ATLAS facility. All major instruments are calibrated periodically in accordance with the quality assurance (QA) programme of the KAERI certificated by the ISO 9001. However, no further recalibration of the thermocouples is performed once they have been installed in the facility. In this report, the measurement capability of capturing multidimensional T/H phenomena is highlighted.

The integrated downcomer enables the reproduction of multidimensional phenomena and reveals unexpected T/H phenomena. Air-water visualisation test results showed that there is no significant difference in flow pattern for a downcomer gap over about 25 mm. A total of 37 thermocouples are installed inside the downcomer to measure the fluid temperature in the ATLAS facility. Figure 5.59 shows a 2D arrangement of the downcomer fluid temperature sensors and an example of the temperature measurement in the LOCA simulation test [5.2.1-7].

Multidimensional non-uniformity in the peak cladding temperature (PCT) can be measured in the ATLAS core by 264 thermocouples at six different elevations, as shown in Figure 5.60. Both a wide- and a narrow-range void fraction (or liquid level) can be measured in the core and downcomer regions of the reactor pressure vessel and in the secondary side of the steam generator, as shown in Figure 5.61. A liquid level inside the U-tube of the steam generator can also be measured, as shown in Figure 5.61.

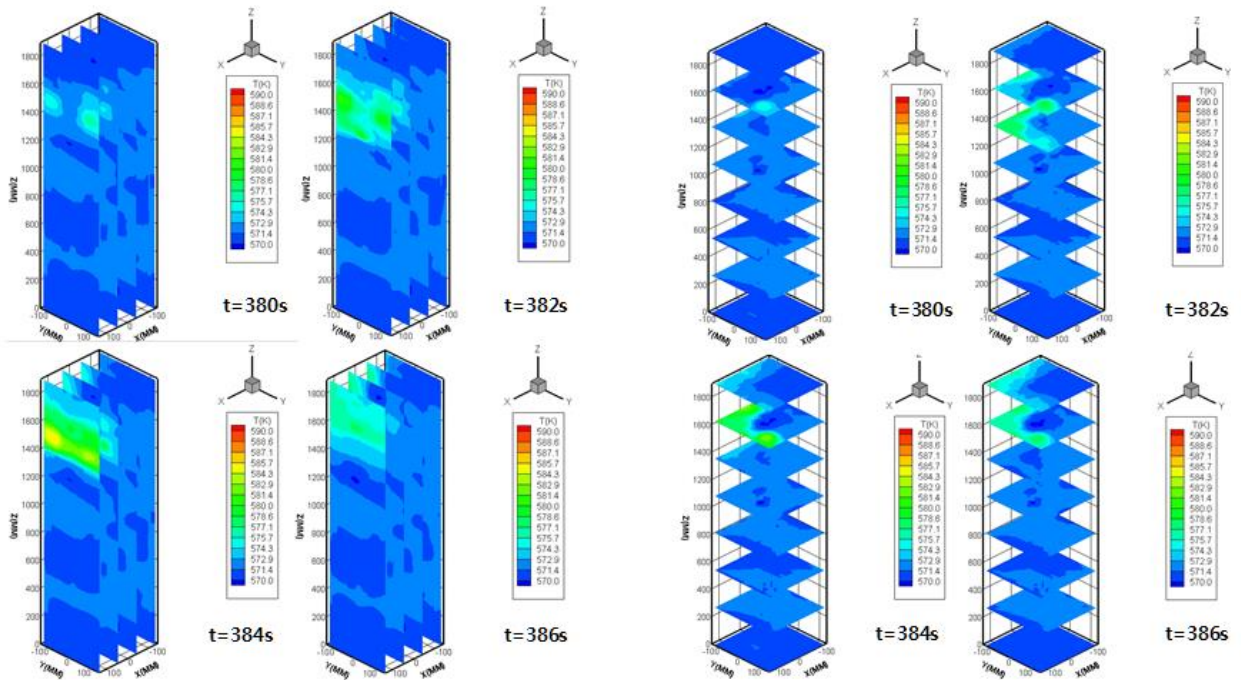
Five internal fluid temperatures can be measured in three and five locations of the hot leg and cold leg, respectively. Figure 5.62 shows a location of profile thermocouples for measurement of fluid temperature in hot leg [5.2.1-5]. These profile thermocouples can give information about the temperature and phase distributions inside the primary loop of ATLAS. The fluid temperature distribution inside the plenum of steam generator can give detailed information about the natural circulation characteristics and reflux condensation phenomenon during accident transients. Detailed temperature distribution inside the plenum of steam generator could be measured in the ATLAS facility by installing 100 thermocouples per each steam generator, as shown in Figure 5.63.

Figure 5.59. 2D arrangement of the DC fluid temperature sensors and example of temperature measurement in the ATLAS test



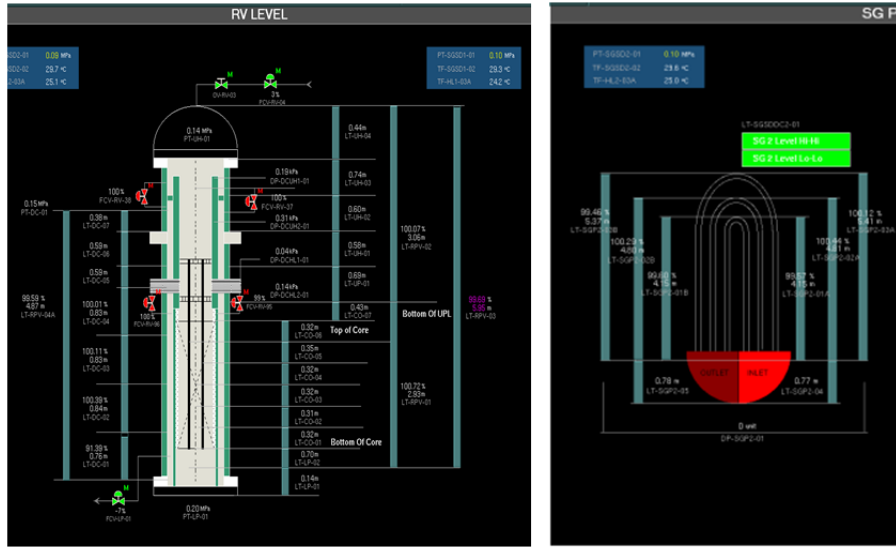
Source: NEA, 2012.

Figure 5.60. Distribution of core wall temperature measured in the ATLAS test



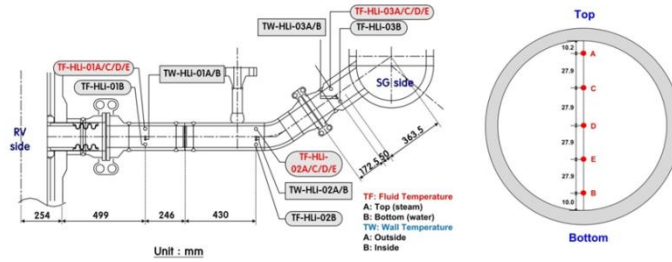
Source: NEA, 2012.

Figure 5.61. Distribution of liquid level measured in the ATLAS test



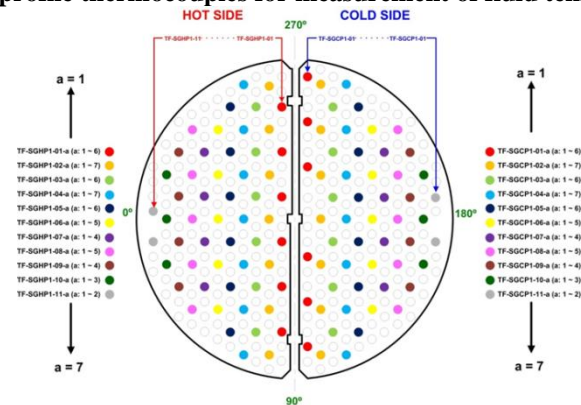
Source: Lee, 2018

Figure 5.62. Location of profile thermocouples for measurement of fluid temperature in hot leg



Source: Lee, 2018.

Figure 5.63. Location of profile thermocouples for measurement of fluid temperature in plenum of SG



Source: Lee, 2018.

5.2.2.3. Tests performed

ATLAS was constructed in 2005 and a series of commissioning tests were successfully completed in 2006. A database of over 134 integral effect tests has been established since 2017, with ATLAS covering various accident scenarios such as design basis accidents

(DBAs) and beyond design basis accidents (BDBAs). This ATLAS test database is being used to resolve the raised safety issues, develop new safety concepts and validate safety analysis codes nationally and internationally. Figure 5.64 shows a roadmap of the ATLAS programme, which includes test items covered by the ATLAS programme [5.2.1-8]. Table 5.32 summarises the ATLAS text matrix.

Figure 5.64. ATLAS roadmap programme

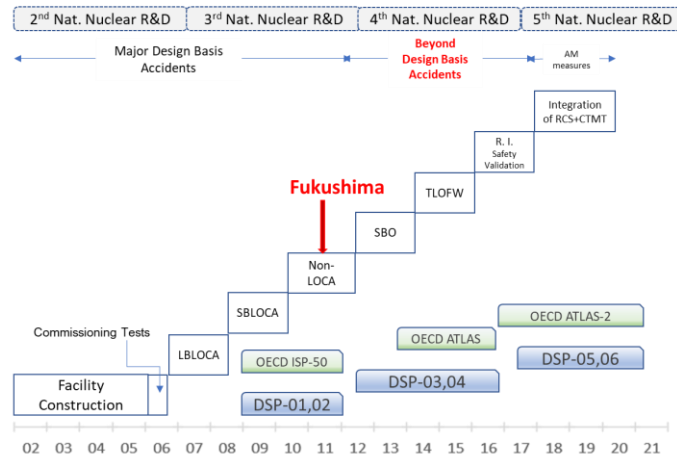


Table 5.32. Test matrix of the ATLAS programme

Year	Test items	# of tests	Remarks	Data usage	Summary
2007 (15)	LB-LOCA reflood parametric test	7	Phase 1: 7	APR1400 DC	LB-LOCA 15 sets 15
	LB-LOCA late reflood test	7	Phase 2: 7	APR1400 DC	
	SET test	1	SET: 1	APR1400 DC	
2008 (10)	DVIB SB-LOCA	8		DSP-01	DVIB SB-LOCA 9 sets including ISP-50 test 10
	CLB SB-LOCA	2			
2009 (12)	CLB SB-LOCA	8		DSP-02	CLB SB-LOCA 10 sets IOPOSRV SBLOCA 2 sets for SPACE 10(2)
	IOPOSRV (for SPACE)	2		SPACE	
	DVIB SBLOCA (ISP-50)	1		ISP-50	
	SGTR	1			
2010 (12)	SGTR	6	Non- LOCA	Multi-dimensional Analysis of Reactor Safety - Korea Institute of Nuclear Safety (MARS-KS) SPACE	SGTR 6 sets SGTR 2 sets for SPACE FLB 4 sets 10 (2)
	SGTG (for SPACE)	2			
	FLB	4			
2011 (15)	FLB	5	Non- LOCA	SPACE	FLB 5 sets FLB 2 sets for SPACE SLB 5 sets SLB 1 set for SPACE Special Test Special Test 12 (3)
	FLB (for SPACE)	2		SPACE	
	SLB	5			
	SLB (for SPACE)	1			
	SLB (for SPACE)	1			
	SBO PRO	1			

Table 5.32. Test matrix of the ATLAS programme (Continued)

Year	Test items	# of tests	Remarks	Data usage	Summary
2012 (13)	SLB FLB with PAFS SLB with PAFS SGTR with PAFS SBO (TMLB') SBO (TDAux) SBO+LOCA IBLOCA (10") SB-CEDM-01	4 1 1 1 1 2 1 1 1	Non-LOCA and SBO	APR+ APR+ APR+ APR1400 APR1400 APR1400 APR1400 APR1400	SLB 1 set for SPACE among 4 SLB sets FLB 1 set for PAFS SLB 1 set for PAFS SGTR 1set for PAFS SBO, repeatability test SBO, turbine-driven aux. (1 & 2 train) SBO+RCP seal failure, 10gpm PZR surge line break, 10" Two CEDM nozzle break (69.3mm*2) 8(5)
2013 (11)	SBO+LOCA SBO+SGTR NCFM LB-LOCA late reflood test LB-LOCA late reflood test LB-LOCA late reflood test (N2)	2 2 2 3 1 1		APR1400 APR1400 APR1400 APR1400 NRC-DC APR1400 NRC-DC APR1400 NRC-DC	SBO+RCP seal failure, 100gpm, 500gpm SBO+SGTR, 1 tube & 5 tubes Natural circulation characteristic tests Electrical 4-train ECC validation LB-CL-09 repeat with different procedure Nitrogen injection tests
2014 (10)	FLB-DS-01, 02 FLB-DSTR-01, 02 FLB-DSBD-01, 02 OECD ATLAS TLOFW	2 2 2 2	TLOFW	DOOSAN DOOSAN DOOSAN APR1400 APR1400	SLB pressure waver propagation Transient test for SG behaviour Primary blowdown from SG A1.1 and A1.2 1ry bleeding & 1ry and 2 nd bleeding
2015 (12)	LTC-CL-01, 02, 03, 04R OECD ATLAS	4 8		APR1400 APR1400	Top slot IBLOCA with loop seal reformation A1.2, A2.1, A2.2, A3.1 and A5.1
2016 (7)	ML-01, 02, 03, 03R OECD ATLAS	4 4		APR1400 APR1400	Loss of RHR during shutdown cooling A4.1 and A5.2
2017 (10)	SLB-SGTR-02 SLB-SIP-02 SGTR-SIP-01 NC-03R, NC-04R HLB-BLK-01 HEMS-SBO-01 PECCS-SBLOCA-01 OECD-ATLAS2 B3.1 Run1, Run2	1 1 1 2 1 1 2		DEC (MOTIE) DEC (MSIT) DEC (MSIT) APR1400 APR1400 iPOWER iPOWER APR1400	SLB + 5 tubes SGTR with 4 SIPs DEGB SLB w/o LOOP + total failure of SIPs 5 tubes SGTR + total failure of SIPs Natural circulation characteristic tests with new RPV HL LB-LOCA + 93.2% partial blockage SBO + single failure of PAFS + 4 H-SITs 2" CL-1A SBLOCA + 2 H-SITs + 2 M-SITs PZR Surgeline break IBLOCA (10")

Table 5.33. Test matrix of the ATLAS programme (Continued)

Year	Test items	# of tests	Remarks	Data usage	Summary
2018 (6)	SB-SIP-02	1		DEC (MOTIE)	2"CL SBLOCA + Total failure of SIPs
	OECD-ATLAS2 B2.1	1		APR1400	SBO + SI injection from 4 H-SITs
	OECD-ATLAS2 B3.2	1		APR1400	DVI line break IBLOCA
	OECD-ATLAS2 B5.1	1		APR1400	1% RPV top break SBLOCA
	SGTR-PAFS-02				5 tubes SGTR + PAFS to SG-2 only
	MLO-PRO-02				Mid-loop + PZR man-way open + RHRS
	Sum		134		

5.2.2. ROSA/LSTF

5.2.2.1. Objective of the experiment

The Rig-of-safety Assessment/ Large Scale Test Facility (ROSA/LSTF) operated by JAEA is designed to simulate T/H phenomena peculiar to LOCAs and operational/abnormal transients of a PWR. ROSA/LSTF has been intensively used for research including Three Mile Island-type experiments, the NEA's experiment for the 26th international standard problem (ISP-26) [5.2.2-1], counterpart tests with other integral effect tests, plant simulation experiments for the Mihama Unit 2 steam generator tube rupture (SGTR) accident, experiments for the AP600 (in collaboration with US NRC), as well as natural circulation tests under various pressure conditions with and without non-condensable gas.

The NEA's ROSA project (2005-2009) [5.2.2-2] and ROSA-2 Project (2009-2012) [5.2.2-3] were performed to resolve issues in T/H analyses relevant to LWR safety by using the ROSA/LSTF. In particular, the projects focused on the validation of simulation models and methods for various complex phenomena. This involves complex multidimensional single-phase and two-phase flow conditions, which may include non-condensable gas in many cases. The test data performed in the projects are provided by the NEA's Data Bank.

5.2.2.2. Description of the test loop

The LSTF [5.2.2-4] shown in Figure 5.65 is a full-pressure and full-height integral test facility constructed in 1985, which simulates a 1 100 MWe four-loop Westinghouse type PWR: Tsuruga Unit-2 reactor. The major design characteristics of the LSTF are summarised in Table 5.33. Multidimensional T/H response during reactor transient is simulated by using a ten MW electrically heated full-size core rod bundle, of about 50 mm width annulus downcomer in the pressure vessel, 207 mm inner diameter hot and cold legs and 141 full-size U-tubes in each of two steam generator. The fuel assembly has mostly the same dimensions for the following points as those of PWR 17x17 fuel assembly; diameter, length and pitch of fuel rod, diameter, length and pitch of control rod guide thimble, and the ratio of number of fuel rods to number of the guide thimbles.

The four primary loops of the reference PWR are represented by two equal-volume loops to simulate two-phase flows during reactor accidents and transients mainly by achieving the large-diameter horizontal legs. The volumetric scaling ratio of the primary loops is 1/48 to those of the reference PWR. The LSTF can handle a wide range of primary and secondary pressures, from reactor nominal operating pressure to atmospheric pressure.

Break flow is simulated by using a break unit that can be connected at 19 locations of the LSTF. The break size is controlled by orifice or nozzle. The break flow rate is measured from the liquid level's increased rate in the suppression tank.

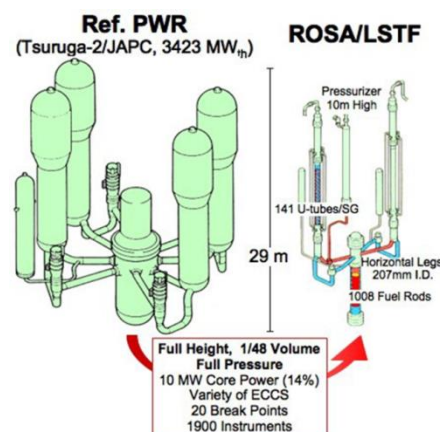
All types of ECCS furnished to the reference PWR are provided; high pressure injection (HPI) system, accumulator injection system (AIS), low pressure injection (LPI) system and RHR system. A gravity-driven injection system (GDIS) as a form of passive safety features is equipped with the LSTF. The LSTF is equipped with all the ECCS with new additional features such as ECCS coolant temperature control and temperature stratification in the accumulator coolant tank for injecting coolant by the flashing of high-temperature coolant portion without N₂ gas pressurisation.

Instrumentation from around 1 900 channels provide detailed information on T/H conditions by measuring parameters such as the temperature, liquid level, pressure loss, flow rate and density. The visual observation of 3D fluid behaviours is possible using a “video-probe”: a periscope that withstands high-temperature steam/water conditions employing glass-fibre image guide or bore scopes. Non-condensable gas detectors and detailed temperature measurement were also furnished.

Table 5.34. Major design characteristics of ROSA/LSTF to reference PWR

Items		LSTF	PWR	PWR/LSTF
Primary/ secondary pressures	(MPa)	16/7.4	16/6.13	1/0.83
Primary/ secondary temperatures	(K)	598/562	598/550	1/0.98
Core height	(m)	3.66	3.66	1
Number of fuel rods	-	1 008	50 952	50.55
Primary fluid volume: V	(m ³)	8.14	347	42.6
Total core power: Q	(MW)	10	3 423(t)	342
Q/V	(MW/m ³)	1.23	8.8	8.0
Core inlet flow	(tonne/s)	0.0488	16.7	342
Pressure vessel downcomer gap	(m)	0.053	0.26	4.91
Number of primary loops		2	4	2
Hot leg inner diameter: D	(m)	0.207	0.737	3.56
Hot leg length: L	(m)	3.69	6.99	1.89
Hot leg: L/D	(m ^{1/2})	8.11	8.14	1.0
Hot leg volume: $p4DL$	(m ³)	0.124	2.98	24.0
Number of tubes in steam generator		141	3 382	24.0
Average length of SG tubes	(m)	20.2	20.2	1

Figure 5.65. Schematic of ROSA/LSTF



Source: NEA, 2013.

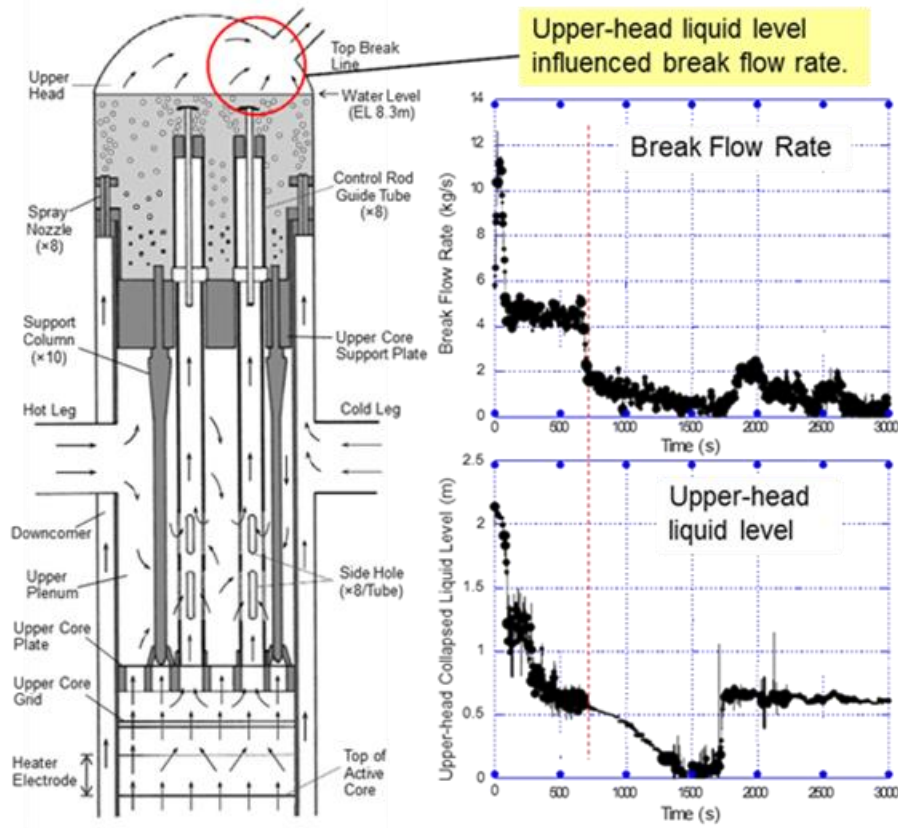
5.2.2.3. Tests performed

Safety issues related to 3D T/H were discussed in the following test series of the NEA's ROSA project and ROSA-2 project.

a) ROSA: test 6-1 PV upper-head break LOCA with AM measure

The objective was to clarify consequences of SB-LOCA due to PV upper-head break with SG depressurisation as a symptom-oriented accident management (AM) measure based on a core exit temperature measured by SETs during core boil-off. Test 6-1 was conducted under assumptions of the total failure of the HPI system and an actuation of auxiliary feedwater, as well as the loss of off-site power concurrent with the scram signal. The break size at the PV upper-head was equivalent to 1.9% cold leg break to simulate the ejection of one whole control rod drive mechanism (CRDM) penetration nozzle. The withdrawal of control rods was not simulated. SG secondary-side depressurisation was started as a symptom-oriented AM operator action when the core exit temperature indicated a certain superheating. The relief valves (RVs) of both SGs were fully opened as soon as the measured core exit temperature reached 623 K.

Figure 5.66. Coolant flow in pressure vessel region at onset of AM action in test 6-1

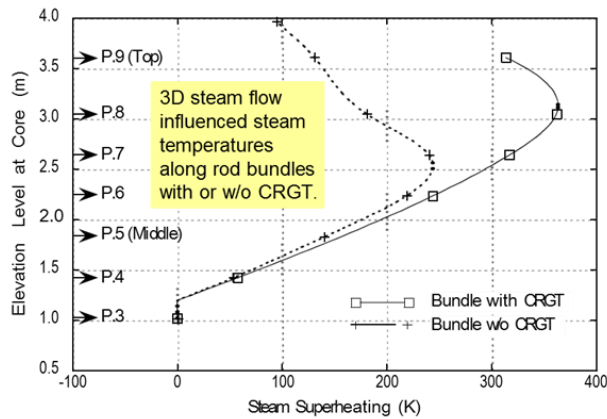


Source: NEA, 2013.

The liquid level in the upper-head was found to control the break flow rate in the experimental results as coolant in the upper plenum entered the upper-head through CRGTs until the penetration holes at the CRGT bottom were exposed to steam in the upper plenum (Figure 5.66). The cycle opening of the SG RVs induced oscillation in the upper-head mixture level. A relatively large-size break resulted in a fast primary depressurisation, especially after the break flow turned into single-phase vapour flow. The primary pressure

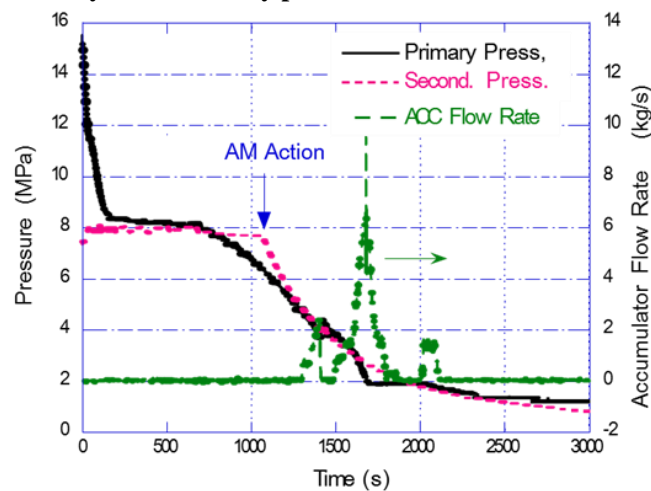
was lower than the SG secondary-side pressure almost simultaneously with the core uncover, resulting in no reflux flow from the SG. However, it took more than 230 s to initiate the AM action after the core temperature excursion started due to a late and slow response of the core exit temperature. The time delay in the detection of steam superheating was influenced by factors such as core power distribution, 3D steam flow in the core due to steam flow towards break through CRGTs, low-temperature steam flow from the core peripheral region and low-temperature metal structure around the core exit. Significant temperature distribution came about in the core and at the core exit, as shown in Figure 5.67. The AM action, to reach the intended primary depressurisation to start accumulator coolant injection, was not effective in the early stage because the primary pressure was lower than the SG secondary-side pressure at the beginning of AM action, as shown in Figure 5.68. Automatic core power decrease procedure to protect the LSTF core was then initiated due to the high core cladding temperature during core boil-off. Loop seal clearing was induced once the accumulator injection started because of significant steam condensation in both cold legs. The experiment was terminated when the long-term core cooling was confirmed by the actuation of the LPI system.

Figure 5.67. Core steam temperature 100s after initiation of AM action in test 6-1



Source: NEA, 2013.

Figure 5.68. Primary and secondary pressure and accumulator flow rate in test 6-1

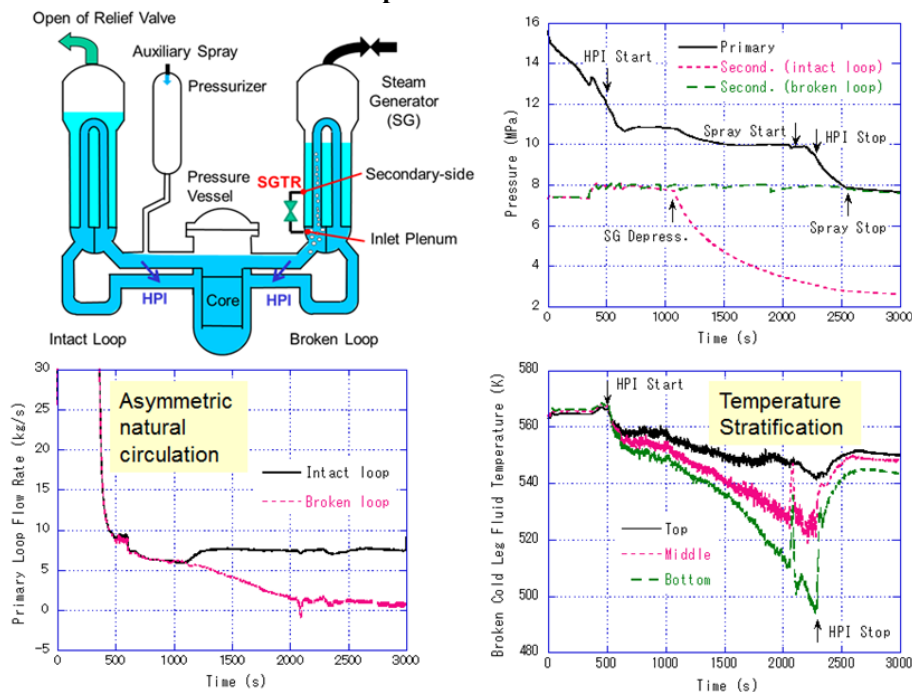


Source: NEA, 2013.

b) ROSA-2: Test 4 steam generator tube rupture (SGTR) accident

The objective was to obtain data for the evaluation of radioactive release to the environment through a broken SG RV and clarify multidimensional coolant behaviour such as temperature stratification in the horizontal leg. The SGTR is simulated by a long nozzle in the break unit, which is in a piping connected between nozzle at inlet plenum and nozzle at secondary boiler section bottom of SG in the broken loop. The nozzle size corresponds to double-ended guillotine break (DEGB) of the 1/21 volumetrically-scaled cross-sectional area of one of SG U-tubes in the 2-loop Mihama Unit-2. Manual depressurisation of the intact SG secondary side was initiated 720 s after the scram signal by fully opening the RV as an AM action and was terminated when the hot leg fluid temperature decreased to 531 K in the intact loop. Auxiliary feedwater (AFW) was initiated in both loops 70 s after the SI signal. AFW was terminated in the broken loop when the broken SG secondary-side collapsed liquid level reached 12.85 m and continued in the intact loop until the end of the test. The HPI system was initiated in both loops ten s after the SI signal, and was terminated in both loops when pressuriser (PZR) liquid level reached one m. PZR auxiliary spray was initiated by using a pump of the HPI system to enhance the primary depressurisation and to recover the liquid level in the PZR, switching over from PJ to PH pumps when the primary pressure was below 10.34 MPa and hot leg fluid temperature decreased to 547 K in the intact loop, and was terminated when the pressure equalisation between the primary and broken SG pressures was achieved.

Figure 5.69. Primary and secondary pressures, primary loop flow rate, broken cold leg fluid temperature in Test 4



Source: NEA, 2017.

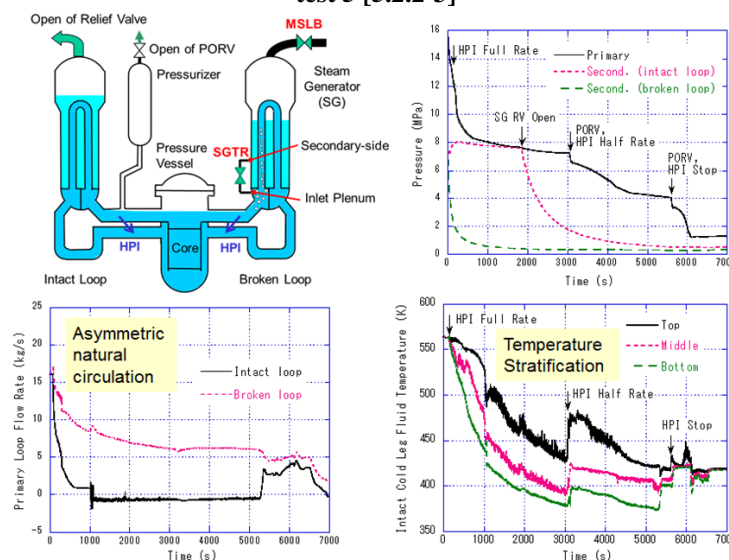
Coolant in the core was kept subcooled through the experiment, while the steam ingress into the intact loop hot leg happened from PZR. The resulting primary depressurisation, however, was significantly limited because major steam condensation on the cooled primary coolant was not enhanced due to temperature stratification. Then, the primary pressure was lowered to the broken SG secondary-side pressure by the termination of the HPI system after the confirmation of liquid level recovery in the PZR by PZR auxiliary

spray. The broken SG RV opened three times after the initiation of manual SG depressurisation. Significant temperature stratification appeared in the cold leg in the broken loop due to flow stagnation, while significant natural circulation prevailed in the intact loop after the initiation of manual SG depressurisation, with some fluid temperature fluctuation along the cold leg in the downstream of ECCS injection nozzle (Figure 5.69). The experiment was terminated when the cold shutdown condition was confirmed by the restart of the primary coolant pump in the intact loop after the pressure equalisation between the primary and broken SG pressures was achieved.

c) ROSA2: Test 5 main steam line break with steam generator tube rupture accident

The objectives of the test series were to obtain data for the evaluation of radioactive release through a ruptured SG U-tube and to clarify multidimensional coolant behaviour such as temperature stratification in the horizontal leg under significantly asymmetric loop behaviour. Test 5 was conducted under assumptions of suppression of the accumulator system actuation to keep primary coolant discharge to the SG secondary side as low as possible and loss of off-site power concurrent with the scram signal. The MSLB was simulated by using a sharp-edge orifice, which mounted at the downstream of a pipe that was connected to the SG main steam line in the broken loop. The orifice size corresponds to 40% of the 1/21 volumetrically-scaled cross-sectional area of 2-loop Mihama Unit-2 main steam tube. The SGTR is simulated in the same manner as Test 4. AFW was initiated in the broken loop after SI signal. The HPI system was initiated in both loops when the pressure vessel lower plenum pressure decreased to 12.27 MPa. As an AM action, intact SG secondary-side depressurisation was initiated by fully opening the RV 30 minutes after the SI signal. The pressure operated relief valve (PORV) was opened to recover the liquid level in the PZR when the primary pressure stagnated after the intact SG depressurisation, and was closed when the PZR liquid level reached one m. The HPI system was terminated in both loops after the 2nd PORV closure.

Figure 5.70. Primary and secondary pressures, primary loop flow rate, intact cold leg fluid temperature in test 5 [5.2.2-3]



Source: NEA, 2017

The primary pressure nearly reached equilibrium with the intact SG secondary-side pressure under the influence of SGTR, while some subcooling occurred, especially in the

broken loop, due to a fast depressurisation of broken SG through MSLB. As an AM action, intact SG secondary-side depressurisation was initiated 30 minutes after the SI signal. However, the primary pressure decreased a little and stagnated again due to the increase in HPI flow rate and decrease in the break flow rate. Significant temperature stratification appeared in the hot and cold legs in the intact loop due to the ingress of low-temperature coolant into the hot leg from upper plenum and the stagnation of high-temperature coolant over HPI coolant that flows at the cold leg's bottom. Significant natural circulation prevailed through the broken loop, with uniform fluid temperatures in the hot and cold legs due to MSLB (Figure 5.70). The experiment was terminated when the continuous core cooling was confirmed due to the coolant injection by LPI system. Consequently, in the two SGTR experiments (tests 4 and 5) there was non-symmetrical behaviour appearing between the two loops. Significant thermal stratification appeared common, but in either of two loops: either the loop with broken SG in test 4, or the loop with intact SG in test 5.

5.2.2.4. Application for system code validation

The test results of test 6-1 of the ROSA project were used to validate 3D system analysis codes for a PV upper-head break LOCA with AM measure. Time delay in the detection of the core exit temperature increase was influenced by 3D steam flow in the core. As an example, RELAP5/MOD3 code successfully predicted the overall trend of the test [5.2.2-5]. It was confirmed that accuracy in the break flow prediction in both the mass flow rate and the energy discharge rate is indispensable to the correct prediction of both the onset timing of core uncover and the primary pressure transient.

The test results of test 5 of the ROSA2 project were used to validate 3D system analysis codes for main steam line break with a steam generator tube rupture accident. Blind calculation was performed in the project for test 5, which was characterised by a strongly asymmetric response between the intact and broken loops in aspects such as natural circulation, thermal stratification and a combination of these phenomena through coolant temperature distribution [5.2.2-6]. Such complicated local and system-integral phenomena led to it being difficult to correctly predict the primary pressure before the AM action by intact SG depressurisation.

5.2.2.5. Main advantages and drawbacks of the facility

The advantage of the ROSA/LSTF is a full-pressure and full-height model of PWR, which is designed to accurately simulate the driving force of natural circulation. The time scale of simulated T/H phenomena is thus one to one to those in the reference PWR. However, the scaling distortion would be expected for the other phenomena as well as other integral effect tests.

Another advantage is the measurement for 3D phenomena. 3D fluid behaviours are detected by a combination of thermocouples, water level measurements and gamma-ray densitometers at the hot and cold legs by visual observation using a video-probe (a periscope that withstands high pressure and temperature steam/water two-phase flows).

5.2.3. LOFT

5.2.3.1. Objective of the experiment

The loss-of-fluid test (LOFT) facility was constructed between 1965 and 1975 at the Idaho National Engineering Laboratory [5.2.3-1] and [5.2.3-2]. It was a 50 MW(th) pressurised water reactor for nuclear safety research which was designed on the principle of volume

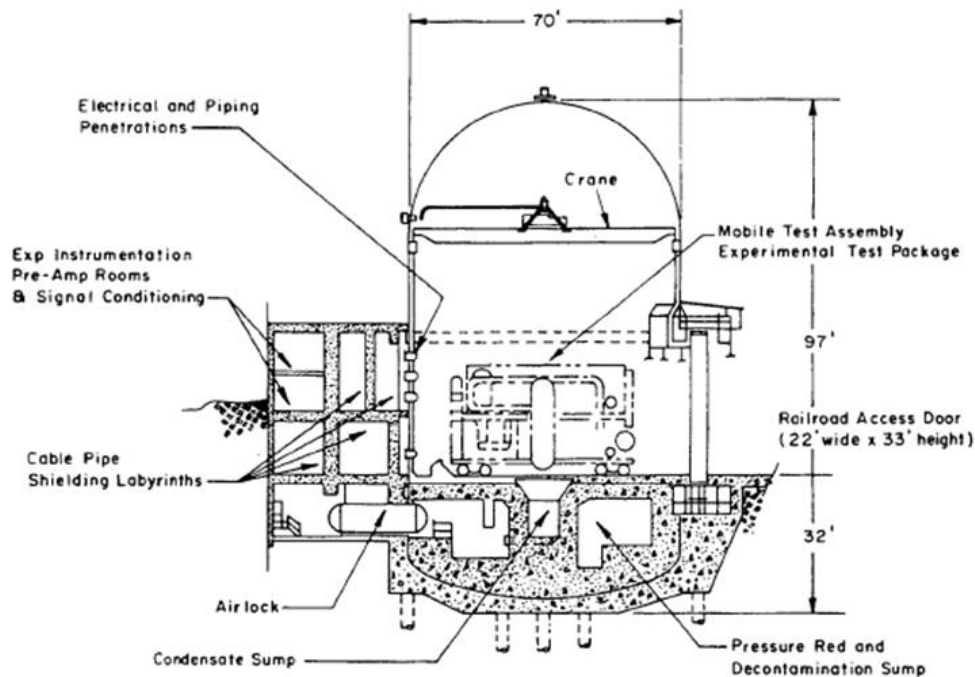
scaling to simulate the major components and system responses of a commercial PWR during a hypothetical LOCA.

Extensive research programmes were conducted at the LOFT facility under the sponsorship of the US NRC between 1978 and 1982 and, later, under the auspices of the OECD between 1983 and 1985. In all, 44 experiments, mainly small and large loss-of-coolant experiments, were carried out over a nine-year period, ending with a severe fuel damage experiment in July 1985 [5.2.3-3]. The decontamination, decommissioning and demolition of the LOFT facility were completed in October 2006.

5.2.3.2. Description of the test loop

The LOFT facility consisted of a containment facility, reactor test assembly and support facility (Figure 5.71). The reactor test assembly had a 50 MW nuclear reactor core. The primary coolant system of the reactor consisted of an intact coolant loop and broken loop. The containment dome was roughly 21 m in diameter and 30 m in height [5.2.3-4]. A detailed description of the test facility is given below.

Figure 5.71. LOFT containment section view



Source: Reeder, 1978.

Geometry

When the LOFT facility was designed in the early 1970s, the scaling issue and 3D flow effects were not of primary concern. Therefore, the scaling and measurement of the LOFT facility might not be satisfactory according to contemporary standards. However, the LOFT experimental data are still valuable for the assessment of 3D system-scale T/H analysis codes. The facility was scaled down but not small; the inner diameters of the LOFT reactor vessel and the core support barrel were about 1.46 m and 0.76 m respectively.

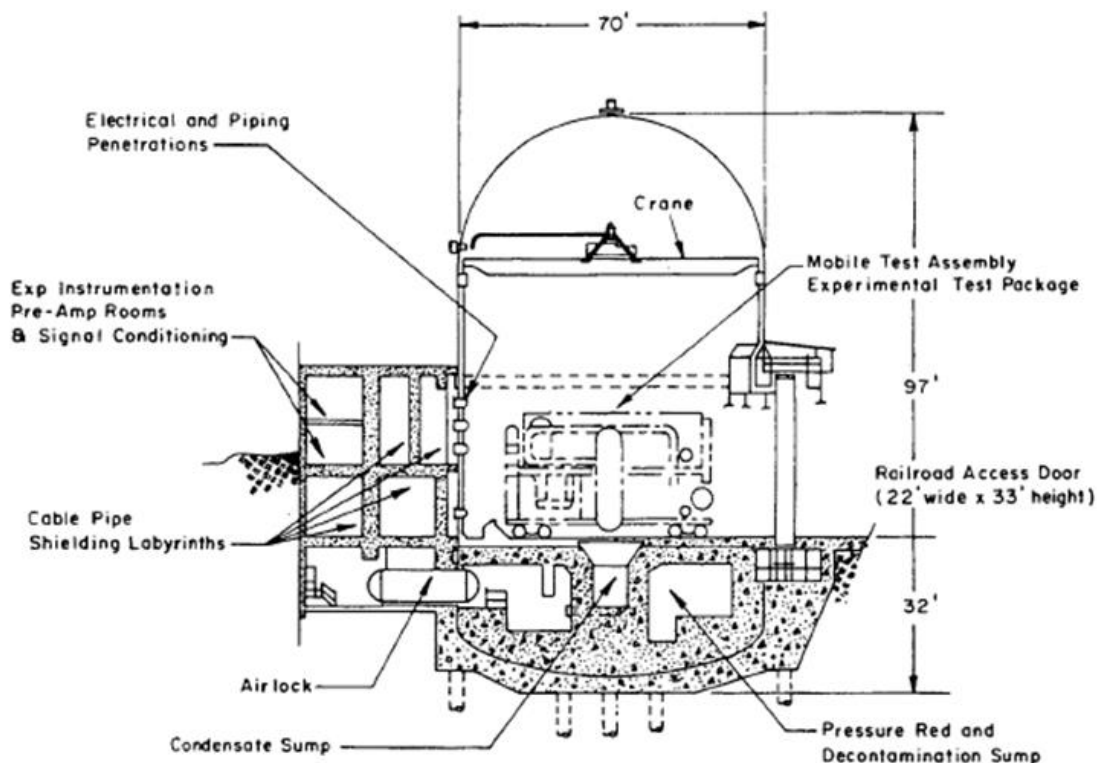
An intact loop and broken loop were symmetrically connected to the reactor vessel assembly. This configuration leads to 3D flows in the downcomer, lower plenum, reactor

core and upper plenum. Various instruments were installed at both the intact- and broken loop sides of the reactor vessel and the downcomer [5.2.3-4]. For the downcomer and lower plenum in particular, there were two downcomer “stalks” on the outer surface of the core barrel set 180° apart (very close to the intact- and broken cold legs respectively) to measure the fluid temperature, absolute pressure, liquid level and coolant velocity/momentum flux. The reactor core consisted of nine fuel assemblies and various measurements installed at the six fuel assemblies. All data involved the 3D flows in the LOFT nuclear reactor.

LOFT major components

Figure 5.72 shows the major components of the LOFT reactor test assembly in the cold leg break configuration. The reactor is a 50 MW(th) PWR scaled to simulate the behaviour of a 1 000 MW(e) commercial PWR. The nuclear core is about 1.7 m long and 0.6 m in diameter and contains 1 300 fuel pins and four control assemblies. The primary system sub-volumes (for example, the inlet plenum, core region, outlet plenum, outlet piping, steam generator and inlet piping) have been designed with relative volumes similar to those of a large PWR's (Table 5.34). The unbroken (intact) reactor coolant loops are simulated by the single unbroken circulating loop in the primary system and the postulated broken loop is simulated by the broken loop. The two 372 KW pumps in the operating loop have variable speed and coastdown inertial capabilities.

Figure 5.72 LOFT major components in cold leg break configuration



Source: Reeder, 1978.

Table 5.35. Dimensional comparison for a PWR and the LOFT facility

Parameter	PWR	LOFT
Volumes (ft³)		
- Total primary coolant system (PCS)	272	12 240
- Reactor vessel (% of PCS Volume)	34	38
- Intact Loop (% of PCS Volume) (Including pressuriser)	48	51
- Broken loop (% of PCS Volume)	18	11
Power (MWt)	55	3 400
Length of active core (ft)	5.5	12
Ratios		
- Volume/ power (ft ³ /MWt)	5.0	3.6
- Break area/ PCS volume (ft ⁻¹ x 10 ⁻⁴)	6.6	6.7
- Core surface area/ PCS volume (ft ⁻¹)	3.5	4.5

The broken loop includes orifices to simulate various break sizes and contains a steam generator and pump simulator to model the effects of these components in the broken PWR loop. The broken loop was designed to be able to simulate both hot and cold leg breaks. Quick-opening valves simulate the initiation of primary coolant piping ruptures. Primary coolant blowdown effluents from the simulated break are collected in a blowdown suppression tank that can model the PWR containment backpressure transients.

ECCS are provided to model the safety injection systems in a PWR, which provide additional capability for upper and lower plenum injection. The emergency coolant is supplied by one of two high pressure injection systems, either by low pressure injection system pumps or one of the two accumulators. Each high pressure injection system (HPIS) pump has a capacity that can be preset between 0.12 and 1.7 litre/s at 99.0 m head, and each accumulator contains ~2.46 m³ of coolant and 1.16m³ of pressurising nitrogen adjustable to pressures of 0 to 6.9 MPa.

LOFT reactor vessel

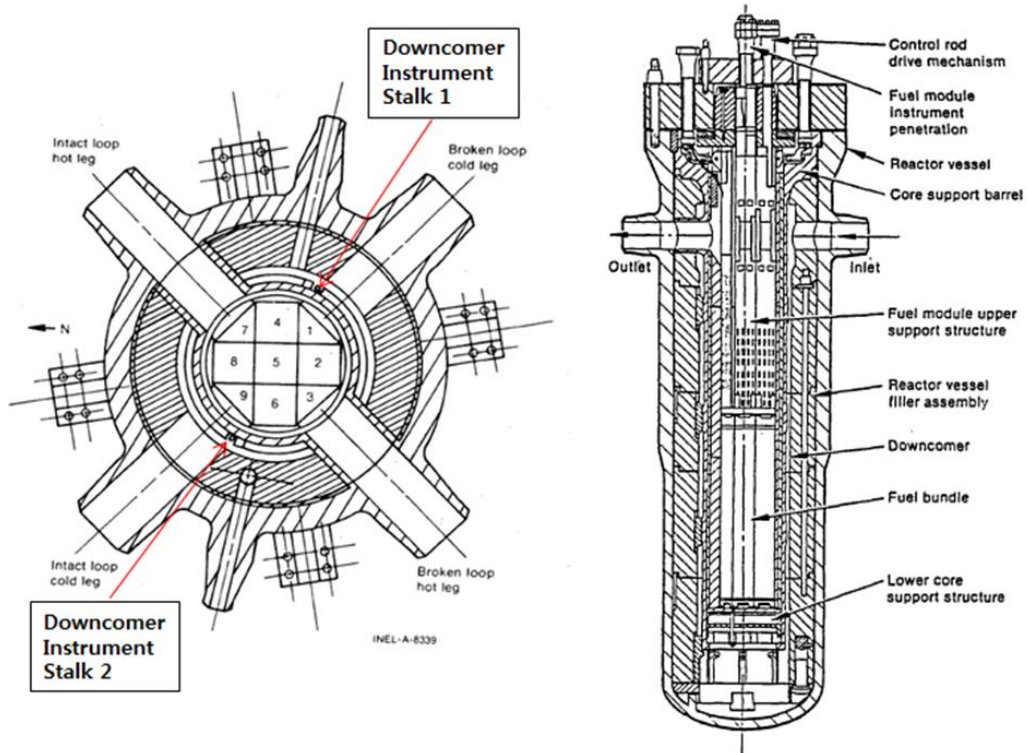
The LOFT reactor vessel and internals arrangement are shown in Figure 5.73. The key components of the reactor system are: (i) reactor vessel and head, (ii) core support barrel, (iii) upper and lower core support structures, (iv) flow skirt, (v) reactor vessel fillers and (vi) 1.68-metre core. The configuration of the reactor vessel upper-head is somewhat different from those of typical commercial PWRs.

The inner diameters of the LOFT reactor vessel and core support barrel were about 1.46 m and 0.76 m respectively. The reactor vessel fillers were installed in the downcomer gap between the reactor vessel and the core support barrel, which is relatively big compared to those of commercial PWRs, to displace excess coolant in the inlet plenum and downcomer regions and maintain the ratio of water in the inlet and outlet plenums to that in the core and primary system as similar to for a PWR. The annular downcomer was therefore divided into an inner 2-inch annulus and outer 0.25-inch annulus. An intact loop and broken loop were symmetrically connected to the reactor vessel assembly.

The 1.68 m core in the LOFT reactor vessel was designed to have the same physical, chemical and metallurgical properties as those in large PWRs. The core was also designed to provide T/H relationships, mechanical response and fission product release behaviour during the LOCEs and ECC recovery, which are representative of large PWRs during a LOCA.

Figure 5.73 shows a cross-sectional layout of the LOFT core. Two basic fuel assembly configurations are used. Five assemblies have a square cross-section with fuel pins and guide tubes. Four assemblies have a triangular cross-section using a portion of the square cross-section structure. The square fuel bundles contain 225 pin locations (15x15 pins). Twenty-one of these locations are occupied by guide tubes, except for in the centre bundle. The triangular assemblies contain 78 pin locations (12 pins along each side). Eight of these locations are occupied by guide tubes. The fuel assemblies are arranged and numbered as shown in Figure 5.73. Assemblies 2, 4, 5, 6, and 8 are square, and assemblies 1, 3, 7 and 9 are triangular. Only assemblies 1, 2, 3, 4, 5 and 6 are instrumented. Fuel assemblies 2, 4, 6 and 8 accommodate the control rods. The centre fuel assembly, assembly 5, is the most active and most heavily instrumented portion of the core.

Figure 5.73. LOFT reactor vessel and internals arrangement



Source: Reeder, 1978.

Instruments and measurements

The primary objective of the LOFT experiment was to provide transient T/H and fuel performance experimental data for a wide spectrum of off-normal and accident conditions. New instrumentation that was not available for a commercial PWR when it was being developed can provide the data necessary to satisfy LOFT's principal objective. This instrumentation must have the capability of measuring the rapidly changing two-phase flow phenomena and also of withstanding the severe nuclear environment that results from accidents [5.2.3-4] and [5.2.3-5].

Over 800 measurements are made in the LOFT facility for a typical loss-of-coolant experiment. These measurements are concentrated in three areas: (i) the primary reactor cooling system; (ii) the reactor vessel; and (iii) the suppression system. As a consequence of the Three Mile Island accident, emphasis in the LOFT Programme shifted from large break LOCAs to small break LOCAs. While the instrumentation available for large break

experiments could be used for small break LOCAs, additional measurements were needed to investigate the small break LOCA phenomena.

In general, the measurement uncertainties for the measured principal variables were determined as:

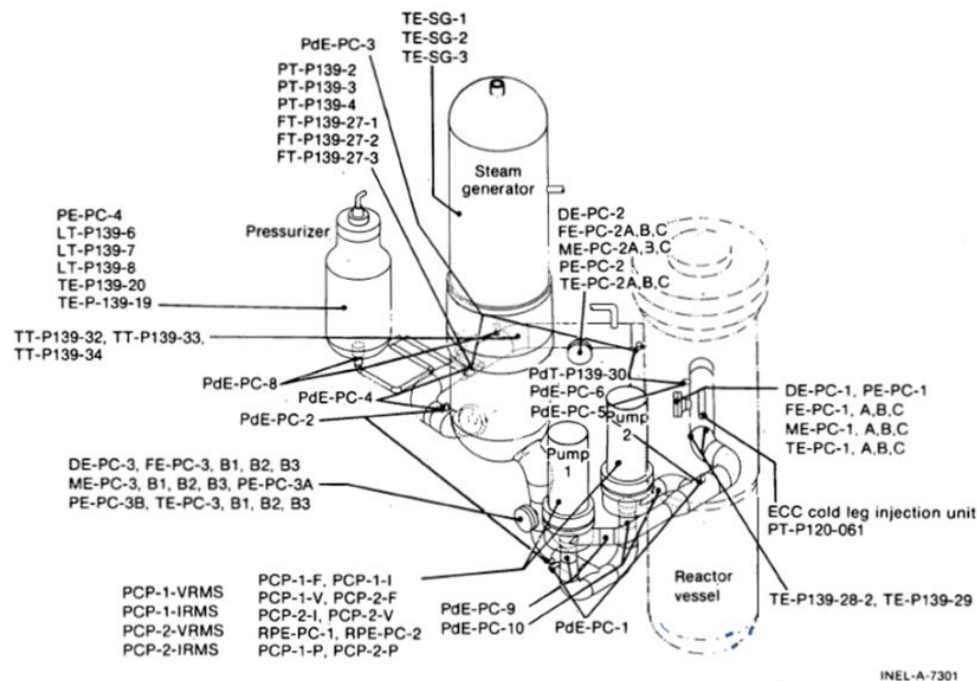
- temperature: ± 3 K;
- pressure: ± 0.03 Mpa;
- differential pressure: ± 0.01 Mpa;
- density: ± 30 kg/m³;
- momentum flux: $\pm 12\,000$ kg/m² s;
- velocity: ± 2.7 m/s.

Primary coolant system (PCS) instrumentation

The LOFT PCS consists of an active intact loop and passive broken loop. The components in the intact loop include pumps, a steam generator, pressuriser and ECC systems.

There are five principal measuring stations in the LOFT piping. Three are located in the intact loop and one in each leg of the broken loop (Figures 5.74 and 5.75 respectively). The measurements and designation at each station consist of: (i) pressure (PE), (ii) temperature (TE), (iii) density (DE), (iv) velocity (FE) and momentum flux (ME).

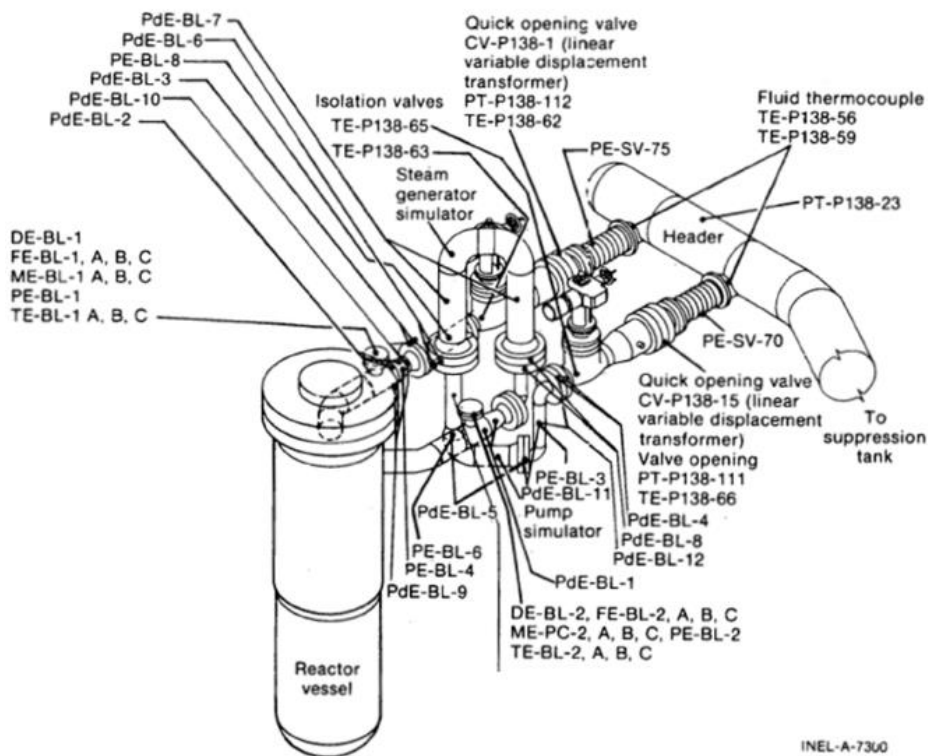
Figure 5.74. LOFT thermo-fluid measurement instrumentation: intact loop



Source: Reeder, 1978.

In addition to the five major measuring stations, instrumentation is included on all major reactor system components, including the pumps, steam generator, pressuriser and ECC systems. Both primary coolant pumps have a pump speed indicator. In addition to pump speed, differential pressure measurements are made across each pump to provide an indication of time varying pump head.

Figure 5.75 LOFT thermo-fluid measurement instrumentation: broken loop cold leg



Source: Reeder, 1978.

Temperature and differential pressure are measured in the steam generator. The fluid temperature measurements are located at the steam generator's inlet and outlet. A bulk fluid temperature measurement is also made on the secondary side. Differential pressure is measured at two different elevations on the secondary side to establish the level, while differential pressure is measured across the inlet and outlet of the primary side of the steam generator.

Like for the steam generator, temperature and differential pressure are measured in the pressuriser. Liquid level is also measured using differential pressures at three different levels. A differential pressure measurement across the surge level is provided to ascertain the single-phase resistance of the surge line and to provide a measure of the flow entering and/or leaving the surge line during all experiments.

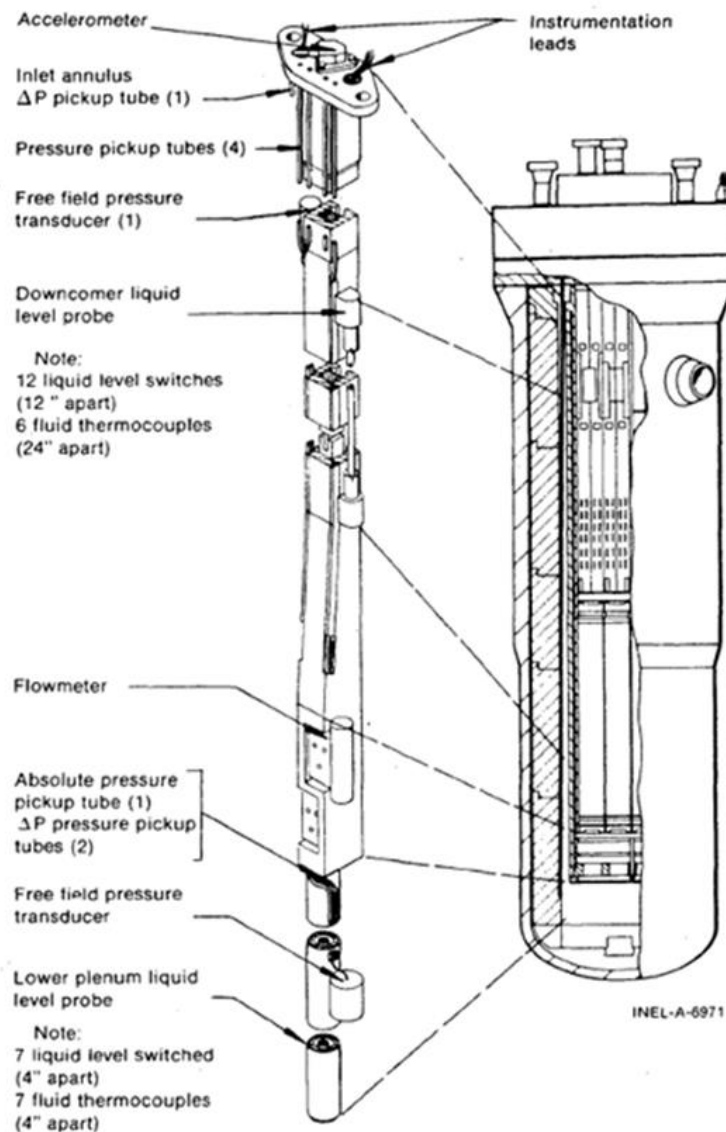
Four basic measurements are installed for the LOFT ECCS: pressure, temperature, flow and level. Pressure and fluid temperature are measured at accumulator A, accumulator B, hot leg injection point, upper plenum injection point, downcomer injection point, cold leg injection point, lower plenum injection point, LPIS A pump discharge and LPIS B pump discharge. Volumetric flow measurements are made at each accumulator's discharge and at the outlet of the high and low pressure injection systems. The levels for each accumulator are derived from differential pressure measurements.

Reactor vessel instrumentation

Thermo-fluid measurements in the LOFT reactor vessel are concentrated in (i) the downcomer and lower plenum, (ii) core and (iii) upper plenum.

The downcomer and lower plenum measurements are concentrated on two downcomer “stalks”, which are on the outer surface of the core barrel at 180° apart (Figures 5.73 and 5.76). The instrumentation on each stalk is identical and consists of fluid temperature, absolute pressure, liquid level, coolant velocity and momentum flux. Fluid temperature is measured in a similar way as the one for measuring the primary piping. These measurements are gathered from 14 discrete elevations. The liquid level is measured at seven elevations in the lower plenum at four-inch intervals between 8.4 and 32 inches above the bottom of the reactor vessel. Downcomer liquid level is measured in 12 inch intervals between 68.4 and 200.4 inches above the reactor vessel’s lower head.

Figure 5.76 Reactor vessel downcomer instrument stalk instrument locations



Source: Reeder, 1978.

Core instrumentation

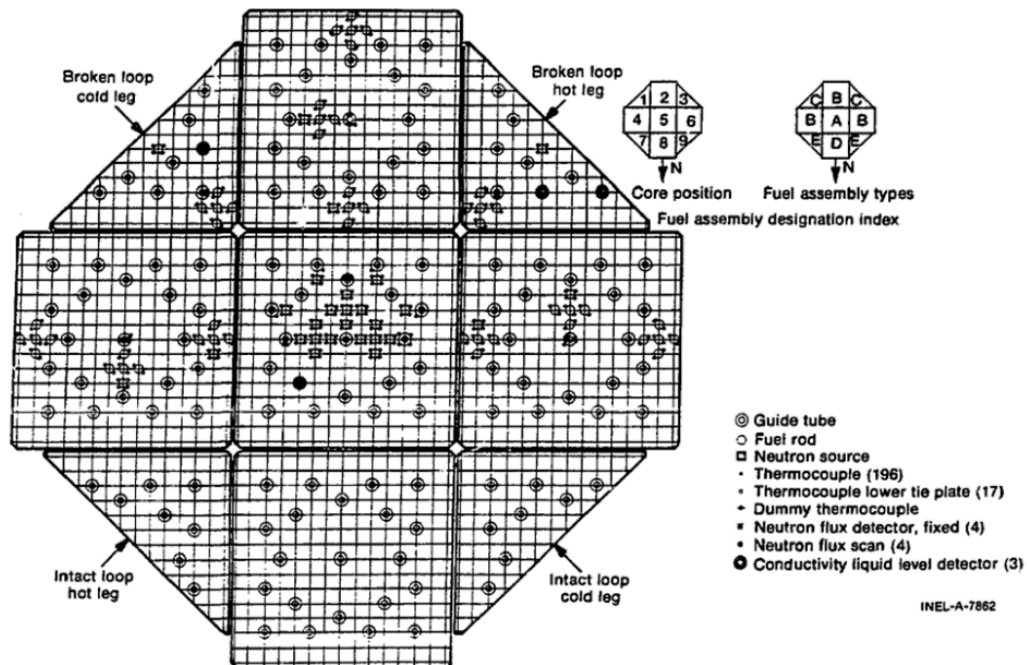
The LOFT core consists of 1 300 fuel rods. The fuel rods are of nominal PWR design, except for their length (1.67 m) and internal pre-pressurisation (0.10 MPa).

Five basic measurements are gathered from or within the boundary of the core region. These measurements are of the fluid temperature, clad temperature, liquid level, mass flow and neutron flux.

There are 38 fluid temperature measurements located in the core. There are 185 measurements of fuel cladding temperatures, which are measured on the outside of the zircaloy clad fuel (Figure 5.77). There are also 11 thermocouples located on the stainless steel guide tubes. Liquid level measurements are gathered from four separate radial locations in the LOFT core. Each level detector counts 19 conductivity probes at four-inch intervals. Fluid velocity and momentum flux are measured at the outlet of the LOFT core in three locations: above the centre fuel module and in the two corner modules adjacent to the cold legs. These measurements are gathered using the drag disc turbine transducer.

Two types of transducers are used for neutron flux measurements: scanning and fixed location detectors. The scanning detector is used to give an accurate measurement of the steady-state power distribution and fixed detectors are used to measure the power transient during a LOCE. The scanning detector (traversing in-core probe [TIP]) is a complete and independent system, which has its own transducer, positioning subsystem, signal conditioning, recording subsystem as well as the required cabling, construction or mechanical details. The system provides graphs of the axial flux distribution at four different locations in the core. There are four fixed neutron flux detectors and four scanning flux detectors.

Figure 5.77 LOFT core configuration and instrumentation



Source: Reeder, 1978.

Upper plenum instrumentation

The upper plenum instrumentation consists of a liquid level detector, four pressure measurements, fluid thermocouples and metal thermocouples.

The liquid level detector in the upper plenum is in the corner fuel module, adjacent to the broken loop hot leg. It contains nine probes spaced at 8 inch intervals. Free-field pressure transducers are located 27 inches above the corner fuel assemblies, adjacent to the intact and broken cold legs respectively. The absolute pressure measurements are 20 inches above the free-field transducers.

There are five coolant thermocouples and two guide tube thermocouples in the upper plenum. Three coolant thermocouples are in the upper end box. The remaining two are 14 and 28 inches above the cold leg nozzle centreline respectively. The metal thermocouples are on the upper core support structure at 10 and 45 inches above the top of the core respectively (62 and 27 inches below the centreline of the cold leg nozzle).

Suppression system instrumentation

Measurements of the suppression system consist of the spray flow velocities and rates, liquid level, pressure, fluid temperature and strain. This instrumentation had been used to determine suppression pool dynamics for the refined control of reflood backpressure.

LOFT instrumentation for SB-LOCE

As a consequence of the Three Mile Island accident, emphasis in the LOFT Programme shifted from large break LOCAs to small break LOCAs. While the instrumentation available for large break experiments were used for small break LOCAs, additional measurements were implemented to investigate the small break LOCA phenomena. These include the accurate measurement of low flows during natural circulation, break flow, pump degradation, upper plenum level and pressuriser behaviour (flow at the PORV and flow behaviour in the surge line).

5.2.3.3. Tests performed

The LOFT research programme was originally set up by the US Nuclear Regulatory Commission. Part of the programme was later broadened into an international collaboration project under the auspices of the NEA. The initial programme addressed several LOCA configurations, carrying out large break tests and intermediate break tests from 1978 to 1982.

The experiment series of the initial programme (from L1 to L7) are listed in Table 5.35 [5.2.3-6]. The NEA's experimental programme of the LOFT project consisted of eight experiments: six T/H experiments and two fission product release experiments, as listed in Table 5.36 [5.2.3-3].

The initial operating conditions of the LOFT experiments were similar to those of a typical PWR. For example, Table 5.37 shows the initial conditions for the LOFT L2-3 experiment [5.2.3-7]. The boundary conditions and the sequence of events were controlled for each experiment.

Table 5.36. LOFT experiment series: 1978-1982²

Experiment series	Type of experiments
L1 (5 tests)	Non-nuclear LOCE: - L1-1: Half size double-ended hot leg - L1-2: Full-size double-ended cold leg, no ECC - L1-3: Full-size double-ended cold leg, lower plenum ECC - L1-4: Full-size double-ended cold leg, cold leg ECC - L1-5: Core installed LI-4 counterpart
L2 (5 tests)	Nuclear power ascension LOCE double-ended cold leg break - L2-2: 26.4 KW/m MLHGR ³ - L2-3: 39.4 KW/m MLHGR - L2-4: 52.3 KW/m MLHGR - L2-5: 39.4 KW/m MLHGR, loss of electric power - L2-6: 39.4 KW/m MLHGR, pressurised fuel
L3 (7 tests)	Nuclear LOCE with small- and intermediate-size breaks - L3-0 Non-nuclear, PORV - L3-1 Nuclear, depressurisation - L3-2 Nuclear, "constant" pressure - L3-3 Nuclear, repressurisation - L3-4 Nuclear, PORV - L3-5 Non-nuclear, intact loop, pumps off - L3-6 Non-nuclear, intact loop, pumps on
L4 (5 tests)	Nuclear LOCE alternate ECCS - L4-1 Lower plenum injection - L4-2 Hot leg injection - L4-3 Combined hot and cold leg injection - L4-4 Direct downcomer injection - L4-5 Cold leg injection with upper plenum/downcomer pressure equalisation.
L5 (2 tests)	Nuclear LOCE hot leg breaks
L6 (6 tests)	Nuclear non-LOCE L7 - L6-1 Loss of steam load - L6-2 Loss of PCS flow - L6-3 Excessive load increase - L6-4 Rod withdrawal - L6-5 Loss of feedwater - L6-6 Uncontrolled boron dilution
L7 (2 tests)	Nuclear LOCE with steam generator tube rupture

Table 5.37. NEA LOFT experiment programme: 1983 – 1985

Experiment Id.	Conditions of experiment (date)
LP-FW-1	Loss-of-feedwater, primary feed and bleed recovery procedure - (20/02/1983)
LP-SB-1	Hot leg SB-LOCA, early pump trip - (23/06/1983)
LP-SB-2	Hot leg SB-LOCA, delayed pump trip - (14/07/1983)
LP-SB-3	Cold leg SB-LOCA, core uncover, secondary feed and bleed recovery procedure, accumulator injection at low pressure differential - (05/03/1984)
LP-02-6	200% large break LOCA, US licensing case - (03/10/1983)
LP-LB- 1	200% large break LOCA, UK licensing case - (03/02/1984)
LP-FP-1	Gap fission product release, large break LOCA, German licensing case - (19/12/1984)
LP-FI-2	Fission product release at high fuel temperatures (above 2 100 K), V-sequence - (03/07/1985)

² In all, 44 experiments were conducted. However, only 40 experiments are listed in Tables 5.35 and 5.36.

Table 5.38. Initial conditions for the LOFT L2-3 experiment

Parameter	Measured value
Reactor vessel	
- Power level (MW)	36 ± 1.0
- Maximum linear heat generation rate (k W/m)	39 ± 3.0
Intact loop	
- Mass flow rate (kg/s)	199 ± 6.3
- Cold leg temp. (K)	560.7 ± 1.8
- Hot leg temp. (K)	592.9 ± 1.8
Broken loop	
- Hot leg temp. near vessel (K)	565.5 ± 1.8
- Hot leg temp. near break (K)	556.5 ± 1.8
- Cold leg temp. near vessel (K)	554.5 ± 1.8
- Cold leg temp. near break (K)	550.3 ± 1.8
Pressurizer	
- Pressure (MPa)	15.06 ± 0.03
- Water volume (m ³)	0.670 ± 0.008
- Water temp. (K)	615.3 ± 3.0
Steam generator secondary side	
- Water level (m)	3.11 ± 0.025
- Water temp. (K)	482.1 ± 3.0
- Pressure (MPa)	6.18 ± 0.08
- Mass flow rate (kg/s)	19.5 ± 0.4

5.2.3.4. Application for system code validation

There are numerous research reports and technical papers related to the LOFT data. Most are concerned with the development and assessment of T/H system codes, such as RELAP5 series, TRAC series, CATHARE2, TRACE, MARS and ATHLET.

The LOFT experimental data are currently available from the US NRC/RSR data bank system [5.2.3-8] and the NEA's Data Bank system [5.2.3-9].

The experimental data have been used extensively for the development and assessment of T/H system codes, such as the TRAC and RELAP5 code series. Some of the experiments, such as the L1-4, L3-1, L3-6/L08-1, and L2-5 experiments, were adopted as the international standard problems (ISPs) exercises, which had been organised by the NEA's CSNI for comparative exercises using various best estimate T/H system codes [5.2.3-10]. These code assessments were generally based on 1D analysis. The 3D analyses of the LOFT experiments and/or code assessment are limited [5.2.3-11], [5.2.3-12] and [5.2.3-13].

5.2.3.5. Main advantages and drawbacks of the facility

The LOFT facility was one of the most prominent reactor safety research facilities in the world. Most of the LOFT experiments focused on experiments for LOCAs. The facility had provided invaluable experimental data, leading to in-depth understanding of integrated two-phase flow phenomena in a PWR during a LOCA.

The LOFT facility was constructed between 1965 and 1975 to simulate the major components and system responses of a commercial PWR during a hypothetical LOCA. At that time there was no special interest in 3D flow phenomenon. The volume scaling law was well followed while reducing and designing a commercial nuclear power plant into a 50 MW research reactor. The installation of various measuring equipment in the reactor downcomer and core allowed for 3D flow phenomenon occurring inside the reactor to be measured. Although this facility was not designed in consideration of 2D/3D flow effects, its experimental data could be useful for 2D/3D code validation.

References

- [5.1.1-1] Grunwald, G., S. Kliem, T. Höhne, U. Rohde, H.M. Prasser, K.H. Richter and F.P. Weiss (2002), “Versuchsanlage ROCOM zur Untersuchung der Kühlmittelvermischung in Druckwasserreaktoren-Ergebnisse quasistationärer Vermischungsexperimente”, Report FZR-348, ISSN 1437-322X, HZDR, Rossendorf.
- [5.1.1-2] Salah, A.B. and J. Vlassenbroeck (2013), “Assessment of the CATHARE 3D capabilities in predicting the temperature mixing under asymmetric buoyant driven flow conditions”, *Nuclear Engineering and Design*, 265, pp. 469.
- [5.1.1-3] Schöffel, P.J., H.V. Hristov and G. Lerchl (2014), “Towards multidimensional thermal-hydraulic simulations with the system code ATHLET”, 45th Annual Meeting on Nuclear Technology 6-8 May, Frankfurt am Main, Germany.
- [5.1.1-4] J. Kurki (2015), “Modelling of ROCOM mixing Test 2.2 with TRACE v5.0 Patch 3”, NUREG/IA-0454, US Nuclear Regulatory Commission, Washington, DC.
- [5.1.1-5] Pandazis, P., S.C. Ceuca, P.J. Schöffel and H.V. Hristov (2015), “Investigation of the multidimensional flow mixing phenomena in the reactor pressure vessel with the system code ATHLET”, NURETH-16, 40 August-4 September, Chicago, United States.
- [5.1.1-6] NEA (2017), “Solving Thermal-Hydraulic Safety Issues for Current and New Pressurised Water Reactor Design Concepts”, OECD Publishing, Paris, NEA/CSNI/R(2017)6, www.oecd-neo.org/jcms/pl_19778.
- [5.1.2-1] Leyer, S. and M. Wich (2011), “The integral test facility Karlstein – INKA”, NURETH-14, 25-30 September, Toronto, Ontario, Canada.
- [5.1.3-1] Damerell, P.S. and J.W. Simons, editors (1993), “2D/3D Program Work Summary Report. GRS Report GRS-100”, US Nuclear Regulatory Commission, Washington, DC.
- [5.1.3-2] Mayinger, F., H.G. Sonnenburg, R. Zipper, J. Liebert, H.P. Gaul and R. Hertlein (1999), “Erkenntnisse aus dem UPTF-TRAM Versuchsvorhaben – Gemeinsamer Bericht von GRS, SIEMENS und TU München”, GRS Report GRS-A-2679, Germany.
- [5.1.3-3] Weiss, P.A., H. Watzinger and R. Hertlein (1990), “UPTF experiment: a synopsis of full-scale test results”, *Nuclear Engineering and Design*, 122(1-3), pp. 219-234.
- [5.1.3-4] Weiss, P.A. and R.J. Hertlein (1988), “UPTF test results: First three separate effect tests”, *Nuclear Engineering and Design*, 108(1-2), pp. 249-263.
- [5.1.3-5] Glaeser, H. (1992), “Downcomer and tie plate countercurrent flow in the Upper Plenum Test Facility (UPTF)”, *Nuclear Engineering and Design*, 133(2), pp. 259-283.
- [5.1.3-6] Wolfert, K. and I. Brittain (1988), “CSNI validation matrix for PWR and BWR thermal-hydraulic system codes”, *Nuclear Engineering and Design*, 108(1-2), pp. 107-119.
- [5.1.3-7] Dor, I. (1994), “Analysis of UPTF downcomer tests with the CATHARE multidimensional model”, *Nuclear Engineering and Design*, 149(1-3), pp. 129-140.
- [5.1.3-8] Jeong, J.J., I. Dor and D. Bestion (1997), “Improvement and Assessment of the CATHARE2 Three-dimensional Module compared with the UPTF Downcomer Test 7”, *Nuclear Technology*, 117(3), pp. 267-280.
- [5.1.3-9] Takeuchi, K. and M.Y. Young (1998), “Assessment of flooding in a best estimate thermal hydraulic code (WCOBRA/TRAC)”, *Nuclear Engineering and Design*, 186(1-2), pp. 225-255.
- [5.1.3-10] Bieder, U. and E. Graffard (2008), “Qualification of the CFD code Trio_U for full-scale reactor applications”, *Nuclear Engineering and Design*, 238(3), pp. 671-679.

- [5.1.3-11] Mériçoux, N., J. Laviéville, S. Mimouni, M. Guingo and S. Bellet (2017), “Verification, validation and application of NEPTUNE_CFD to two-phase Pressurised Thermal Shocks”, *Nuclear Engineering and Design*, 312, pp. 74-85.
- [5.1.4-1] Ichikawa, M. (1995), “2D/3D Program Work Summary Report”, JAERI-1335, Japan.
- [5.1.4-2] Ichikawa, M. (1995), “Reactor Safety Issues Resolved by the 2D/3D Program”, JAERI-1335, Japan.
- [5.1.4-3] US NRC (2006), “TRACE V5.0 ASSESSMENT Appendix C: Integral Effects Tests”, US Nuclear Regulatory Commission, Washington, DC.
- [5.1.5-1] Reinhardt, H.J. (1989). *A study of 2Dimensional Effects in the Core of a PWR during the Reflooding Phase of a LOCA. Analysis of Data of PERICLES Experiments with the COBRA-NC code.* NC code (No. EUR--12408). Commission of the European Communities.
- [5.1.5-2] Deruaz, R., P. Clément and J.M. Veteau (1985), “Effects in the core during the reflooding phase of a LOCA, Safety of Thermal Water Reactors”, in *Safety of Thermal Water Reactors*, Graham & Trotman Limited: Springer, Dordrecht, pp. 103-113.
- [5.1.5-3] Morel, C. and P. Boudier (1999), “Validation of the CATHARE code against PERICLES 2D REFLOODING Tests”, NURETH-9, 3-8 October, San Francisco.
- [5.1.5-4] Morel, C. and D. Bestion (1999), “Validation of the CATHARE code against PERICLES 2D BOIL-UP Tests”, NURETH-9, 3-8 October, San Francisco.
- [5.1.6-1] Yoon, S.J., S.B. Kim, G.-C. Park, H.Y. Yoon and H.-K. Cho (2018), “Application of CUPID for subchannel-scale thermal-hydraulic analysis of pressurised water reactor core under single-phase conditions”, *Nuclear Engineering and Technology*, 50(1).
- [5.1.6-2] Kim, S., H.S. Choi, Y.J. Youn, I.C. Chuh and D.J. Euh (2017), “Experimental study on flow visualization inside subchannels of PWR rod bundle”, Transactions of the Korean Nuclear Society Spring Meeting, 18 May, Jeju, Korea.
- [5.1.6-3] Bestion, D., M. Valette, P. Fillion and P. Gaillard (2017), “3D Core thermal-hydraulic phenomena in PWR SBLOCAs and IBLOCAs”, NURETH-17, 3-8 Sept, Xian, China
- [5.1.7-1] Kim, K., D.J. Euh, I.C. Chu, Y.J. Youn, H.S. Choi and Y.S. Kwon (2013), “Experimental study of the APR+ reactor core flow and pressure distributions under 4-pump running conditions”, *Nuclear Engineering and Design*, 265, pp. 957-966.
- [5.1.8-1] Euh, D.J., S. Kim, B.D. Kim, W.M. Park, K.D. Kim, J.H. Bae, J.Y. Lee and B.J. Yun (2013), “Identification of Two-dimensional Void Profile in a Large Slab Geometry Using an Impedance Measurement Method”, *Nuclear Engineering and Technology*, 45(5), pp. 613-624.
- [5.1.9-1] Euh, D.J., B.G. Huh, B.J. Yun, C.H Song and I.G. Kim (2008), “Performance Evaluation of the Safety Analysis Codes for the Subcooled Boiling Phenomena in a Nuclear Reactor Downcomer during the Late Reflood Phase of an LBLOCA”, *Nuclear Technology*, 164(3), pp. 368-384.
- [5.1.9-2] Yun, J., D.J. Euh and C.H Song (2008), “Downcomer boiling phenomena during the reflood phase of a large break LOCA for the APR1400”, *Nuclear Engineering and Design*, 238, pp. 2064-2074.
- [5.1.10-1] Yun, B.J., H.K. Cho, T.S. Kwon, C.H. Song, J.K. Park and G.C. Park (2001), “Air-Water Test on the Direct ECC Bypass during LBLOCA Reflood Phase with DVI: UPTF Test 21D Counterpart Test”, *Nuclear Engineering and Technology*, 33(3), p. 315.
- [5.1.11-1] NEA (2012), “OECD/NRC Benchmark Based on NUPEC PWR Sub-channel and Bundle Tests (PSBT) Volume I: Experimental Database and Final Problem Specifications”, OECD Publishing, Paris, NEA/NSC/DOC(2012)1, www.oecd-nea.org/jcms/pl_19106.

- [5.1.11-2] NEA (2016), “International Benchmark on Pressurised Water Reactor Sub-channel and Bundle Tests Volume II: Benchmark Results of Phase I: Void Distribution”, OECD Publishing, Paris, NEA/NSC/R(2015)4, www.oecd-nea.org/jcms/pl_19660.
- [5.1.11-3] NEA (2016), “International Benchmark on Pressurised Water Reactor Sub-channel and Bundle Tests Volume III: Departure from nucleate boiling”, OECD Publishing, Paris, NEA/NSC/R(2015)7, www.oecd-nea.org/jcms/pl_19676.
- [5.1.11-4] Mishima, Y., T. Okubo, T. and M. Oishi (1989), “Proving test on reliability of PWR fuel assembly”, *Nippon Genshiryoku Gakkai-Shi*, 31(10), pp. 1129-1143.
- [5.1.11-5] Hori, K., K. Miyazaki, T. Kurosu, S. Sugiyama, J. Matsumoto and Y. Akiyama (1993), “In bundle void fraction measurement of PWR fuel assembly.” ICONE-2, 21-24 March, San Francisco.
- [5.1.12-1] NEA (2005), “NUPEC BWR full-size fine-mesh bundle test (BFBT) benchmark Volume I: Specifications”, NEA/NSC/DOC(2005)5, OECD Publishing, Paris, http://www.oecd-nea.org/jcms/pl_14238.
- [5.1.12-2] Inoue, A., T. Kurosu, T. Aoki and M. Yagi (1995), “Void fraction distribution in BWR fuel assembly and evaluation of sub-channel code”, *Journal of Nuclear Science and Technology*, 32(7), pp. 629-640.
- [5.1.12-3] Gluck, M. (2008), “Validation of the sub-channel code F-COBRA-TF Part II. Recalculation of void measurement”, *Nuclear Engineering and Design*, 238(9), pp. 2317-2327.
- [5.1.13-1] Glantz, T. and R. Freitas (2008), “Improvement of the CATHARE 3D code prediction on PIERO transient”, ICONE 16, 11-15 May, Orlando, Florida, United States.
- [5.1.13-2] Freitas, R. and Y.D. Pasquale (2015), “Validation of CATHARE 3 code on the PIERO experiment”, NURETH-16, 30 August-4 September, Chicago.
- [5.1.13-3] Herer, C., A. Beisegel, P. Imbert, D.A. Farnsworth and F. Burtak, (2005) “Comparison of PWR fuel assembly CHF test obtained at three different test facilities”, NURETH-11, 2-6 October, Avignon, France.
- [5.1.13-4] Park, H.Y., K.H. Kim, E.J. Park, P. Clément and G. Cubizolles (2013), “Verification of OMEGA-2 CHF loop reliability via benchmarking CHF tests”, ICAPP 2013, 14-18 April, Jeju Island, Korea.
- [5.1.13-5] Cubizolles, G., T. Chataing, P. Clément and D. Groeneveld (2009), “PWR Bundle Heat Transfer Tests in the OMEGA-2 Test Facility”, NURETH-13, 27 September- 2 October, Kanazawa, Japan.
- [5.1.13-6] Cubizolles, G., P. Clément and D. Groeneveld (2013), “Repeatability of heat transfer tests in a 5×5 bundle geometry”, *Nuclear Engineering and Design*, 264, pp. 89-96.
- [5.1.13-7] De Crécy, F. (1994), “The effect of grid assembly mixing vanes on critical heat flux values and azimuthal location in fuel assemblies”, *Nuclear Engineering and Design*, 149(1-3), pp. 233-241.
- [5.1.13-8] Bergeron, A., D. Caruge and Ph. Clément (1999), “Assessment of the 3D thermal-hydraulic nuclear computer code FLICA-IV on rod bundle experiments”, NURETH-9, 3-8 October, San Francisco, California.
- [5.1.13-9] Garnier, J. (1997), “Isokinetic sampling of boiling R12 in a rod bundle: methodology and first results”, Fourth International Seminar on Subchannel Analysis, 25-26 September, Tokyo.
- [5.1.13-10] Chandesris, M., M. Mazoyer, G. Serre and M. Valette (2013), “Rod bundle thermalhydraulics mixing phenomena: 3D analysis with CATHARE 3 of various experiments”, NURETH-15, 12-17 May, Pisa, Italy.

- [5.1.13-11] Falk, F. and A. Momponteil (1998), “Détermination d’un champ de vitesse 3D en géométrie complexe par vélocimétrie laser 2D [Determination of a 3D velocity field in complex geometry by 2D laser velocimetry]”, 6e congrès francophone de vélocimétrie laser, 22-25 September, Saint-Louis, France.
- [5.1.13-12] Bieder, U., F. Falk and G. Faucher (2014), “CFD analysis of the flow in the near wake of a generic PWR mixing grid”, *Progress in Nuclear Energy*, 75, pp. 15-24.
- [5.1.13-13] Bieder, U., F. Falk and G. Faucher (2015), “LES analysis of the flow in a simplified PWR assembly with mixing grid”, *Annals of Nuclear Energy*, 82, pp. 169-178.
- [5.1.13-14] Serre, G., M. Chandesris and D. Bestion (2013), “Modelling the heat transfer enhancement by grids in rod-bundle using a turbulence model in the CATHARE-3 code”, NURETH-15, 12-17 May, Pisa, Italy.
- [5.1.13-15] NRC, U. (1998), “Compendium of ECCS research for realistic LOCA analysis”, US Nuclear Regulatory Commission, Washington, DC, p. 1230.
- [5.1.13-16] Bestion, D., P. Fillion, R. Pr ea and G. Bernard-Michel (2018), “Improved PWR LOCA Simulations Through Refined Core 3D Simulations – An Advanced 3D Modelling and the Associated METERO Validation Program”, NUTHOS-12, 14-18 October, Qingdao, China.
- [5.2.1-1] Baek, W.P., C.H. Song, B.J. Yun, T.S. Kwon, S.K. Moon and S.J. Lee (2005), “KAERI integral effect test program and the ATLAS design.”, *Nuclear Technology*, 152(2), pp. 183-195.
- [5.2.1-2] Ishii, M. and I. Kataoka (1983), “Similarity analysis and scaling criteria for LWRs under single-phase and two-phase natural circulation”, NUREG/CR-3267, Argonne National Lab., Illinois, United States.
- [5.2.1-3] NEA (2018), “Summary Report of the NEA- Advanced Thermal-Hydraulic Test Loop for Accident Simulation Joint Project”, OECD Publishing, Paris, NEA/CSNI/R(2017)9, www.oecd-nea.org/jcms/pl_19794.
- [5.2.1-4] Kim, Y.-S., K.-Y. Choi, C.-H. Song and W.-P. Baek (2014), “Overview of the standard problems of the ATLAS facility”, *Annals of Nuclear Energy*, 63, pp. 509-524.
- [5.2.1-5] Lee, J.B. (2018), “Description Report of ATLAS Facility and Instrumentation (second revision)”, KAERI/TR-7218/2018.
- [5.2.1-6] Ryu, S.U., S.I. Lee, Y.N. Kim, S. Cho, K.H. Kang and S.J. Yi (2018), “Experimental Study on the Cooling Performance of Passive Emergency Core Cooling System”, KAERI/TR-7221/2018.
- [5.2.1-7] NEA (2012), “OECD/NEA/CSNI International Standard Problem No. 50 Final Integration Report”, OECD Publications, Paris, NEA/CSNI/R(2012)6/VOL1, www.oecd-nea.org/jcms/pl_19144.
- [5.2.1-8] Choi, K.Y., K.H. Kang and C.H. Song (2019), “Recent achievement and future prospects of the ATLAS Program”, *Nuclear Engineering and Design*, 354, pp. 110-168.
- [5.2.2-1] NEA (1991), “ISP-26. OECD/NEA/CSNI International Standard Problem No.26. ROSA-IV LSTF Cold Leg Small- Break LOCA Experiment. Comparison Report. February 1992”, OECD Publications, Paris, NEA/CSNI/R(91)13, www.oecd-nea.org/jcms/pl_15898.
- [5.2.2-2] NEA (2013), “Final Integration Report of OECD/NEA ROSA Project 2005-2009”, OECD Publications, Paris, NEA/CSNI/R (2013)1, www.oecd-nea.org/jcms/pl_19244.
- [5.2.2-3] NEA (2017), “Final Integration Report of OECD/NEA ROSA-2 Project 2009-2012”, OECD Publications Paris, NEA/CSNI/R (2016)10, www.oecd-nea.org/jcms/pl_19728.
- [5.2.2-4] Suzuki, M., H. Nakamura and I. Ohtsu (2003), “ROSA-V large scale test facility (LSTF) system description for the third and fourth simulated fuel assemblies.”, JAERI-Tech 2003-037 Report, Japan Atomic Energy Research Institute.

- [5.2.2-5] Nakamura, H., T. Watanabe, T. Takeda, H. Asaka, M. Kondo, Y. Maruyama, I. Ohtsu, I. and M. Suzuki (2008), “RELAP5/MOD3 Code Verifications through PWR Pressure Vessel Small Break LOCA Tests in OECD/NEA ROSA PROJECT”, ICONE-16, 11-15 May, Orlando, Florida, United States.
- [5.2.2-6] Nakamura, H., T. Takeda, A. Satou, M. Ishigaki, S. Abe and D. Irwanto (2013), “Major Outcomes from OECD/NEA ROSA and ROSA-2 Projects”, NURETH-15, 12-17 May, Pisa, Italy.
- [5.2.3-1] Floerke, J.P., T.F. Borschel and L.K. Rhodes (2007), “The Decontamination, Decommissioning, and Demolition of Loss-of-Fluid Test Reactor at the Idaho National Laboratory Site”, WM’07 Conference, 25 February-1 March, Tucson, AZ, United States.
- [5.2.3-2] Modro, S.M., S.N. Aksan, V.T. Berta and A.B. Wahba (1989), “Review of LOFT Large Break Experiments - OECD LOFT Project”, NUREG/IA-0028, US Nuclear Regulatory Commission, Washington, DC.
- [5.2.3-3] NEA (1990) “An account of the NEA LOFT Project”, OECD Publications, Paris, OECD LOFT-T-3907, www.oecd-nea.org/jcms/pl_18922.
- [5.2.3-4] Reeder, D.L. (1978), “LOFT System and Test Description (5.5-Ft Nuclear Core 1 LOCES)”, No. NUREG/CR-0247; TREE-1208, Idaho National Engineering Lab., Idaho Falls, United States.
- [5.2.3-5] Bixby, W.W. (1979), “An Overview of LOFT Instrumentation”, GRS-Fachgespräch, Munich, Germany.
- [5.2.3-6] McPherson, G.D. (1979), “The LOFT Facility and Test Program”, (No. CONF-791124-1), US Nuclear Regulatory Commission, Washington, DC.
- [5.2.3-7] Prassinis, P.G. (1979), “Experimental Data Report for LOFT Power Ascension Experiment L2-3”, NUREG/CR-0792, US Nuclear Regulatory Commission, Washington, DC.
- [5.2.3-8] NRC/DPRS Reactor Safety Data Bank, ENCOUNTER, EGG-RTH-7285.
- [5.2.3-9] OECD NEA Data Bank (2016), www.oecd-nea.org/dbprog/ccvm/loft.htm.
- [5.2.3-10] NEA (1997), “International Standard Problems, Brief descriptions (1975-1997)”, OECD Publications, Paris, NEA/CSNI/R(97)3, www.oecd-nea.org/jcms/pl_16160.
- [5.2.3-11] Jeong, J.J., S.K. Sim, C.H. Ban and C.E. Park (1997), “Assessment of the COBRA/RELAP5 code using the LOFT L2-3 large-break loss-of-coolant experiment”, *Annals of Nuclear Energy*, 24(14), pp. 1171-1182.
- [5.2.3-12] Jeong, J.J., K.S. Ha, B.D. Chung and W.J. Lee (1999), “Development of a multi-dimensional thermal-hydraulic system code, MARS 1.3.1”, *Annals of Nuclear Energy*, 26(18), pp. 1611-1642.
- [5.2.3-13] Davis, C.B. (1998), “Assessment of the RELAP5 multi-dimensional component model using data from LOFT test L2-5”, No. INEEL/EXT-97-01325, Idaho National Lab., Idaho Falls, ID, United States.

6. Verification and validation matrix for 3D T/H Codes

Significant progress has been made in the last few decades in the knowledge of phenomena and their analytical representation, as well as in numerical methods. Nevertheless, the computer code simulations provide only an approximation of reality. Their inherent limitations must be understood and addressed as part of the development of the codes, followed by extensive verification and validation (V&V) of the embedded models.

According to Requirement 18 of the IAEA requirements for safety assessment [6.1-1]:

- “Model verification is the process of determining that a computational model correctly implements the intended conceptual model or mathematical model; that is, whether the controlling physical equations and data have been correctly translated into the computer codes.
- System code verification is the review of source coding in relation to its description in the system code documentation.
- Model validation is the process of determining whether a mathematical model is an adequate representation of the real system being modelled, by comparing the predictions of the model with observations of the real system, or with experimental data.
- System code validation is the assessment of the accuracy of values predicted by the system code against relevant experimental data for the important phenomena expected to occur.”

Three-dimensional (3D) phenomena predictions are nowadays almost essential for correctly reproducing the system behaviour attaining to recent nuclear power plants’ generation. The need for a more detailed and accurate simulation of the multidimensional hydrodynamic features of reactor applications led to the development of multidimensional components in system thermal-hydraulics (SYSTH) codes. The 3D formulation of the mass, internal energy and momentum equations has been added in the cylindrical and Cartesian forms. As for any other code models, the correct functioning of this new multidimensional flow model was subject to verification procedures.

The V&V of a code ensures the numerical tool has been delivered on its purpose in an error-free way. Specifically, the verification process is intended to check that the code meets a set of specifications or requirements, while the validation tests how well the needs that led to those requirements have been addressed [6.1-2]. Model verification is the process of determining whether a computational model correctly implements the intended conceptual model or mathematical model [6.1-1].

The developmental assessment and V&V of SYSTH codes use a combination of phenomenological tests, modelling of separate effects experiments and modelling of integral experiments to qualitatively check the performance of selected code models and the appropriateness of these tools against specific applications. Numerical scheme features of the code models are also tested (for example, the consistency, stability, numerical accuracy, robustness and central processing unit (CPU) time efficiency), where the main goal is the assessment of the differences between a system of equations and its numerical (discretised) solution. Judgements are formulated for each case by comparing the code results against experimental or analytical data according to pre-established criteria fixed by either the code developers or a code user in the case of internal or independent code

assessment respectively. Some general information on V&V, which is not specific to 3D modelling, can be found in [6.1-6].

6.1. Verification tests

Verification is often an internal process during the developmental assessment phase of a code, especially during the debugging process. The verification procedures involve performing special tests to simulate a portion or a complete system, followed by a critical analysis of the obtained results. In the code post-development phase, verification procedures involve regularly repeating tests devised specifically to ensure the code's compliance with the initial design specifications, as time progresses and hence new versions appear.

This section focuses on the typical phenomenological and numerical problems of an exact analytical solution that is meant to test the multidimensional flow model and component of SYSTH codes.

As reported in Table 6.1, the verification problems are designed to check (some of) the fundamental terms in the multidimensional component flow model, such as:

- momentum flux terms;
- mass and momentum distribution in a 3D space (Cartesian and/or cylindrical coordinate);
- gravitational terms;
- specific correlation (e.g. interphase drag, heat transfer).

Table 6.1. List of typical verification tests for checking 3D features of SYSTH codes

No.	Verification Test ID	Objective of the verification	Notes
1	Rigid body rotation problem	Azimuthal momentum flux terms	
2	Pure radial symmetric flow problem	Radial momentum flux terms	
3	R-Theta symmetric flow	3D momentum equations	
4	Fall problem	Momentum flux, correlation (Interphase drag, heat transfer), gravitational terms	Named also "water over steam"
5	Rest problem	Mass and momentum distribution in a 3D space	To test unphysical behaviour occurrences
6	Water faucet	Momentum flux, gravitational terms Numerical diffusion	Named also "ransom's faucet" (1D problem solved by 3D equations)
7	Gravity wave problem	Mass and momentum distribution in a 3D space, flow regime map Capability to predict void waves	Similar to "shock tube case"
8	Tank drain problem	All the momentum flux terms except z-direction velocity	No description
9	Basic heat conduction problem	Fluid heat conduction	Special feature relevant under limited flow conditions Not already treated in test 10 (laminar flow in heated tube)
10	Laminar flow in a heated tube	Wall heat flux	

Source: Serre and Bestion, 2001.

Table 6.1. List of typical verification tests for checking 3D features of SYSTH codes (Continued)

No.	Verification Test ID	Objective of the verification	Notes
11	Boiling in a channel	Momentum flux, Interfacial heat transfer and wall heat flux	
12	Propagation of a passive scalar front	Momentum flux (rather scalar transport and diffusion) Measure of the numerical diffusion as a function of mesh size and time steps	
13	Dam break	Momentum equation	Asymptotic (steady state) solution known
13	Oscillating manometer	Motion of the interface between liquid and gas, gravitational terms, liquid level, oscillations Evaluation of the numerical dissipation	Other models could be tested: wall friction, interfacial friction, flow stratification and liquid level tracking.

Source: Serre and Bestion, 2001.

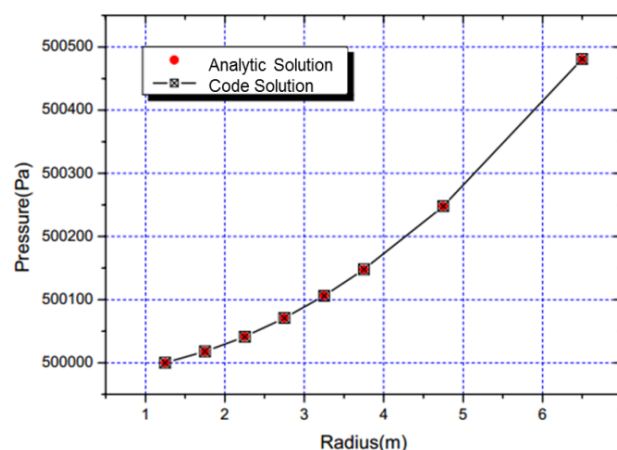
A few examples of typical verification tests are briefly discussed below, with one for each of the listed items.

The momentum flux terms can be tested either separately (in each co-ordinate direction) or in the 3D space. A test case that verifies the azimuthal momentum flux term is briefly described: the rigid body rotation problem.

The **rigid body rotation** problem involves a hollow cylinder with a symmetric flow pattern in the azimuthal direction. No radial flow, gravity and loss due to friction are assumed. Such simplifications yield an easy analytical formulation of the problem (and the related exact solution).

An azimuthal flow pattern is imposed in the code run by proper boundary conditions in the outer ring. The azimuthal velocities in the inner rings are consistently input with the rigid body rotation assumption; given the correct azimuthal velocity profile, the correct pressure profile will be computed by the code.

Positive verification implies that the code essentially predicts the same results as the exact solution regarding the azimuthal velocity profile and the radial pressure behaviour. The latter is shown in Figure 6.1.

Figure 6.1. Comparison of the radial pressure distribution

Source: Chung et al., 2010.

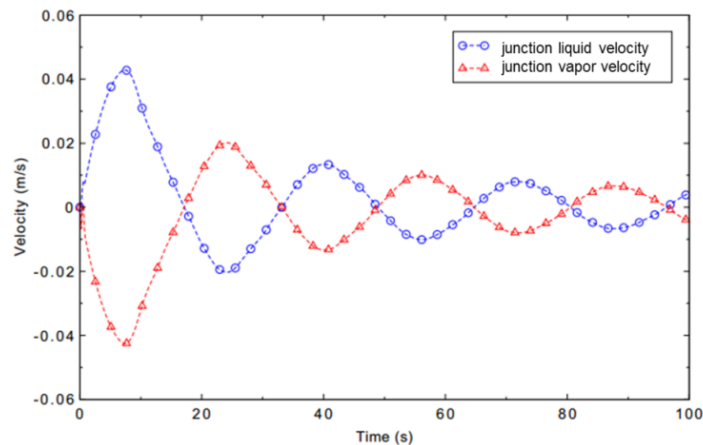
The **gravity wave** problem allows for the assessment of the distribution of mass and momentum in a 3D space in the multidimensional component. The test challenges the flow regime map model and momentum equations.

The gravity wave problem examines the propagation of a wave introduced in a system that is initially at rest. In this test, a column of water is represented by a lower void fraction in one or a set of volumes, with the remaining volumes at a higher void fraction. The body forces on the column of liquid introduce a variation in hydrostatic pressure in the system, which produces a force on the liquid in all directions parallel to the surface of the liquid. The solution for the wave speed in the one-dimensional (1D) horizontal square or rectangular duct case is well known and can often be applied to certain 3D cases. It is necessary to force the code, ignoring the influence of the interfacial drag force and dynamic drag (virtual mass) force, or wave speed would be reduced.

The gravity wave problem can be performed to verify different geometries and components (1D or 3D).

Positive verification implies that the code can predict the phenomenon of the gravity wave and that the prediction is accurate in terms of proper flow direction and reflection from hard boundaries. Figure 6.2 shows the calculated liquid and vapour velocities in the middle of a rectangular duct.

Figure 6.2. Calculated liquid and vapour velocities in the mid-duct, gravity wave 3D



Source: Bayless (ed.), 2014.

The momentum flux terms, programmed correlations (interphase drag and interphase heat transfer) and gravitational terms are altogether challenged by the **fall problem**. The fall problem is developed to demonstrate that the liquid falls evenly and similarly for both the 3D and the 1D components.

The fall problem consists of a closed vertical tube that is initially filled with one-third saturated liquid and two-thirds saturated steam, with the liquid on the top. The gravity force causes inversion of the position of the two fluids. The water in the upper volumes depletes quickly and drops into the lower volumes.

The multidimensional coding exercised by the falling problem is correctly implemented when the void fraction behaviours are the same as in the 1D case. For a free-fall scenario, an analytical solution of the time needed by the liquid to drop a certain distance (h) can be obtained and compared to the computational results.

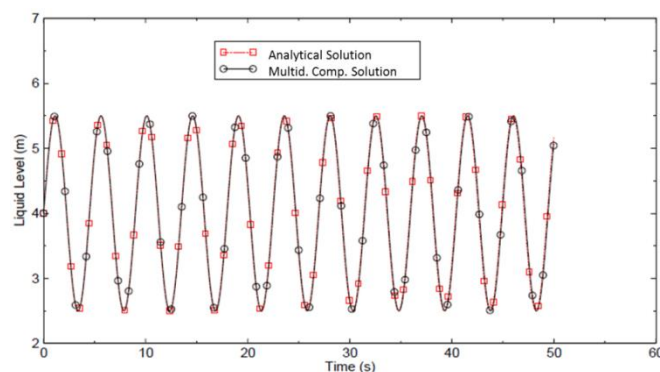
The capability of the codes to predict the motion of the interface between liquid and gas is assessed by the oscillating manometer case. The oscillating manometer consists of a U-tube

shaped frictionless pipe of constant cross-sectional area containing a water column. The water column is set in motion by applying a small initial displacement and an initial velocity to the fluid, while the gravitational head provides the driving force for the flow oscillation.

An exact analytical solution for the problem can be obtained from the governing equation of motion for the liquid interface motion derived by Moody [6.1-5], assuming an incompressible fluid. Moody also gives the equations from which the pressure can be determined at the ends of the horizontal section at the bottom of the manometer.

Positive verification implies that the code essentially calculates the same liquid level values as the exact solution (Figure 6.3), with fluid velocity and pressure at the bottom of the U-tube.

Figure 6.3. Liquid level vs. time for multidimensional component oscillating manometer



Source: US NRC, 2007.

The solution for the oscillating manometer should be independent of the type of components in order for this problem to be useful for the verification of 1D and 3D components. Other models that could be tested with this problem include: wall friction model (inducing the dumping of the oscillations), interfacial friction model, horizontal and vertical stratification model and liquid level tracking models.

Together with the phenomenological problems, which are used to verify that the code is in qualitative agreement with the physics of a problem, the separate effects and integral problems are designed to provide data for the developmental assessment of SYSTH codes as well. The next section addresses the separate effects tests (SETs) and integral effect tests (IETs).

6.2. Validation procedure

The validation process should provide confidence in the ability of the code to predict the values of the safety parameters of interest and to allow for the evaluation of uncertainties associated with the calculated values in a best estimate plus uncertainty (BEPU) approach. The assessment and validation of the models and computer codes should be performed against experimental data from separate and integral effect tests to assess the codes' simulation accuracy. The codes' outputs are compared to relevant experimental data and operational transients, if possible, for all important phenomena that are expected to occur.

The code validation is presented in two sets: the development phase, in which the code developer carries out the assessment, and the independent applications, in which the code users perform the assessment. Code developers must demonstrate the validation of their codes within defined areas of applications. Code developers establish guidance and

recommendation for the best use of computational tools in accordance with the selected models and the comparison with experiments they performed. The first part of this chapter summarises the bases of their demonstration. The validation performed during the development of a code can consist of hundreds of test simulations, which are repeated for each version of the code, and which include basic tests, separate effect tests and integral tests. These calculations are often automated. The validation of the code is also discussed in the code manuals and other documents.

A validation matrix should be developed for nuclear power plant simulation in normal or accident conditions to comprehensively address expected phenomena in their expected ranges and boundary conditions.

The creation of the validation matrix is a process of collection and selection (and documenting) of tests appropriate for the validation purpose. A comprehensive validation programme is mainly based on pre- and post-test calculations of separate effects tests and integral system tests (including the major international standard problems and on real plant transients). The tests cover phenomena which are expected to be relevant for all types of events of the envisaged code range of application.

Independent comparisons provide another aspect of the codes' capability. These comparisons are presented in the chapter's second part. The work relating to the independent validation of computer codes is vast and therefore it is impossible to summarise it all. A few examples are reported in Section 0

The assessment and validation problems for testing SYSTH codes' 3D capabilities are reported in the following sections.

6.2.1. MARS-KS code: validation

The objective of the Multi-dimensional Analysis of Reactor Safety - Korea Institute of Nuclear Safety (MARS-KS) code assessment is to determine the qualitative and quantitative accuracy of the code for problems that are consistent with the intended application of the code. This is accomplished using three types of problems: conceptual problems, modelling of separate effects experiments and modelling of integral experiments. The phenomenological problems demonstrate that the code is in qualitative agreement with the physics of the problem and, in cases where analytical solutions exist, the qualitative accuracy of the code can also be judged. The separate effects tests are designed to provide data on a primary physical effect. These problems are selected to test a key model or models of the code. Qualitative agreement with the data is the first criteria that must be satisfied, i.e. the correct trends must be predicted. If this condition is met, the code results can then be quantitatively compared to the data. The integral problems prove that the collection of models in the code function in concert. The code predictions of integral system parameters – such as pressure, clad temperature and mass inventory – are used to assess the code's overall accuracy.

Thirteen assessment calculations were performed for the multidimensional (MULTID) component (cf. Section 4.4.2). Table 6.1 shows the assessment matrix, which includes a brief description of each problem's objective. The matrix contains five separate effects problems and one integral effect test problem.

Nine assessment calculations were performed for the 3D vessel component, which is a subchannel analysis module. Table 6.3 shows the assessment matrix, which includes a brief description of each problem's objective. The matrix contains seven separate effects problems, one integral effect test problem and one plant application problem [6.2-1].

Table 6.2. MARS-KS code assessment problems for MULTID Component

Problem type	Problem	Assessment objective
Separate effects problem	RPI air-water experiment	Multidimensional two-phase flow, multidimensional flow regime
	UPTF test 7	Multidimensional full-scale bypass
	KAERI MIDAS bypass tests	Multidimensional flow pattern; film spread and tear-off
	KAERI IRWST tests	Thermal mixing phenomena
	OECD PANDA tests	Multidimensional steam injection flow
Integral effect problem	LOFT L2-5	Large break LOCA

Source: Chung et al., 2010.

Table 6.3. MARS-KS code assessment problems for 3D vessel component

Problem type	Problem	Assessment objective
Separate effects problem	RPI air-water experiment	Multidimensional two-phase flow, multidimensional flow regime
	CREARE 1/15 Downcomer ECC Bypass Tests	Downward penetration of emergency core cooling water against the up-flow steam in a PWR downcomer
	CREARE 1/5 Downcomer ECC Bypass Tests	
	UPTF Test 7	Multidimensional full-scale ECC bypass
	KAERI IRWST tests	Thermal mixing phenomena
	GE 9-Rods experiments	Subchannel phenomena (mass flux, enthalpy distribution in rod bundle)
	ISPRA 16-Rod EUROP tests	
Integral effect problem	LOFT L2-5	Large break LOCA
Plant applications	YGN3 (Yeonggwang)MSLB Simulation with 3D Kinetics	Postulated non-LOCA Application

Source: Chung et al., 2010.

6.2.2. SPACE code: validation

The objective of the space and performance analysis code (SPACE) code assessment is to determine the qualitative and quantitative accuracy of the code for problems that are consistent with the code's intended application. This is accomplished using three types of problems: conceptual problems, modelling of separate effects experiments and modelling of integral experiments. The phenomenological problems demonstrate that the code is in qualitative agreement with the physics of the problem and, in cases where analytical solutions exist, the qualitative accuracy of the code can also be judged. The separate effect tests are designed to provide data on a primary physical effect. These problems test a key model or models of the code. Qualitative agreement with the data is the first criteria that must be satisfied, i.e. the correct trends must be predicted. If this condition is met, the code results can then be quantitatively compared to the data. The integral problems prove that the collection of models in the code function in concern. The code predictions of integral system parameters – such as pressure, clad temperature and mass inventory – are used to assess the code's overall accuracy.

Thirteen assessment calculations were performed for the multidimensional component. Table 6.4 shows the assessment matrix, which includes a brief description of each problem's objective. The matrix contains three separate effects problems. However, no integral effect test problems have been performed so far.

Table 6.4. SPACE code assessment problems for 3D component of SPACE

Problem type	Problem	Assessment objective
Separate effects problem	RPI air-water experiment	Multidimensional two-phase flow, multidimensional flow regime
	UPTF 20 ECC bypass	Multidimensional full-scale bypass
	KAERI DYNAS test	Multidimensional air-water flow pattern in vertical plate

Source: Bae et al., 2016.

6.2.3. ATHLET code: validation

The Analysis of THERmal-hydraulics of LEaks and Transients (ATHLET) code development is accompanied by continuous and comprehensive code validation measures. The validation is mainly based on pre- and post-test calculations of separate effects tests and integral system tests (including the major international standard problems and on real plant transients). The tests cover phenomena that are expected to be relevant for all types of events of the envisaged ATHLET range of application for all common light water reactors (LWRs) and advanced reactor designs. The comprehensive validation of the recently implemented 3D multidimensional flow model against small and large-scale experiments is still underway. As shown in Table 6.5, the application has so far focused on the investigation of 3D single-phase and two-phase water mixing phenomena occurring in the reactor pressure vessel (RPV) of a LWR [6.2-8] and [6.2-9]. For that purpose, experimental data from the Rossendorf Coolant Mixing Model (ROCOM), upper plenum test facility (UPTF) and Advanced Thermal-Hydraulic Test Loop for Accident Simulation (ATLAS) test facilities were used. The 3D flow model was also validated against experiments performed in the TALL-3D facility (lead-bismuth facility). The facility contains a well-instrumented 3D test section and provides data with high spatial and temporal resolution for the validation of computational fluid dynamics (CFD) codes for pool-type liquid metal reactor applications. With regard to passive safety systems, experimental data from ATLAS and INtegral Test Facility KARlstein (INKA) facilities were used to investigate the 3D model applicability for the simulation of water pools.

Table 6.5. ATHLET code validation cases for 3D model

Facility	Test no.	Test description
ROCOM	Test T1.1, T1.2, T1.3, T2.1 and T2.2 (OECD PKL-2)	MSLB: mixing in RPV with respect to recriticality and PTS
	Test T2.1 and T2.3 (OECD ROCOM PKL-3)	ECC injection: Mixing in RPV
UPTF	UPTF-6 and 7 ; UPTF-Z3	LB-LOCA: CCFL in downcomer
	UPTF-TRAM C1	ECC mixing in cold leg and downcomer
ATLAS	SB-DVI-09 (ISP-50) Tests A1-2 and A2.1 (OECD ATLAS)	50% break of a DVI line of APR-1400 SBO
TALL-3D	Tests T01, T02, T03, T06 and T11	Transition between forced and natural convection (for pool-type liquid metal reactors, lead-bismuth)
INKA	NOKO_1_10_85_13-1 NOKO_1_09_80_5_1 NOKO_1_3C_85_5_1 PCFS_1_1_02	BWR KERENA (AREVA): passive heat removal to water pool (emergency condenser) and passive core flooding

6.2.4. CATHARE code: validation

A specific validation programme has been developed for the 3D vessel application including both SETs and IETs, considering full-scale or large-scale tests facilities as much as possible.

In the frame of analysis of loss-of-coolant accidents (LOCAs), it includes PIERO tests for lower plenum voiding [6.2-11], UPTF tests (6 and 7) and Japan Atomic Energy Research Institute's (JAERI's) downcomer refilling tests, UPTF test 10c for the upper plenum behaviour [6.2-12] and JAERI-SUDO for the downcomer level evolution during late reflooding [6.2-13]. PERICLES two-dimensional (2D) tests are dedicated to studying core uncovering and reflooding, and SCTF test are used for this phase of the LOCA to analyse 2D thermal-hydraulic (T/H) behaviour in the core and more specifically the effects of radial power and temperature distribution [6.2-14]. IETs' matrix includes two loss-of-fluid test (LOFT) experiments (L2-5 and LP02-6) to cover a full large break loss-of-coolant accident (LB-LOCA) transient [6.2-12] and [6.2-15] and the ROSA 2/ Large Scale Test Facility (LSFT) test 1, 2 and 7 for the intermediate break (IB)-LOCA [6.2-15], [6.2-16] and [6.2-17].

The Code for Analysis of THERmalhydraulics during an Accident of Reactor and safety Evaluation (CATHARE) validation matrix for the 3D module includes also CEGB, ACHILLES, FLECHT, FEBA and SEFLEX test facilities, allowing the assessment of fuel ballooning models [6.2-12].

The 3D validation programme includes two OECD/NRC benchmarks for core application: BWR Full-size Fine-Mesh Bundle Test (BFBT) and PWR Subchannel and Bundle Tests (PSBTs), with 3D subchannel calculations using CATHARE 3 [6.2-19] and [6.2-20]. Such a subchannel validation matrix is completed by some rod bundle experiments, OMEGA, GRAZIELLA and AGATE [6.2-19] and [6.2-20].

Additional validations have been performed by CATHARE partners or CATHARE users. UPTF transient and accident management programme (TRAM) C3 test were used to assess mixing phenomenon, simulating a boron dilution which may occur during a small break loss-of-coolant accident (SB-LOCA) [6.2-21]. The assessment of CATHARE 2 3D capabilities on PKL-2 ROCOM tests were carried out by Bel V (cf. Section 6.4.1), for the prediction of the coolant mixing in the downcomer and the lower plenum under buoyant asymmetric conditions [6.2-22]. As part of the NUClear REactor SAFETY simulation platform (NURESAFE) project, subchannel calculations with PERICLES 2D tests were performed by VTT (Teknologian tutkimuskeskus, research centre in Finland) with CATHARE 3 to assess the dispersion and diffusion terms of the 3D module.

Table 6.6 gives some examples of the SETs and IETs used for the CATHARE 3D module validation.

Table 6.6. Examples of SET and IET used for the CATHARE 3D module validation

Application	Phase / component	Test	Type
LB-LOCA	Blowdown phase, lower plenum voiding	PIERO	SET
	Downcomer refilling phase	UPTF tests 6 and 7	SET
	Boiling phenomena in downcomer (late reflooding phase)	JAERI-SUBO	SET
	Reflooding phase: 3D effects in core	PERICLES 2D reflooding, SCTF	SET
	Transient	LOFT L2-5 and LP02-6	IET
IB-LOCA	Cold leg 13% break	ROSA 2/LSTF test 7	IET
LOCA	Countercurrent flow limit (CCFL) at the core upper plate	UPTF test 10c	SET
	Core uncovering	PERICLES 2D boil-up	SET

Table 6.6. Examples of SET and IET used for the CATHARE 3D module validation (Continued)

Application	Phase / component	Test	Type
Fuel ballooning	Core	CEGB, ACHILLES, FLECHT, FEBA, SEFLEX	SET
Mixing effects in core	Core	BFBT, PSBT, OMEGA, GRAZIELLA, AGATE, PERICLES	SET

6.3. Examples of code validation prepared by the developers

6.3.1. Validation cases done for CATHARE

A first computation of a 3-inch break LOCA with CATHARE 3 using a modular multi-3D modelling of a PWR vessel and non-conformal junctions is described in [6.2-23].

6.3.2. Validation cases for MARS-KS

Rensselaer Polytechnic Institute (RPI) air-water experiment

Test description

Steady-state flow experiments were performed in a 2D test section in a low pressure air/water loop at RPI [6.3-2]. The test section consisted of a thin vertical channel that simulated a 2D slice through the core of a pressurised water reactor. The test section was 0.91 m tall, 0.91 m wide and 0.013 m thick. Flow was supplied to or received from the test section through four separate ports, as shown in Figure 6.4. Port one supplied single-phase liquid to the upper right corner of the test section. Port two and three received two-phase flow mixtures from the upper left and lower right corners respectively. Port four supplied a two-phase mixture to the bottom centre of the test section. Port five, which was in the lower left corner of the test section, was closed during these tests.

The void fraction measurements were averaged over a six-minute period to minimise the effects of the fluctuating flow. The maximum error in the averaged void fraction was estimated to be 0.014. The total liquid flow was constant and evenly divided between Ports one and four for all three tests. The air flow, which was supplied through Port four, varied between tests. Port three removed a substantial portion (about 40%) of the total liquid supplied to the test section but removed only a small fraction (less than 5%) of the total gas flow for these tests. The remainder of the liquid and gas flow supplied to the test section exited through Port two.

Figure 6.4 also provides a qualitative schematic of the flow pattern in the test section. The test section was divided into eight regions, labelled (A) to (G). The boundaries between regions varied between test and fluctuated within a test. Test 1AN4, 2AN4 and 3AN4, were selected for comparison with MARS. Test parameters are shown in Table 6.7.

Table 6.7. RPI flow test parameters

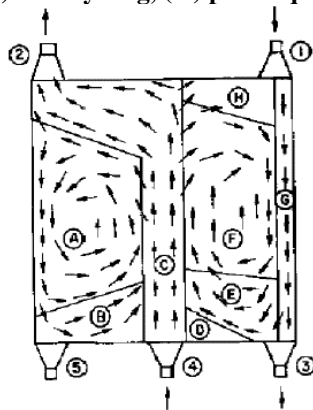
Test	Total liquid mass flow rate (kg/s)	Fraction of total liquid flow to Port 4	Total air flow (kg/s)	Pressure (kPa)
1AN4	1.81	0.50	0.00273	133
2AN4	1.81	0.50	0.00547	133
3AN4	1.81	0.50	0.00821	133

MARS-KS modelling

Figure 6.5 shows a MARS-KS modelling which consists of a rectangular 2D multidimensional slab with 1 717 volumes, four time-dependent junctions and one inlet 1D pipe for Port 4. This nodalisation was developed so that the location of each void fraction measurement coincided with the centre of a control volume.

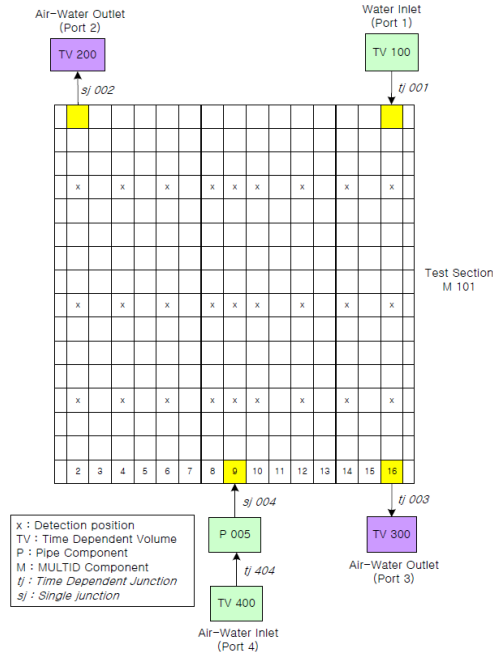
The RPI flow tests were simulated for 200 s. The initial velocities were set to zero in the test section. The liquid flow rates at Ports 1, 3 and 4 were increased from zero to the measured values over a 5 s period, and then the air flow rates were increased to the measured values over 15 s period. The flow rates were then held constant for the duration of the calculation. Even though the boundary conditions were held constant, oscillations were observed in the calculated void fractions.

Figure 6.4. RPI test section and qualitative flow pattern (region (A) bubbly/slug, (B), (D) single-phase, (C) slug, (E) bubbly, (F) bubbly/slug, (G) pure liquid and (H) air-pocket)



Source: Bukhar and Lahey Jr., 1984.

Figure 6.5. MARS nodalisation of the RPI test section



Source: Chung et al., 2010.

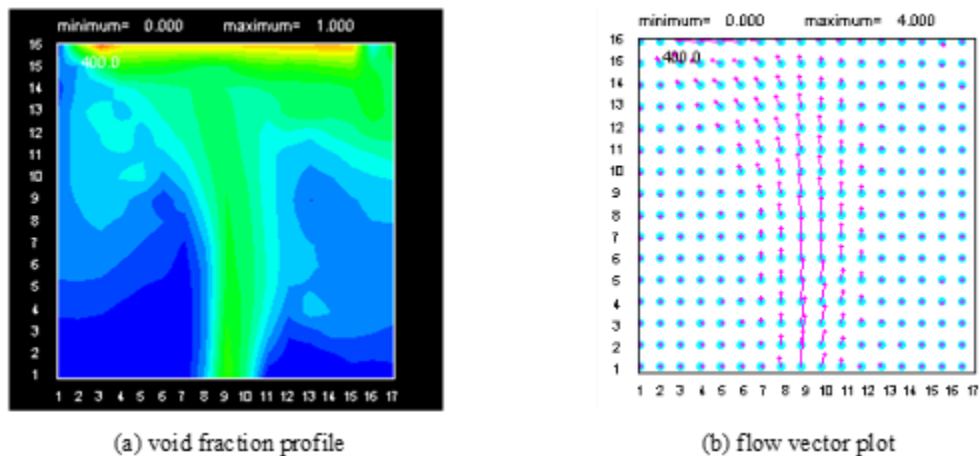
Results of the calculation

The results of first time run were not successful. The calculated void fraction distribution is highly dispersed and diffusive. It was revealed that the main reason for this is horizontal stratified force in horizontal stratified flow regimes. Stratified flow regime is not expected in multidimensional flow and therefore the horizontally stratified flow regimes are deleted. However, level gradient terms are always set to be active, resulting from the horizontally different void fraction.

Obtained results after modification are shown in Figure 6.6 and Figure 6.7. The calculated void fractions of all tests are compared with the measured void fraction in Figure 6.7.

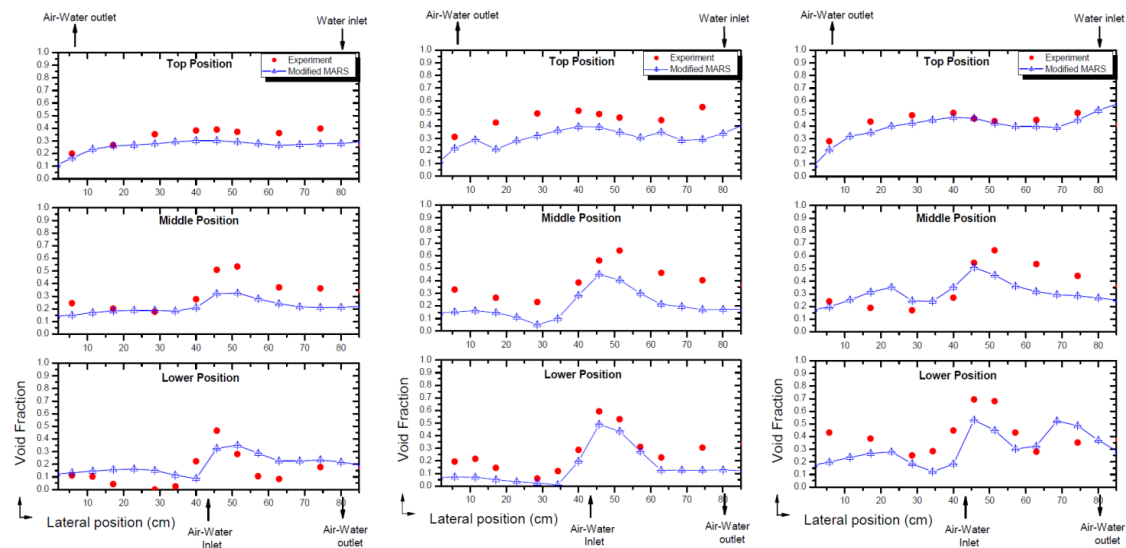
Two-phase multidimensional models in MARS are assessed with the simulation of an RPI air-water test. It was found that the modification of the horizontal flow regime map is needed in a multidimensional model. Following the modification of the flow regime, the predicted flow patterns and void fraction profiles are in good agreement with measured data.

Figure 6.6. MARS-KS simulation results for test 2AN4



Source: Chung et al., 2010.

Figure 6.7. Comparison of void fractions from the RPI test



Note: (a) 1AN4

Source: Chung et al., 2010.

(b) 2AN4

(c) 3AN4

MIDAS bypass tests

Test description

The test matrix of Multi-dimensional Investigation in Downcomer Annulus Simulation (MIDAS) (cf. Section 5.1.10) consists of the ECC (emergency core cooling) direct bypass and void height tests. In the present assessment, the MARS-KS is evaluated against the direct ECC bypass test, which excludes the water sweep out from the top of a water level. The direct ECC bypass test was performed in cases of direct vessel injection (DVI)-4 (the nearest to the broken cold leg), DVI-2 (the farthest from the broken cold leg) and DVI-2&4 respectively. The test was performed in steady-state conditions. The downcomer water level was maintained lower in the test to exclude the water sweep-out phenomena and the bypass flow rate and condensation flow rate were adjusted depending on the steam injection flow rate at the intact cold legs.

Test results show that the direct bypass fraction of ECC water significantly depends on the injected steam mass flow rate. DVI-4 tests show that the direct bypass fraction increases drastically as the steam flow rate increases. However, in the DVI-2 test most injected ECC water penetrated into the lower downcomer. The direct bypass characteristic in the DVI-2 and DVI-4 tests is reflected into the direct bypass characteristic curve of the DVI-2&4 tests. The steam condensation reaches a theoretically allowable maximum value.

MARS-KS modelling

Figure 6.8 shows a schematic of the MARS-KS nodalisation for the direct bypass test of the MIDAS simulation. The annulus downcomer is 3D modelled by the MULTID component. The 3D input model in Figure 6.8 consists of 95 hydrodynamic volumes and 184 junctions. The direct vessel injection nozzle, intact cold leg and containment tank are modelled by “time-dependent volumes” and “time-dependent junctions”. The downcomer wall is divided into six sections in radial direction and 14 vertical sections. The hot leg was simulated by a porous media option of the volume and a loss coefficient of the related junctions in order to consider the flow blockage effect. The porosity and loss coefficients

were set to 0.4 and 10, respectively. A control valve was implemented at the bottom of the downcomer to control the water level. The heat structure was not modelled because the structure of a downcomer wall was maintained at a saturated temperature in the test and the heat transfer to the fluid from the downcomer wall is negligible compared to the interfacial heat transfer in an annulus.

Results of the calculation

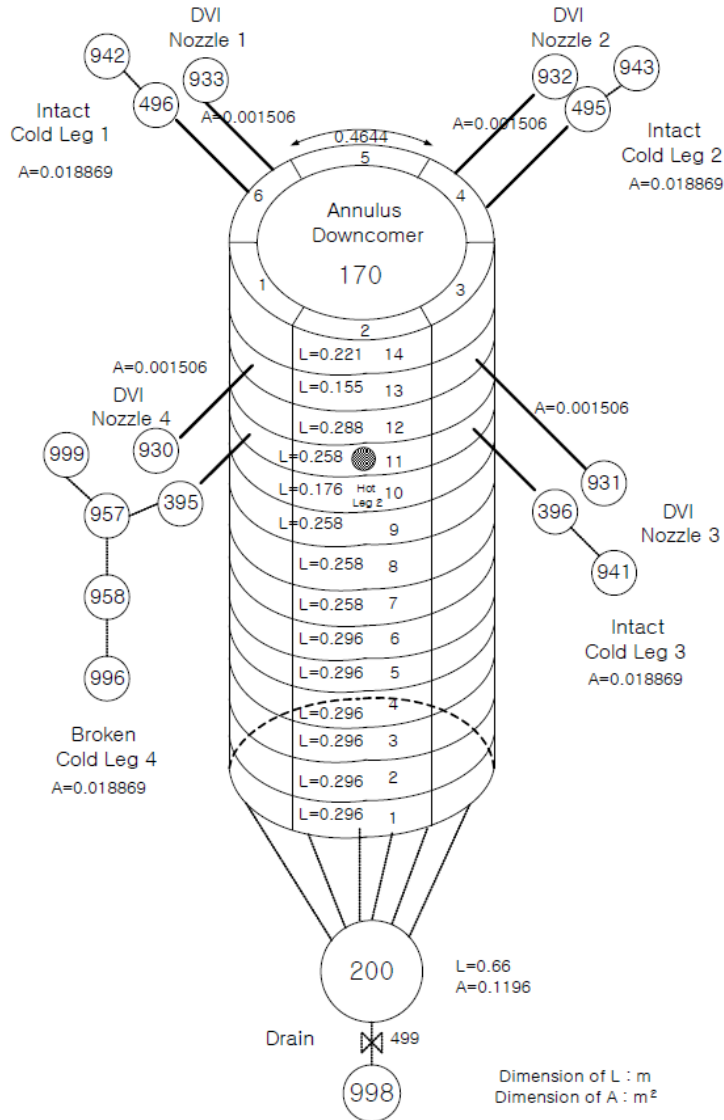
The MIDAS test was performed in steady-state conditions and thus the calculation results of the MARS-KS code were taken after steady-state conditions were established for a given flow condition. The steam injection flow rate was gradually increased to the target value to obtain a steady-state condition. There is not much severe oscillation in the parameters such as pressure, water level, or break flow rate throughout the calculation against the experimental data. The calculation was carried out changing the droplet on/off option of the MULTID component.

Figure 6.9 shows the comparison between experiment and MARS calculation of the direct ECC bypass fraction. In the figure, the direct ECC bypass fraction is calculated by the fraction of mass flow rates as follows,

$$\text{Bypass fraction} = 1 - \frac{m_{f,penetration}}{m_{Total,ECC,in} + m_{Total,steam,in} - m_{steam,break}}$$

The figure shows that the MARS-KS code over-predicts the bypass fraction in the less than 0.9 kg/s of steam flow rate. However, the code predicts comparatively well for above 0.9 kg/s of steam flow rate in the case of DVI-2&4 injection mode. The figure also shows that the generation of droplets makes more ECC bypass flow than the non-droplet generation mode. In case of a single DVI-4 (the nearest to the broken cold leg) injection, the same trends are found as with those of the DVI-2&4. However, the MARS under-predicts in the DVI-2 (the farthest from the broken cold leg) injection mode.

Figure 6.8. MARS-KS nodalisation for the MIDAS test



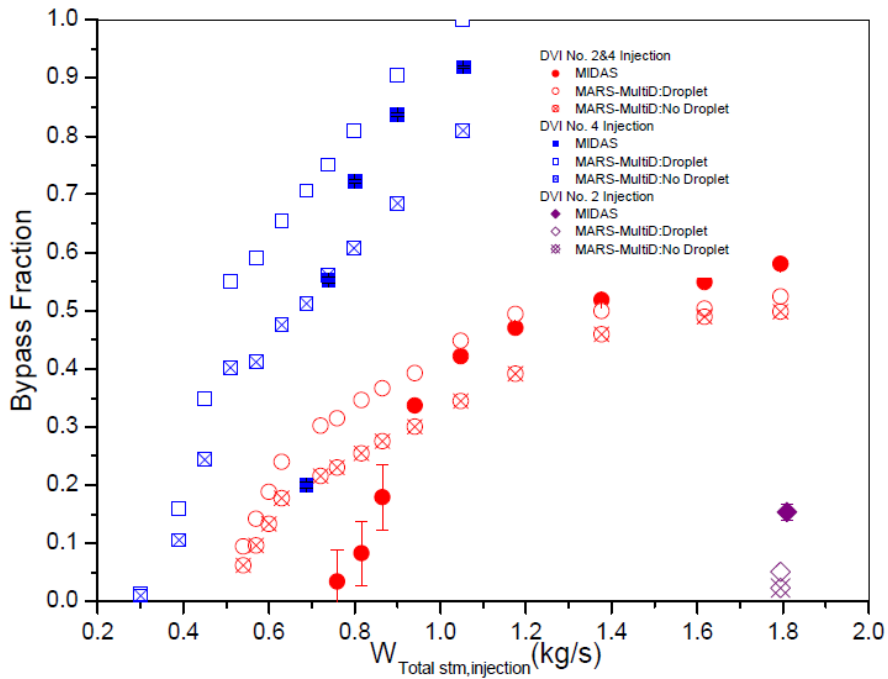
Source: Chung et al., 2010.

The steam condensation rate is also evaluated. Figure 6.10 shows the comparison of the condensation fractions. In the figure, the steam condensation fraction is calculated as follows:

$$\text{Condensation fraction} = 1 - \frac{m_{\text{steam,break}}}{m_{\text{Total,steam,in}}}$$

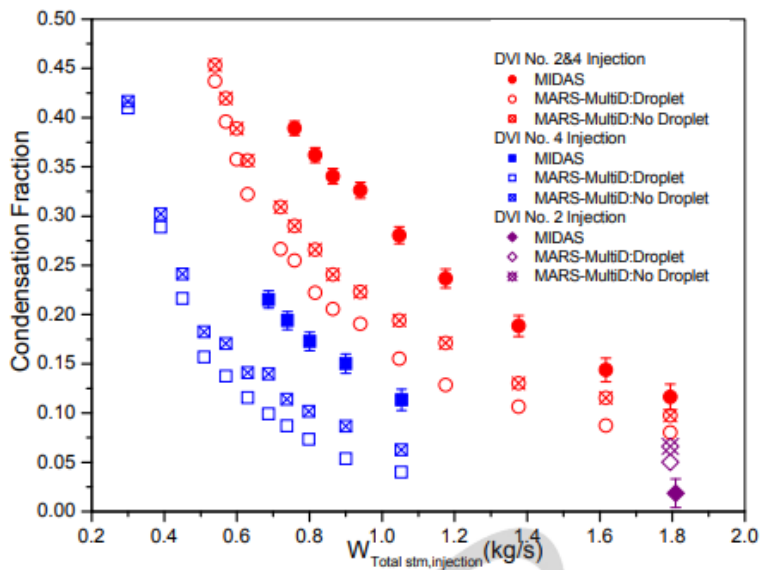
As shown in the figure, the steam condensation fraction of the MARS-KS code severely under-predicts for all cases. Figure 6.11 confirms this once more. The droplet makes no enhancement of a steam condensation, which results from the fact that the heat transfer calculation is not performed for the droplets in the present MULTID component.

Figure 6.9. Comparison of direct ECC bypass fraction

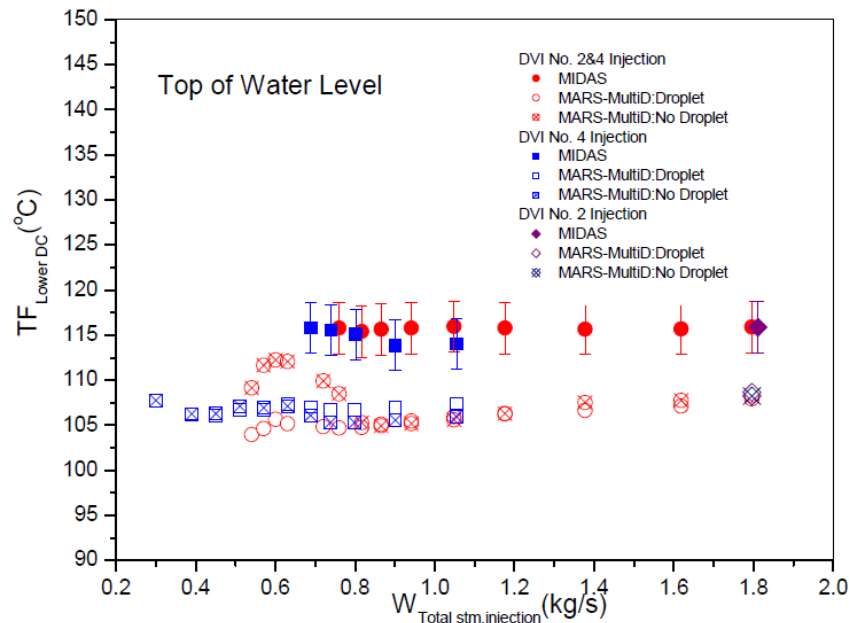


Source: Chung et al., 2010.

Figure 6.10. Comparison of condensation fraction



Source: Chung et al., 2010.

Figure 6.11. Comparison of water temperature at the lower downcomer

Source: Chung et al., 2010.

LOFT L2-5 test

Test description

LOFT L2-5 (cf. Section 5.2.3) was performed in June 1982 and was the third nuclear LB-LOCA experiment. The main objective was to investigate the effects of a 200% double-ended cold leg break with an immediate primary coolant trip. The experiment was initiated by opening two quick-opening blowdown valves in the broken loop. The operator tripped the primary coolant pump shortly after the initiation of the test. The pumps were disconnected from flywheel during coastdown, differing from previous LOFT tests, L2-2 and L2-3.

MARS-KS modelling

The input model that was used in the developmental assessment of the Reactor excursion and leak analysis programme 5 (RELAP5)/MOD3 was the starting point for the MARS-KS input model. The original 1D model represented the intact and broken loops, steam generator secondary of the intact loop, pressuriser, ECC system and reactor vessel. The discharge coefficient, 0.95, was applied at both break junctions. The 3D model of the LOFT vessel was developed. The vessel was divided into four 90° azimuthal sectors and four radial rings, as shown in Figure 6.14.

The four azimuthal sectors corresponded to the four nozzles connecting the loop and the vessel. Sector one corresponded to the broken loop cold leg, sector two to the broken loop hot leg, sector three to the intact loop cold leg and sector four to the intact loop hot leg. The inner ring of the vessel represents the hot channel including the hot rod. The second ring represents the averaged core channel, and the third ring represents the core and filler block bypass. The fourth ring also represents the downcomer region. Heat structures for the filler block, reactor vessel and core support structures are also modelled as four sectors and connected to hydraulic volumes according to each geometry. The 3D vessel model contains total 272 volumes, 564 junctions and nine fuel structures. The bypass leak in the core and

the filler blocks was modelled as third ring region of 3D core, which was connected to each of the four volumes in the third ring of the lower plenum and the upper plenum region. The loss coefficients in the leakage path were adjusted to provide the designed values. The core fuel rods were modelled with eight heat structures for assembly, located in a given ring and sector. An additional hot rod was simulated in the inner ring and the sector of the broken side. The fuel power and volume fraction of the inner channel correspond to the hot channel properties and the remaining core power and volumes are assigned in the second ring.

The qualification during nodalisation generation was done through the work of the OECD's Best-Estimate Methods Uncertainty and Sensitivity Evaluation (BEMUSE) Phase II [6.2-34]. Figure 6.12 shows the results of input deck nodalisation qualification. The nodalisation errors are well within the acceptance criteria, except for the heat transfer volume. The effective heat transfer volume can be simulated by considering the stagnant volumes in the flowing system.

Figure 6.12. Results of input deck nodalisation qualification

Item	Description	Unit	Acceptance	Exp.	Calculation	Errors	Error/ Acceptance
1	Primary circuit volume	m ³	1%	7.94	7.982	0.53%	0.5290
2	Secondary circuit volume	m ³	2%	6.65	6.624	0.39%	0.1955
3	Non Active structures heat transfer area (overall)	m ²	10%	NA	---	---	---
4	Core heat transfer surface area	m ²	0.10%	73.39	73.505	0.16%	1.5670
5	SG U-tubes heat transfer external surface area (without tube sheet)			335	347.5	3.73%	37.3134
6	Core heat transfer volume	m ³	0.20%	0.1932	0.293	51.66%	258.2816
7	SG U-tubes heat transfer volume (without tube sheet)			0.693	0.781	12.70%	63.4921
8	Maximum of the axial power distribution for the average rod in average channel (zone 2)	KW/m	1%	25.60	25.26	0.00%	0.0000
9	Maximum of the axial power distribution for the hot rod in hot channel (zone 4)	KW/m	1%	36.03	35.36	0.00%	0.0000

Source: NEA, 2006.

Results of the calculation

The measurement sequence of events is presented in Figure 6.13. The test was initiated by opening quick valves at 0.0 s. Reactor scram time, pump trip time, the initiation time of HPSI and low pressure safety injection (LPSI) were modelled as input data. The calculated events were generally in reasonable agreement with the data, except for the accumulator behaviour. The accumulator started earlier and emptied later than reflected by the measurement.

A comparison of calculated and measured primary system pressure is presented in Figure 6.15. The calculated primary system pressure was under-predicted after five s. Thereafter, the under-predicted pressure initiated the accumulator injection earlier at 13 s. Figure 6.16

shows the liquid level trends of the accumulator. The accumulator empty time was delayed by seven s.

The mass flowrate at the broken loop cold leg and hot leg are compared to measurement data in Figure 6.17. The steam discharge flowrate from the hot leg was well predicted. However, the two-phase discharge flow rate from cold leg side was over-predicted throughout the transient.

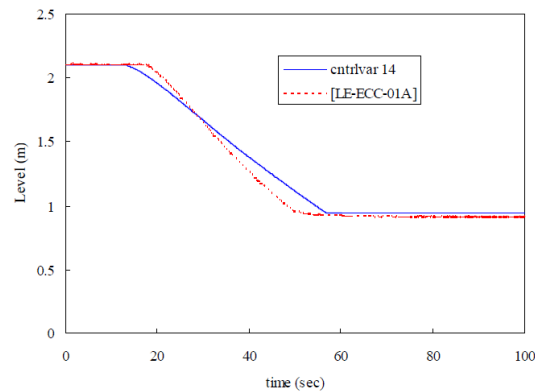
The cladding temperatures at node four of the hot rod are shown in Figure 6.18. As shown in the figure, the starting time of heat-up was well predicted but turn-around time was predicted too early and heat-up rate was slower than the measurements. The possible reason of early turn-around time is the over-prediction of discharge flow from cold leg side. The backward flow enhances the drain-back of liquid from hot leg, upper plenum into the core, and results in the early top-down rewet.

After the maximum clad temperature was reached, the cladding temperature slowly decreased until complete core quenching. The calculated quenching time is similar to the measurement, but the cladding temperature during the reflood was generally lower than the measurement.

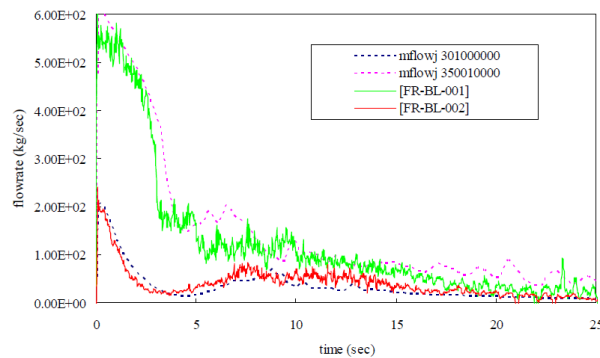
Figure 6.13. Sequence of events for LOFT L2-5

EVENTS	TIME AFTER EXPERIMENT INITIATION (s)	CALCULATED TIME AFTER TRANSIENT INITIATION (s)
Experiment L2-5 initiated	0	0 (input)
Subcooled blowdown ended	0.043 ± 0.01	0.1
Reactor scrammed	0.24 ± 0.01	0.24 (input)
Cladding temperatures initially deviated from saturation (DNB in core)	0.91 ± 0.2	1.2
Primary coolant pumps tripped	0.94 ± 0.01	0.94 (input)
Subcooled break flow ended in cold leg	3.4 ± 0.5	3.2
Partial top-down rewet initiated	12.1 ± 1.0	9.1
Pressurizer emptied	15.4 ± 1.0	15.3
Accumulator A injection initiated	16.8 ± 0.1	12.9
Partial top-down rewet ended	22.7 ± 1.0	14.4
HPIS injection initiated	23.90 ± 0.02	23.9 (input)
Maximum cladding temperature reached	28.47 ± 0.02	39.1
LPIS injection initiated	37.32 ± 0.02	37.32 (input)
Accumulator emptied	49.6 ± 0.1	57.1
Core cladding fully quenched	65 ± 2.0	65.7
Blowdown Suppression Tank maximum pressure reached	72.5 ± 1.0	72 (input)
LPIS injection terminated	107.1 ± 0.4	

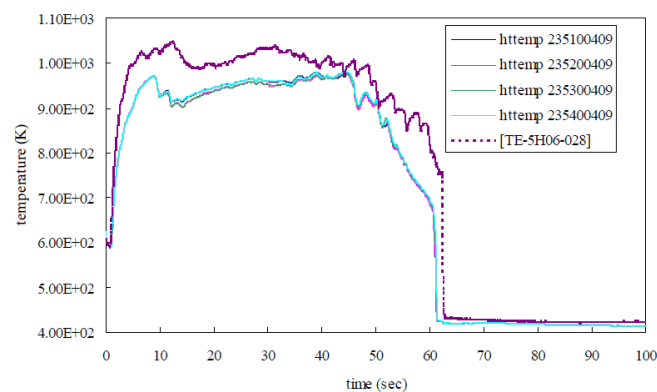
Source: NEA, 2006.

Figure 6.16. Comparison of accumulator liquid level

Source: Chung et al., 2010.

Figure 6.17. Break flowrate through the hot and cold leg side

Source: Chung et al., 2010.

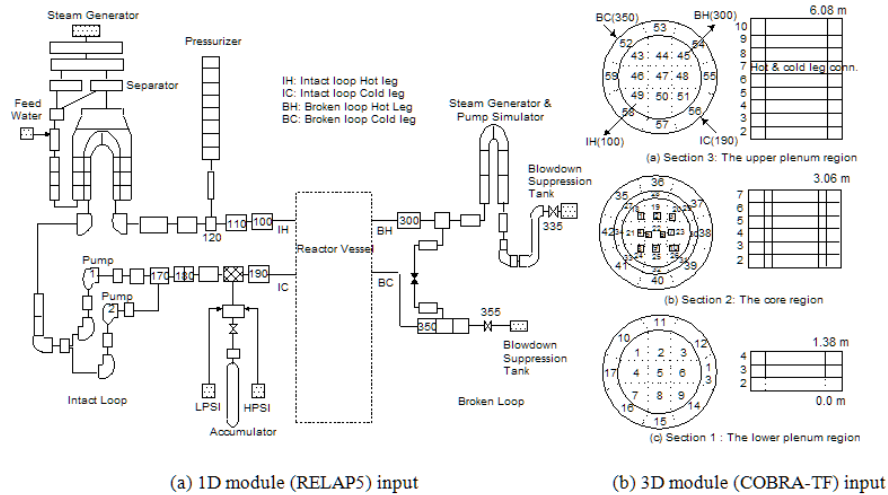
Figure 6.18. Clad temperature at hot rod node four of nine

Source: Chung et al., 2010.

The 3D analyses of the LOFT experiments and/or code assessment were very limited [6.2-29] and [6.2-30]. One of the examples is the MARS code assessment. Figure 6.19 shows the MARS nodalisation for the LOFT L2-5 experiment simulation [6.2-30]. The MARS code has been developed by consolidating and restructuring the RELAP5/MOD3.2.1.2 and COBRA-TF codes. The reactor vessel was modelled using the 3D module (COBRA-TF), which consists of 354 hydrodynamic cells (3 sections, 59 channels and 76 gaps). Each channel of the core region, channels 18 through 26, contains a “rod” component representing the average rods of the fuel bundle. Channel 22 contains an additional “rod”

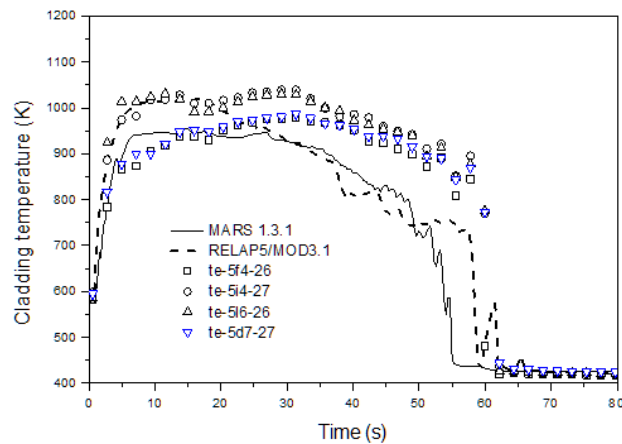
component to simulate the hottest rod. Figure 6.20 shows that both MARS and RELAP5/MOD3.1 predict the cladding temperature at 0.64 m above the bottom of the active core reasonably well. However, MARS tends to under-predict the temperature. This seems to be caused by the blowdown heat transfer model of the MARS 3D module. Figure 6.21 shows that both codes failed to capture the blowdown peak. Nevertheless, the results of MARS seem qualitatively better.

Figure 6.19. MARS nodalisation for the LOFT L2-5 experiment simulation

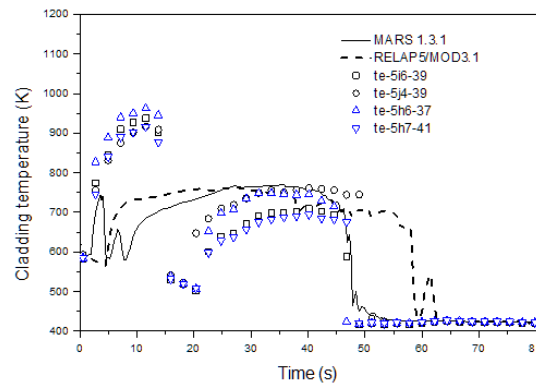


Source: Chung et al., 2010.

Figure 6.20. Hot rod cladding temperatures at 0.64 m



Source: Chung et al., 2010.

Figure 6.21. Hot rod cladding temperatures at 1.0 m

Source: Chung et al., 2010.

6.3.3. Validation cases for SPACE

Validation tests have been performed for the validation of SPACE against three SETs of RPI, MIDAS and DYNAS. Among the tests, the RPI and MIDAS simulation were almost the same as those for MARS-KS and therefore the simulation results are not included in this report.

DYNAS experiment

Test description

The DYNAS is a SET facility (cf. Section 5.1.8) that generates an experimental database for a multidimensional two-phase void distribution in 2D slab geometry. Two separated test sections were prepared for visualisation and impedance measurements, respectively. The shape and scale of the test section points to the phenomena of two-phase multidimensional behaviour at the downcomer region. The simulation matrix for the SPACE validation is summarised in Table 6.8 below.

Table 6.8. Simulation matrix for SPACE validation

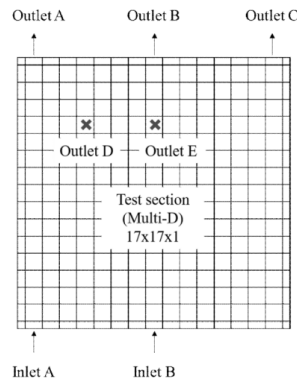
Case	AB / AC / BB / BC*				AE / BE*	
	01	02	03	04	01	04
Water (kg/s)	4.0	4.0	20.0	20.0	4.0	10.0
Air (g/s)	2.0	20.0	2.0	20.0	2.0	10.0

Note: *location of inlet and outlet

SPACE modelling

The SPACE input model for the DYNAS consists of 17x17 rectangular cells on the Cartesian co-ordinate as shown in Figure 6.22.

Figure 6.22. SPACE DYNAS nodalisation



Source: Lee et al., 2018.

Results of the calculation

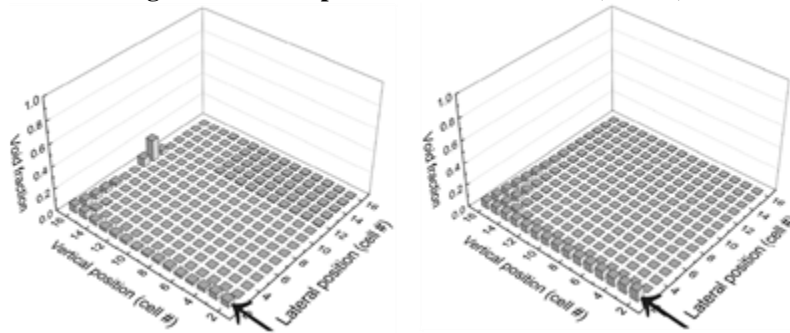
Figures 6.23 and 6.24 show the measured void fraction and calculated void fraction of AC01 and AC02, respectively. SPACE underestimated the void fraction of AC01 relative to small gas flow injection, whereas SPACE overestimated the void fraction of AC02 relative to high gas flow injection. The average error to experimental value is compared in Table 6.10. The average error is defined as follows:

$$\text{Average error} = \frac{\sum_{i=1}^n |C_i - M_i|}{n}$$

where C_i and M_i are calculated value and measured value respectively and n is the number of measurement locations and its value is 225 for all test conditions. Table 6.9 shows the void fraction’s overall average error in all tests of the DYNAS. The table indicates that the average error has a low value in low void fraction cases compared to those in high void fraction cases.

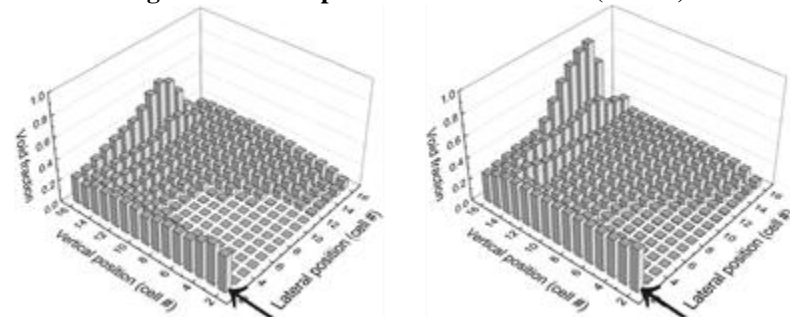
Table 6.9. Average void fraction error

Case	No.	Error (%)	Case	No.	Error (%)	Case	No.	Error (%)	
AB	01	1.37	BB	01	1.87	AE	01	7.32	
	02	4.77		02	29.60		04	9.24	
	03	4.24		03	6.49		BE	01	13.30
	04	10.8		04	10.50			04	14.70
AC	01	0.83	BC	01	2.81				
	02	3.83		02	18.10				
	03	1.34		03	7.25				
	04	8.28		04	16.50				

Figure 6.23. Comparison of void fraction (AC-01)

Note: (a) Experimental data of void fraction
Source: Lee et al., 2018.

(b) Estimated void fraction by SPACE

Figure 6.24. Comparison of void fraction (AC-02)

Note: (a) Experimental data of void fraction
Source: Lee et al., 2018.

(b) Estimated void fraction by SPACE

6.3.4. Validation cases for ATHLET

6.3.4.1. ROCOM test 1.1

ROCOM test 1.1 - motivation

Several experiments were chosen in the ROCOM facility (a well-instrumented facility for 3D applications, see Section 5.1.1) for the validation of the 3D fluid dynamic model ATHLET. The experiments were conducted as part of the OECD's PKL-2 project [6.2-24] as complementary tests to the PKL G3.1 integral test (main steam line break [MSLB]). The tests investigate the MSLB scenario, which results in an asymmetric flow behaviour in the RPV. The simulation of the flow processes requires a multidimensional description.

The validation work related to ROCOM test 1.1 involved two major aspects:

- Firstly, ATHLET 1D (parallel channel) and 3D model capabilities to adequately capture the coolant mixing behaviour in the RPV of the ROCOM test facility.
- Secondly, model performance with respect to different nodalisation schemes for the RPV: grids with eight and 16 nodes along the downcomer perimeter were investigated.

ROCOM test 1.1 - Test description

Based on the G3.1 PKL tests related to the MSLB event (see Section 5.1.1), two ROCOM experimental scenarios were designed for detailed analyses of the coolant mixing within the RPV. In the first ROCOM test, labelled test 1.1, the recriticality problem was investigated. The second test, test 1.2, was oriented towards the analysis of the coolant mixing in relation to pressurised thermal shock (PTS). Both scenarios are characterised by asymmetric loop flow rates and overcooling as a result of the postulated main steam line break and emergency core coolant injection.

The following chapters provide details on the results achieved within the ATHLET model validation against the ROCOM test 1.1. Information on results achieved for test 1.2 can be found in [6.2-9].

The G3.1 PKL experimental conditions, at which a minimum temperature in loop one (affected by MSLB) during the overcooling phase was monitored, were taken as initial conditions for the ROCOM test 1.1. Water with higher density was injected into loop one. The water is at room temperature at the ROCOM test facility and therefore the necessary amount of sugar was diluted into the injected water to achieve the density difference corresponding to the temperatures measured at PKL.

Table 6.10. Initial and boundary conditions for ROCOM test 1.1

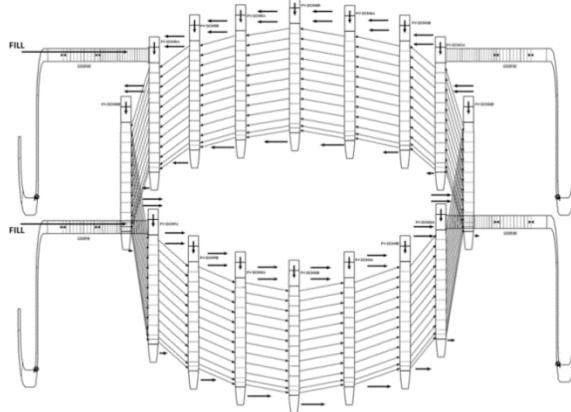
<i>Experimental conditions</i>				
Loop	1	2	3	4
Normalised volume flow rate, [-] (nominal value: 185 m ³ /h)	12.21	3.15	3.15	3.15
Volumetric flow rate, [l/s]	6.27	1.62	1.62	1.62
Relative density, [-]	1.12	1.00	1.00	1.00
<i>Experimental procedure</i>				
Time	Task			
Experiment preparation	Preparation of the water/sugar solution with the desired density value Labelling the water with salt			
t = - 30 seconds	Establish stationary flow conditions in loops 2 to 4			
t = 0 seconds	Start of injection of the water with the higher density			
t = 150 seconds	End of injection			

ROCOM test 1.1 - modelling approach

For this test case (see Table 6.10), the main focus was on the modelling of the flow in the RPV downcomer. The downcomer was represented by two different grids with either eight or 16 nodes in azimuthal direction (Figure 6.25). The grids were generated for both multidimensional modelling approaches available in ATHLET (pseudo-3D and 3D) from a corresponding number of parallel pipe objects connected by junctions to capture azimuthal flows.

The nodalisation of the lower plenum was rather coarse for this test case. The lower plenum was modelled by three rings of control volumes with 8 or 16 nodes along the azimuthal direction according to the discretisation of the downcomer.

Figure 6.25. The 16 azimuthal nodes model: nodalisation of the reactor downcomer (together with the four loops) used for pseudo-3D as well as 3D calculations



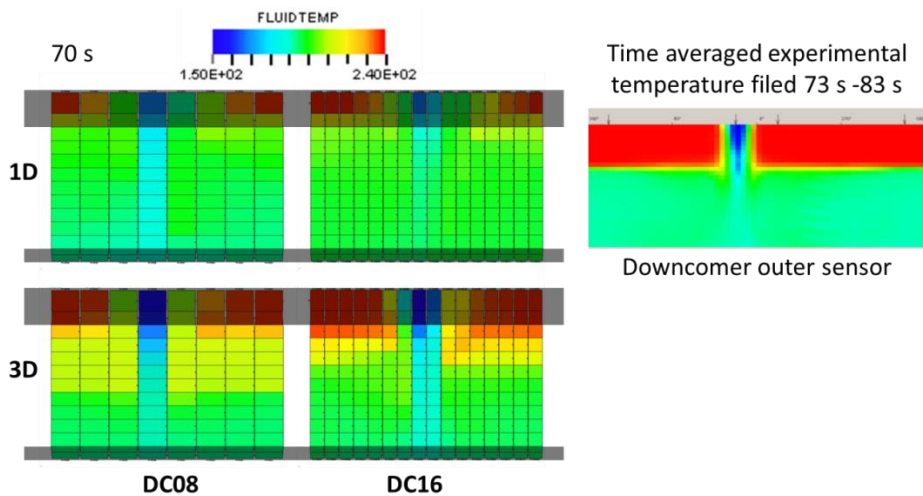
Source: Schöffel et al., 2014.

ROCOM test 1.1 - results

A comparison of the experimental temperature field recalculated from the measured local conductivity and the ATHLET models' predictions is shown in Figure 6.22 for 70 s. The presented experimental results cover the reactor downcomer region, where the two vertically aligned wire mesh sensors are placed. DC08 and DC16 stand for the downcomer resolution with 8 and 16 azimuthal grid cells, respectively. The topmost and the lowermost two-node lines, which are covered by the grey see-through boxes, are beyond the range of the sensors and inappropriate for comparison. The experimental results indicate that the injected cold water slug sinks down after entering the reactor with a negligible degree of mixing. There is then mixing at the lower part of the RPV, which fills the downcomer upwards with subcooled water. As a result, two hot and cold regions with nearly homogeneous temperature distribution can be distinguished. The boundary between those regions is quite sharp, as confirmed by the experiment.

According to the colour coded temperature in Figure 6.26, the two 1D ATHLET models estimated that the coolant mixing was homogeneous enough that after 70 s the entire reactor downcomer was practically filled with subcooled water. The nodalisation (8 or 16 azimuthally aligned channels) do not lead to major difference in the 1D model predictions. In contrast, the simulations with 3D model exhibited a lower degree of mixing. The experimentally observed hot and cold regions are qualitatively well captured by the two 3D models. The coarser ATHLET 3D model (DC08) failed to predict a defined boundary between the hot and the cold regions, whereas the 16 nodes model (DC16) performed much better in this respect. The boundary predicted by the latter is located lower and correspondingly closer to the experimental one.

**Figure 6.26. Qualitative comparison of the downcomer temperature field.
Left: Four ATHLET models. Right: outer sensor measurement**



Source: Schöffel et al., 2014.

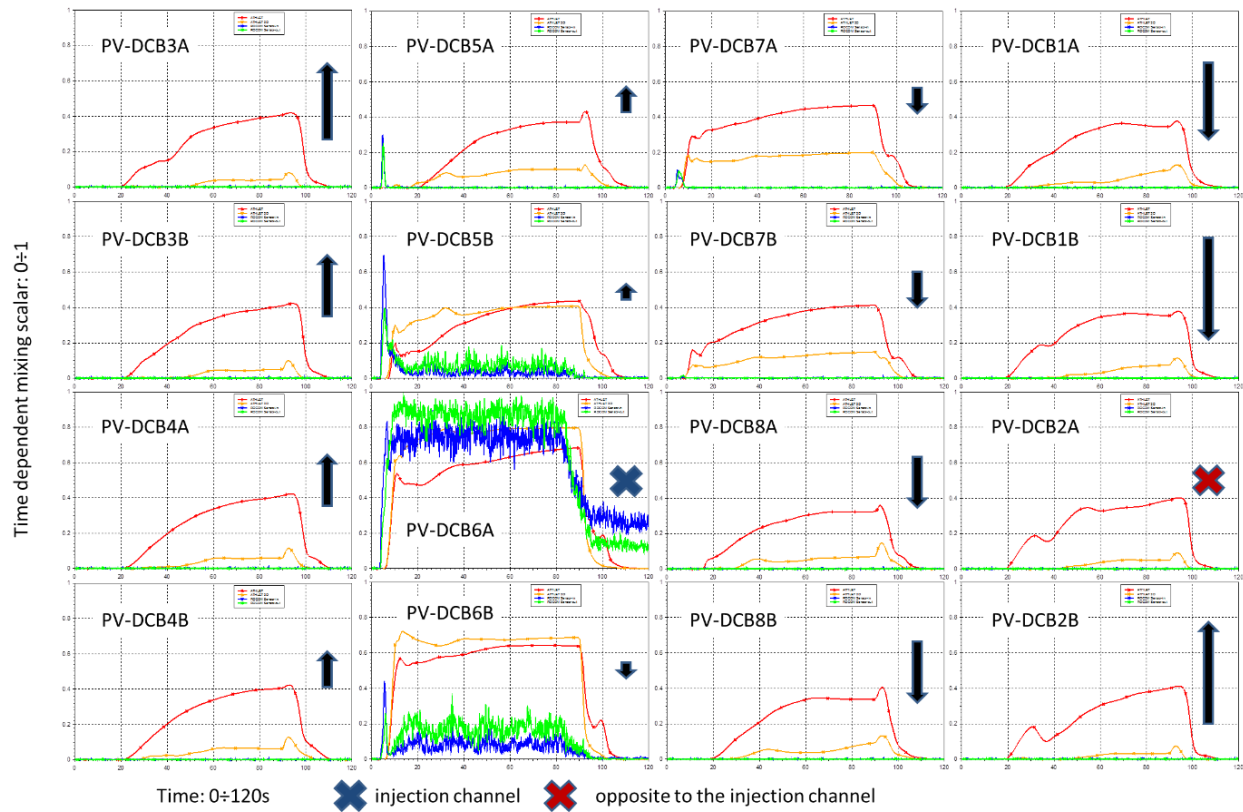
An overview of the ATHLET 16 nodes 1D and 3D models predictions against the experimental observations for the dynamics of the mixing process in the downcomer is presented in Figure 6.27. The experimental values are spatially averaged for the four (out of 64 azimuthal) wire mesh measuring points, which happen to lie within the corresponding node of the ATHLET model.

The mixing scalar predictions for the second topmost node of the downcomer channel connected to the injecting loop is presented in Figure 6.27 by the plot marked by a blue cross. The 3D model appears to capture the injected colder water sinking vertically down in a lean stream in the reactor downcomer quite well. It can generally be anticipated that the results would improve when more detailed or finer nodalisation is used.

A time shift between the experimental and the theoretical curves of about 2.5 s can be observed. The cold loop wire mesh sensor suggests that the injected cold water settles in the lower part of the pipe, which could lead to slightly higher fluid velocity and an earlier entrance into the reactor pressure vessel by the injected water. Similar behaviour cannot be captured by the pure 1D approach employed in ATHLET for the modelling of the loops.

The mixing scalar is overestimated outside the cold stream (a higher amount of admixed cold water) for the upper nodes of the downcomer channels, as seen in Figure 6.27. The arrows in the plots indicate how far a given node is from the injection one. Both ATHLET curves lay above the experimental ones, but with clearly improved predictions obtained by the 3D model. The measurements remain close to zero throughout the entire experiment, which corresponds to the presence of separate hot and cold zones, as mentioned above. The values predicted by the 3D model align with the experimental ones for a significant amount of time, close to zero. This is also reflected by the sharper boundary that appears between the hot and the cold fluid regions, as shown in Figure 6.26.

Figure 6.27. Mixing scalar comparison in second top most nodes of the downcomer channels for the DC16 ATHLET models



Note: (green: outer wall sensor; blue: inner wall sensor; red: 1D-model; orange: 3D-model).
Source: Schöffel et al., 2014.

ROCOM test 1.1 - conclusions

ROCOM test 1.1 was employed for the validation of ATHLET eight (DC08) and 16 (DC16) downcomer nodes models. The ability of both nodalisation schemes to capture the 3D process was analysed with and without the ATHLET 3D fluid dynamic model. The following specific conclusions on the models' performance can be drawn:

- All ATHLET models perform qualitatively well but tend to overestimate the coolant mixing in the reactor downcomer for ROCOM test 1.1. ATHLET 3D models reproduce the experimentally investigated mixing behaviour and hot-cold coolant regions better than ATHLET 1D ones.
- The ATHLET model with an activated 3D model and refined nodalisation scheme DC16 clearly demonstrates improvements in its predictions. The DC16 3D model not only captures the hot-cold regions of ROCOM test 1.1, but also calculates the defined boundary between them well.
- The overestimation of the coolant mixing within the reactor downcomer is partially due to the inadequate modelling of the cold legs in which hot-cold separated regions were experimentally observed. All ATHLET models apply 1D transport equations to that region and consequently the injected cold water is perfectly mixed with the hot one within the loops.
- The nodalisation scheme of 8 or 16 parallel channels does not influence the "classic" 1D model performance.

6.3.4.2. ROCOM test 2.1

ROCOM test 2.1 - motivation

The 3D model was employed not only to the downcomer, but also to the lower plenum to capture the flow processes of the ROCOM test 2.1 [6.2-8]. The post-test calculation of test 2.1 aimed to validate the 3D fluid dynamic model on topologically both the 2D cylindrical grid (downcomer) and 3D cylindrical grid (lower plenum). The code version ATHLET 3.0B was used for this application.

ROCOM test 2.1 - test description

Test 2.1 is dedicated to the overcooling phase after a MSLB event. The initial and constant boundary conditions slightly differ compared to test 1.1. There is a decreased coolant density difference between the loop one, which is assigned to the affected steam generator and loops two to four. The loop mass flow rates were also closer together, as presented in Table 6.11.

Table 6.11. Initial and boundary conditions for ROCOM test 2.1

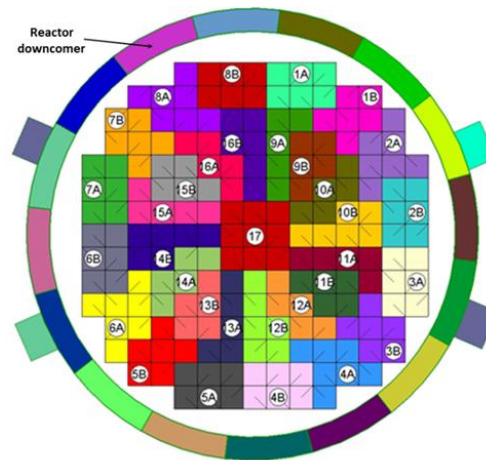
Experimental conditions				
Cooling circuit loop	1	2	3	4
Normalised volume flow rate, [-] (nominal value: 185 m ³ /h)	10.2	4.8	4.8	4.8
Volumetric flow rate, [l/s]	5.24	2.47	2.47	2.47
Relative density, [-]	1.067	1.00	1.00	1.00
Experimental procedure				
Time	Task			
Experiment preparation	Preparation of the water/sugar solution with the desired density value Labelling the water with salt			
t = - 30 seconds	Stationary flow conditions in loops 2, 3, 4 established			
t = 0 seconds	Start of injection of the water with the higher density into the loop 1			
t = 90 seconds	End of injection			

ROCOM test 2.1 - modelling approach

Two cylindrically shaped grids were used for the geometrical representation of the downcomer and the lower plenum. Both consisted of 16 azimuthal nodes. The lower plenum grid was generated by a so-called central channel (representing the central part of the cylindrical grid) and three subsequent rings, with the outermost ring connected to the downcomer grid. Figure 6.28 schematically represents the downcomer grid and the assignment of the 193 core inlet openings (each equipped with one wire mesh measuring node) to the rings and segments of the cylindrical lower plenum grid.

A second, simplified nodalisation was also tested to assess the advantage of the 3D approach to the lower plenum. Within this “classical” 1D approach, a set of branch objects interconnected by junctions was used to represent the lower plenum.

Figure 6.28. Downcomer grid and assignment of 193 core inlet openings to the central channel and two innermost rings of the cylindrical grid



Source: Pandazis et al., 2015.

ROCOM test 2.1 - results

The assessment of the simulation results will start with the qualitative comparison against the measurements in the downcomer (DC) and lower plenum (LP) regions. A direct comparison is presented in Figure 6.29. The two modelling approaches adopted to the lower plenum are named 3DLP (3D) and BRLP (1D). The colour schemes used to represent the temperature field for downcomer and core entry are different. The colour “blue” always corresponds to the temperature 241°C (recalculated from the measured mixing scalar) and the colour “red” corresponds to the values 198.3°C and 214.8°C in the downcomer and core entry, respectively.

The interpretation of the measurement data reveals a non-uniformly mixture of the coolant at the RPV inlet nozzle of the affected loop (AL) in the first few seconds of the experiment. This detail influences the degree of coolant mixing in the DC of the RPV. Due to the ATHLET’s 1D description of the coolant flow in the cold legs, this effect could not be observed in any of the numerical simulations.

The denser liquid creates a plume of approximately 90° azimuthal width below the RPV’s inlet nozzle of the AL. This flow behaviour can be observed in the experiment between 12.4 s and 15.1 s. Subsequently, the denser liquid flows downwards to the LP in form of two diverging strands. The ATHLET simulation, which employs the genuine multidimensional flow description, captures the effect of the liquid strand separation. The two resulting strands still flow in a more compact pattern towards the LP in the 3DLP simulation than in the experiment. However, the BRLP model failed to capture this effect because the denser liquid flows in form of a plume through the DC of the RPV.

The denser liquid reaches the LP over almost the entire periphery in the experiment and starts to enter the core. Both ATHLET simulations show a similar behaviour at that point for the denser liquid plume as it reaches the LP in a compact pattern. The plume temperature is overestimated due to too-high hot coolant admixing in the region of the nozzle, which can result from numerical diffusion. Yet the point when the first overcooled liquid reaches the core tie plate is well predicted by the 3DLP model. However, the BRLP simulation shows a slightly different flow behaviour: the denser fluid reaches the lower plenum earlier and the denser liquid is redirected into the core channels neighbouring the downcomer region linked with the affected loop.

The point at which the denser liquid bulk started to form in the core centre is well captured by the 3DLP simulation, at around 55.0 s. In comparison, the time delay by which the denser liquid reaches the core inlet and the temperature distribution pattern at the CI highlight ATHLET's multidimensional capability to transport the fluid realistically along and within the hemispherical shaped lower plenum.

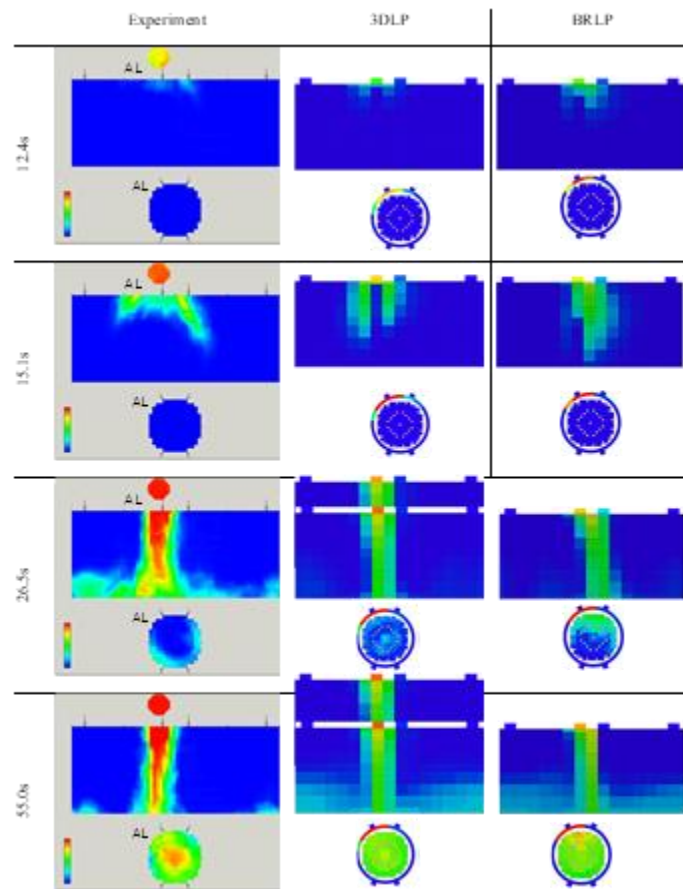
The temperature trends at the core inlet of two representative flow channels and the average core inlet temperature are presented in Figures 6.30, 6.31 and 6.32. The 3D lower plenum model predicts the overall behaviour better, for even the point at which the denser fluid reaches the CI is accurately captured. This capability is underlined by the comparison of the temperature trends in the core channels neighbouring the AL. However, the comparison of the temperature trends for the core central channel provides only minor advantages of the genuine multidimensional flow model: both computer simulations overestimate the degree of mixing and, hence, the resulting temperature shows higher values than in the experiment.

ROCOM test 2.1 - conclusions

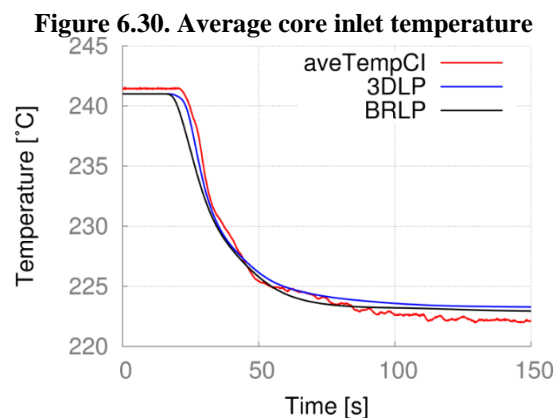
ATHLET's multidimensional model was validated against ROCOM test 2.1 data acquired in the downcomer region and at the core inlet, showing the typical behaviour of a coolant mixing process. ATHLET yields good results for the temperature distribution during the overcooling transient in complex geometries such as the RPV, provided that the multidimensional flow model is employed together with an advanced nodalisation scheme of the lower plenum. Both enable a clearly improved and realistic flow modelling in annular and hemispherical geometries, thereby increasing ATHLET's prediction capabilities. The formation and shape of the denser coolant plume in the DC could be simulated satisfactorily. In particular, only the 3D lower plenum model could reproduce a coolant temperature distribution across the CI, with a low-temperature bulk in the central core region, thus highlighting the improvement compared to the "classical" 1D description of the LP. However, the degree of mixing was overestimated, which is most likely due to the coarse nodalisation used to represent the lower plenum.

ATHLET simulations have also been performed on ROCOM tests 1.1 and 2.1 in [6.2-25].

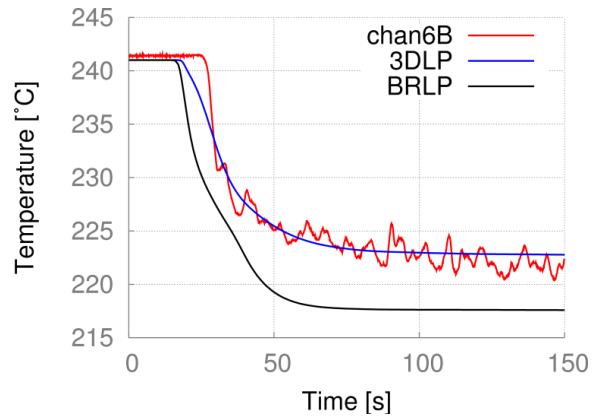
Figure 6.29. Comparison of the temperature fields derived from measured data and simulated by means of the 3DLP and BRLP models, in the downcomer and at the core inlet at temporal key points of the experiment



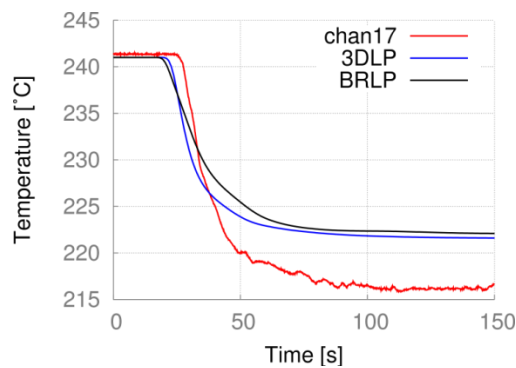
Source: Pandazis et al., 2015.



Source: Pandazis, et al., 2015.

Figure 6.31. Temperature trends at the CI for channel 6B adjacent to MSLB affected loop

Source: Pandazis et al., 2015.

Figure 6.32. Temperature trends at the CI for central channel

Source: Pandazis et al., 2015.

6.3.4.3. UPTF test 7

UPTF test 7 - motivation

The 3D fluid dynamic model was also adopted to two-phase flow situations as part of ATHLET's validation. Experiments were selected from the full-scale test facility UPTF (see Section 5.1.3). The UPTF-7 test investigated the multidimensional flow processes during the refill/reflood in the downcomer and lower plenum after a LB-LOCA. Condensation effects played a minor role because ECC injection was nearly at saturated conditions. The focus of the experiment and the according post-test simulation were therefore on multidimensional flow processes in the downcomer, such as CCFL and ECC bypass flow.

UPTF test 7 - test description

UPTF test 7 was performed to obtain full-scale information on the downcomer and lower plenum refill and reflood behaviour during the end-of-blowdown phase of LOCA. Four runs were conducted: run 200, run 201, run 202 and run 203. Steam and ECC water were injected into the core and the intact cold legs respectively at controlled rates. The main objective of the tests was to determine the penetration of the ECC coolant through the downcomer into the lower plenum as a function of the uprising steam flow.

Steam and ECC injections were regulated as function of time. Table 6.12 summarises the steam and the ECC injection mass flow rates for the different phases of UPTF test 7's

experimental runs. The ECC injection was at saturation (slightly subcooled). According to [6.2-27] and the phases highlighted in red in Table 6.12, the liquid level in the lower plenum was so high that the steam was further accelerated in the region due to the reduced free cross-section. Consequently, the flow was no longer considered to be a subject of the countercurrent flow limitation (CCFL) study objectives of the experiment for these experimental phases. These phases were not therefore considered for the assessment of the code to reproduce CCFL situation in the RPV downcomer.

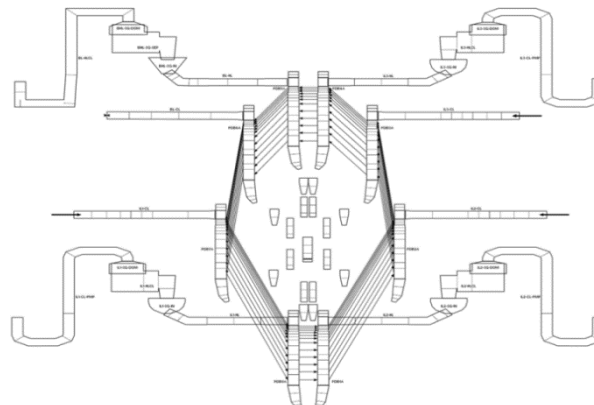
Table 6.12. Steam and ECC injection mass flows for UPTF test 7

Run, phase	Steam [kg/s]	ECC in cold leg 1 [kg/s]	ECC in cold leg 2 [kg/s]	ECC in cold leg 3 [kg/s]
Run 200, phase I (75s – 97s)	104	495	14	12
Run 200, phase II (125s – 155s)	53	737	31	12
Run 200, phase III (175s – 205s)	102	735	17	14
Run 200, phase IV (235s – 265s)	102	493	15	488
Run 200, phase V (300s – 345s)	148	687	25	483
Run 201, phase I (85s – 105s)	102	-	487	489
Run 201, phase II (140s – 160s)	101	271	727	732
Run 201, phase III (192s – 225s)	102	491	486	490
Run 202, Phase I (65s – 100s)	102	-	726	730
Run 202, phase II (125s – 155s)	127	-	487	490
Run 202, phase III (unstable)	unspecified	unspecified	unspecified	unspecified
Run 203, phase I (68s – 98s)	70	734	35	16
Run 203, phase II (131s – 171s)	30	738	25	16
Run 203, phase III (220s – 250s)	71	737	32	733
Run 203, phase IV (290s – 330s)	51	493	484	487

UPTF test 7 - modelling approach

Two different nodalisations [6.2-26] were again employed for the 3D simulation region to analyse the grid sensitivity effect: 8 and 16 azimuthally aligned channels nodalisation schemes were investigated for the representation of the reactor downcomer and lower plenum. Figure 6.33 presents an overview of the eight channels nodalisation scheme. The reactor downcomer was modelled in the input model, with eight vertical pipes connected by horizontal junctions. The pipes of the lower plenum, consisting of a central channel and three rings with eight pipes each, is also depicted in Figure 6.33. The model with 16 azimuthal segments employed an analogous nodalisation scheme.

Figure 6.33. The eight segments model nodalisation scheme for the DC and LP

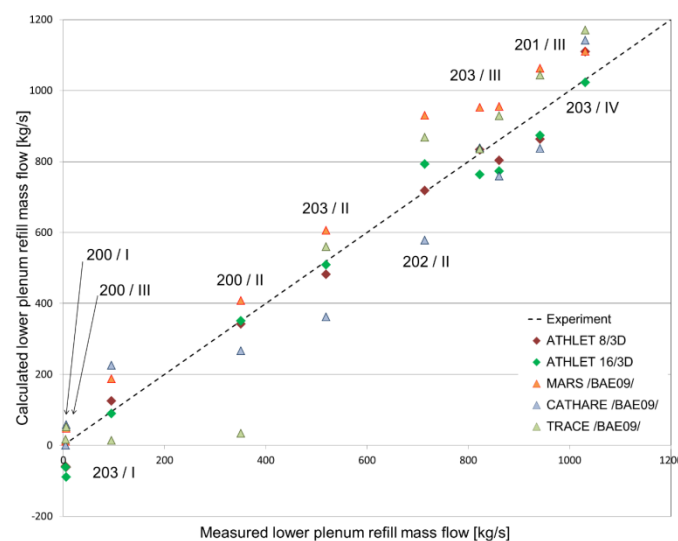


Source: Austregesilo et al., 2013.

UPTF test 7 - results

The mass flow towards the reactor lower plenum indicates if and how the reactor core can be cooled during the end-of-blowdown LOCA refill and reflood phases. The main goal of the UPTF test 7 was to assess this mass flow experimentally. Bae and Chung [6.2-28] compared MARS-KS, CATHARE and TRACE numerical codes during their studies for the theoretical assessment of the lower plenum refill mass flow. Their results were employed in the evaluation of the ATHLET input model performance. The lower plenum refill mass flow results are shown in Figure 6.34.

Figure 6.34. Mass flow towards the lower plenum at different experimental phases



Source: Austregesilo et al., 2013.

There is good agreement between the 3D ATHLET models and the experimental observations for mass flow towards the reactor lower plenum, as shown in Figure 6.31. The biggest differences are observed for phase I and phase III of run 200, for which a minimum mass flow of five and six kg/s respectively was experimentally observed. The 16 channels 3D capture most closely the experiment at higher mass flows for less than 600 kg/s. The eight channels 3D model performs most successfully in the range of 700 to 900 kg/s.

UPTF test 7 - conclusions

UPTF test 7's downcomer countercurrent flow experiments were analysed with the ATHLET 3.0A code version. Both ATHLET models, using 8 or 16 segments for the cylindrical RPV grid, produced good qualitative predictions with respect to the coolant level in the reactor lower plenum. No clear advantage of the highly resolving 3D approach with 16 azimuthal segments could be demonstrated for the entire experimental set and time. Therefore, no final recommendation for finer grid nodalisation can be derived from UPTF test 7 simulations.

6.4. Independent code validation

Independent validation is an important activity in the life cycle of a code because many more models and integral system simulations are performed that significantly exceed the developing organisation's capability. The goal is to receive feedback on code/model strengths and deficiencies from expert code users (via independent assessment).

6.4.1. CATHARE 3D natural circulation flow mixing

The CATHARE 3D capability in predicting the flow mixing under asymmetric natural circulation flow conditions was assessed against the PKL-2/ROCOM test series (T1.1, T1.2, and T1.3).

The ROCOM facility [Section 5.1.1] was built to investigate the coolant mixing phenomenon in the RPV downcomer and core inlet zones, as well as the thermal stratification phenomenon that can take place in the connecting legs. Advanced instrumentation that delivers high resolution information was installed for this purpose. The downcomer sensors consist of two grids at the inner and outer sides of the downcomer's walls. The wire mesh sensor measures the instantaneous local water conductivity and derives the corresponding density difference with a measurement error of about 3.5%. The RPV of the ROCOM facility is filled with demineralised water at atmospheric temperature and pressure conditions. The desired water density could be changed by injecting an adequate amount of sugar or ethanol according to the test requirements. The mixing in the RPV downcomer and the core inlet plenum are then implicitly evaluated at a ten Hz frequency (each 0.1s) using the following mixing scalar (MS) formula:

$$MS_{measured}(r, \theta, z) = \frac{\sigma_{measured}(r, \theta, z) - \sigma_{intact-loops}}{(\sigma_{affected-loop} - \sigma_{intact-loops})} \quad (\text{Eq. 1})$$

$\sigma_{measured}(r, \theta, z)$ is the instantaneous local water conductivity measured through the sensors.

Table 6.13 summarises the tests conditions where the fluid density and mass flow rates are changed at the RPV inlet.

Table 6.13. Boundary conditions of ROCOM runs

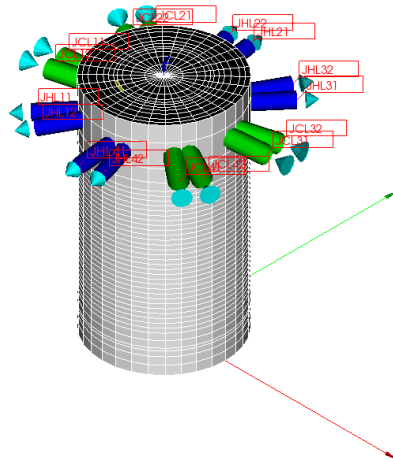
Run N	T1.1		T1.2		T1.3	
Loop number	1, 2, 4	3	1, 2, 4	3	1, 2	3, 4
Density (kg/m ³)	838.2	815.7	888.1	863.5	930	898.5
Mass flow rate (l/s)	3.3	2.14	3.28	0.58	3.51	0.68
Relative density	1.0	0.974	1.0	0.972	1.0	0.966

CATHARE modelling

The CATHARE-2/V2.5_2/mod8.1 nodalisation is built up based on former calculations. The current base case model, as shown in Figure 6.35, has 11 radial meshes, 32 azimuthal and 16 axial nodes. Concerning the vessel connections with the cooling loops, external and internal junctions are considered as in Figure 6.35. In order to take the geometry effects of the different components of the vessel into account, surface and volume porosity are introduced. Surface porosity is considered to represent the cold and hot leg connections to the vessel. The volumetric porosity is considered to take into account the geometry effects of the core grid support plate, the core basket, the lower plenum sieve drum, and the lower plenum semi-spherical shape.

The test conditions as specified in Table 6.13 are used as boundary conditions at the RPV nozzles. The latter are translated into temperature and mass flow rate in which the mixing scalar is calculated using the following formula:

$$\Psi(r, \theta, z) = \frac{(T(r, \theta, z) - T_{average-intact-loops})}{(T_{affected-loop} - T_{average-intact-loops})} \quad (\text{Eq. 2})$$

Figure 6.35. 3D CATHARE nodalisation model for the ROCOM vessel

Source: Salah and Vlassenbroeck, 2013.

Calculation vs. experimental results

All the CATHARE simulations were carried out within a pseudo-steady-state period of 400 s with a maximum time step of 0.1 s.

On the one hand, the calculated and experimental fluid temperature distributions in the RPV downcomer are sketched together in a 2D plan representation in Figure 6.36. Each line corresponds to the ROCOM T1.1, T2.1 and T3.1 tests, respectively. On the whole, from the qualitative point of view, the descending plumes and even the turbulence in the downcomer are qualitatively well predicted by the CATHARE code.

In T1.1, a clear mixing level takes place in the upper zone of the downcomer (see Figure 6.34). Furthermore, two distinct hot and cold descending plumes are clearly simulated. The hot plume, coming from the affected loop, follows an azimuthal flow path, before going downward to the bottom zone of the downcomer.

In T1.2, the mixing level in the RPV downcomer is less pronounced. The descending cold plumes are more diffused in the downcomer and prevent the hot plume coming from the affected loop to easily reach the bottom of the downcomer. In T1.3, the mixing level in the RPV downcomer is clearly emphasised. The hot fluid coming from the affected loop mixes in the zones where the cold water is injected before reaching the lower part of the downcomer.

On the other hand, Figure 6.37 presents the maximal and mean value of the mixing scalar (MS) in the downcomer and core inlet plenum. It is observed that the mean value of the MS is well predicted in the downcomer zone, while the maximal value of the MS is predicted with larger discrepancy. However, a better agreement is observed at the core inlet zone.

Conclusion

The 3D features of the T/H system code CATHARE2_V2.5_2mod8.1 have been assessed against the OECD/PKL-2 ROCOM tests T1.1, T1.2 and T1.3. The focus was on the evaluation of mixing in the RPV under asymmetric conditions. The main phenomena taking place in the RPV downcomer and core inlet zone were well predicted. The CATHARE code agrees with the experimental measurements with respect to the mean values of the

mixing. Nevertheless, larger discrepancies are observed in predicting local values of the mixing.

Figure 6.36. CATHARE vs. experimental temperature distribution in the downcomer

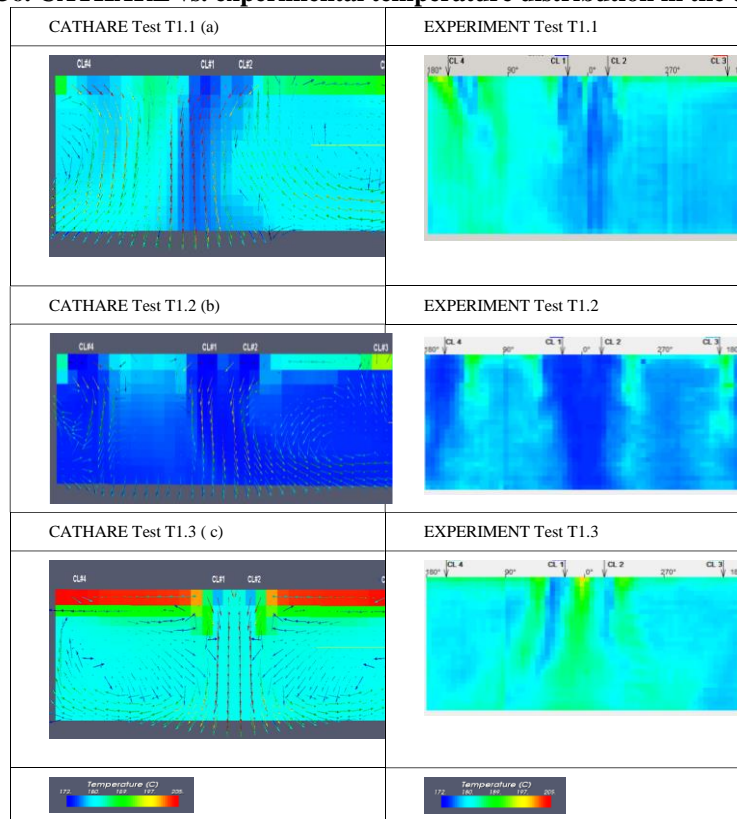
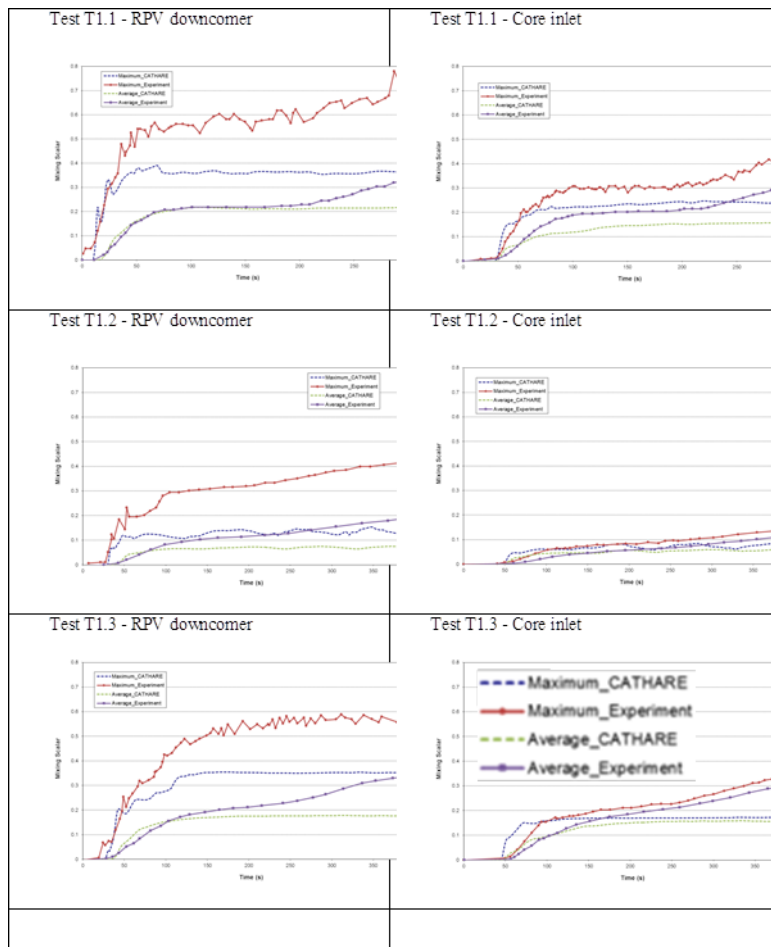


Figure 6.37. CATHARE vs. experimental mixing scalar

6.4.2. Validation of CATHARE with the SPES-2 facility

SPES2 is a full-height and full-pressure experimental facility scaled at 1/395 of the Westinghouse AP600 plant [6.2-31]. This facility can simulate the behaviour of the typical passive safety systems of the AP600. The passive safety systems are: two core make-up tanks (CMTs), an in-containment refuelling water storage tank (IRWST), a passive residual heat removal (PRHR) system, two accumulators (ACCs) and an automatic depressurisation system (ADS).

The present work deals with the development and validation of a numerical model of SPES2 integral facility using the CATHARE code. The model's capability to simulate the transient behaviour of the facility in its present configuration has been verified against a SB-LOCA transient test conducted in the SPES facility in the 1990s.

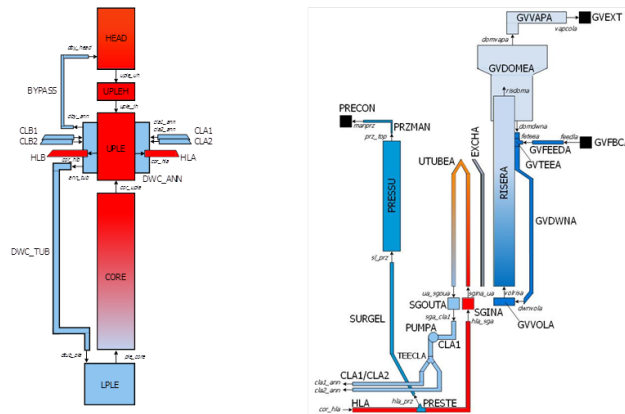
CATHARE model

The latest version V2.5_2 of CATHARE 2 has been adopted to simulate the SPES-2 facility behaviour; the related nodalisation has been developed by respecting the geometrical dimensions of different parts and components, as well as the circuits' topology. The nodalisation schemes of the primary vessel and loop A, which includes the pressuriser, are reported in Figure 6.38.

Some choices about the nodalisation of the facility can strongly influence the results of the simulation [6.2-32]. The vessel annular downcomer has been represented, in a first nodalisation, by a zero-dimensional or “volumes” (0D) component (DWC_ANN) in order to easily describe the high number of connections in this part of the circuit (four cold legs, downcomer upper-head bypass, passive safety systems injection and tubular downcomer). This component does not take the inertial forces (the internal velocity is neglected) and the possible multidimensional effects into account, and therefore it has been decided to update the nodalisation by introducing 3D components to describe the behaviour of the annular downcomer (Figure 6.39). The annular downcomer was represented by one mesh in radial direction, 15 meshes in Z direction and eight meshes in azimuthal direction.

The nodalisation of IRWST has been carefully developed (Figure 6.40). The IRWST is represented by two “volumes” -0D- and two “axials”-1D- (TEP2, TP2) connected by a transversal junction at different elevations, which simulates as many of the phenomena observed in this part of the facility as possible (aiming to simulate 2D recirculation). The axial TEP2 is thermally coupled with a PRHR C-shaped tube to remove residual heat from the primary system by natural circulation at any pressure.

Figure 6.38. Vessel and loop A nodalisations



Source: D’Amico et al., 2015.

Figure 6.39. Annular downcomer 3D component

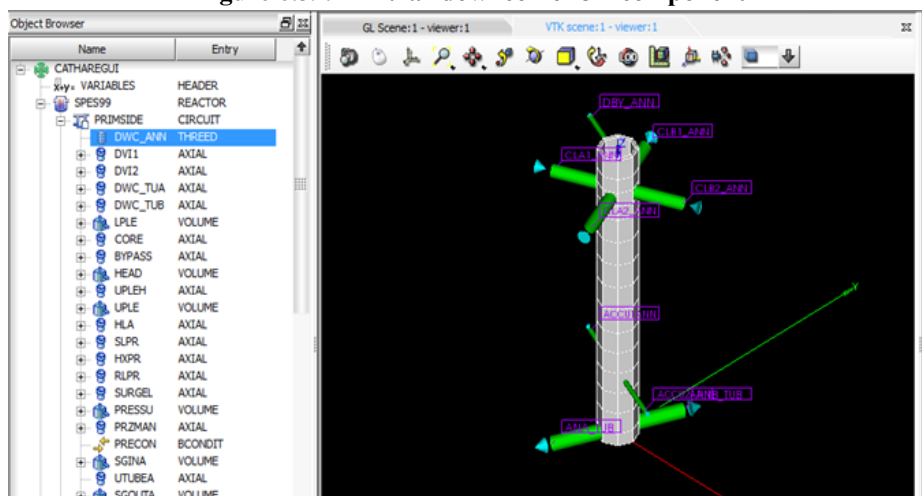
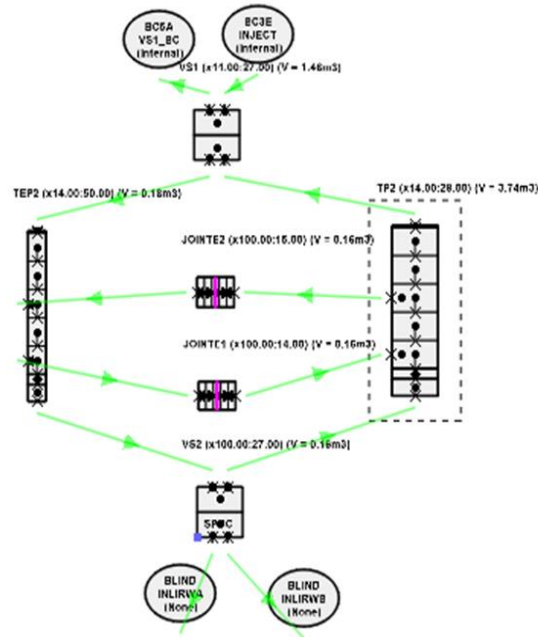


Figure 6.40. IRWST nodalisation



“2-inch direct vessel injection line break” in SPES

The test simulated is part of the SPES2 test’s matrix [6.2-33]. The test of this matrix has been conducted by SIET in Piacenza (Italy), with the aim of examining the AP600 passive safety system response for a range of SB-LOCAs at different locations on the primary system and passive system lines. All experimental data obtained in this campaign belong to Westinghouse. As a result, all results reported in this paper are shown in a non-dimensional form. The test’s aim was to investigate the response of the passive safety systems during the whole transient. The test is characterised by a single failure event: one of the two ADS stage four valves had to remain closed. The sequence of the events is reported in Table 6.14.

Table 6.14. Sequence of events

EVENT	SET POINT
REACTOR TRIP	P (PRZ) < 12.41 MPa + 5.73s
S SIGNAL	P (PRZ) < 11.72 MPa
STEAM LINE A/B CLOSURE	P (PRZ) < 12.41 MPa + 2s delay
FEED WATER A/B CLOSURE	P (PRZ) < 11.72 MPa + 2 s delay
CMT A/B INTERVENTION	P (PRZ) < 11.72 MPa + 2 s delay
PRHR INTERVENTION	P (PRZ) < 11.72 MPa + 2 s delay
PUMP A/B TRIP	P (PRZ) < 11.72 MPa + 16.2 s delay
ADS STAGE I	L (CMT A o B) < 67% +30 s
ACC INJECTION	P (PRZ) < 4.87 MPa
ADS STAGE II	L (CMT A o B) < 67% +125 s
ADS STAGE III	L (CMT A o B) < 67% +245 s
ADS STAGE IV	L (CMT A o B) < 20% +60 s

The test starts at 0s by opening the break valve from full power steady-state conditions. The CMT flow rates are slightly asymmetric during recirculation and drain down phases. The pressuriser level rises after ADS stage one opening and continues to increase until

ACC injection stops. After ADS stage three opening, the primary system depressurisation becomes more rapid due to the increased amount of steam in the system. About 30 minutes after the beginning of the transient, ADS stage four opens and the pressuriser empties again. IRWST injection begins about 100 s later: this signals the end of the SB-LOCA transient and beginning of the long-term cooling phase.

Comparison between experimental data and CATHARE results

The main calculated parameters compared to the experimental trends are reported from Figure 6.41 to Figure 6.44. In all reported figures, the red line represents the experimental data, the blue (CATHARE_OLD) and green (CATHARE_NEW) lines represent the results of CATHARE calculation with the 0D and 3D components for annular downcomer respectively. The CATHARE_NEW simulation presents an early stop, probably due to calculation convergence problem.

Figure 6.41 shows the primary pressure. The fast depressurisation of the primary system after the break opening is well predicted by CATHARE in the first seconds of the transient in both simulations. The CATHARE_NEW results are in better agreement with the experimental depressurisation results than the CATHARE_OLD results.

Figure 6.41. Primary pressure

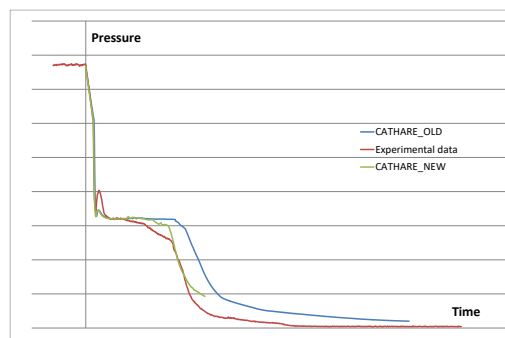


Figure 6.42 shows the mass flowrate discharged by the break located in the DVI2, near the connection with annular downcomer. A good prediction by CATHARE_NEW is showed in the first part of the transient until the simulation stops. In the second part, the CATHARE_OLD simulation overestimates the experimental result.

Figure 6.42. Break mass flow rate

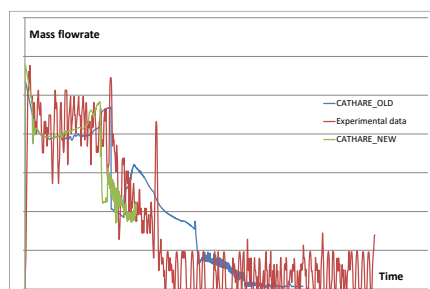


Figure 6.43 shows the mass flow rate flowing in the PRHR. This flow rate is a function of natural circulation and in accidental conditions will provide the residual heat removal from the primary side of the facility. While the PRHR intervention time is exactly predicted, the natural circulation stops in both CATHARE simulations. The CATHARE_NEW simulation shows a restart in natural circulation and better prediction of the PRHR behaviour than the CATHARE_OLD simulation. It is clear in this facility where the annular downcomer extends into the inlet plenum that the cold water injected by DVIs is able to

reach the lower plenum, while the hot water is recirculated to the upper part of the downcomer. The update of the nodalisation using a 3D element therefore can represent this behaviour.

Figure 6.43. PRHR mass flow rate

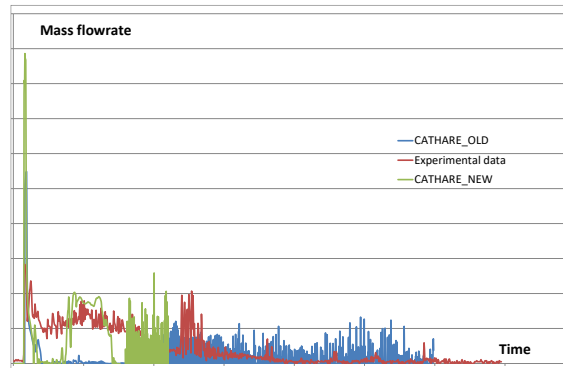
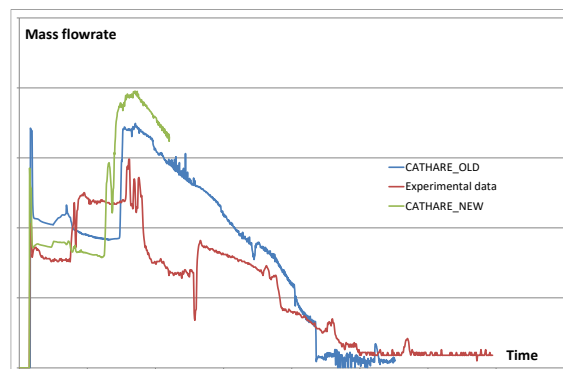


Figure 6.44 reports the mass flowrate discharged by CMTB in the primary side. The new nodalisation shows a better capacity to describe the behaviour of this passive safety system.

Figure 6.44. CMTB mass flow rate



The following can be drawn from these results:

- The 3D module of CATHARE has better capability for describing the real situation of the SPES2 annular downcomer, which will be a subject of further investigation.
- The presence of stop in PRHR natural circulation is predicted by CATHARE simulation and not showed by experimental results.

The results of these calculations suggest deepening the phenomena occurring in the passive safety systems (i.e. the stop in natural circulation observed in PRHR that could be a consequence of the nodalisation adopted for the IRWST) and verifying the T/H codes' ability to describe these phenomena (i.e. the exact evaluation of pressure and heat losses).

Conclusions

SPES2 is a full-height and full-pressure experimental facility scaled 1/395 respect to the Westinghouse AP600 plant. This facility can simulate the behaviour of the typical passive safety systems of the AP600. The present work deals with the development and validation of a numerical model of the SPES2 integral facility using a CATHARE code. The capability of the model to simulate the transient behaviour of the facility has been verified against an SB-LOCA transient test, which was conducted in the SPES2 facility at the end of the 1990s.

A comparison of the CATHARE model predictions and experimental data presented in this work shows a good ability of the 3D element of CATHARE code to describe the relevant phenomena occurring in this facility. This comparison has suggested some possible improvements of the model, such as the updated nodalisation adopted for the IRWST.

Moreover, the comparison of the code predictions and experimental data is very useful to identify input data limitations and improve the CATHARE nodalisation.

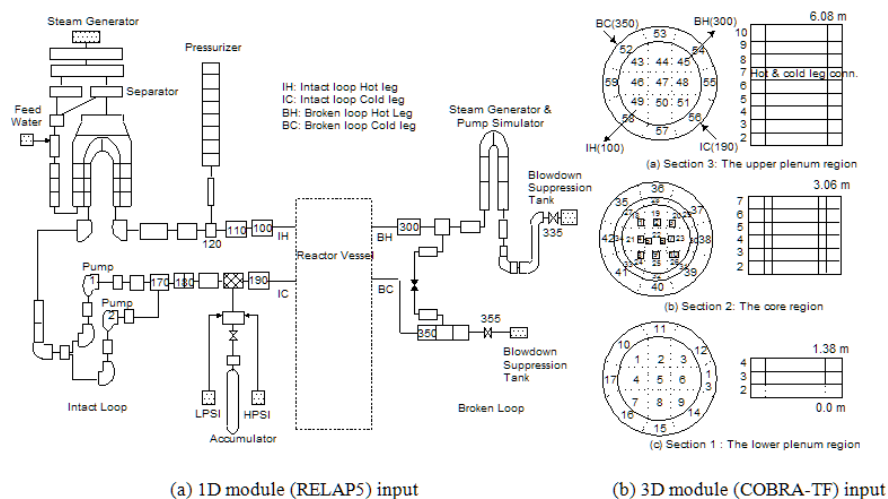
Acknowledgements

The authors appreciate the financial support of the Italian Minister of Economic Development through the ENEA-MSE agreement.

6.4.3. Validation of MARS with the LOFT facility

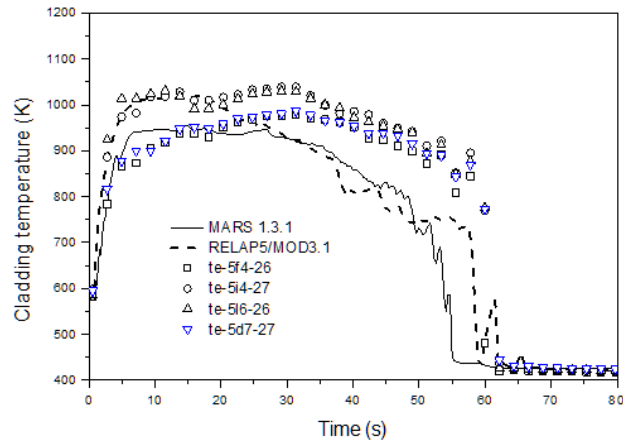
The 3D analyses of the LOFT experiments and/or code assessment were very limited, see [6.2-29] and [6.2-30]. One of the examples is the MARS code assessment. Figure 6.45 shows the MARS nodalisation for the LOFT L2-5 experiment simulation [6.2-30]. The MARS code has been developed by consolidating and restructuring the RELAP5/MOD3.2.1.2 and COBRA-TF codes. The reactor vessel was modelled using the 3D module (COBRA-TF), which consists of 354 hydrodynamic cells (3 sections, 59 channels and 76 gaps). Each channel of the core region, channels 18 through 26, contains a “rod” component representing the average rods of the fuel bundle. Channel 22 contains an additional “rod” component to simulate the hottest rod. Figure 6.46 shows that both MARS and RELAP5/MOD3.1 predict the cladding temperature at 0.64 m above the bottom of the active core reasonably well. However, MARS tends to under-predict the temperature. This seems to be caused by the blowdown heat transfer model of the MARS 3D module. Figure 6.47 shows that both codes failed to capture the blowdown peak. Nevertheless, the results of MARS seem qualitatively better.

Figure 6.45. MARS nodalisation for the LOFT L2-5 experiment simulation



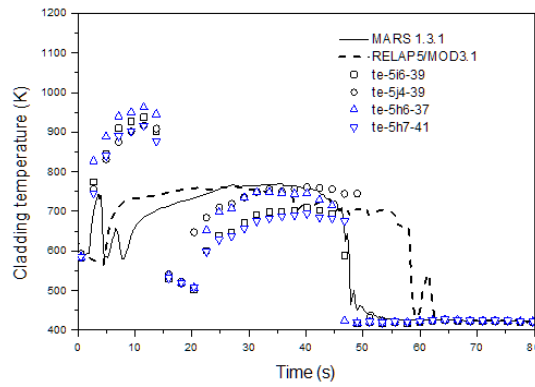
Source: Chung et al., 2010.

Figure 6.46. Hot rod cladding temperatures at 0.64 m



Source: Chung et al., 2010.

Figure 6.47. Hot rod cladding temperatures at 1.0 m



Source: Chung et al., 2010.

References

- [6.1-1] International Atomic Energy Agency (2019), *IAEA Safety Glossary: 2018 Edition*, Non-serial Publications, IAEA, Vienna.
- [6.1-2] IEEE Standards Association (2010), *Systems and software engineering-Vocabulary*, Iso/Iec/Ieee, 24765, pp.1-418.
- [6.1-3] Bayless, P.D., editor (2014), “RELAP5-3D Code Manual - Volume III: Developmental Assessment”, INEEL-EXT-98-00834 Revision 4.2., Idaho Falls, Idaho, United States.
- [6.1-4] US NRC (2007), “TRACE V5.0 ASSESSMENT MANUAL - Appendix A: Fundamental Validation Cases”, US Nuclear Regulatory Commission, Washington, DC.
- [6.1-5] Moody, F.J. (1990), “Introduction to Unsteady Thermofluid Mechanics”, John Wiley & Sons, New York, p.589.
- [6.1-6] D’Auria, F. and M. Lanfredini (2019), “V&V&C in nuclear reactor thermal-hydraulics”, *Nuclear Engineering and Design*, 354.
- [6.1-7] Serre, G. and D. Bestion (2001), “Benchmarks calculated with the ICE numerical method using CATHARE and TRIO_U codes”, ECUME project report, CEA/EDF.
- [6.2-1] Chung, B.D., J.J. Jeong, M.K. Hwang, W.J. Lee, Y.J. Lee, S.W. Lee, K.D. Kim and S.W. Bae (2010), “MARS CODE MANUAL VOLUME IV-Developmental Assessment Report”, No. KAERI/TR--3042/2005, Korea Atomic Energy Research Institute.
- [6.2-2] Bukhar, K.M. and R.T. Lahey Jr. (1984), “The Measurement of Countercurrent Phase Separation and Distribution in a Two-Dimensional Test Section”, NUREC/CR-3577 R2, Rensselaer Polytechnic Inst., Dept. of Nuclear Engineering, Troy, NY (United States).
- [6.2-3] Park, C.K., C.K. Song, S. Cho, S.Y. Chun and M.K. Chung (1997), “Construction of the blowdown and condensation loop”, No. KAERI/TR--941/98, Korea Atomic Energy Research Institute.
- [6.2-4] Auban, O., D. Paladino and R. Zboray (2005), “OECD/SETH Project, PANDA Test Facility: Description and Geometrical Data”, PSI TM-42-05-06, ALPHA-05-01.
- [6.2-5] Rothe, P.H. and C.J. Crowley (1978), “Scaling of pressure and subcooling for countercurrent flow”, Creare, Inc., Hanover, NH, United States.
- [6.2-6] Herkenrath, H., W. Hufschmidt, U. Jung and F. Weckermann (1981), “Experimental investigation of the enthalpy and mass flow distribution in 16-rod clusters with BWR-PWR geometries and conditions.”, Final Report Joint Research Centre of the European Communities, Ispra, Italy.
- [6.2-7] Bae, S.W., K.D. Kim, B.D. Jeong, S.W. Lee, B.J. Kim J.S. Heo and J.H. Lee (2016), “Development and Verification of SPACE Code 3D Component”, KAERI technical report, KAERI/TR-6369/2016.
- [6.2-8] Pandazis, P., S.C. Ceuca, P.J. Schöffel and H.V. Hristov (2015), “Investigation of the Multidimensional Flow Mixing Phenomena in the Reactor Pressure Vessel with the System Code ATHLET”, NURETH-16, 30 August-4 September, Chicago, United States.
- [6.2-9] Schöffel, P.J., H.V. Hristov and G. Lerchl (2014), “Towards Multidimensional Thermal-hydraulic Simulations with the System Code ATHLET”, Proc. of 45th Annual Meeting on Nuclear Technology, Frankfurt, Germany, pp. 6-8.
- [6.2-10] M. Valette (2007), “Analysis of boiling two-phase flow in rod bundle for NUPEC BFBT benchmark with 3-field NEPTUNE system code”, NURETH-12, 30 August-4 September, Pittsburgh, Pennsylvania, United States.

- [6.2-11] Glantz, T. and R. Freitas (2008), “Improvement of the CATHARE 3D code prediction on PIERO transient”, ICONE 16, 11-15 May, Orlando, Florida, United States.
- [6.2-12] Geffraye, G. O. Antoni, M. Farvacque, D. Kadri, G. Laviaille, B. Rameau and A. Ruby (2011), “CATHARE 2 V2.5 2: A single version for various applications”, *Nuclear Engineering and Design*, 241, pp. 4456-4463.
- [6.2-13] Jeong, J.J., I. Dor and D. Bestion (1997), “Improvement and assessment of the CATHARE 2 three-dimensional module compared with the UPTF downcomer test 7”, *Nuclear Technology*, 117(3), pp. 267–280.
- [6.2-14] Dor, I. and P. Germain (2011), “Core radial profile effect during reflooding, validation of CATHARE-2 3D module using SCTF tests”, NURETH-14, 25-30 September, Toronto, Ontario, Canada.
- [6.2-15] Bazin, P., I. Dor and C. Morel (2005), “Assessment of the CATHARE 3D module for LBLOCA simulation”, NURETH-11, 2-6 October, Avignon, France.
- [6.2-16] Carnevali, S. and P. Bazin (2012), “Validation of CATHARE code on the 3D ROSA-LSTF pressure vessel”, NURETH 16, 30 August-4 September, Chicago, United States.
- [6.2-17] Carnevali, S. (2016), “Comparison of CATHARE code using a 3D Reactor Pressure Vessel modelling approach and experimental results on intermediate break LOCAs of ROSA 2 program”, NUTHOS-11, 9-13 October, Gyeongju, Korea.
- [6.2-18] Mazgaj, P., J.-L. Vacher and S. Carnevali (2016), “Comparison of CATHARE results with the experimental results of cold leg intermediate break LOCA obtained during ROSA-2/LSTF test 7”, *EPJ Nuclear Science and Technologies*, 2(1).
- [6.2-19] Valette, M. (2012), “Analysis of Subchannel and Rod Bundle PSBT Experiments with CATHARE 3”, *Science and Technology of Nuclear Installations*, Article ID 123426, 10 pages.
- [6.2-20] Chandesris, M., M. Mazoyer, G. Serre and M. Valette (2013), “Rod bundle thermalhydraulics mixing phenomena: 3D analysis with CATHARE 3 of various experiments”, NURETH-15, 12-17 May, Pisa, Italy.
- [6.2-21] Glantz, T. and R. Freitas (2008), “Validation of CATHARE 3D Code against UPTF-TRAM C3 transients”, *Journal of Power and Energy Systems*, 2(1), pp. 397-408.
- [6.2-22] Salah, A.B. and J. Vlassenbroeck (2013), “Assessment of the CATHARE 3D capabilities in predicting the temperature mixing under asymmetric buoyant driven flow conditions”, *Nuclear Engineering and Design*, 265, pp. 469-483.
- [6.2-23] Ruby, A., P. Emonot, V. Figerou, D. Baloge, A. Fèvre, B. Velly and G. Vigé (2013), “CATHARE-3: First computations of a 3 inches break Loss-Of-Coolant Accident using a modular multi-3D modelling of a PWR vessel”, NURETH-15, 12-17 May, Pisa, Italy.
- [6.2-24] Kliem, S. and R. Franz (2012), “OECD PKL-2 Project – Final Report on the ROCOM Tests”, HZDR/FWO.
- [6.2-25] Diaz-Pescador, E., F. Schäfer and S. Kliem (2021), “Modelling of multidimensional effects in thermal-hydraulic system codes under asymmetric flow conditions – Simulation of ROCOM Tests 1.1 and 2.1 with ATHLET 3D-Module”, *Nuclear Engineering and Technology*, 53.
- [6.2-26] Austregesilo, H., C. Bals, J. Herb, T. Hollands, A. Papukchiev, P. Schöffel and S. Weber (2013), „Validierung von Rechenprogrammen zur Simulation von Stör- und Unfällen im Reaktorkühlsystem”, Final Report, RS1195.

- [6.2-27] Weiss, P. et. al. (1990), “Test No. 7 Downcomer Countercurrent Flow Test”, 2D/3D Program Upper Plenum Test Facility Quick Look Report, prepared by Siemens/KWU, E314/90/003, Erlangen, Germany.
- [6.2-28] Bae, S. W. and B.D. Chung (2009), “Development of the multi-dimensional hydraulic component for the best estimate system analysis code Mars”, *Nuclear engineering and technology*, 41(10).
- [6.2-29] Jeong, J.J., S.K. Sim, C.H. Ban and C.E. Park (1997), “Assessment of the COBRA/RELAP5 code using the LOFT L2-3 large-break loss-of-coolant experiment”, *Annals of Nuclear Energy*, 24, 14, pp. 1171-1182.
- [6.2-30] Jeong, J.J., K.S. Ha, B.D. Chung and W.J. Lee (1999), “Development of A Multi-dimensional Thermal-Hydraulic System Code, MARS 1.3.1”, *Annals of Nuclear Energy*, 26, pp. 1611-1642.
- [6.2-31] Rigamonti, M. (1995), “SPES-2 facility description” SIET report 00183R192 Piacenza, Italy.
- [6.2-32] L.E. Conway and R. Hundal (1996), “SPES-2, AP600 integral systems test results”, Westinghouse Electric Corporation.
- [6.2-33] Lavialle, G. (2006), “CATHARE 2 V2.5_1 User’s guidelines”, DER/SSTH/LDAS/EM/2005-034, Grenoble, France.
- [6.2-34] NEA (2006), “BEMUSE Phase II Report: Re-Analysis of the ISP-13 Exercise, Post-Test Analysis of the LOFT L2-5 Test Calculation”, OECD Publications, Paris, NEA/CSNI/R(2006)2, www.oecd-nea.org/jcms/pl_18346.
- [6.2-35] D’Amico, S., C. Lombardo, I. Moscato, M. Polidori and G. Vella (2015), “Transient analysis of ‘2 inch Direct Vessel Injection line break’ in SPES-2 facility by using TRACE code”, *Journal of Physics: Conference Series*, 655(1).
- [6.3-1] Lee, D.H., S.W. Lee and J.J. Jeong (2018), “Improvement of the SPACE Multi-dimensional Thermal-hydraulic Module using Semi-conservative Form of Momentum Equations”, *Journal of Computational Fluids Engineering*, 23(1), pp.37-44.
- [6.3-2] Barasch, M. and R. Lahey (1981), “The measurement of two-dimensional phase separation phenomena”, NUREG/CR-1936, US Nuclear Regulatory Commission, Washington, DC.

7. Main challenges to the improvement of 3D capabilities of SYSTH codes

7.1. 3D phenomena

Numerous three-dimensional (3D) phenomena have been identified in the components or pipes of a nuclear reactor, including pools [7-1]. This multidimensional behaviour is typical of many transients and is not restricted to multiphase flows. Some typical examples for which the implementation of 3D capabilities is expected to provide more reliable simulations are provided below. These examples are mainly related to loss-of-coolant accidents (LOCAs). However, other situations of interest have been identified in Section 2.2. These phenomena and the driven parameters (velocity, pressure, power distribution, geometry, etc.) have to be identified in detail. Some indications from experiments and simulations are available and are provided below, but they are insufficient.

7.1.1. Flow in the core with radial power distribution

3D phenomena occurring in a pressurised water reactor (PWR) core with radial power differences lead to modelling and validation issues that must be addressed for more precise and reliable simulations [7-2]:

- Gravity-driven and friction driven crossflows – due to a radial power profile – exist and depend on velocity flows and low or high pressure pure vapour flows. The direction of crossflows (from cold to hotter or hot to colder assemblies) influences the peak clad temperature (PCT) for LOCAs. The sensitivity to radial pressure losses seems weak, but the uncertainty is high.
- The radial distribution of fluid velocity and temperature is primarily due to diffusion and dispersion of momentum and energy. However, turbulent diffusion induces less mixing than dispersion in presence of spacer grids with mixing vanes. If both are smaller than the crossflow effects originating from the radial power profile, this explains the reasonable success of the simulation of LOCA transients without any diffusion and dispersion modelling.

7.1.2. Flow in the downcomer

Analyses of the 3D phenomena occurring in a PWR downcomer during emergency core cooling systems (ECCS) injection in a LOCA with azimuthal non-homogeneities identified a list of local phenomena:

- azimuthal thermal mixing between cold water from ECCS and boiling saturated water due to heat release from the pressure vessel (PV) wall;
- azimuthal void mixing between boiling regions and subcooled liquid downflow regions;
- condensation of bubbly flow.

Such phenomena are difficult to predict with coarse 2D downcomer modelling and a rather high uncertainty has to be applied to current models and nodalisations. Some mixing

problems in the downcomer in the presence of strong density differences (due to temperature gradients) can be approximated by 3D modules of system codes using a very coarse two-dimensional (2D) nodalisation at a very small central processing unit (CPU) cost compared to classical computational fluid dynamics (CFD) in open medium, which requires millions of meshes.

7.2. Limitation of PIRT

Existing system phenomena identification ranking tables (PIRTs) do not usually focus on local 3D processes. Table 7.1 shows an illustration extracted from the TRACE PIRT [7-3] establishing the validation matrix for large break loss-of-coolant accidents (LB-LOCAs), where only the phenomenon “3D flow “is mentioned for the core component and for refill and reflood phases.

Table 7.1. Example of PIRT for validation matrix for large break loss-of-coolant accidents

Phenomena	Components	Blowdown	Refill	Reflood
Stored Energy	Fuel rod	x		
Entrainment / de-entrainment	Upper plenum, hot leg			x
Steam binding	Steam generator			x
Critical flow	Break	x	x	
Three-dimensional flow	Core		x	x
Voiding	Core			x
Pressuriser early quench	Pressuriser	x		
...	...			

The one-dimensional (1D) approach to 3D phenomena involves a consideration of macroscale phenomena only. This simplification can include compensating errors and the conditions for extrapolating a physical modelling to reactor scale are not clear. Large-scale data exist – such as from the upper plenum test facility (UPTF), slab core test facility (SCTF), cylindrical core test facility (CCTF) and PERICLES-2D tests for LB-LOCA – and therefore it is possible to validate the 3D model and determine the prediction accuracy or uncertainty. However, there can be compensating errors between numerical errors due to a coarse nodalisation and physical model errors. There can also be compensating errors between the processes that are modelled and those that are not. The sub-grid processes, particularly all the ones occurring at a smaller scale than the mesh size, are not explicitly modelled. The weaknesses of such modelling can be acceptable with the assumption that the compensating errors in reactor application are the same as in the validation tests (provided that the same nodalisation is used and the scaling effects are properly identified).

When such large-scale data are not available for applications of a 3D model (for example, for steam line break [SLB], small break [SB] LOCA, IB-LOCA, loss of residual heat removal [LORHR], boron dilution), it is not possible to rely on extrapolation to the reactor application. All 3D processes must be identified in a revisited detailed PIRT and each basic process must be validated on separate effect tests (SETs), provided they exist. If such SETs do not exist, a new experimental programme addressing the processes of interest should be designed. For example, this is the approach followed for local mixing processes (buoyancy-driven and friction driven crossflows, diffusion and dispersion processes) in a PWR core, which will be investigated in the in-PWR Rod bundle Investigation of Undeveloped mixing flow across Subchannel (PRIUS) (see Section 5.1.6) and METERO-V experiments (see Section 5.1.13.10). Ideally, experiments should be performed up to a significant pressure (20-40 bar) and provide 3D velocity measurements. Steam is preferable to using air as a surrogate. Heating rods with adjusted radial distribution would increase transverse

velocities, which are key parameters in heat transfer in rod bundles for increasing the reliability of core modelling.

7.3. Field equations and closure laws

The porous media approach brings very interesting features that are compatible with thermal-hydraulic system codes. The geometry's precise definition is not only very difficult to achieve but is also not commensurate with the system codes' objectives. A global definition of flow area and space occupied by solid structures is therefore acceptable. However, the drawback is the rough definition of local 3D flows. There is neither a detailed presentation nor a known reference document discussing the derivation of 3D two-fluid equations used in system thermal-hydraulics (SYSTH) codes. The derivation induces specific new terms (diffusion-dispersion) to be modelled and terms to be neglected (for example, tortuosity in porous media).⁴ A rigorous derivation of 2-fluid equations requires the identification and justification of all simplifications with the order of magnitude analysis to justify it.

The possibility to use either a homogenised porous approach or space integration approach should be investigated. This investigation could lead to different treatments of porosity (volumetric and surface porosity).

The best choice among the various forms of momentum and energy equations is unclear.

There are several closure laws showing limitations. Suggested developments are described in Chapter 8.

7.4. Mesh size dependence

The dependence of predictions on the mesh size may be seen in two different ways, depending on the adopted strategy.

If a homogenised porous 3D model is used, the use of non-converged meshing induces a numerical error for some terms of the equations. This error decreases with smaller meshes. The mesh convergence is controlled by the convergence of the dominant terms of equations. The following sources of numerical errors can be identified:

- Wall heat transfer in the core depends on axial and radial power distribution and a fine description of this power distribution might be necessary to accurately predict peak clad temperature.
- Wall friction and form losses depend on local geometry (grids, upper tie plate, etc.) and small meshes might be needed to calculate form losses, depending on local conditions (and not averaged over a too long distance in case of sharp gradients of void fraction and/or velocity).
- Interfacial friction, heat and mass interfacial transfers are non-linear functions of principal variables: the convergence depends on the presence of sharp gradients of these principal variables and degree of non-linearity of the term.
- Momentum convection and energy convection: first-order scheme induces numerical diffusion.

⁴ Tortuosity is an intrinsic property of a porous material usually defined as the ratio of actual flow path length to the straight distance between the ends of the flow path (Jacob Bear, Dynamics of Fluids in Porous Media American Elsevier Publishing Co, New York [1988]).

The following comments should be considered:

- Axial momentum convection term is often negligible for low axial velocity gradients in a core.
- Transverse momentum convection in a core can induce a significant radial numerical diffusion for crossflow, which depends on the radial mesh size.
- Momentum convection terms can be dominant in lower plenum voiding in the gas phase, creating a wave and inducing a Kelvin-Helmholtz instability, which led to water entrainment to the break in the case of a LB-LOCA. A rather fine nodalisation was found necessary for converged predictions.
- Momentum and energy diffusion in open medium (downcomer [DC] and lower plenum [LP]) can be highly sensitive to mesh size. If their effect is dominant on the safety figure of merit (temperature, boron concentration, etc.), other tools such as CFD in an open medium tool with an advanced turbulence model (SLB, boron dilution) might be required. However, there may be a much lower turbulent mixing in the presence of high density gradients and a coarse nodalisation may be sufficient.
- Momentum and energy dispersion in porous medium (core) can be modelled depending on the space integration scale (i.e. the mesh size) in the same way as sub-grid turbulent diffusion in large eddy simulation.

The mesh dependence has to be considered when developing models, during validation and uncertainty quantification.

The issue of mesh dependence of the results may be treated in three ways:

- Homogenised 3D equations can be used with the support of mesh and time step convergence studies. This might be too expensive if diffusive processes are playing a significant role because they require rather small meshes, particularly in first-order numerical schemes. The diffusive Courant limit also leads also to rather small time step limitations.
- Adopting a control volume approach with meshes clearly related to the geometry (for example, subchannel analysis or assembly-scale modelling) and developing physical models for this space resolution. This requires validation experiments to validate the physics at the same scale (i.e. the same mesh size) as for reactor application. This approach can lead to very expensive experiments.
- The new concept of multiscale validation can compensate for the lack of large-scale validation experiments using finer scale 3D tools (such as CFD in open medium), which must be validated in a separate effect way on smaller scale SETs as reference to develop models adapted to larger meshes. This requires a robust validation methodology.

References

- [7-1] Song, C.-H., H.C. No and J.H. Kim (2021), “Progress in light water reactor thermal-hydraulics research in Korea”, *Nuclear Engineering and Design*, 372.
- [7-2] Bestion, D. and L. Matteo (2015), “Scaling considerations about LWR core thermalhydraulics”, NURETH-16, 30 August-4 September, Chicago, United States.
- [7-3] US NRC (2008), “TRACE V5.0 Developmental Assessment Manual”, US Nuclear Regulatory Commission, Washington, DC.

8. Recommendations for future R&D activities

8.1. Revisiting the PIRT

A new phenomena identification ranking table (PIRT) is necessary for identifying and ranking local three-dimensional (3D) processes. The identification of key parameters can be based on the terms of 3D equations. For example, specific 3D diffusion and dispersion terms should be considered. The real 3D effects on terms extrapolated from one dimension (1D), such as the interfacial and wall transfers, must also be evaluated. New formulations could be implemented if necessary, which take 3D effects with a specific validation into account.

The ranking might require iterations between expert judgement, sensitivity tests and experiment analyses.

The new and detailed PIRT should depend on:

- the component and sub-component (e.g. downcomer, lower plenum [LP], core, upper plenum [UP], upper-head, etc.);
- each phase in each transient (e.g. blowdown, refill, reflood for large break loss-of-coolant accident [LB-LOCA], loss of reactor cooling pump [RCP], forced convection, natural convection for steam line break [SLB]).

The porous media approach is currently the best compromise for system thermal-hydraulics (SYSTH) codes and therefore the inherent simplifications in the PIRT have to be considered. The relative weight of each process in the field equations depends on the porosity and hydraulic diameter (D_h).

The following indications seem acceptable in a relatively open medium (with high porosity) and with large D_h (in the lower plenum, upper plenum, annular downcomer):

- a small effect of wall transfers (but possible effect of local form losses);
- a possibly significant effect of inertial forces (e.g. lower plenum voiding in blowdown phase of a LB-LOCA);
- a possibly significant effect of turbulent diffusion (mixing in downcomer and lower plenum in a SLB, or in boron dilution transient, or during emergency core cooling systems' [ECCS'] injection of a small break [SB]-LOCA);
- possibly significant effects of complex geometry on phase repartition (entrainment/de-entrainment in the upper plenum).

The following indications seem acceptable in a porous medium with relatively low porosity, and with small D_h (the core):

- a significant effect of wall transfers (with possible 3D effects);
- a small effect of inertial force (in liquid flow because of non-significant acceleration);
- a small effect of turbulent diffusion (LOCAS, SLB, etc.);
- a possibly medium effect of dispersion (LOCAS, SLB, etc.);
- possibly significant effects of mixing by gravity-driven or friction-driven crossflows.

These indications should be verified by a systematic order of magnitude analysis of the relative terms of equations, depending on the component and flow conditions.

The trend to use more and more refined modelling and nodalisation encourages a revisiting of the PIRT of accidental transients to consider both macroscale 3D processes and more local flow processes, which are now seen by the code. For example, PIRT was made for LB-LOCA a long time ago with a limited identification of macroscale phenomena. “3D flow” was mentioned for downcomer refill and core reflooding without any additional details, which led to UPTF, SCTF and CCTF 2D-3D experimental programmes. Local 3D processes were not listed. Only a global validation of the combined effects of all 3D processes was made. Nevertheless, the first applications of 3D system codes in a best estimate plus uncertainty (BEPU) approach were made possible thanks to acceptable validation results on large-scale experiments, although using very coarse nodalisation.⁵

This might still include compensating errors between modelled and non-modelled processes and between numerical and physical errors. The code uncertainty in LOCAs remains rather high, as shown in the Best-Estimate Methods Uncertainty and Sensitivity Evaluation (BEMUSE) benchmark exercise [8-1], where the uncertainty on peak clad temperature (PCT) was estimated at 150 K to 200 K.

Currently, much finer nodalisations are possible than smaller scale 3D phenomena that can be modelled, numerical errors will thus be lower and improved prediction can be expected.

The degree of confidence in the modelling can be evaluated for any reactor component or sub-component and for all transients or transient phases. For example, Table 8.1 lists the processes during a SB-LOCA, providing an estimation of the sensitivity (low, medium or high L/M/H) on the figure of merit (FoM) and model uncertainty. The effect of the geometry on the process and validation data status are mentioned (OK when data are sufficient and no when data are missing). This type of information shows the need to improve some sensitive models and identify additional validation.

Table 8.1. 3D effects in an uncovered PWR core during a SB-LOCA

Process	Sensitivity on FoM (H,M,L)	Model uncertainty (H, M, L)	Geometry effect	SET or global validation
Flow regime identification	H	L in axial flow	not known	No
Interfacial friction	H	M	not known	Axial flow: OK Radial flow : no
Wall friction and form loss	M	L in axial flow H in radial flow	spacers	Axial flow: OK Radial flow : no
Void dispersion	L	H	not known	No
Interfacial H&M transfers	L		spacers	No
Wall HT regime identification	H	L		Axial flow: OK
Convection to liquid	L	L	spacers	Axial flow: OK
Nucleate boiling	L	M		Axial flow: OK
CHF (DNB or dryout)	H	L		to be determined
Convection to vapour	H	L	spacers	Axial flow: OK

Source: Bestion and Fillion, 2018.

⁵ For example, 20 vertical meshes, five radial meshes and six or eight azimuthal meshes for a three loop or four loop PWR pressure vessel with cylindrical co-ordinates

Table 8.1. 3D effects in an uncovered pwr core during a sb-loca (Continued)

Process	Sensitivity on FoM (H,M,L)	Model uncertainty (H, M, L)	Geometry effect	SET or global validation
Heat diffusion-dispersion in liquid	L	M	spacers	PSBT
Heat diffusion-dispersion in steam	L or M	M	spacers	No
Specific 3D processes	M	M	spacers	No
Chimney effect	M	M	spacers	PERICLES
Diverging crossflow				

Source: Bestion and Fillion, 2018.

An example of the kind of table to be filled for a revisited PIRT that addresses 3D local phenomena is provided in Figure 8.1.

Figure 8.1. Typical revisited PIRT table

Matrix 1: Cross Reference Matrix for 3D Phenomena in Intermediate Break LOCAs

- **3D phenomena vs. phase (missing component ?)**
 - + occurring : specify component
 - o partially occurring
 - not in list
- **3D phenomena vs. test facility**
 - + suitable for code validation
 - o limited suitability for code validation
 - not suitable for code validation
- **System tests vs. phase**
 - + already performed
 - o performed but of limited use
 - not performed

	Phase	Test Facility																
		System Tests				Separate Effects Tests												
		ATLAS	ROSA	LOFT	ROCOM	INKA	IPTF	DYNAS	DOBO	ACOP	MIDAS	PSBT	BFET	CCTF & SCTF	MATIS	PERICLES	PIERO	MR2 & MR-2A
Core	Initial single phase depressurization																	
Downcomer	Creation of void and stratification																	
UP	Decrease in RPV water level																	
LP	Accumulator injection, reactor coolant filling and core refueling																	
3D Phenomena	Flow regime identification																	
	Interfacial friction in bubbly-slug-churn																	
	Wall friction & singular P loss																	
	Void dispersion																	
	Cross flows chimney effect mainly controlled by axial and radial friction terms																	
	Wall HT regime identification																	
	Forced convection to liquid																	
	Nucleate boiling																	
	CHF at low quality (DNB)																	
	CHF at high quality (Dry-out)																	
	Film boiling																	
	Forced convection to vapor																	
	Heat diffusion-dispersion in liquid																	
	Heat diffusion-dispersion in vapor																	
System Tests	ATLAS																	
	ROSA																	
	LOFT																	

8.2. Physical models

The main closure laws showing known limitations are:

- **Wall friction and form losses**, which require validated models in the core for non-axial flows.
- **Momentum and energy diffusion-dispersion models**, which exist but need further validation. The dispersion associated with space averaging contains the effects of the sub-grid geometrical effects. The model therefore depends on the geometry of the component (e.g. spacer grids in a core have strong effects) and on the space filter or mesh size. The effect of mesh size should be further investigated. Several cases may be considered:

- Diffusion-dispersion have to be modelled in the **annular downcomer** geometry for a 2D nodalisation where only one mesh is used in the radial direction. Such downcomer modelling using a coarse nodalisation is still rather common because the cold legs are connected to one mesh. Either large-scale experiments should be considered, or a multiscale validation approach could be used. 3D CFD in open medium model could be used as a reference for developing and validating the coarse 2D modelling, provided sufficient validation is available for multiphase CFD calculations in the downcomer. Although 3D CFD uses turbulence models, which require additional transport equations (e.g. $k-\epsilon$, $Rij-\epsilon$), a simple algebraic diffusivity model might be better adapted to coarse 2D modelling. However, this approach may be insufficient for two-phase flow in the downcomer.
- Diffusion-dispersion has to be modelled in the **core** geometry for a given nodalisation. In the short and medium term, a modelling at the assembly scale (e.g. one mesh per assembly for a square lattice core) could become standard. Diffusion-dispersion models at the subchannel analysis scale (one mesh per subchannel) exist with some validation (PWR Subchannel and Bundle Test [PSBT], GRAZIELLA, OMEGA, in-PWR Rod bundle Investigation of Undeveloped mixing flow across Subchannel [PRIUS], etc.) and can be used as a reference for developing and validating the models at the assembly scale using an upscaling method.
- **The void dispersion model** requires more validation in the core and downcomer.
- **The interfacial friction for non-axial flow** in a core is not well known. However, a rather small effect is expected because radial flow is currently predicted without visible defect in the reflooding below the quench front and below a swell level in the boil-up condition, see 3D code validation on SCTF (cf. Section 5.1.4) and PERICLES 2D (cf. Section 5.1.5).

8.3. Suggestions for verification and numerical improvements

A matrix of verification tests must be defined and used to check the correct implementation of the equations, models and solver. These tests should also evaluate the capabilities of the numerical scheme and control and evaluate numerical errors.

The verification tests presented in Section 6.1 form a generally accepted basis. In principle, there is no specific method for the verification of the correct implementation of 3D modules. The same methods are used as for other modules. Specific 3D tests are necessary for checking the code's overall numerical 3D capability.

The code developers should agree on a set of specific requirements for the numerics of the 3D modules and on a matrix of benchmarks for checking how requirements are met by current solvers.

For example, no axial diffusion is used in 1D model and 3D diffusion can be used in 3D models, which require a specific verification for the numerics.

The following improvements are suggested from existing benchmark results:

- The first-order upwind schemes used in 3D SYSTH codes induce some numerical errors when associated with a coarse meshing. Higher order schemes exist, but for single-phase flow. These could be implemented for single-phase problems. The extension of such schemes to two-phase is recommended.

- The treatment of vertical stratification with a moving free surface or swell level may require (at least for some codes) more attention for avoiding artificial pressure perturbations.

8.4. Suggestions for validation

The strategy concerning the mesh dependence of results (see Section 3.2) must be first established before defining the validation needs for a 3D modelling with system codes. Two cases are considered:

1. A set of homogenised porous 3D equations is used and a converged meshing must be used for both validation and reactor application.
2. An engineering approach consists of using a space integration over volumes that are linked to the solid structure (e.g. the subchannel analysis or assembly scale for the core, or a 2D modelling of a downcomer with integration over the radial direction). In such cases no mesh convergence is needed, but models are scale-dependent or mesh-size-dependent and the same mesh size should be used for both validation and reactor application, or the scale dependence should be validated.

The first approach, which requires experimental validation, leads to very fine nodes and prohibitive central processing unit (CPU) costs. The second approach is more convenient for a pressure vessel with many internal structures that define various zones or components (lower plenum, core, upper plenum, downcomer, etc.), with each having a specific geometry, porosity and hydraulic diameter that cannot be easily homogenised without losing information about the geometrical effects. This approach will therefore be specific to a single component and cannot be extended to other components but can also apply to other types of the same component with different internals or scales.

Only the second approach (space integration) is considered.

The main difficulty in this approach is that the physical model and meshing must be validated together and then the same mesh size should be used for the reactor application. This has been possible for LB-LOCA thanks to the 2D-3D experimental programme, which produced scale one tests. However, this approach becomes more difficult for other transients in the absence of such large-scale tests. The solution may need a combination of several steps and tools:

- a validation of basic processes in a separate effect and combined effect way;
- a validation on integral effect tests (IETs);
- the possible use of multiscale validation.

As for 1D models, both “separate effect” validation and “integral effect” validation are required for 3D models of system codes. A “combined effect” validation could be added between these.

The separate effect validation measures the quality of separate models or closure laws in particular conditions, which can be very simplified (to be able to use advanced instrumentation techniques) compared to reactor situations. For example, mechanical laws about pressure losses can be first validated in single-phase adiabatic flow and then in heated flow. Interfacial friction can be first validated in air-water conditions and then in steam-water condition. Turbulent diffusion and dispersion can also be validated in single-phase liquid or single-phase gas adiabatic flow.

Combined effect validation includes situations sensitive to several basic processes together and can have a lower level of instrumentation. However, the validation provides information on how several models work together.

Integral effect validation uses IETs, which represent the entire reactor cooling circuit in reactor conditions but often at a reduced scale. The local measurements are also more difficult to implement in such experiments. IET measures the global quality and consistency of the set of models in T/H conditions (two-phase steam-water with heating and cooling). The pressure vessels in IETs are often geometrically distorted because the scale reduction factor is not the same in all directions. Many IETs used a scale one in vertical direction and a factor of ten or more in horizontal directions. Reduced-scale IETs also exist (APEX, ATLAS, etc.) but the scale factor is still (less) distorted in horizontal and vertical directions. 3D effects therefore exist with some distortion. For example, azimuthal mixing in a downcomer during ECCS injection (IB-LOCA) is probably overestimated in IETs with annular downcomer due to smaller azimuthal distances between the up-flow and downflow zones. Concerning the core, IETs radial dimensions are smaller than in a reactor. IETs do not provide a reliable representation of the radial power differences between assemblies with the right assembly dimensions. Rig-of-safety Assessment/ Large Scale Test Facility (ROSA/LSTF) and ATLAS facilities have a radial power distribution with the assemblies having a reduced number of rods of different power [8-3]. Despite these drawbacks, IETs must be used to validate a 3D pressure vessel modelling in some specific transients, such as SB-LOCA or IB-LOCA, even if all 3D processes are not fully representative because there are no other full-scale tests.

8.4.1. Separate effect validation for 3D applications

Several SETs are suggested for the validation of 3D applications in SYSTH codes. The highest priority ones should address the following aspects:

- friction pressure losses for crossflows in the core;
- diffusion-dispersion of momentum and energy in the core and downcomer;
- dispersion of the void in the core and downcomer;
- heat exchanges and thermal stratification in pool.

Lower priority validation may be useful for the following models:

- the validation of a more general interfacial friction formulation for non-axial flow in a bundle;
- the influence of velocity vectors' directions on the interfacial and wall heat transfers.

Some of these needs will be addressed by the PRIUS (see Section 5.1.6) and METERO-V tests (see Section 5.1.13.10).

8.4.2. Combined effect validation for 3D applications

Combined effect tests are often necessary to test the efficiency of several models together and the extrapolation to other parameter ranges (pressure, fluids, flow rate, space dimensions, etc.). For example, DYNAS tests (cf. Section 5.1.8) are air-water tests sensitive to:

- momentum turbulent diffusion;
- interfacial friction;
- void dispersion forces.

All of these processes contribute to the void fraction mixing and space repartition and can be useful for validating models that play a significant role in some flow conditions encountered in an annular downcomer.

SUDO ([8-4]) and DOWncomer BOiling (DOBO) (cf. Section 5.1.9) tests add boiling in steam-water conditions to the above phenomena.

The general principle to apply to a validation matrix is therefore that every process which was identified in a PIRT should be validated first in a separate effect way and then possibly in a combined effect way.

If no separate effect validation is available for a physical process, it should be at least validated in a combined effect way or using multiscale validation (see the below Section 8.4.3).

8.4.3. Role of multiscale validation

Multiscale validation can be used to complement existing experimental data by small-scale simulations validating the macroscopic 3D modelling used in system codes [8-2]. The validation of the local 3D processes in a pressure vessel (PV) in prototypic reactor transient conditions such as SB-OLCA, IB-LOCA or SLB would require significant resources. Facilities like UPTF and SCTF with high pressure capabilities and multiple instrumentation have therefore thus far only been implemented in reduced dimension low pressure SETs. One possible option is to validate, using a “small-scale” simulation tool (e.g. CFD or computational multi-fluid dynamics [CMFD]), a small-scale 3D model in a separate effect way in rather small dimension SETs and to use this model as a reference to validate the 3D system code for larger scale situations. The uncertainty of the small-scale simulation tool can be determined by validation on small dimension SETs. The uncertainty of the 3D system code can be determined by considering the comparison error between the two different-scale models at the reactor scale and taking into account the uncertainty of the small-scale model, which plays the role of the experimental uncertainty of the normal validation. This technique assumes that the small-scale simulation tool can reliably predict the scale effect between small-scale experiments and reactor scale phenomena.

Examples of this multiscale validation are:

1. The use of the subchannel model as a reference for an assembly-scale core modelling. Subchannel models have some validation for the diffusion and dispersion of momentum heat and void fraction thanks to the OMEGA, AGATE, GRAZIELLA, BWR Full-size Fine-Mesh Bundle Tests (BFBTs) and PSBTs. Situations including several assemblies with power differences are then simulated with a subchannel model and the results are used as a reference for an assembly-scale model.

2. The use of a 3D two-phase CFD to simulate a typical situation with mixing in a PWR downcomer during the ECCS injection phase of an IB-LOCA. The same situation is then simulated by a coarse 2D downcomer modelling and the CFD results are used as a reference.

Some conditions for the applicability of a multiscale validation are proposed [8-2] for each step of the method, including a PIRT, the validation matrices of the fine scale and macroscopic scale models and the uncertainty quantification of both scales. The proposed conditions must still be clearly identified and then commonly agreed and accepted by safety authorities. Although multiscale validation seems a reasonable approach, it still requires effective justification. A consistent set of experimental data would likely be required to provide a full coverage of all processes occurring at each scale and modelled by specific different models. Past experience shows that validated codes on several SETs have discrepancies with new SETs describing the same processes.

References

- [8-1] Reventos, F., H. Glaeser, F. D'Auria and A.D. Crecy (2013), “Main Results of the OECD BEMUSE Programme”, in “OECD/CSNI Workshop on Best Estimate Methods and Uncertainty Evaluations: Workshop Proceedings Barcelona, Spain 16-18 November 2011 - Part 2”, NEA/CSNI/R(2013)8/PART 2, OECD Publishing, Paris, www.oecd-nea.org/jcms/pl_19377.
- [8-2] Bestion, D. and P. Fillion (2018), “The concept of multiscale validation”, NUTHOS-12, 14-18 October, Qingdao, China.
- [8-3] Pr ea, R. (2019), “Validation of CATHARE 3D module on LSTF core”, NURETH-18, 18-23 August, Portland, United States.
- [8-4] Sudo, Y. and H. Akimoto (1982), “Downcomer Effective Water Head during Reflood in Postulated PWR LOCA”, *Journal of Nuclear Science and Technology*, 19(1), pp. 34-45.

9. Conclusion

Considering the ever-increasing performance of computers, thermal-hydraulic system codes are currently undertaking a new development of their capabilities. The thermal-hydraulic models of two-phase flow are improving their accuracy and reliability. [9-1] provides a general status and proposes some directions (not specific to multidimensional capabilities). Multidimensional capabilities for pressurised water reactor large break loss-of-coolant accidents (PWR LB-LOCAs) were introduced into the codes in the 1980s with reasonable success considering the simplifications and limited models. Large-scale three-dimensional (3D) effects were identified in the PWR downcomer, core and upper plenum. 3D pressure vessel modelling therefore brings the achievement of more realistic physical description than one-dimensional (1D) or multi-1D modelling a step closer. Achieving finer resolution 3D simulations could be a new step with regards to the upgrading of the realism of thermal-hydraulic system codes.

However, an extensive application of 3D capabilities was hindered by some known limitations, simplifications and deficiencies. The more general conditions for a consistent use were not clearly identified. These include the effects of the complex non-isotropic geometry of the various components in a pressure vessel, the selection of a space resolution of the physical modelling and the selection of a modelling and validation strategy in relation to the results' mesh dependence. The lack of proper turbulence modelling and non-converged meshing raised questions without leading to clear answers.

Although a significant volume of experimental data already exists, some gaps remain. A revisited phenomena identification ranking table (PIRT) of 3D flows, which looks at all local 3D effects and mixing processes (especially in loss-of-coolant accident situations), is the preliminary task to perform.

A gap analysis with available experimental information led to new ongoing experimental programmes that seek missing information (e.g. the METERO-V CEA/EDF/Framatome/IRSN experiment, see Section 5.1.13.10, and the Korea Atomic Energy Research Institute's PWR rod bundle investigation of undeveloped mixing flow across subchannel [KAERI's PRIUS] experiment, see Section 5.1.6). One key issue lies in the modelling and validation of all mixing effects due to radial power distribution in the core. The range of thermal-hydraulic parameters encountered with the operation of passive systems may also require additional experimental support. Several projects related to these topics are currently under consideration at the Working Group on the Analysis and Management of Accidents (WGAMA).

The current 3D tools of system codes and available verification and validation (V&V) matrices allow PWR LB-LOCA simulation with validation on the upper plenum test facility (UPTF), slab core test facility (SCTF) and cylindrical core test facility (CCTF) using the same mesh size for validation and application. There may be some imperfect physical modelling and significant numerical errors, but the resulting uncertainty on reactor application can be estimated from the validation errors.

PWR small break (SB-)LOCAs and intermediate break (IB-) LOCAs can be simulated by either coarse or finer nodalisation with conservative uncertainty quantification for some closure laws in the core (e.g. pressure losses for crossflows) and downcomer (DC) (condensation, interfacial friction, etc.) due to the lack of a precise validation of 3D effects in the high pressure range.

This document provides suggested clarification regarding some issues and recommends future research and development (R&D) activities.

This document presents several options concerning the mesh size dependence. Once mesh and time convergence have been achieved, a full 3D treatment (homogenised field equations) will require huge computing resources to capture diffusive effects, when they are predominant. A “geometry” dependent approach will require large experimental support. The promising concept of multiscale validation needs robust justification alongside experimental support and needs to be approved by the safety authorities.

Concerning 3D phenomena and particularly crossflows in the core with radial power distribution, the competing effects of gravity and friction (which are highly pressure dependent), radial pressure losses, and diffusion and dispersion modelling must be investigated in detail to achieve more precise and reliable simulations. Another typical issue concerns mixing in the downcomer. Such phenomena are difficult to predict precisely with coarse 2D modelling and a rather high uncertainty must be applied using current models and nodalizations

However, mixing problems in the downcomer in the presence of strong density differences (due to temperature gradients) can be rather well approximated by 3D modules of system codes, which use a coarse 2D nodalisation at a small central processing unit (CPU) cost compared to classical computational fluid dynamics (CFD) in an open medium that would require millions of meshes. Similar situations can be encountered with applications to passive systems with mixing in the presence of thermal stratification. A coarse nodalisation may be also sufficient. However, the conditions that should be respected for such coarse nodalisation should be more deeply analysed and their application criteria defined.

To conclude, some recommendations for future R&D activities are suggested:

- A reference document should be developed on the derivation of equations in the porous 3D approach, which should provide a clear identification and justification of all the simplifications and assumptions made.
- Some guidance should be provided to revisit the PIRT following a systematic approach. All processes that are dependent on the geometry of a component and encountered flow conditions, which can be based on a non-dimensional form of equations, should be identified and ranked.
- Clear numerical requirements for the numerical scheme should be established and an exhaustive verification matrix defined that addresses all requirements, including mesh convergence.
- Numerics should be improved, with particular attention being paid to obtaining better accuracy and CPU efficiency in the presence of diffusive processes. Methods for the estimation of the numerical errors should also be considered, alongside those existing for CFD in open medium.
- Additional validation should be provided, when needed, for a set of transients.
- The role of multiscale validation with agreed requirements should be specified.
- The methodology for uncertainty qualification and licensing and regulatory requirements for best-estimate plus uncertainty applications should be considered when 3D capabilities of thermal-hydraulic system codes are used for safety demonstration.

Although relative improvements in 3D capabilities and numerics can be achieved, significant investments in experimental support and specialists’ resources are needed to

achieve a breakthrough. Ideally, experiments should be performed up to a significant pressure (20-40 bar), which should provide 3D velocity measurements. Steam is preferable to using air as a surrogate. Heating rods with adjusted radial distribution would increase the transverse velocities, which are key parameters in heat transfer in rod bundles and increase the reliability of core modelling. On a more theoretical level, the derivation of equations for a porous 3D approach in two-phase flows must be documented in detail. All assumptions and simplifications should be clearly identified and the justification for their treatment should be given. Beyond considerations of 3D, the current efforts being made in numerics and uncertainty qualification should continue.

References

- [9-1] Bestion, D. (2017), “System thermalhydraulics for design basis accident analysis and simulation: Status of tools and methods and direction for future R&D”, *Nuclear Engineering and Design*, 312.

10. Glossary

Accuracy (qualitative and quantitative)

The accuracy of a simulation tool is a measure of the differences between the code predictions and the actual transient performance of a real facility or reactor. Qualitative accuracy is defined by qualitative criteria, for example fairly good agreement or unacceptable error. Quantitative accuracy is measured through quantitative functions, such as the difference between code prediction and reference value, with statistical parameters such as bias and standard deviation.

Adequacy of evaluation model (EM)

The definition of EM implies the definition of related adequacy. The adequacy of the EM implies a series of actions (or as “process”, see below) that are requested by the code user and deal with the code, concerning transient scenario, nodalisation and initial conditions at various levels or steps within the framework of using system thermal-hydraulic codes in nuclear reactor safety. This is summarised with suitable detail in the US NRC RG 1.203, where the “Adequacy of EM” is reported as evaluation model development and assessment process (EMDAP).

Assessment

See code assessment.

Balance equations

See also field equations.

Basic test

A basic test is a rather simple test checking the capability of a numerical tool, aiming to correctly simulate a simple physical problem. A basic test can be a simple test with an analytical solution that checks a capability of the numerical scheme. The test can also be a simple physical test with a trivial solution, or an experimental test in some prototypical conditions with measurements for comparing against predictions.

Benchmark

A benchmark problem is a test problem for code comparison (either numerical scheme or physical model comparison) which does not necessarily have experimental results, but a generally agreed numerical solution.

Best-estimate code

A code which: (1) is free of conservative assumptions in the modelling (deliberate pessimism regarding selected acceptance criteria), and (2) contains a sufficiently detailed model for describing the relevant processes that require modelling.

Bias of calculation result

A bias is a measure of the systematic difference between an actual or true value and a predicted or measured value. Bias is the tendency of a model to systematically over-predict or under-predict data that are representative of an assigned phenomenon.

Blind ISP

This is an international standard problem (ISP) where concerned experimental data are unknown to the code user before the processes of developing the nodalisation and performing the calculation to simulate the assigned test.

Boiling crisis

There are several steps between heating a liquid and overheated steam occurring. When the temperature at the wall slightly exceeds saturation temperature, local subcooled nucleate boiling occurs (the onset of nucleate boiling followed by the onset of significant void). When nucleate boiling is insufficient for removing all local heat flux at the wall, a blanket of steam insulates the wall from the remaining liquid. This phenomenon is called departure from nucleate boiling and corresponds to the occurrence of a boiling crisis.

Cliff-edge (effect)

When there are discontinuities in physical models, a small change in a parameter can lead to a great change in the evolution of an entire physical process. This is called the cliff-edge effect. For example, some phenomena such as loop seal clearing, flow regime and heat transfer near critical heat flux condition, are highly sensitive to the values of certain parameters. These phenomena are thus characterised by the “cliff-edge effect”. This effect evokes some challenges in the numerical simulation of those phenomena.

Closure laws (or relations)

After averaging local instantaneous fluid balance equations, many terms of the resulting equations are new unknowns or contain new unknowns. At this step, the number of unknowns is larger than the number of equations and the system of equations is not closed. In particular, the averaged equations exhibit terms for transfers of mass, momentum and energy at the walls and interfaces (in two-phase or multi-fluid flow conditions). Constitutive relations are mathematical expressions for these phase transfer terms as functions of the selected averaged principal variables. These are part of closure relations. Other relations are also necessary to express the average of non-linear terms as functions of averaged main variables. The terminology “closure relations” derives from considering them as necessary to close the system of equations. Some closure relations are simplifying assumptions, for example $\langle \rho(P,T) \rangle = \rho(\langle P \rangle, \langle T \rangle)$.

Code assessment

Code assessment is the process of validation and verification that proves the ability of the physical models and numerical scheme of a code to simulate the physical behaviour in a given domain of application with sufficient accuracy and confidence.

Code manual

Code manuals are a set of documents for the code users that have been written by the code developers. The code manual usually consists of a theory manual, a models and correlation manual, user’s guideline, an assessment report, an installation manual and a programmer’s manual, etc.

Code qualification

Code qualification is the set of procedures used to prove that a code can do what it is designed for and can meet all associated requirements. Code qualification includes quality assurance, validation and verification, full documentation, and validated tools for uncertainty evaluation for best-estimate codes.

Coast down

The coast down is the rotating inertia of a motor and, more specifically, that of a pump, which results by a remaining flow rate when the pump is stopped. In case of a locked rotor, the rotation of the pump is blocked and no coast downflow rate is available.

Computational (multi) fluid dynamics (CFD) (counter posed to system thermal-hydraulics)

CFD (or computational multi-fluid dynamics [CMFD] for multiphase simulations) is the simulation of fluid dynamics with a numerical tool that solves multidimensional fluid dynamic equations (local instantaneous equations, or averaged equations, or filtered equations) and is mainly used for single fluid models. CMFD was also recently introduced to extend the capability of CFD to multi-fluid models. CFD or CMFD tools can use either the open medium approach or the porous medium approach. CFD and CMFD are commonly understood to refer to a fine resolution. The terminologies in CFD and CMFD are therefore not applicable to system thermal-hydraulics (SYSTH) codes because SYSTH codes use 0D and 1D models and they can also use 3D models with the porous body approach, and a rather coarse nodalisation.

Confidence in validation

In statistics “the confidence level” refers to the likelihood that the true parameter value lies within the range specified by the confidence interval. The confidence level is usually expressed as a percentage. 95% confidence level thus implies that the probability that the true parameter value lying within the confidence interval is 0.95. The confidence level here implies the probability 0.95. In the area of V&V for system thermal-hydraulic codes, the confidence in validation indicates the level of satisfaction based on the results of the validation process by an observer. The confidence in validation should therefore be based on the quantitative evaluation of accuracy where proper thresholds of acceptability for the calculations (i.e. a comparison between measured and predicted values) are fixed and fulfilled.

Conservative calculation

A conservative calculation is a calculation carried out that leads to pessimistic results relative to specified acceptance criterion/criteria by using a conservative code and unfavourable input data set, including conservative initial and boundary conditions.

Conservative code

This term designates a safety analysis code that was designed to lead to pessimistic results relative to specified acceptance criterion/criteria. Some phenomena are modelled in a way to overestimate the severity of the accident sequence (e.g. a wall-to-fluid heat transfer coefficient is minimised to overestimate a rod clad temperature).

Constitutive equations (see also closure relationships)

Averaged fluid balance equations exhibit terms for the transfers of mass, momentum and energy at the walls and interfaces. Constitutive relations are expressions for these transfers as functions of principal variables. These are also called closure relations because they are necessary for closing the system of equations.

Convergence

See mesh convergence.

Courant limit (Courant–Friedrichs–Lewy) condition

See material Courant limit.

Critical heat flux (CHF)

Critical heat flux corresponds to the value of local heat flux generated at the wall for which a boiling crisis (see this term) occurs.

Departure from nucleate boiling (DNB)

See boiling crisis.

Departure from nucleate boiling ratio (DNBR)

DNBR is formed by the ratio of the calculated critical heat flux (CHF) to the local heat flux. Until local heat flux is lower than CHF, no boiling crisis is expected (DNBR>1).

Developmental assessment

Developmental assessment is the assessment performed by code developers during the development phase of the code that selects appropriate physical models and numerical algorithms to check they have a good behaviour and are properly implemented.

Evaluation model development and assessment process (EMDAP)

See adequacy of EM.

Evaluation model (EM)

EM is the calculation framework for evaluating the behaviour of the reactor system during a postulated transient or design basis accident. The EM may include one or more computer programs, special models and all other information needed to apply the calculation framework to a specific event.

Explicit numerical scheme

An explicit numerical scheme is a numerical scheme for which unknown quantities (i.e. the quantities at the next time step) are evaluated in terms of known quantities at only the current time step. In the fully explicit scheme, all unknowns of all terms are taken at beginning of time step, except for in the time derivative term.

Field equations

Field equations are the equations that are solved with the aim of determining the transport of mass, energy and momentum throughout the system.

Frozen

The condition whereby the analytical tools and associated facility input decks remain unchanged and under configuration control throughout a safety analysis, thereby ensuring traceability and consistency in the final results.

Hydraulic diameter

The concept of hydraulic diameter has been proposed, for example by Chezy (1820), as a simple way of using any hydraulic relationship established for a given geometry for another one. For example, the usual hydraulic pressure loss equations (such as Darcy-Weisbach) that were established for a circular pipe of diameter D can be used for other geometries. The hydraulic diameter is generally formed by the ratio of four times the flow area to the wetted diameter. In the case of a circular duct, hydraulic diameter is the same as actual diameter. However, other formulas exist, especially for given types of geometries such as a rectangle or annulus.

IET (integral effect test)

Integral- effect tests are experimental tests that aim to simulate the behaviour of a complex system with all interactions between various flows and heat transfers processes occurring in various system components. IET relative to reactor accidental thermal hydraulics simulate the entire primary cooling circuit and accidental scenario through initial and boundary conditions.

Ill-posed equations

Ill-posed equations are equations that do not satisfy the conditions of the well-posedness (see well posed equations). Non-hyperbolic formulations of fluid dynamics are ill-posed equations.

Implicit numerical scheme

An implicit numerical scheme is a numerical scheme for which unknown quantities (i.e. the quantities at the next time step) are evaluated in terms of unknown quantities. The implicit formulation requires the simultaneous solution of several coupled equations involving the unknowns. In the fully-implicit scheme, the unknowns of all terms are taken at the end of the time step, except for in the time derivative term.

Independent assessment

Verification and validation by an organisation that is both technically and managerially separate from the organisation responsible for developing the software or code.

International standard problem (ISP)

A selected problem, in the framework of the independent assessment of codes, namely system codes, that is used for accident analysis. The ISPs are selected by proper committees from inside OECD/NEA/CSNI and are based on experiments performed in facilities available within OECD member countries. One host institution manages the ISP and is responsible for issuing related documents. Participants perform calculations and contribute to the preparation of the document. The ISP issued documents that are approved by the CSNI, following proper review processes.

Loop seal filling and clearing (or clearance)

Whenever the crossover legs downstream from the steam generator are filled with liquid water, steam is blocked and the cooling capacity of the core reduced. This can happen after the blowdown phase of a loss-of-coolant accident (especially small or intermediate break). Water levels in the core decrease and increase in the downcomer, finally resulting in the clearance of the water seal and equalising of the two levels.

Lumped model (or lumped parameter model)

A zero-dimensional or “point” model aiming to simulate the steady state or transient performance of a finite space (dimensions are typically consistent with the entire nuclear power plant or a significant part of it) is known as lumped model, or lumped parameter model. A lumped model is also constituted by the coupling of different lumped models defined above: for example, a point neutron kinetics model coupled with a point hydraulic model for the core and a point model for conduction heat transfer of fuel rods still constitute a lumped model.

Manufactured solution (method of manufactured solution)

The method of manufactured solution is a method for testing the capabilities and accuracy of a numerical solution algorithm for a given set of equations. The first step is to select a “manufactured solution” as a closed analytic form for the solution for the final test problem. Then, the analytic solution is substituted into the base partial differential equations (PDEs) to generate new or modified source terms in the equations. Finally, initial and boundary conditions for the test problem are obtained by evaluating the selected solution form at zero time and at spatial boundaries of the problem.

Material courant limit (or CFL limit)

Material courant limit is a time step limit for numerical stability imposed by the explicit treatment of the convective terms. When the convective quantities are treated explicitly, the time step should be equal to or less than $\text{Min}(dz/U)$ for numerical stability, where dz and U are the mesh size and fluid velocity, respectively. This is also called convective limit. The origin of this term is a famous paper written by Courant, Friedrichs, and Lewy (CFL) that addressed the stability requirement for the numerical solution of hyperbolic PDEs.

Mesh convergence

Mesh convergence is the process of decreasing the mesh size of a nodalisation to the point where the solution does not change any more. When the numerical scheme is consistent and convergent, the convergence is obtained when the exact solution of the PDE is reached. In practice, convergence tests are made up to a given tolerance limit by defining a convergence criterion. In system thermal-hydraulic codes, mesh convergence is possible in 1D modules that use a well posed system of equations.

Module

The module of a thermal-hydraulic code is a part of the code that models a reactor component or of a test facility with a given set of physical assumptions and physical models. A module of a system code can be 0D, 1D or multi-dimensional. A system thermal-hydraulics code generally includes several modules and sub-modules to model all components of a reactor. Sub-modules represent parts of a code that model systems of a reactor, such as pumps, sources, sinks or valves, which are coupled to a module.

Nodalisation

The nodalisation of a thermal-hydraulic system is the schematisation of the system so that it may be reduced to a finite number of nodes or control volumes, to which the governing equations are applied and solved. In practice, it particularly consists of defining a simplified geometry of the system and defining nodes or control volumes for modelling the fluid flow and heat conduction in solids. The nodalisation is the interface between the code and the reality constituted by the nuclear power plant or a test facility. The main function of the nodalisation is to transfer the peculiarities of the nuclear power plant into a format suitable for the system thermal-hydraulic code. Thus, the choice of the nodalisation must take the real system characteristics (for example, the nuclear power plant and boundary conditions), code features, objective of the analysis and available computational resources into account.

Numerical consistency

Numerical consistency is the extent to which the discretised equations approximate the PDEs. A discretised representation of a PDE is considered consistent if it can be shown that the difference between the exact solution of a PDE and its discretised representation (i.e. truncation error) vanishes as the mesh size tends to zero.

Numerical convergence

Numerical convergence is achieved when, as the mesh is refined, the solution to the discretised equation by a numerical scheme approaches the true solution (or a constant one) to the PDE having the same initial and boundary conditions. A consistent and stable scheme is convergent.

Numerical diffusion

Numerical diffusion is the numerical feature when a first-order approximation is used for the discretised equation. In this case, the discretised equation of a PDE possesses an artificial diffusion term. This term corresponds to the leading term in the truncation error of a PDE discretised equation that has second-order derivatives when a first-order approximation is used. The truncation error then behaves like an artificial diffusion term and this is thus called numerical diffusion, false diffusion or numerical dissipation.

Numerical stability

Numerical stability is the numerical feature whereby errors from any source are not permitted to grow in the sequence of numerical procedures as the calculation proceeds from one marching step to the next. This concept is only applicable to transient problems in the strictest sense.

Open ISP

This is an ISP where concerned experimental data are known to the code user before starting the process of developing the nodalisation and performing the calculation to simulate the assigned test.

Open medium (media) approach

Open medium (media) approach in CFD is applied when local instantaneous equations are either not averaged (direct numerical simulation [DNS]) are simply time-averaged or ensemble-averaged (Reynolds-averaged Navier-Stokes [RANS] equations) or are space averaged (or filtered) over a space scale much smaller than the dimensions of the fluid domain to be simulated. Equations are only written in the fluid domain and solid walls can only exist at the boundaries of the simulation domain. The space resolution of the fluid flow simulation is much finer than the hydraulic diameter or the dimensions of the flow domain.

Partial differential equations

Partial differential equations (PDEs) are relations involving an unknown function (or functions) of several independent variables and their partial derivatives with respect to those variables. Basic fluid equations are PDE with space co-ordinates and time as independent variables. The use of the term PDE for the resulting equations after the space and time averaging of basic equations is controversial. There are no PDEs after space discretisation that result in a SET of ordinary differential equations with time as only independent variable. However, in this document the PDE term has been extended to system code thermal-hydraulic equations.

PDE

See partial differential equations.

Phenomena identification

Phenomena identification is the process of analysing and subdividing a complex thermal-hydraulic scenario system (depending on a large number of thermal-hydraulic quantities) into several simpler processes or phenomena that mainly depend on a limited number of thermal-hydraulic quantities.

Porous body

See porous media approach.

Porous media approach

The porous medium (media) approach is applied when three-dimensional equations are written in a space domain containing both fluid and solid structures. Equations include a porosity factor representing the ratio of fluid volume to total volume and transfers with walls that are modelled at every calculation node or in every mesh through source terms. The space resolution of the fluid flow simulation is at least equal to, if not larger than, the hydraulic diameter.

Reflux condensation

Reflux condensation occurs when the coolant in the core boils off with the generated steam escaping from the core into the steam generator through the hot legs and then is condensed by the cold water in the secondary side of the steam generator (SG). When this condensation occurs in the ascending part of the SG tube, a countercurrent flow appears with the liquid flow returning to the core and steam flow.

Robustness

A code or a numerical scheme is said to be robust if it can cope well with various physical situations without numerical failure. This includes the quality of being able to withstand numerical perturbations due to sudden changes in physical processes

Safety analysis

Safety analysis is an analytical study usually performed by computer codes, which is used to demonstrate the extent to which safety requirements are met.

Scaling (and scaling issue)

The word scaling can be used in a number of contexts: two of these are hereafter described.

The scaling of an experiment is the process of demonstrating how and to what extent the simulation of a physical process (such as a reactor transient) by an experiment at a reduced scale (or at different values of some flow parameters such as pressure and fluid properties) can be sufficiently representative of the real process.

Scaling applied to numerical simulation tools is the process of demonstrating how and to what extent the numerical simulation tool validated on one or several reduced-scale experiments (or at different values of some flow parameters such as pressure and fluid properties) can be applied to the real process with sufficient confidence.

Furthermore, the words “scaling issue” should be used when performing a licensing study, which mainly refers to the scaling capabilities of codes.

Semi-implicit numerical scheme

A semi-implicit numerical scheme is a numerical scheme for which unknown quantities (i.e. the quantities at the next time step) are evaluated in terms of known and unknown quantities. This term sometimes indicates a specific numerical scheme in which the convected quantities are explicitly treated and the sonic quantities are implicitly treated, with the result that the time step is limited by the material Courant limit but not limited by the sonic Courant limit.

SET

Separate effect tests are experimental tests that aim to investigate a single physical process either in the absence of other processes, or in conditions which enable the measurement of the effects of the process of interest. SETs can be used to validate a constitutive relation independently from the others.

Software quality engineering (SQE)

SQE is the activity related to the management of the quality of software. It includes QA procedures for code development, code testing (including portability tests), code assessment (including V&V), code delivery, code documentation, configuration management, the management of the life cycle of the code, code debugging, code maintenance, correction of defects and the delivery of versions and updates.

Steam binding

During the reflood phase of a LOCA, fuel is re-wetted by liquid and steam generated, entraining liquid droplets. The vapourisation of entrained droplets in the SG tubes creates an additional pressure drop that further inhibits the gravity-driven reflooding of the core. This is the “steam binding effect”, which represents the flow resistance between the core and the break

Swell level

Swell level is defined as the top of the two-phase mixture in the core.

System

A system is an ensemble of material elements coupled together to perform a given functionality (for example, a reactor cooling circuit is a system made of all the components of the reactor that allows the cooling fluid to cool the reactor core).

System code

A system code is a computer model capable of simulating the transient performance of a complex system like a nuclear power plant. A system code typically includes equations for thermal hydraulics and heat transfer, and/or neutronics and must be equipped with special models to simulate the performance of components such as pumps and separators. The code should typically also simulate the control logic implemented in the plant and be able to predict an accident's evolution.

System modelling

System modelling is the processes of input development of a system thermal-hydraulic code and of building a nodalisation, including the needed assumptions.

System thermal-hydraulics (SYSTH) code

A system thermal-hydraulics code is a thermal-hydraulic simulation tool that can model an entire thermal-hydraulic system made of several subsystems and components and simulate design basis accident scenarios. The system is modelled by modules and sub-modules, which are assembled to describe the circuits. System codes' main modules are 0D lumped, 1D and 3D in porous media approach. Sub-modules model heat conduction in solids, heat exchangers, sources, sinks, breaks, pumps and turbines, etc.

Uncertainty (see also “uncertainty analysis”)

Uncertainty is a measure of the expected error range in experimental data or in calculated values by a code. Uncertainty can ideally be defined by a probability density function (PDF) of the considered output parameter. It is often more simply expressed by two percentiles (for example, the 2.5 and 97.5% percentiles) of the output parameter, from which a variation interval is deduced. The uncertainty can also be described by a bias and standard deviation.

Uncertainty analysis (see also “uncertainty”)

Uncertainty analysis is an analysis for estimating the uncertainties (expected error range) of the quantities involved in, and the results from, the solution of a problem. If the applied method is based on the propagation of the uncertainties of input parameters, uncertainty analysis includes the estimation of individual modelling or overall code uncertainties, representation uncertainties, numerical inadequacies, user effects, computer/compiler effects and plant data uncertainties for the analysis of an individual event.

User or code user

A code user is a person, group of persons or organisation who will use the software product under concern (which is here the system thermal-hydraulic code). The users' roles are the development of the nodalisation for an experimental facility or a nuclear power plant, independent assessment and code application. Normally, the code user is also the analyst who interprets the data obtained from a calculation.

User effect

A user effect is what makes the difference between two sets of calculation results obtained by two code users (or two groups of code users) who use the same code to simulate the same problem (which is here a thermal-hydraulic system with initial and boundary conditions), and can access the same information for setting up the nodalisation and determining the needed input and boundary condition values.

User's guidelines

User's guidelines are provided to code users to give them the necessary recommendations for building an adequate nodalisation and input deck, in order to carry out an appropriate simulation of a thermal-hydraulic problem.

User guidelines of a system code mainly address:

- the choice of modules (0D, 1D and 3D) and sub-modules (pumps, sources, sinks, valves, breaks, HX and neutron kinetics models, etc.) to model the components of a system (test facility or reactor);
- the space resolution, by giving recommendations on the mesh size for hydraulic meshes and for heat conduction in solids;
- the time resolution by giving recommendations on the time step and time step control.

User guidelines are necessary to eliminate, or reduce as far as possible, the user's effect

User qualification

The process aiming to reduce the user effect constitutes the user qualification. User qualification is based on extensive training and performing a suitable number of code calculation involving the comparison with experimental data. A well-qualified user might require at least five years' experience in the area (the continuous-documented application of codes) or even ten years' if he/she is responsible for interpreting the results of system analyses relevant to the licensing process.

Validation

Validation is a process for accessing the accuracy of a physical model in a SYSTH code based on comparisons between computational simulations and experimental data. In a broad sense, the validation is performed to provide confidence in the ability of a code to predict the values of the safety parameter or parameters of interest realistically or conservatively. The process can also quantify the accuracy. The results of a validation can be used to determine the uncertainty of some constitutive laws of the code. The validation can be conducted by the code developers and/or by the code users. The former is called a developmental assessment and the latter an independent assessment.

Validation matrix (code, user, specific system and application)

Validation matrix is a set of selected experimental data for the purpose of carrying out extensive and systematical validation of a code. The validation matrix usually includes (i) basic tests, (ii) separate effect tests, (iii) integral effect tests and (iv) nuclear power plant data. Various validation matrices can be established by code developers and/or code users for their own purposes.

Verification

Verification is a process to assess the software's correctness and the numerical accuracy of the solution to a given physical model defined by a set of equations. In a broad sense, the verification is performed to demonstrate that the design of the code numerical algorithms conforms to the design requirements, that the source code conforms to programming standards and language standards, and that its logic is consistent with the design specifications. The verification is usually conducted by the code developers and, sometimes, independent verification is performed by the code users.

Versatility (of a numerical scheme)

Versatility is the ability to simulate all physical conditions that need to be modelled to meet the code's requirements. The versatility of system codes should cover the domain of safety analyses of a nuclear power plant.

Water-packing

Water-packing is related to predicting pressure spikes that are not related to known physical phenomena. These fictitious pressure spikes are sometimes calculated when steam or even gas is disappearing from, and water is about to fill, a control volume.

Well posed problem

According to Hadamar, a problem is well posed when a solution exists, is unique, and depends continuously on the initial condition values. A problem in thermal hydraulics is defined by a set of PDE and initial and boundary conditions. A heat conduction equation with specified initial conditions to predict future temperature fields is well posed. However, the inverse problem of predicting the past temperature field from final temperatures is ill-posed because the solution is highly sensitive to small changes in final data.

The hyperbolicity is a condition of the well-posedness for fluid dynamic equations. A system of equation is hyperbolic when all eigenvalues (solutions of the characteristic equation) are real.

Annex A. Synthesis of the answers to the questionnaire

Table A.1. Geometries simulated with 3D capabilities

Organisation	TH code	3D	Applications of 3D capabilities Components					
			Core	PV	SG	Cold Leg	HL	Others
AREVA	CATHARE-2	Y	Y	Y	N	N	N	DC
Bel V	CATHARE-2	Y	Y	Y	Y	N	N	N
CEA_1	CATHARE-2 and CATHARE-3	Y	Y	Y	Possible and contemplated	Used for some particular analyses of PTS	N	N
CEA_2	CATHARE-2 and CATHARE-3	Y	Y	Y	Y	N	N	N
CNSC	CATHENA	Y	Y	N	N	N	N	N
EDF	CATHARE-2 and THYC V5	Y	Y	N	N	N	N	N
ENEA	CATHARE-2 and TRACE V5.0	Y	N	Y	N	N	N	Y Containment in SMR, pool (RWST) in advanced passive reactor
GRS_1	ATHLET 3.1A	Y	Y	Y	N	N	N	Y (Emergency condenser, passive auxiliary feedwater system)
GRS_2	ATHLET 3.1A	Y	N	Y	N	N	N	Y (Pools of passive safety systems)
Westinghouse	WCOBRA/ TRAC-TF2 WCOBRA/TRAC	Y	Y	Y	N	N	N	N
KAERI	SPACE 1.6 MARS-KS 1.3	Y	Y	Y	N	N	N	N
KINS	MARS-KS 1.3	Y	Y	Y	N	N	N	N
NINE	RELAP5-3D	Y	Y	Y	N	N		Moderator tank in PHWR, Pool, Downcomer
NRA	TRACE5.0	Y	Y	Y	N	N	N	N

Table A.2. Transients simulated with 3D capabilities

Organisation	TH code		Applications of 3D capabilities Transients				
		LB- LOCA	IB-LOCA	SGTR	SLB	Boron dilution transient	Other situations
AREVA	CATHARE-2	Y	Y	N	N	N	N
Bel V	CATHARE-2	N	N	N	N	N	Y
CEA_1	CATHARE-2 and CATHARE-3	Y	Y	If necessary in future	Y (in future)	Y (in future)	N
CEA_2	CATHARE-2 and CATHARE-3	Y	Y	N	Y	N	Y
CNSC	CATHENA	N	N	N	N	N	Y
EDF	CATHARE-2 and THYC V5	N	Y	N	Y	N	N
ENEA	CATHARE-2 and TRACE V5.0	N	Y	N	Y	Y	Y (SB-LOCA, SBO)
GRS_1	ATHLET 3.1A	Y	Y	N	N	Y	Y (SBO)
GRS_2	ATHLET 3.1A	Y	N	N	Y	N	N
Westinghouse	WCOBRA/ TRAC-TF2 WCOBRA/TRAC	Y	Y	N	N	N	DNBR analysis for transient accidents
KAERI	SPACE 1.6 MARS-KS 1.3	Y	Y	N	N	Y	N
KINS	MARS-KS 1.3	Y	Y	N	N	Y	N
NINE	RELAP5-3D	Y	Y	N	N	Y	CR ejection, protected loss of flow
NRA	TRACE5.0	Y	Y	N	N	N	N

Table A.3. Simulations performed with 3D capabilities

Organisation	TH code	Note				
AREVA	CATHARE-2	Plant types: PWR	<u>Validation:</u>	Analytical tests → partial	Separate-effect tests → expanded	Integral effect tests → expanded
Bel V	CATHARE-2	Plant types: PWR	<u>Validation:</u>	Analytical tests → none	Separate-effect tests → expanded	Integral effect tests → partial
CEA_1	CATHARE-2 and CATHARE-3	It uses a 3D modelling in porous medium and has not models for an extension to CFD in open medium (no wall function, no general turbulence modelling,...).				
CEA_2	CATHARE-2 and CATHARE-3	Analytical tests → partial	Separate-effect tests → partial	Integral effect tests → partial	Proposal of new development: Theoretical physical models: Diffusion/dispersion terms, friction terms in rod bundles	
CNSC	CATHENA	System code (TUF, CATHENA, CAMP codes)		Others (GOTHIC, COMSOL)	Plant types: CANDU, Research Reactors	<u>Validation:</u> none
EDF	CATHARE-2 and THYC V5	Plant types: PWR	<u>Validation:</u>	Analytical tests → partial	Separate-effect tests → partial	Integral effect tests → partial
ENEA	CATHARE-2 and TRACE V5.0	Plant types: Advanced passive small modular reactor; plant application				<u>Validation:</u> Integral effect tests
GRS_1	ATHLET 3.1A	Plant types: PWR/BWR/VVER	<u>Validation:</u>	Analytical tests → partial	Separate-effect tests → expanded	Integral effect tests → expanded
GRS_2	ATHLET 3.1A	Plant types: Test facilities	Validation based on separate effect tests, research	Analytical tests → partial	Separate-effect tests → expanded	Integral effect tests → expanded
Westinghouse	WCOBRA/TRAC-TF2 WCOBRA/TRAC	There is simplification from N-S equation, for example, diffusion term, and further simplification to a subchannel model for reactor core thermal-hydraulic analysis.		Plant types: PWR (Westinghouse 2-loop, 3loop, and 4loop plants) PWR with passive safety design, AP1000/SMR	Validation: Analytical tests: expanded: Manometer problem, steam expulsion tests, boil-off test, Faraday way test. Separate-effect tests: expanded: large break LOCA, UPTF tests 6, 8, 25, 29. Integral effect tests: expanded: CCTF IETs, ROSA/LSTF IETs	
KAERI	SPACE 1.6 MARS-KS 1.3	Both simplification (based on 1D flow regime map and physical models, etc.) and restriction (not applicable for large pool).		Plant types: PWR 3D module is not fully validated	Validation: Analytical tests: partial separate-effect tests: partial integral effect tests: none for SPACE, partial for MARS-KS	Proposal of new development: Theoretical physical models: flow regime map (annular, stratification), physical models for pressure drop. Experiments in 3D conditions: bundle region, downcomer, etc.
KINS	MARS-KS 1.3	Both Simplification (based on 1D flow regime map and physical models, etc.) and restriction (not applicable for large pool).		Not validated		
NINE	RELAP5-3D	No open tanks, simplified turbulence model, limited number of volume subdivision in one direction (<9).		Plant types: PWR, BWR, PHWR, CANDU, SFR, ITF Research Reactors	Validation: Analytical tests: Yes, as in the code manual Separate-effect tests: UPTF downcomer refill tests, UPTF-Upper Plenum tests, BFBT, ROCOM Integral Effect Tests: LOFT, EBR	
NRA	TRACE5.0	Plant types: PWR, BWR, Spent fuel pool, etc.	The above classification is based on analyses for PWR. 3D TH codes are also used for analyses of Anticipated Operational Occurrence (AOO), Reactivity Initiated Accident (RIA) and Anticipated Transient without scram (ATWS) for BWR.			